Investigation of combustion instabilities in annular combustors combining injector dynamics and flame describing functions in simplified configurations

Preethi Rajendram Soundararajan

université PARIS-SACLAY

Investigation of combustion instabilities in annular combustors combining injector dynamics and flame describing functions determined in simplified configurations

Etude des instabilités de combustion dans les foyers annulaires en considérant la dynamique des injecteurs et les fonctions descriptives des flammes déterminées dans des configurations simplifiées

Thèse de doctorat de l'université Paris-Saclay

École doctorale n° 579, Sciences mécaniques et énergétiques, matériaux et géosciences (SMEMaG)
Spécialité de doctorat : Combustion
Graduate School : Sciences de l'ingénierie et des systèmes.
Référent : CentraleSupélec

Thèse préparée dans l'unité de recherche du Laboratoire EM2C (Université Paris-Saclay, CNRS, CentraleSupélec)
sous la direction de Sébastien Candel, Professeur des université émérite et le co-encadrement de Antoine Renaud, Maître de conférences et Daniel Durox, Ingénieur de recherche

Thèse soutenue à Gif-Sur-Yvette, le 07 July 2022, par

Preethi RAJENDRAM SOUNDARARAJAN

Composition du jury

James Dawson Professor, Norwegian University of Science and Technology	Président
Thierry Poinsot Research director, CNRS, Université de Toulouse, IMFT	Rapporteur
Nicolas Noiray Associate professor, ETH Zürich	Rapporteur
Françoise Baillot Professor, Université de Rouen	Examinatrice
R. I. Sujith Professor, Indian Institute of Technology, Madras	Examinateur
Christian Oliver Paschereit Professor, TU Berlin	Invité
Sébastien Candel Professeur des université émérite, CentraleSupélec, Université Paris-Saclay	Directeur de thèse
Antoine Renaud Maître de conférences, CentraleSupélec, Université Paris-Saclay	Co-encadrant
Daniel Durox Ingénieur de recherche, Consultant	Co-encadrant

THESE DE DOCTORAT
NNT : 2022UPAST090

Abstract

This thesis addresses some of the central issues in the combustion dynamics of annular systems, essentially focusing on understanding, interpreting, and predicting combustion instabilities coupled with azimuthal modes. These modes are the most detrimental among those encountered in gas turbines and aero-engines as they correspond to the lowest eigenfrequencies where the flame is most sensitive to incoming disturbances. The work specifically considers the case where the flames established in the combustor are formed by a spray of liquid fuel and on injection systems generating a swirling flow, idealizing those found in practical applications. Systematic experiments are carried out on a multiple-injector annular combustor (MICCA-Spray), allowing full optical access to the combustion region and equipped with multiple microphones for identifying the pressure field. These are complemented with measurements of flame describing functions (FDFs) using a single-sector combustor (SICCA-Spray) and another facility featuring an array of three injectors (TICCA-Spray) to better represent the flame environment and boundary conditions corresponding to the annular case. This combination of experiments is used to explore the effects of injection geometry and operating parameters on the occurrence of combustion instabilities. The domains of instability are documented for three fuel types (premixed propane and air, heptane and dodecane) and different values of injector head loss and swirl number. In addition, the instabilities are also found to be sensitive to the location of the atomizer with respect to the injector outlet. Several questions are considered in this work, including the possibility of representing the response of a multi-dimensional flame using the FDF framework and methods to suitably determine FDFs for the class of injectors used, which are weakly transparent to acoustic waves. The comparison between measured FDFs in the single sector and the linear array of three injectors is used to reveal the limitations of data corresponding to an isolated flame in representing the dynamics of flames surrounded by neighboring flames. The data interpretation based on low-order modeling indicates that many of the features observed experimentally can be predicted by making use of measured FDFs. This, however, requires that the swirling injectors be suitably represented by an injector impedance and that the damping rate be estimated. The analysis underlines the importance of the swirling injector parameters and injection conditions on the

occurrence of combustion instability and provides guidelines in sorting out their influence.

Résumé

Cette thèse aborde des questions centrales de la dynamique de la combustion des systèmes annulaires, en se concentrant essentiellement sur la compréhension, l'interprétation et la prédiction des instabilités de combustion couplées aux modes azimutaux. Ces modes sont les plus dangereux parmi ceux rencontrés dans les turbines à gaz et les moteurs d'avion car ils correspondent aux fréquences propres les plus basses où la combustion est la plus sensible aux perturbations auxquelles elle est soumise. Le travail considère spécifiquement le cas où les flammes établies dans la chambre de combustion sont formées par une atomisation du combustible liquide et sur les systèmes d'injection générant un écoulement «swirlé», en rotation idéalisant ceux des applications pratiques. Des expériences systématiques sont réalisées sur une chambre de combustion annulaire comportant des injecteurs multiples (MICCA-Spray), permettant un accès optique complet à la région de combustion et équipée de plusieurs microphones pour identifier le champ de pression. Ces expériences sont complétées par des mesures des fonctions descriptives de flamme (FDF) à l'aide d'une chambre de combustion à secteur unique (SICCA-Spray) et d'une autre installation comportant un réseau linéaire de trois injecteurs (TICCA-Spray) pour mieux représenter l'environnement de la flamme et les conditions aux limites correspondant à la configuration annulaire. Cette combinaison d'expériences permet d'explorer les effets de la géométrie d'injection et des paramètres de fonctionnement sur l'apparition d'instabilités de combustion. Les domaines d'instabilité sont documentés pour trois types de combustible (propane et air prémélangés, heptane et dodécane) et différentes valeurs de perte de charge d'injecteur et de nombre de swirl. De plus, les instabilités se révèlent également sensibles à la position de l'atomiseur par rapport à la sortie de l'injecteur. Plusieurs questions sont envisagées dans ce travail, dont la possibilité de représenter la réponse d'une flamme multidimensionnelle à l'aide d'une représentation par FDF et des méthodes permettant de déterminer convenablement les FDF pour la classe d'injecteurs utilisés, qui sont faiblement transparents aux ondes acoustiques. La comparaison entre les FDF mesurées dans le secteur unique et le réseau linéaire de trois injecteurs est réalisée pour révéler les limites des données obtenues dans le cas d'une flamme isolée dans la représentation de la dynamique de flammes entourées par d'autres flammes. L'interprétation des données basée sur la modélisation d'ordre réduit indique que beaucoup des caractéristiques observées ex-

périmentalement peuvent être prédites en utilisant les FDF mesurées. Ceci nécessite cependant que les injecteurs swirlés soient convenablement représentés par une impédance d'injecteur et que le taux d'amortissement du système soit estimé. L'analyse souligne l'importance des paramètres de l'injecteur swirlé et des conditions d'injection sur l'apparition de l'instabilité de combustion et fournit des lignes directrices pour cerner leur influence.

Contents

General introduction

1 Introduction

The phenomenon of combustion instabilities raises a wide variety of fundamental questions and gives rise to many practical problems during the development and operation of combustion systems. This dynamical phenomena arise in high-performance devices like aircraft engines, gas turbines, liquid rocket thrust chambers, in lower power devices like domestic or industrial boilers, matrix burners used in various processes, and in a wide variety of other practical configurations (Candel 2002; Lieuwen and Yang 2005b). Combustion dynamics and instabilities, therefore, constitute one of the central issues in combustion research and application. Historically, high-pressure oscillations were encountered in the developmental stages of several early rocket programs (Oefelein and Yang 1993; Culick and Yang 1995). These instabilities pose serious problems, leading to undesirable consequences, including intense noise and vibrations, excessive heat loads to the combustor walls, flashback, blow-off, and in some cases, they may even lead to spectacular failures (Huang and Yang 2009). This focused the attention of engineers and scientists leading to considerable research and development efforts aimed at understanding and avoiding combustion instabilities and their consequences. Significant work has been performed to derive predictive tools and control techniques for the suppression of these instabilities. There are, however, difficult issues that still need to be resolved since combustion instabilities occur as a result of a complex coupling between flow, combustion, and acoustics. Unsteady combustion generates acoustic waves, and when this happens in a resonant environment, it may induce flow perturbations. Through intermediary mechanisms, this further leads to heat release rate disturbances, which under certain conditions, may grow, making the system unstable. This situation is often encountered in modern gas turbine engines operating in lean premixed regimes to reduce NO_x emissions. In these devices, the flames are aerodynamically anchored by swirling injectors, producing compact combustion regions with relatively high power densities in a low damping environment. The flames are receptive to resonant coupling, eventually leading to combustion instabilities (Candel 2002; Poinsot 2017). As solutions to such problems are not easy to develop, they may induce painstak-

ing engineering modifications, and costly trial-and-error testing (Poinsot 2017). With the aviation industry swiftly transitioning toward low-carbon combustion, the need to understand these instabilities with newer fuels has become all the more important (Beita et al. 2021). Although laboratory-scale studies have focused on simpler conditions where only the combustion chamber is considered, these studies have brought in several insights in the past years, greatly advancing the existing knowledge on instabilities. One important advance in this field has been made in experimentation with the development of lab-scale annular combustors, comprising multiple injectors (Worth and Dawson 2013b; Dawson and Worth 2014; Bourgouin et al. 2015a; Prieur et al. 2017) studying turbulent flames (Bourgouin et al. 2013) and spray combustion (Prieur et al. 2018; Rajendram Soundararajan et al. 2021). The annular geometry has allowed studies of instabilities coupled by azimuthal modes, which are the most dangerous in practical systems. These azimuthal instabilities occur at frequencies that fall in the range where flames are most sensitive to disturbances. Azimuthal coupling is also a serious issue because the corresponding modes are less well-damped. Work on annular combustor dynamics at the EM2C laboratory has been supported by Safran, underlining the industrial interest in this kind of research. This has led to the thesis of Bourgouin (2014) and Prieur (2017). Further work was carried out by Vignat (2020) with support from Safran and the European network ANNULIGhT. As a continuation of such efforts, the present investigation is meant to contribute to this domain by providing new data and model developments that are essentially focused on understanding, interpreting, and predicting combustion instabilities coupled by azimuthal modes. These types of instabilities are of special interest because they arise combustors having annular geometries such as in aircraft engines or gas turbines. The annular geometry is because the combustor is placed around the engine shafts connecting the fan, low and high-pressure compressor stages to the low and high-pressure turbine stages. It is clearly essential to advance the understanding of the coupling between combustion and acoustics, and take into account the azimuthal structure of the coupling modes. This work is focused on flames formed by sprays of liquid fuel droplets and on injectors defining a swirling flow. These choices are made to align with aircraft engines that use liquid fuel (typically kerosene or the future sustainable aviation fuels), introduced as a spray in the combustor with swirling injectors. Of course, it is not possible to use injectors having a complex geometry similar to those found in real systems. It is preferable to idealize the injector configuration, and define a family of swirlers in which some simple geometrical variations can be made to change the head loss and swirl number. This will allow sorting out the main effects without dealing with the complexities that are inherent to real units.

The available research on combustion instability is quite substantial, and significant advances have been made in this field; however, the capacity to carry out experiments in an annular configuration comprising multiple injectors and to do

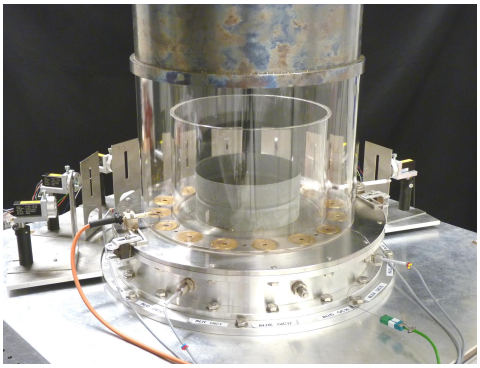

(a) MICCA-Spray

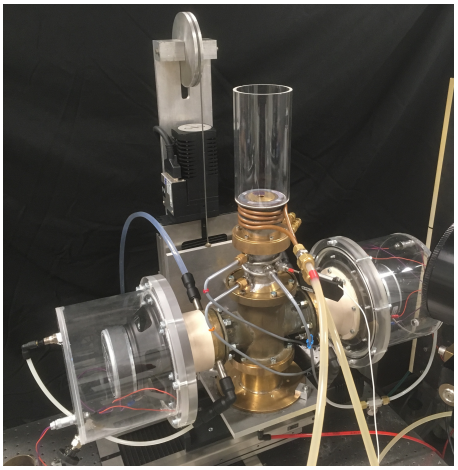

(b) SICCA-Spray

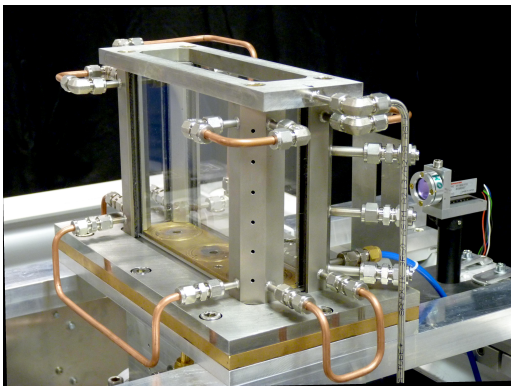

(c) TICCA-Spray

Figure 1. *Photograph of the three experimental test rigs used in the present work.*

so with multiple diagnostics including pressure sensors, photomultipliers arrays, intensified cameras allowing high-speed imaging is more recent. There are now a few test rigs that comprise annular chambers with transparent walls allowing optical access to the combustion region. One of the systems designed at an early stage which has been operating for nearly ten years, is the MICCA annular combustor. This facility, conceived at the EM2C laboratory in the framework of a research project supported by the French national research agency (ANR), has been used extensively to characterize instabilities coupled by azimuthal modes. The initial version of MICCA, developed during the thesis of Bourgouin (2014), was equipped with a system of swirling injectors using a blade row to impart an azimuthal rotation to the flow. These swirling injectors were then replaced by matrix injectors forming small conical laminar flames (Bourgouin et al. 2015b). The combustor was later modified to operate with liquid fuels injected as a spray, with the new version named as MICCA-Spray (photograph shown in Fig. 1 (a)), during the thesis of Prieur (2017) and was further improved in the thesis of Vignat (2020). Following this train of research efforts, the present investigation uses the MICCA-Spray version in the context of studying combustion instabilities. MICCA has also

allowed investigations of the light-round process that takes place when the ignition is obtained with a spark plug, and the initial flame propagates from the initial kernel and travels from injector to injector, eventually leading to the initiation of a flame in all the injectors (Bourgouin et al. 2013; Philip et al. 2015; Prieur et al. 2017). During the same period, another facility was developed independently by the group of James Dawson at the University of Cambridge (Worth and Dawson 2013b; Worth and Dawson 2013a; Dawson and Worth 2014). Dawson's group, including Nicolas Worth, later moved to NTNU in Norway and continued work on annular combustion systems (Indlekofer et al. 2021; Indlekofer et al. 2021; Mazur et al. 2021; Ahn et al. 2021). There are now other such configurations at different research labs around the world (Zhong et al. 2021; Fang et al. 2021; Roy et al. 2021; Singh et al. 2021), and some of them are inspired by the MICCA design. Efforts were also focused in parallel on performing numerical simulations of annular combustors with some pioneering work using large eddy simulations (LES) at CERFACS by Poinsot and his co-workers (Staffelbach et al. 2009; Wolf et al. 2009; Wolf et al. 2012). In addition, there has also been a number of theoretical studies carried out on annular combustors studying azimuthal modes (Morgans and Stow 2007; Parmentier et al. 2012; Ghirardo and Juniper 2013; Noiray and Schuermans 2013; Bauerheim et al. 2015; Ghirardo et al. 2016; Magri et al. 2016). Other notable works include that of Pankiewitz and Sattelmayer (2003), Blimbaum et al. (2012), with certain studies focusing on network modeling approaches (Kopitz et al. 2005; Bellucci et al. 2005) along with some analyses carried out on real engines (Bothien et al. 2015).

One of the original aspects of research carried out at EM2C has been to establish a dialog between experiments carried out in the multiple-injector annular combustor MICCA-Spray and a single-injector test facility designated as SICCA-Spray (photograph shown in Fig. 1 (b)). The central idea of this dialog is that one could obtain important information on the flame response in a single-injector configuration, in particular, determine the flame describing function, and use this knowledge to guide the experiments in the more complex annular system. This strategy shown in Fig. 2 has been exploited quite effectively, producing meaningful results (Prieur 2017; Vignat 2020), and is pursued in the present investigation. However, one is led to ask whether a configuration comprising an isolated flame placed in a cylindrical chamber like that of SICCA-Spray is representative of the situation that prevails when each flame is surrounded by adjacent flames and is facing an inner and outer wall on the lateral side, as in the case of MICCA-Spray. This leads to the idea that an array of three injectors could perhaps constitute an improved representation of the full annular geometry. This geometry is adopted in the newly developed TICCA-Spray combustor (photograph shown in Fig. 1 (c)), a recent addition to the combustion dynamics experimental platform at EM2C. The TICCA-Spray test rig consists of a linear array of three injectors with important geometrical parameters such as inter-injector distance and injector-to-backplane

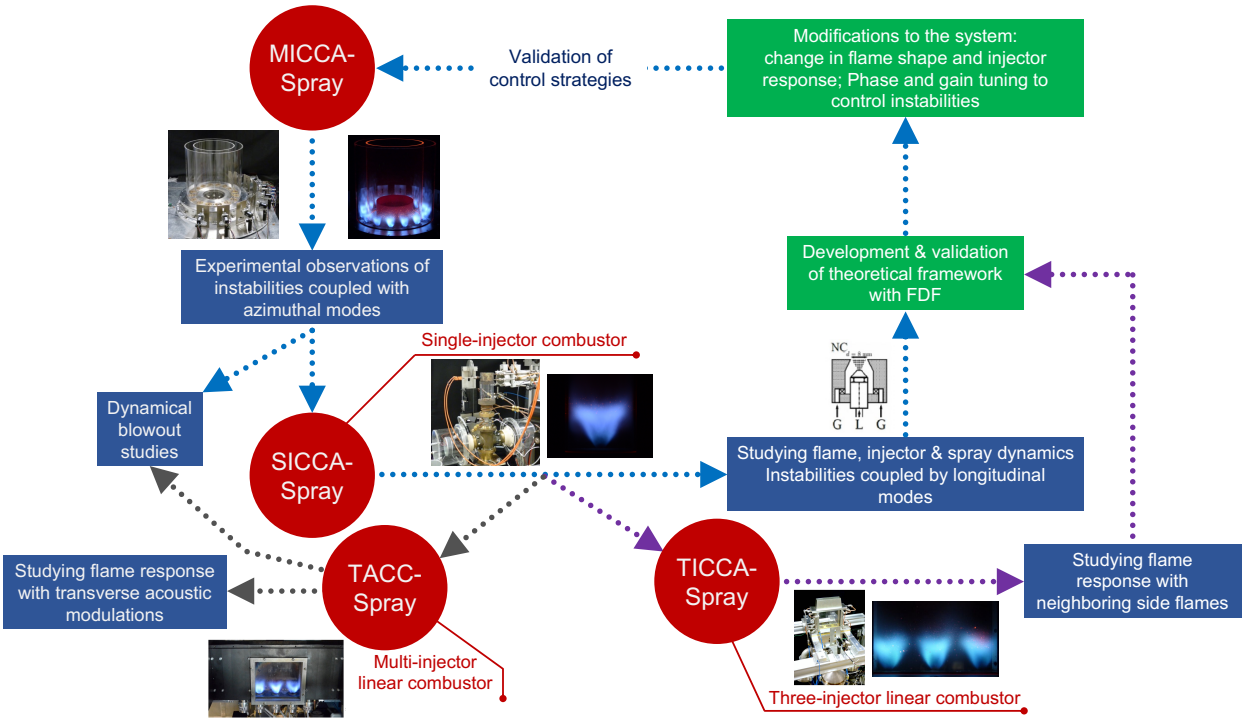

Figure 2. *Experimental methodology adopted in the present work. The MICCA-Spray annular is studied in a closed-loop framework consisting of investigations carried out in the single-injector combustor SICCA-Spray and three-injector linear combustor TICCA-Spray present at the EM2C laboratory. In addition, a complementary test rig located at the CORIA laboratory, namely TACC-Spray, with the facility to conduct transverse acoustic excitation, is also encompassed in the context of ANR project FASMIC, but these results are not elaborated in this thesis. Image of TACC-Spray adapted from Patat et al. (2021).*

surface area ratio, being the same as that of the annular combustor, allowing to reproduce the same environment as MICCA-Spray for the central flame. The three experimental setups are used in this work in a comprehensive framework (shown in Fig. 2) to understand the nature of combustion instabilities, the role of injection units in the processes leading to instabilities, and develop simplified tools and techniques for instability prediction and control. Although TICCA-Spray closely resembles the annular combustor, it only allows axial modulation of the flames using a set of driver units and does not include the capacity to modulate the flames in the transverse direction, like in the case of an annular combustor undergoing azimuthal instabilities. This is possible in another facility, designated as TACC-Spray, operated at CORIA laboratory by the team of Françoise Baillot. The TACC-Spray facility comprises five injectors, out of which three injectors operate with flames, and is equipped with system allowing high-amplitude transverse excitation of the flames. The injectors used in TACC setup are copies of the injectors used at EM2C for the three test rigs —MICCA, SICCA and TICCA. A collabo-

ration between CORIA and EM2C carried out in the framework of the FASMIC project supported by ANR has allowed fruitful exchanges between the two groups on special issues, including the determination of injector impedance and analysis of flame extinction by large amplitude oscillations, a process designated as dynamical blow out. The results from this configuration are, however, not discussed in this thesis.

The present research effort thus integrates systematic experimentation using three test facilities combined with low-order modeling in which the flame response is represented in terms of its describing function. The work will include, in essence, the following aspects.

- The MICCA-Spray annular combustor equipped with sixteen swirling injectors will be used to examine instabilities coupled by azimuthal modes. MICCA is a versatile annular test combustor allowing optical access to the flames and acoustic identification of modal structures in the plenum and chamber. This combustor has a flexible design and can be fitted with a variety of injectors. Investigations have been carried out with a broad set of swirlers allowing a detailed examination of effects related to the swirl number and injector head loss. In the current setup of MICCA-Spray, fuel is mainly injected as a spray through pressure atomizers, but it also has the facility to operate in premixed mode. This unique experimental configuration allows investigations of dynamical phenomena and, more specifically, of self-sustained thermoacoustic oscillations coupled by azimuthal modes, which in reality are the most dangerous. Using modal identification, it is possible to distinguish spinning, standing, or mixed modes that can be characterized by the spin ratio.

- The SICCA-Spray cylindrical test rig comprises a single injector that is geometrically identical to those used in MICCA-Spray, and it will be used to examine flame dynamics. This setup is equipped with driver units and different acoustic and optical diagnostic tools to analyze the forced flame response to longitudinal acoustic perturbations or examine the longitudinal self-sustained oscillations obtained by changing the combustor size. This setup is operated with a variety of swirlers and different fuels, particularly, the liquid fuels heptane and dodecane and premixed propane. Flame describing functions (FDFs) are conveniently obtained in this configuration. Any change, such as modifying the flame or injector geometry, tuning the gain and phase of FDF, etc., as a means of instability control is first tested in this simpler setup and later validated in the annular combustor.

- FDFs will also be determined in TICCA-Spray, a new facility comprising three injectors such that the central flame is surrounded by two side flames, a situation that is close to that found at a pressure antinode in the annular sys-

tem. The FDFs from TICCA-Spray will be compared with those measured in the single-injector configuration featuring an isolated flame.

At this stage, it is worth listing the questions of interest that will be investigated in this research:

- One of the central themes of the current effort will be to examine the **influence of the injector unit** on azimuthal instabilities. This study initiated in the thesis of Guillaume Vignat (Vignat 2020) with the development of different injector units is systematically pursued here. These injectors notably differ from the previous ones used in the MICCA combustor and are named in this work as "acoustically weakly transparent" in accordance with their response to acoustic waves. It is, in particular, interesting to quantify the effects associated with the injector swirl number and pressure loss and see how these parameters influence the development of instabilities. The injector impact will be investigated in the three test rigs: MICCA-Spray, SICCA-Spray and TICCA-Spray. A special study will also concern the effect of the location of the spray atomizer with respect to the injector outlet. This will be considered in a configuration of SICCA-Spray, where the atomizer position is continuously varied.

- One important item in combustion instability analysis is to quantify the **influence of the fuel** that is being used and of the combustion mode. For this, a situation is considered where the fuel (propane) and oxidizer (air) are fully premixed, a second case where fuel (heptane) is injected as a spray and is highly volatile and convected into the chamber by the air stream, and a third situation where fuel (dodecane) is also injected as a spray but is much less volatile. From this comparison, one expects to find how the vaporization delay affects the development of instabilities.

- Another item that is of fundamental nature is to ask if it is possible to **represent the dynamics of a multi-dimensional combustion process with an FDF** relating an input, typically the incident volume flow rate fluctuations, and an output, namely the heat release rate fluctuations. Such input/output descriptions are typically found in the control system domain. "Black box" transfer function and describing functions have been used extensively in the combustion instability and control literature. However, the basic question is worth investigating. This is accomplished by experimentally comparing a situation where the flame is acoustically modulated and where the flame is coupled with acoustics, and self-sustained oscillations are produced. It is then possible to see whether the FDF does represent the flame response when the system features self-sustained oscillations.

- The experimental results gathered from the various configurations form a

database that can guide modeling. This is used to see if the **low-order model derived in the present work can identify regimes of instability**. It is shown that this requires a suitable representation of the injector response and that this can be conveniently achieved by assigning an impedance to the injector outlet. In turn, this impedance has to be measured or modeled or may be inferred from a combination of measurements and modeling. The model that combines experimentally determined FDFs, injector impedance information and estimated damping rates is then used to predict the occurrence of unstable oscillations and these predictions are compared with experimental observations.

- One question encountered during this research pertains to the **determination of the FDF** itself. In most experiments, where fuel and oxidizer are premixed and the flames have a simple structure, this determination is based on a direct method in which the relative heat release rate fluctuation is measured together with the relative velocity fluctuation. The ratio of these two quantities is then calculated to determine the value of the FDF. This is repeated for the frequency range of interest and for a set of input amplitude levels. Such determination is adequate in the case of laminar conical flames or inverted "V" flames or in the case of multiple conical flames formed by a matrix injector unit. The velocity disturbance is generally determined upstream of the flame where its spatial distribution is uniform or approximately uniform. When the flame is more complex, and the velocity profile on the upstream side of the flame is non-uniform, such as for flames formed by swirling injectors that are acoustically weakly transparent, it is not straightforward to define a suitable point for measuring the relative velocity disturbance. Of course, it is possible to measure the velocity on the upstream side of the injector before the swirler, where the velocity and velocity fluctuation profiles are uniform. However, this provides a describing function that combines the injector dynamics with the flame response. It is then necessary to account for the injector transfer function to extract the FDF, but this raises further issues which are discussed in this thesis. Another method that has been used quite extensively is to determine a flame transfer matrix (FTM). This is generally accomplished by placing an array of microphones on both sides of the injector and flame and exciting the system from upstream and downstream. The multi-microphone method is then used to determine the transfer matrix. To obtain the transfer function from this method, one needs to extract the flame transfer matrix from the combined injector and flame transfer matrix, but this raises the additional issue of determining the injector transfer matrix. In the present investigation, a direct FDF determination is opted for, which relies on the measurement of the relative velocity fluctuation at a point where these relative fluctuations are equal to the relative volumetric fluctuation rate.

2 Thesis structure and organization

This thesis is based on research carried out at the EM2C, CNRS laboratory. Much of this work has been supported by two research networks:

- ANNULIGhT, a European research network associating ten different research groups working on the problem of combustion instabilities and ignition dynamics of annular combustors coordinated by Prof. James Dawson from NTNU.

- FASMIC, a network formed by CORIA, EM2C and CERFACS in the framework of an ANR research contract dealing with flame-acoustic coupling in swirling two-phase flames coordinated by Prof. Françoise Baillot from CORIA.

Most of the material contained in the following pages has been published in the form of articles or as conference proceedings. The author has also participated in research efforts that have resulted in publications but are not included in what follows. Publications that constitute a particular chapter are mentioned at the beginning of that chapter. A consolidated list of all the publications is provided at the end of the present chapter. The thesis is written such that each chapter can mostly be read as a standalone work without much need for referring to other chapters. This naturally results in certain overlaps and repetitions between several chapters, which might be redundant for a reader glancing through the entire thesis. For such readers, possible repetitions are mentioned at the beginning of each chapter so that they may skip through them. Each chapter also includes a detailed literature survey and motivation in addition to the broad and short overview of combustion instabilities provided in this chapter. In addition, appendices are provided at the end of most chapters to provide supplementary information on the subject of a particular chapter.

The organization of this document, graphically shown in Fig. 3, is described below.

- The first part of this thesis deals with the description of experiments and modeling framework. In the first chapter, a detailed description of the different experimental setups is provided, along with information on instrumentation and diagnostics used for the various measurements. An emphasis is provided in the second chapter of this part concerning the chemiluminescence emission and its validation for the spray flames considered here. A comparison of the present spray flames is made with that of premixed flames by measuring the equivalence ratio fluctuations using the ratio of CH^* and

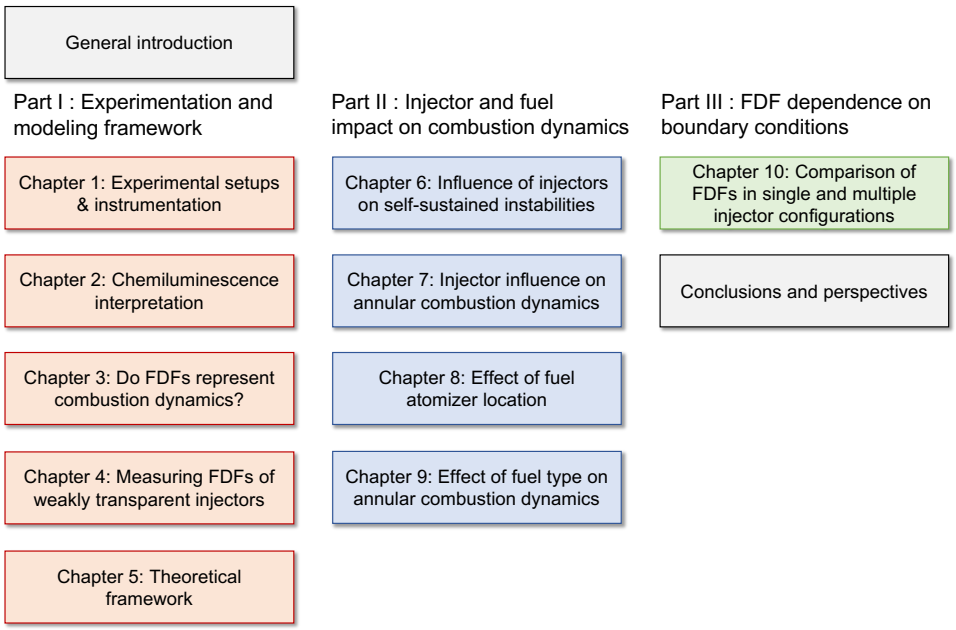

Figure 3. *Organization of the thesis.*

OH^* radicals. It is found that the spatial and temporal equivalence ratio fluctuations exhibited by these specific spray flames are negligible compared to the velocity fluctuations due to the specific location of the fuel atomizer inside the injector. The results from this chapter are exploited in the measurement of FDFs discussed in the subsequent chapters. The third chapter is concerned with the role of FDFs. Experiments are carried out to validate the use of FDFs in representing the complex dynamical response of swirl-spray flame undergoing self-sustained oscillations. Although several studies have successfully exploited FDFs in low-order models, it is believed that a direct experimental validation has never been provided. After this verification, the next chapter firstly describes the peculiar nature of the injectors studied here and, eventually, the experimental methodology that needs to be adopted for deducing the FDFs of such injectors. The specific injectors considered here feature a high pressure drop value, acting as an acoustic loss element, thus leading to their designation as "acoustically weakly transparent". The final chapter of this part deals with a theoretical framework combining the flame response, in terms of FDF, and injector response, in terms of an impedance imposed at the outlet, to analyze the linear stability of a combustor system equipped with an injector that is weakly transparent to acoustic waves.

- The second part of this thesis deals with the influence of the injector and fuel on self-sustained combustion instabilities. The first two chapters in this part primarily discuss the effect of varying the swirl number and pressure drop on instabilities. The first chapter discusses this using the single-injector combustor SICCA-Spray featuring longitudinal instabilities and considers the

theoretical framework used in Part I to predict instabilities. The theoretical framework provides the growth rates and oscillation frequencies that are compared with the amplitude and frequency of instabilities from the experiments while also accounting for the measured damping rate of the system. The next chapter deals with experiments carried out in MICCA-Spray with different swirling injectors to identify their effect on azimuthal instabilities. The stability maps obtained with the different swirlers are discussed, and a simple analysis using the FDFs obtained from SICCA-Spray is examined. The third chapter of this part deals with the effect of atomizer position on combustion instabilities in the SICCA-Spray combustor. By varying the atomizer position with respect to the injector backplane, a change in the stability behavior is observed. Changing the atomizer position modifies the spray-wall interaction mechanism, resulting in a change in the spatial dispersion of the droplets and possibly their convection time. The above chapters included in this part could together constitute an interesting test case in the development of instability prediction tools and may serve in devising techniques for instability suppression. The final chapter of this part deals with the effect of fuel type or, alternatively, time lag on combustion instabilities in the MICCA-Spray annular combustor. Liquid fuels heptane and dodecane are used along with the reference case of premixed propane to determine the stability map of the combustor. A subsequent analysis is also carried out on the SICCA-Spray combustor to identify the effect of fuels on the FDFs.

- The third and final part of this thesis deals with the experiments carried out in the newly developed three-injector linear combustor TICCA-Spray, which more closely resembles the environment of a flame in the MICCA-Spray annular combustor. In a first-of-its-kind study, FDFs measured in an isolated flame formed by the single-injector SICCA-Spray combustor are compared to those corresponding to a flame surrounded by neighboring side flames to identify the effect of lateral boundary conditions on the flame response.

Finally, several appendices are provided at the end of this document that includes results not reported in other chapters but would serve as a reference for future studies. Appendix A provides a note on the comparison of a transfer function obtained with an acoustic method and a transfer function obtained directly using OH^* chemiluminescence approximated to heat release rate fluctuations. Appendices B and C provide a database of FDFs and flame images measured with different swirlers. In addition, Appendix D provides cold flow damping rates and stability map of other swirlers in SICCA-Spray not reported in the main text. The following appendix (Appendix E) reports the low frequency FDFs at different atomizer positions. Appendix F includes a comparison between large eddy simulations that were carried out using the AVBP code during a secondment with CERFACS. This simulation effort is a continuity of the work of Guillaume Vignat, and

a validation for the steady flame is provided by comparing it with experiments.

Publications

List of publications that are part of this thesis:

- *Effect of different fuels on combustion instabilities in an annular combustor*
  P. Rajendram Soundararajan, G. Vignat, D. Durox, A. Renaud, S. Candel
  Journal of Engineering for Gas Turbines and Power, 143(3), **2021**, p. 031007
  https://doi.org/10.1115/1.4049702

- *Swirler effects on combustion instabilities analyzed with measured FDFs, injector impedances, and damping rates*
  P. Rajendram Soundararajan, D. Durox, A. Renaud, G. Vignat, S. Candel
  Combustion and Flame, 238(4), **2022**, p. 111947
  https://doi.org/10.1016/j.combustflame.2021.111947

- *Azimuthal instabilities of an annular combustor with different swirling injectors*
  P. Rajendram Soundararajan, D. Durox, A. Renaud, S. Candel
  Accepted at the ASME Turbo Expo **2022**, paper number GT2022-82281. *Recommended for publication in the Journal of Engineering for Gas Turbines and Power.*

- *Comparison of flame describing functions measured in single and multiple injector configurations*
  P. Rajendram Soundararajan, D. Durox, G. Vignat, A. Renaud, J. Beaunier, S. Candel
  Accepted at the ASME Turbo Expo **2022**, paper number GT2022-80577. *Recommended for publication in the Journal of Engineering for Gas Turbines and Power.*

- *Do flame describing functions suitably represent combustion dynamics under self-sustained oscillations?*
  P. Rajendram Soundararajan, G. Vignat, D. Durox, A. Renaud, S. Candel
  Under review in the Journal of Sound and Vibration (**2022**).

- *Impact of injector on combustion instabilities in a spray-swirl combustor*
  P. Rajendram Soundararajan, G. Vignat, D. Durox, A. Renaud, S. Candel
  Presented at the Initiative sur la combustion avancée (INCA) colloquium, Online, April **2021**.

- *The flame describing function and flame dynamics under self-sustained oscillations*

G. Vignat, P. Rajendram Soundararajan, A. Renaud, D. Durox, S. Candel
Presented at the Initiative sur la combustion avancée (INCA) colloquium, Online, April **2021**.

List of publications that are not part of this thesis:

- *A joint experimental and LES characterization of the liquid spray in a swirl injector*
  G. Vignat, P. Rajendram Soundararajan, D. Durox, A. Vie, A. Renaud, S. Candel
  Journal of Engineering for Gas Turbines and Power, 143 (8), **2021**, p. 081019
  https://doi.org/10.1115/1.4049771

- *Improvement of lean blow out performance of spray and premixed flames using nanosecond repetitively pulsed discharges*
  G. Vignat, N. Minesi, P. Rajendram Soundararajan, D. Durox, A. Renaud, V. Blanchard, C. O. Laux, S. Candel
  Proceedings of the Combustion Institute, 38(4), **2020**, pp. 6559-6566
  https://doi.org/10.1016/j.proci.2020.06.136

- *Swirling spray flames dynamical blow out induced by transverse acoustic oscillations*
  C. Patat, F. Baillot, J.B. Blaisot, E. Domingues, G. Vignat, P. Rajendram Soundararajan, A. Renaud, D. Durox, S. Candel
  Accepted for presentation at the 39th International Symposium on Combustion (**2022**).

- *Dynamical blow-out of swirling spray flames induced by transverse acoustic oscillations*
  C. Patat, F. Baillot, J.B. Blaisot, E. Domingues, G. Vignat, P. Rajendram Soundararajan, A. Renaud, D. Durox, S. Candel
  Presented at the Initiative sur la combustion avancée (INCA) colloquium, Online, April **2021** and at the Symposium on Thermoacoustics in Combustion: Industry meets Academia, TU Munich –Virtual venue, September **2021**.

Part I

Experimentation and modeling framework

Chapter 1

Experimental setups and instrumentation

Contents

This chapter contains a detailed description of the three experimental setups and the various diagnostic tools used in this work. A first experimental setup, the MICCA-Spray annular combustor, is a multiple injector configuration that idealizes aircraft engine combustors. The azimuthal instabilities exhibited by such systems are the main focus of this work because they are the most dangerous in terms of oscillation levels and impact on the structural integrity. Being a fully transparent combustor, this configuration allows for inspection of the flame dynamics during instability through an array of photomultiplier tubes fitted with appropriate optical filters. A set of microphones plugged on the chamber and plenum allows acoustic field identification. However, a complex multiple-injector test rig might often pose limitations in terms of experimentation and diagnostics. To overcome this, a single-injector test setup, namely SICCA-Spray, comprising only a single injector of the annular combustor was developed. Several diagnostic tools are mounted on this simplified combustor to examine the flow and flame behavior. This setup is used, in particular, to characterize the injector behavior and obtain the flame response through measurements of flame describing functions (FDFs). This facility is also used to investigate longitudinal self-sustained oscillations exhibited by this system when the chamber length, swirler characteristics, and operating parameters are varied. The annular combustor MICCA-Spray and the single-injector combustor SICCA-Spray are used in an interactive framework where the experiments in each setup complement and guide the experiments in the other. Finally, a newly developed multi-injector array combustor, namely TICCA-Spray, is employed for the first time. This setup, comprising three injectors, supplements the FDF measurements carried out in SICCA-Spray to answer the question of whether the flame response of a wall-bounded isolated flame measured in the single-injector setup represents the flame dynamics of annular combustors that are surrounded by other flames. The three test facilities are first described. This is followed by a review of optical and acoustic instrumentation implemented in the various configurations.

1.1 MICCA-Spray, a multi-injector annular combustor

The MICCA-Spray (Multiple Injector Combustor Coupled with Acoustics–spray version) experimental setup shown in Fig. 1.1 is a laboratory-scale annular system equipped with multiple injection units. This geometry represents a helicopter engine in an idealized and scaled-down fashion. Several generations of MICCA systems have been operated at the EM2C laboratory, starting from a system equipped with matrix injectors (Bourgouin et al. 2015a; Bourgouin et al. 2015b; Prieur et al. 2017; Aguilar et al. 2021), followed by several configurations of swirling

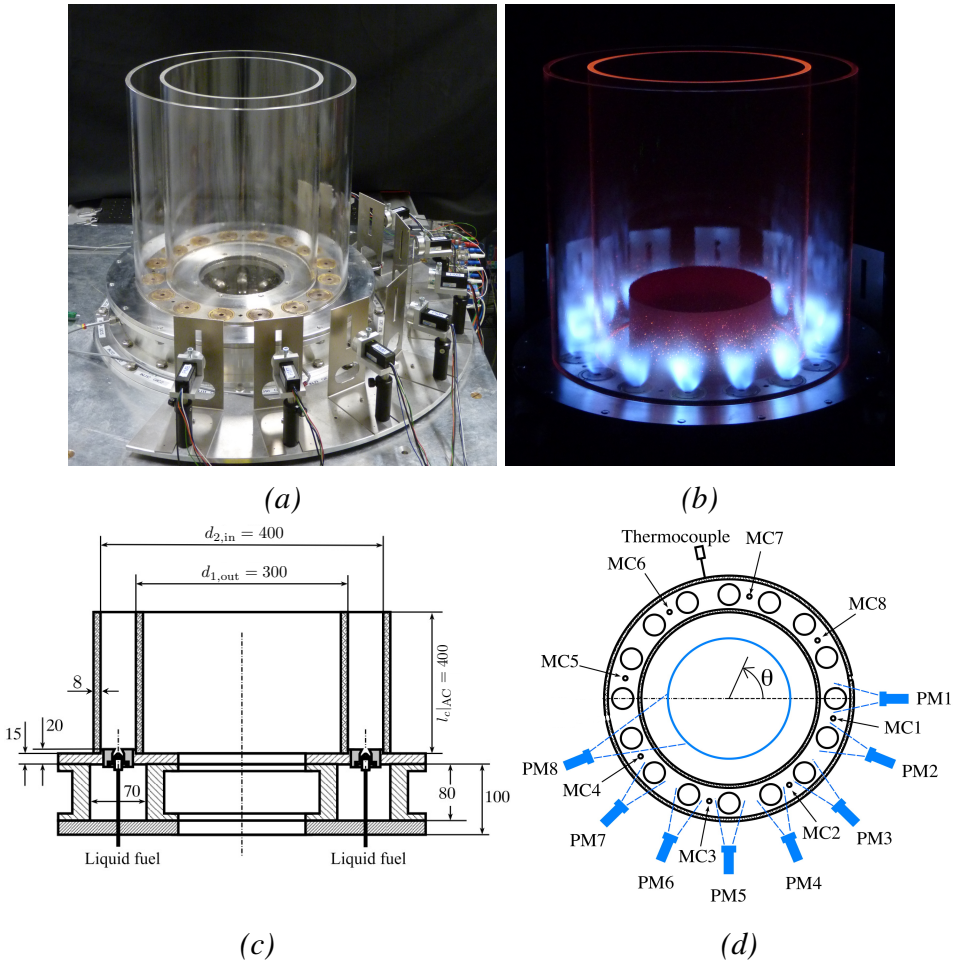

Figure 1.1. *(a) A photograph of MICCA-Spray annular combustor equipped with sixteen swirling injectors. The chamber walls, in this case, are of equal lengths. An array of eight photomultipliers (in black) record light emission from the flames in one half of the chamber. Each photomultiplier is equipped with a spatial filter in the front to prevent acquiring signals from adjacent flames. (b) A photograph of MICCA-Spray under operation. (c) A schematic of the experimental setup marked with the different dimensions in* mm. *Reproduced from Vignat (2020). (d) A schematic top view of the combustion chamber showing the locations of the chamber microphones (MCx), the arrangement of photomultipliers (PMx), and the position of the wall-mounted thermocouple. The blue dashed lines show the field of view of each PM. A steel tube, marked as a blue circle and seen glowing in (b), placed inside the inner chamber acts as a screen, preventing light transmission from opposite flames.*

injectors operated with premixed fuel (Bourgouin et al. 2013; Durox et al. 2016) and finally to the latest spray version of the combustor (Prieur et al. 2018; Vignat et al. 2020; Rajendram Soundararajan et al. 2021). In addition to studies of longitudinal, spinning, standing, and slanted azimuthal instabilities, this combus-

tor has also been used to examine the ignition dynamics using both experiments (Bourgouin et al. 2013; Prieur et al. 2017; Prieur et al. 2019) as well as numerical simulations (Philip et al. 2015; Philip et al. 2015; Lancien et al. 2018; Puggelli et al. 2021; Töpperwien et al. 2022).

The MICCA-Spray combustor comprises an annular plenum that is $80\,\mathrm{mm}$ in height with an internal diameter of $280\,\mathrm{mm}$ and an outer diameter of $420\,\mathrm{mm}$. The combustion chamber consists of two concentric, cylindrical, and vertical quartz walls of height $l_c|_{\mathrm{AC}} = 400\,\mathrm{mm}$ (AC stands for annular combustor), each with a thickness of $8\,\mathrm{mm}$. The transparent quartz walls provide optical access for observing the combustion region. In most previous investigations (Bourgouin et al. 2013; Prieur et al. 2018; Vignat et al. 2020), azimuthal instabilities were obtained by making use of unequal height for the side walls, the inner wall being shorter than the outer wall, similar to the first such experiments by Worth and Dawson (2013a). This was found to promote high amplitude combustion instabilities. In the present investigations, the chamber walls have equal heights. The inner quartz wall has an outer diameter of $d_{1,\mathrm{out}} = 300\,\mathrm{mm}$, while the outer quartz wall has an inner diameter of $d_{2,\mathrm{in}} = 400\,\mathrm{mm}$, resulting in a wall separation distance of $50\,\mathrm{mm}$. The relatively large circumferential dimension of MICCA-Spray allows conducting studies for understanding combustion instabilities coupled by azimuthal modes at frequencies that fall around 800 Hz. Air flow to the combustor is controlled by means of a Bronkhorst EL-FLOW mass flow controller with a relative accuracy better than 1% and a full scale of $150\,\mathrm{m_n^3/h}$ ('n' in the unit indicating normal conditions). The plenum is connected to the chamber via sixteen swirling injectors, the construction of which is detailed in Section 1.4. Each injector is separated by a distance of $69\,\mathrm{mm}$. The combustor can be operated with gaseous propane fuel fully premixed with air or with liquid fuels, heptane, and dodecane in the so-called technically premixed mode. When operating in fully premixed mode, propane is mixed with air well ahead of the plenum, and the liquid fuel supply lines remain inactive. Propane, being a gaseous fuel, is supplied through a Bronkhorst EL-FLOW mass flow controller and is premixed with air at ambient temperature before it enters the plenum. The flow meter has an accuracy of 0.5% and a full scale of $5.7\,\mathrm{m_n^3/h}$. The liquid fuels are supplied through a pump connected to a Bronkhorst CORI-FLOW controller, which has a relative accuracy of 0.2% and a full scale of $10\,\mathrm{kg\,h^{-1}}$. The fuel is supplied through eight equally spaced tubes, each tube feeding two fuel lines. The air and the fuel flow rate to the combustor can be systematically varied to study the instabilities at different operating points. Ignition of MICCA-Spray is obtained by a spark plug introduced from the top of the chamber and removed when combustion is self-sustained. This ensures rotational symmetry in the system geometry.

1.2 SICCA-Spray, a single-injector counterpart combustor

Although the MICCA-Spray annular combustor closely resembling a real aeronautical combustor is quite useful in studying azimuthal instabilities, understanding the flow and flame dynamics in such a complex system is difficult. In addition, examining possible control strategies for instability mitigation can be both laborious and costly in the annular configuration. Obtaining the flame response by external modulation to determine the flame transfer/describing functions is also difficult to implement in MICCA-Spray. The above issues may be addressed with a single-injector test rig, namely SICCA-Spray, which geometrically resembles one sector of MICCA-Spray. The photograph of the SICCA-Spray test bench is shown in Fig. 1.2 (a), along with an image of the flame in Fig. 1.2 (b). The two combustors are used in a closed-loop complementary framework, where the experiments from each guide the studies conducted on the other. Such an experimental framework (shown in Fig. 2) was successfully used in the previous research efforts, notably by Prieur (2017) and Vignat (2020). The SICCA-Spray combustor is used to understand the flame and injector dynamics in addition to studying the flow and the fuel spray behavior. The response of an isolated flame to acoustics obtained through external modulation is used to represent the flame in reduced-order models. SICCA-Spray, being a modular setup, not only allows the determination of FDFs but also studying instabilities coupled by longitudinal modes leading to self-sustained oscillations (SSOs). This gives the possibility of testing and tuning the low-order models and validating them with the SSOs of this configuration, with the eventual aim of using the reduced-order model for instability prediction in the annular system MICCA-Spray. In turn, the reduced-order model, in combination with measured FDF gains and phases, can be tuned to devise stable configurations. The system tested in SICCA-Spray can be further investigated in the annular combustors to test the instability control strategy. To ensure that the flame response obtained in SICCA-Spray suitably represents the flame dynamics of the annular combustor, one has to see whether the flame in a single sector interacting with the combustor wall has the same dynamics as a flame in MICCA-Spray, where the flame is surrounded by side flames and interacts with the inner and outer walls. For dynamical similarity, it is generally considered that the confinement ratio, i.e., the ratio of injection surface area to backplane surface area A_I/A_{BP} should take identical values in the single-sector and annular configurations. Since the injector outlet A_I is kept constant, one has to assure that A_{BP} in SICCA-Spray corresponds to the surface area of one injector in MICCA-Spray. It is also necessary to ensure that the distance of the chamber wall from the center of the single-injector combustor should be half the inter-injector distance of the annular combustor. This would be equivalent to considering a single injector of an unwrapped annular combustor but with a cylindrical cross-section. This results in a chamber diameter of $d_c = 69\,\mathrm{mm}$ for SICCA-Spray.

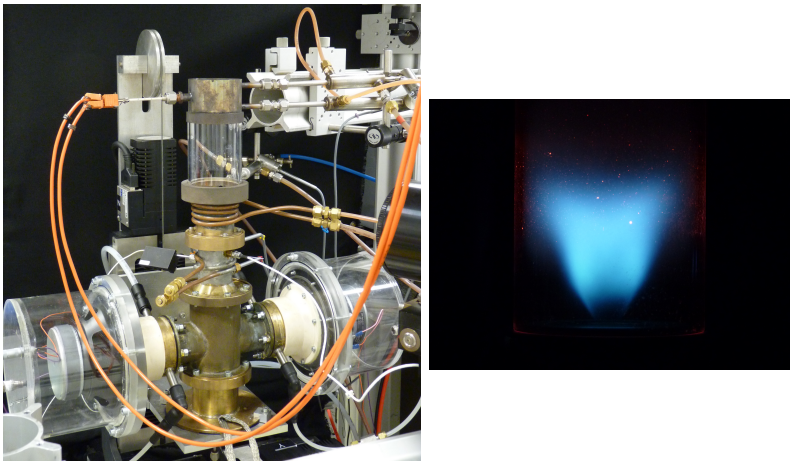

(a) *(b)*

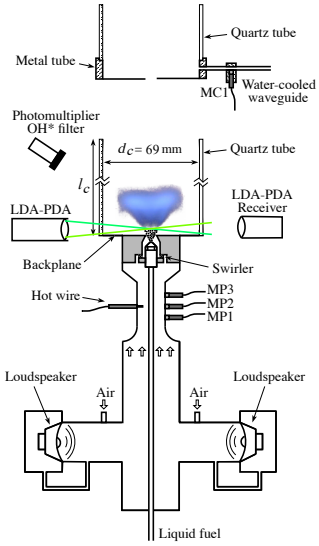

(c)

Figure 1.2. *(a) A photograph of SICCA-Spray comprising a single sector of the annular configuration. A single flame of the annular combustor is placed in an isolated environment surrounded by a combustion chamber. The setup shown here is equipped with different diagnostic tools such as microphones, hot wire, and thermocouple. (b) A photograph of the flame in SICCA-Spray during operation. (c) Schematic of the experimental setup of SICCA-Spray. The figure shows the position of the microphones marked as MPx and the hot wire in the plenum. For the LDA/PDA measurements, a full transparent quartz chamber is used. When measuring the chamber pressure, a metal ring or metal cap is mounted on the chamber to hold the microphone fixed on a waveguide, as shown (a).*

The experimental setup of SICCA-Spray shown schematically in Fig. 1.2 (c) comprises a plenum fed by air at atmospheric conditions by a Bronkhorst EL-

FLOW mass flow controller with a relative accuracy of 0.6% and a full scale of $150\,\mathrm{l_n/min}$. The plenum is connected to the combustor through a spray-swirl injector, the same as the ones used in MICCA-Spray. Like MICCA-Spray, SICCA-Spray can also be operated with premixed propane as fuel or with liquid fuels delivered as a spray. When operating in premixed conditions, propane is mixed with air at a distance of nearly $1\,\mathrm{m}$ from the plenum by a cyclone mixer and the spray atomizer mounted on the injector remains unused. Propane is controlled by a Bronkhorst EL-FLOW mass flow controller with a relative accuracy of 0.6% and a full scale of $20\,\mathrm{l_n/min}$. Liquid fuels are supplied by a central tube traversing the plenum, and their mass flow rates are controlled by a Bronkhorst CORI-FLOW controller having a relative accuracy of 0.2% and a full scale of $1\,\mathrm{kg\,h^{-1}}$. Flow modulation is achieved using two driver units, each confined in a cylindrical enclosure mounted at the bottom of the plenum and producing axial perturbations of the air flow at different amplitudes and frequencies. The driver units are connected to a HiFi wave amplifier and a signal generator that can be programmed to produce a linear frequency sweep signal at different amplitudes. The possibility of using the flame response from a single-injector combustor where the axial velocity is modulated to represent the annular combustor that exhibits azimuthal instabilities stems from the fact that azimuthal instabilities essentially induce axial velocity perturbations at the base of the flame when this flame is at a pressure antinode (Staffelbach et al. 2009). However, the transverse velocities that also accompany azimuthal modes and are particularly strong in the pressure node region cannot be reproduced in this single-sector configuration. Thus, the SICCA-Spray measurements represent the flame dynamics only near the pressure antinode, but it is known that this region plays a central role in driving the instability. If one wishes to examine the effect of transverse velocities, it is necessary to use facilities that are not available at EM2C. One such configuration designated as TACC operating at CORIA has been used in the framework of the ANR FASMIC project to examine the flame dynamics at a velocity or intensity antinode, in addition to a pressure antinode position (Patat et al. 2021). Two types of chambers are used in SICCA-Spray depending on the type of measurement (see Fig. 1.2 (c)). For measurements that require optical access to the base of the flame, a full cylindrical quartz tube that gives access to the complete flame is used. This includes velocity measurements at the injector outlet using laser Doppler anemometry (LDA) or droplet size measurements based on phase Doppler anemometry (PDA), flame visualization, chemiluminescence detection, etc., which are described in Section 1.6. For measuring the pressure fluctuations close to the chamber backplane, the full quartz tube is replaced by a cylindrical metal bottom ring of $15\,\mathrm{mm}$ height which holds a waveguide equipped with a microphone that measures the pressure near the chamber backplane. Quartz tubes of required heights are then placed on top of this metal ring providing optical access to the rest of the flame zone. If pressure measurements are needed in other regions of the chamber, then a metal top hat $50\,\mathrm{mm}$ in height is placed further on top of the quartz tube to complete the combustion

chamber (see Fig. 1.2 (a)). The top metal hat has provisions for holding additional microphones and an R-type double bead thermocouple for measuring the exhaust gas temperature. The total length of the combustion chamber is also chosen depending on the kind of measurement to be carried out. For measurements that require studying the stable flame response (using a stable flame modulation or SFM), the length is chosen such that the combustor is stable and there is no positive coupling between the flame and chamber acoustics. The length for such measurements is generally chosen between $l_c = 115\,\mathrm{mm}$ to $165\,\mathrm{mm}$. For experiments on self-sustained oscillations coupled by longitudinal modes, the length of the combustion chamber is varied between $l_c = 215\,\mathrm{mm}$ and $465\,\mathrm{mm}$ to produce different amplitude and frequencies of oscillation. The SICCA-Spray system is mounted on a motorized traverse enabling the acquisition of velocity and droplet information at different locations in the chamber.

1.3 TICCA-Spray, a three-injector, linear, counterpart combustor

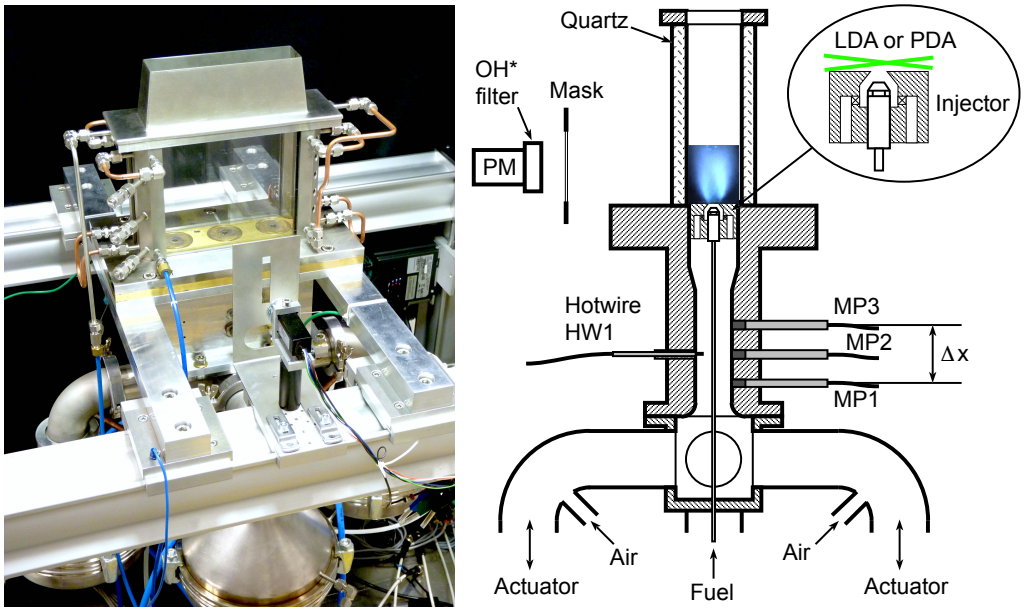

(a) *(b)*

Figure 1.3. *(a) Photograph of TICCA-Spray, a linear combustor equipped with three injectors. Acoustic actuators are visible at the bottom of the photograph. A photomultiplier (in black) is installed in front of the window, behind a mask with a vertical rectangular slot serving as a spatial filter. (b) The sectional view of TICCA-Spray combustor in a plane perpendicular to the length and passing through the central burner axis. The zoomed-in portion near the injector displays the velocity measurement technique described in Section 1.6.*

Even though the injector surface area to backplane surface area ratio is maintained the same between SICCA-Spray and MICCA-Spray, this alone may be inadequate because there is a notable difference in the boundary conditions: a rigid wall cannot properly reflect possible interactions with the adjacent flames. Even if the interactions between the neighboring flames appear to be weak (Staffelbach et al. 2009; Wolf et al. 2012; Bourgouin et al. 2013), there is evidence that the proximity and arrangement of injection units (co- or counter-rotating) may influence the dynamics of the annular combustor (Worth and Dawson 2013a; Worth and Dawson 2019). In addition, the flames are generally swirling, causing a strong rotation of the burnt gases between the flames. To address the above issues, a new test bench, namely TICCA-Spray, was designed to complement the existing single-injector SICCA-Spray and annular combustor MICCA-Spray. This device comprises an array of three injectors in a rectangular geometry. The central flame is surrounded by two side flames in an arrangement that portrays in a linear fashion the situation that prevails in the annular system. In addition to maintaining the injector outlet surface area to backplane surface area ratio A_I/A_{BP} same as MICCA-Spray, the relative injector spacing s_I/d_I is also maintained the same. In the present thesis, TICCA-Spray is only used to study the flame response under SFM, and no SSOs are examined. The recently built TICCA-Spray linear combustor is shown in Fig. 1.3. It comprises an array of three injectors, identical to those used in MICCA-Spray and SICCA-Spray, with a spacing of $69\,\mathrm{mm}$ between injectors. The combustion chamber is formed by four transparent windows with a length of $205\,\mathrm{mm}$, a width of $50\,\mathrm{mm}$, and a height of $175\,\mathrm{mm}$. The width equals the distance between the two sidewalls in MICCA-Spray and the length to the curvilinear distance corresponding to three adjacent injectors in MICCA-Spray. The height of TICCA-Spray is chosen such that the flames are stable and also sufficiently confined as in the annular chamber. The central flame in the linear array is, therefore, in a configuration close to that of the annular chamber, with neighboring swirling flames on either side. A slightly converging metallic hat placed on top of the transparent chamber prevents the entrainment of outside air and its inflow into the chamber. The backplane and the metallic corner structures supporting the lateral windows are cooled by circulating cold water. Air is fed to the common manifold at the bottom of the test rig, and the total air flow rate is controlled by a Bronkhorst EL-FLOW® mass flow meter of $500\,\mathrm{l_n/min}$. Like the other two combustors, TICCA-Spray can also be operated with premixed propane or liquid fuels. Premixed propane is controlled by a Bronkhorst EL-FLOW® mass flow meter of $50\,\mathrm{l_n/min}$, and the liquid fuels are controlled by a Bronkhorst CORI-FLOW™ mass flow meter with a full-scale of $10\,\mathrm{kg\,h^{-1}}$. The common air manifold branches into the individual plenum for the three injection systems which is identical to the plenum of SICCA-Spray. Four driver units are used for modulating the air flow and are connected through elbow channels to the common air manifold (see Fig. 1.3 (a)). A partition is made in the common air manifold such that the two lateral driver units majorly modulate the air flow rate of the two side flames

while the other two driver units modulate the air flow to the central flame. Such an arrangement resembles the situation of an azimuthal instability where the adjacent flames in an annular combustor do not oscillate with the same amplitude at a particular instant. The central plenum houses the instrumentation for acoustic measurements upstream of the injector (see Fig. 1.3 (b)). The measurement of flame response to acoustic modulation is only carried out on the central flame and compared with the flame response of an isolated flame in SICCA-Spray.

1.4 Swirling injector design

The injector represents the portion of the combustor that holds the fuel nozzle (or fuel atomizer), air distributor, and swirler unit and acts as the flame holding element. These injectors were first introduced in the thesis of Prieur (2017) for operation mainly with liquid fuels and further developed during the thesis of Vignat (2020). In the current work, detailed investigations are carried out to understand the dynamics induced by such injectors when they are equipped with different swirlers and their impact on combustion instabilities. The exploded view of an injection unit is shown in Fig. 1.4 left, and the schematic of the top view of the swirler is shown in Fig. 1.4 right. The injector assembly consists of an air distributor which is connected to the plenum, followed by a radial swirler comprising six tangential channels. The liquid fuel atomizer is mounted at the center of the air distributor. The passage of air through the swirler typically results in a clockwise rotation of the incoming air flow. The injector houses a terminal plate (also referred to as exit nozzle) after the swirler that has a hole with a conical section $5\,\mathrm{mm}$ in height followed by a $1\,\mathrm{mm}$-long straight section. The conical section of the terminal plate has an inlet diameter of $14.5\,\mathrm{mm}$ and an outlet diameter of $8\,\mathrm{mm}$ and forms the backplane of the test rigs. The injector's modular construction enables to swiftly change the swirler unit. Different swirlers are used in the present work, and they are primarily distinguished in terms of two parameters, the dimensionless swirl number S_N, which quantifies the extent of rotational motion imparted to the incoming air flow, and the pressure drop Δp between the injector upstream and downstream sections. These two parameters are experimentally obtained in the SICCA-Spray test rig. The swirl number is the ratio of the axial flux of angular momentum to the axial flux of axial momentum (Gupta et al. 1984) and is given by the classical formula:

$$S_N = \frac{\int_0^{2R_{\text{inj}}} \overline{u}_\theta \overline{u}_x r^2 dr}{R_{\text{inj}} \int_0^{2R_{\text{inj}}} \overline{u}_x^2 r dr} \tag{1.1}$$

where $R_{\text{inj}} = 4\,\mathrm{mm}$ is the radius at the injector outlet. The swirl number is obtained by measuring axial $\overline{u}_x$ and tangential $\overline{u}_\theta$ velocity profiles using LDA described

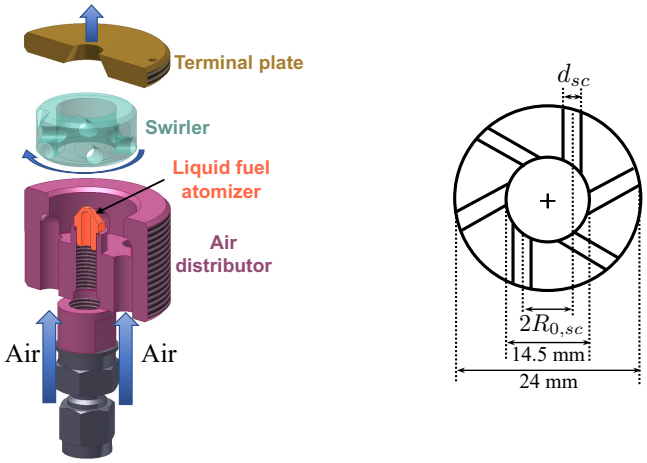

Figure 1.4. *Exploded view of the swirling injector showing its various components. Adapted from Vignat (2020). The injector unit comprises an air distributor, a hollow cone atomizer, a swirler, and a terminal plate. The terminal plate features a converging conical section having a diameter of* $8\,\mathrm{mm}$ *at the outlet. The schematic of the swirler is shown on the right. The channel diameter* d_{sc} *and radial location* $R_{0,sc}$ *can be changed to vary the swirl number and pressure drop.*

in section 1.6. The catalog of the velocity profiles reported in Vignat (2020) is recalled here in Fig. 1.5, along with the swirl number values in Tab. 1.1. The injector pressure drop with various swirler units is measured using a differential pressure sensor (make: *KIMO Instruments*, type: *MP111*) placed between the plenum (corresponding to the location of microphone MP2 in Fig. 1.2 (c)) and the atmosphere in an unconfined experimental test rig under cold flow conditions. In addition to the pressure drop value, a dimensionless pressure drop coefficient σ is obtained as:

$$\sigma = 2\Delta p/\rho_0 u_b^2 \tag{1.2}$$

where ρ_0 is the density and u_b is the bulk velocity at the injector outlet.

The two characteristic parameters, swirl number and pressure drop, can be changed by modifying the two geometrical dimensions d_{sc}, which is the diameter of the swirler channels, and $R_{0,sc}$, which is the distance between the axis of a channel to the axis of the swirler (see Fig. 1.4 right). These two parameters are systematically varied to obtain ten distinct swirler units. The swirler units are designated as 707, 712, 713, 714, 715, 716, 726, 727, K and T, and were initially studied in the thesis of Vignat (2020), where the characterization of the swirlers in terms of different velocity components, swirl numbers, and pressure drops were measured and reported. The swirler K was introduced in the thesis of Prieur (2017) to study instabilities in MICCA-Spray. It exhibited strong self-sustained oscillations, and the first occurrence of dynamical blow out was observed with this swirler (Prieur et al. 2018). However, this unit is phased out due to certain manufacturing con-

Table 1.1. *Injector characteristics measured in an unconfined SICCA-Spray test rig under cold flow conditions. The swirl number S_N is measured at a height $h = 2.5\,\mathrm{mm}$ above the outlet. Δp is the pressure drop, and σ is the head loss coefficient calculated using Eq. 1.2. These values are shown at two air mass flow rates used in this thesis. d_{sc} is the diameter of the swirler channels, and $2R_{0,sc}$ is the distance separating the axis of two opposing channels. Adapted from Vignat (2020).*

Swirler	$\dot{m}_a$	S_N	Δp	σ	d_{sc}	$R_{0,sc}$
	$\mathrm{g\,s^{-1}}$	(-)	(kPa)	(-)	(mm)	(mm)
707/807	2.3	0.60	2.81	3.30	4.0	4.6
	2.6		3.65			
712	2.6	0.59	4.50	4.10	3.0	2.3
713	2.6	0.69	4.96	4.52	3.5	3.9
714	2.6	0.70	5.30	4.83	3.5	4.1
715	2.6	0.71	5.64	5.14	3.5	4.4
716/816	2.3	0.70	4.41	5.23	3.5	4.7
	2.6		5.74			
726	2.6	0.74	6.00	5.47	3.5	5.5
727	2.6	0.74	5.70	5.20	3.5	5.1
K	2.6	0.68	3.73	3.40	4.5	5.0
T	2.6	0.76	10.8	9.84	3.0	5.0

straints and is not presently used. The swirler T was introduced in the thesis of Lancien (2018) and was mostly used to study ignition in some of the previous works carried out in MICCA-Spray. The characteristics of the different swirlers, along with their geometrical parameters, are given in Tab. 1.1. Apart from the ten swirler units, two additional swirlers are also considered, namely 807 and 816, that impart counterclockwise rotation to the incoming air flow. These two swirlers are the counterclockwise replicas of the clockwise swirlers 707 and 716, respectively, and possess the same characteristics and geometry. These counterclockwise swirlers are used to identify the effect of swirl direction on flame dynamics (discussed in Chapters 7 & 10).

The mean velocity profiles of the different swirlers previously reported by Vignat (2020) are shown in Fig. 1.5. In the figure, $\overline{u}_x$ represents the mean axial

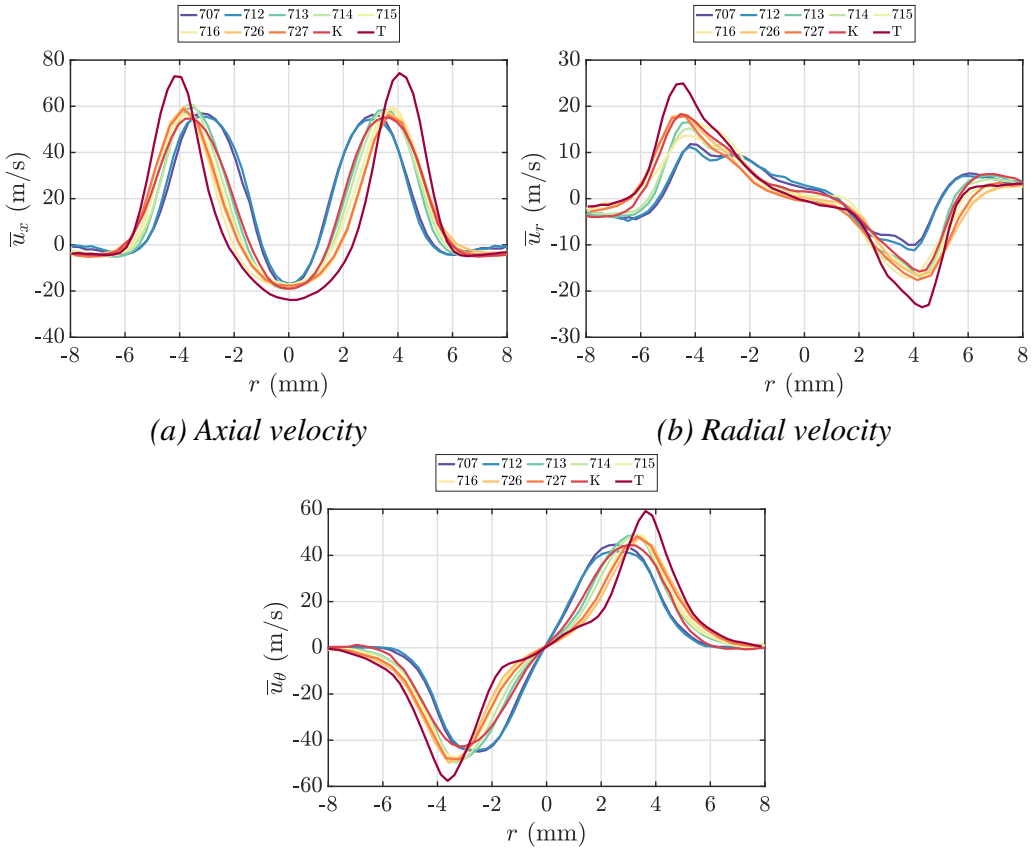

(a) Axial velocity *(b) Radial velocity*

(c) Tangential velocity

Figure 1.5. *Mean velocity profiles of the various swirlers considered in this work. $\overline{u}_x$ is the axial velocity, $\overline{u}_r$ is the radial velocity, and $\overline{u}_\theta$ is the tangential velocity, measured at a distance of $h = 2.5\,\mathrm{mm}$ above the backplane under cold flow conditions at an air mass flow rate of $\dot{m}_a = 2.6\,\mathrm{g\,s^{-1}}$. Adapted from the thesis of Vignat (2020).*

velocity, $\overline{u}_r$ is the mean radial velocity, and $\overline{u}_\theta$ is the mean tangential velocity, all measured using laser Doppler anemometry (presented later in Section 1.6.2) at a distance of $h = 2.5\,\mathrm{mm}$ above the backplane under cold flow conditions by seeding the flow with fine oil droplets. The profiles for the different swirlers are nearly similar except for some minor changes based on which they can be grouped. The type-1 (T1) category comprises swirlers 707 and 712, which have the same velocity profiles and a relatively narrow inner recirculation zone. The location of peak mean axial velocity occurs close to $r = 3.5\,\mathrm{mm}$ for these swirlers, and they have the smallest peak value for all three velocity components. These two swirlers also have the same swirl number value but a different pressure drop (see Tab. 1.1). The type-2 (T2) category comprises swirlers 713, 714, 715, 716, 726, 727, and K that have a wider inner recirculation zone due to their higher swirl number values. The peak of mean axial velocity occurs close to $r = 3.5\,\mathrm{mm}$ for 713 and 714, and at $r = 4\,\mathrm{mm}$ for the rest of the swirlers. The maximum value of the three velocity

components for these swirlers is slightly higher than the T1 category, except for swirler K, which has nearly the same peak velocity as the T1 category. The location of peak velocities also occurs at a higher radial point for these swirlers. The swirlers in this category have similar values of swirl number but varying pressure drops. This is achieved by retaining the same hole diameter for the swirler channels (i.e., same $d_{0,sc}$) but varying the distance between the axis of two opposing swirler channels (i.e., $2R_{0,sc}$). Only the swirler K has a different value of $d_{0,sc}$ in this category. Among these swirlers, 726 and 727 have the same value of swirl number, but different pressure drops, allowing to study the effect of pressure drop on combustion instabilities. Additionally, the swirlers 716 and 727 have almost the same pressure drop but different swirl numbers, which would help in examining the effect of swirl number on combustion instabilities (discussed in Chapter 7). The final category, namely type-3 (T3), consists only of swirler T, which takes the highest value of both the pressure drop and swirl number. This unit naturally has a broader inner recirculation zone and also takes the highest value for peak velocity for all the velocity components. The location of peak velocities occurs at almost the same point as the swirlers of the T2 group, at $r = 4\,\mathrm{mm}$. As the swirler T was mainly developed for ignition studies, it is not used much in the present thesis.

The injectors described here have strong pressure drops and feature abrupt area changes in the air pathway. This construction causes a substantial change in the acoustic state before and after the injector. Thus, these injectors are designated as “acoustically weakly transparent" as opposed to more traditional injectors that have been considered, for example, by Palies et al. (2011), which are relatively transparent to acoustic waves. Further discussion on the nature of these injectors is provided in Chapter 4.

1.5 Operating points

In the MICCA-Spray annular combustor, experiments are performed systematically by varying the thermal power $\mathcal{P}$ and equivalence ratio ϕ. Five levels of thermal powers are considered $\mathcal{P} = 93, 99, 103, 110, 118\,\mathrm{kW}$ and at each thermal power level, six different equivalence ratios are explored $\phi = 0.75, 0.85, 0.9, 0.95, 1.0, 1.05$. The operating points are systematically varied to obtain the combustor stability map. From the operating points of MICCA-Spray, three points are selected for measurements in the simplified test rigs SICCA-Spray and TICCA-Spray. These operating points are designated as F1, F2, and F3, and their details are provided in Tab. 1.2.

Table 1.2. *Different operating points of the simplified test rigs derived from MICCA-Spray operating domains. The mass flow rate of air $\dot{m}_a$ corresponds to that of a single injector.*

Operating point	$\mathcal{P}_{\text{micca}}$	$\mathcal{P}_{\text{sicca}}$	$\mathcal{P}_{\text{ticca}}$	ϕ	$\dot{m}_a$
-	kW	kW	kW	(-)	$\mathrm{g\,s^{-1}}$
F1	103	6.4	19.3	0.85	2.6
F2	103	6.4	19.3	0.95	2.3
F3	118	7.4	22.2	0.95	2.6

1.6 Instrumentation

The various diagnostic tools mounted on the test rigs are described in this section along with details of their implementation.

1.6.1 Pressure measurements

1.6.1.1 Sensor details

Acoustic pressure measurements are performed using *Brüel & Kjær* type 4938 1/4-inch pressure-field microphones mounted with type 2670 preamplifiers having a relative accuracy of 1%. These microphones have a dynamic pressure range between 30 and $172\,\mathrm{dB}$, a frequency range between 4 and 70,000 Hz, and a sensitivity of $1.6\,\mathrm{mV\,Pa^{-1}}$. The microphone signals are conditioned using a *NEXUS*™ conditioning amplifier and are filtered between the frequency range of $15\,\mathrm{Hz}$ and $20\,\mathrm{kHz}$. The microphones are regularly calibrated using a *Brüel & Kjær* type 4231 calibration source. They are typically flush-mounted on the measuring section except when the sensor is exposed to a high-temperature environment (i.e., in the combustion chamber), as they can only operate until $150\,^{\circ}\mathrm{C}$ before incurring damage. In such situations, the microphones are mounted in waveguide tubes. Two types of waveguides are used in the present study depending on the test rig in which they are used. The waveguides mounted on SICCA-Spray are generally water-cooled and consist of a straight metallic tube with an inner diameter of $6\,\mathrm{mm}$ enclosed in a continuously circulated cold water network terminated by a $25\,\mathrm{m}$ long tube that is closed at the end to damp wave reflections. The microphones are located at a distance of $276\,\mathrm{mm}$ or $283\,\mathrm{mm}$, depending on their location in this test rig. In MICCA-Spray, waveguides are formed by straight metallic tubes without water cooling. Microphones are plugged into these tubes at a distance of $170\,\mathrm{mm}$ from the orifice. These tubes are also terminated by a $25\,\mathrm{m}$ long tube, which is closed at its end. The microphone positioning inside a waveguide results in distortion of the measured acoustic pressure record, which needs to be accounted for. The

waveguide possesses a transfer function of its own, the phase of which just corresponds to a constant time delay associated with the travel time of the pressure waves in the tube. In MICCA-Spray, the waveguide results in a propagation time lag of $0.46\,\mathrm{ms}$, considering a temperature of $55\,^{\circ}\mathrm{C}$ for the hot gases in the waveguide tube. In SICCA-Spray, due to the water cooling, the gas temperature in the waveguide is considered to be $30\,^{\circ}\mathrm{C}$ based on measurement by Prieur (2017). The propagation delay associated with the acoustic pressure records is $0.79\,\mathrm{ms}$ when considering a tube length of $276\,\mathrm{mm}$ and $0.81\,\mathrm{ms}$ when considering a length of $283\,\mathrm{mm}$ for the waveguide. Concerning the waveguide transfer function gain, a study carried out by Gaudron (2018) (pp.119-122) with similar waveguide tubes indicates that the amplitude is decreased by less than 8% at $1000\,\mathrm{Hz}$. This deviation would be further reduced at lower frequencies of interest here (maximum being $850\,\mathrm{Hz}$), and one may, therefore, consider that the amplitude distortion is negligible.

1.6.1.2 Deployment in the test rigs

In the MICCA-Spray annular combustors, a total of twelve microphones, eight of which are plugged on the chamber (designated as MC1 to MC8 in Fig. 1.1) and four of which (MP1 to MP4) are mounted on the plenum (not shown), are used to reconstruct the acoustic fields in the chamber and plenum. The microphones in the plenum are flush-mounted on the side wall, while the chamber microphones are mounted on waveguides. The waveguide ports are located between every two injectors.

In SICCA-Spray, three microphones are flush-mounted in the plenum and separated by a distance of $\Delta x|\mathrm{SIC} \approx 20\,\mathrm{mm}$. In the chamber, close to the backplane, a microphone is mounted on a water-cooled waveguide at a distance of $276\,\mathrm{mm}$ from the waveguide port, which is, in turn, flush-mounted on the cavity wall. The waveguide is held by the bottom metal ring of height $15\,\mathrm{mm}$ (see Fig. 1.2 (c) top). Two additional microphones are placed close to the chamber exit and mounted on water-cooled waveguides at a distance of $283\,\mathrm{mm}$ from the chamber wall. The two waveguides are in turn supported on a top metal hat (seen in Fig. 1.2 (a)), and the waveguide ports are separated by a distance of $\Delta x|\mathrm{SIC} \approx 30\,\mathrm{mm}$. An additional waveguide port can also be placed at the center of this metal hat replacing the R-type thermocouple, if needed.

In TICCA-Spray, like in the plenum of SICCA-Spray, three microphones are flush-mounted on the plenum wall and separated by a distance of $\Delta x|\mathrm{TIC} \approx 25\,\mathrm{mm}$. Although there is a provision for measuring the chamber backplane pressure in TICCA-Spray, this has not been used in this work.

1.6.2 Velocity measurements

Velocity measurements are quite important in the analysis of combustion dynamics as they form the input of the flame describing function, which is extensively exploited in this work. Three kinds of instrumentation are used to measure the velocity at different locations in the test rigs, and their details are given in what follows.

1.6.2.1 Sensor details

Hot wire anemometry
The first method relies on constant temperature hot wire anemometry used for measuring the instantaneous velocity signal using a 1D hot wire probe inserted into the flow. It is then possible to obtain the mean and extract the velocity fluctuation by subtracting its mean from the instantaneous signal. This sensor is based on the principle of the convective cooling effect produced by the fluid flow over a heated body (i.e., measurement probe). The probe used here is a plated tungsten wire with a diameter of $5\,\mu\mathrm{m}$ and length of $1.25\,\mathrm{mm}$ from *Dantec Dynamics* (reference: 55P16), welded to a set of prongs. The velocity component that is measured is the one perpendicular to the wire. The probe is conditioned by the electronic circuitry MiniCTA from *Dantec Dynamics*, which keeps it heated at a constant temperature by suitably adjusting the current supplied to the probe wire. This current can then give a direct measure of the flow velocity. The voltage of the electronic circuitry can be related to the velocity through King's law (King 1914) as:

$$E^2 = a + bU^n \tag{1.3}$$

where E is the measured voltage, U is the velocity to be measured, and a, b, and n are constants. The constants are obtained by a calibration setup with an $8\,\mathrm{mm}$ outlet diameter which accommodates the velocity range typically expected in these test rigs. Although the measurement with hot wires is quite simple, there are, however, certain drawbacks associated with this technique. Some of them are:

- The hot wire positioning is crucial as it decides the component of velocity that is being measured. If not placed exactly perpendicular to the flow, it might also include the measurement of other unwanted velocity components.
- Hot wire probes are thin and delicate, and the handling of these probes must be done cautiously.
- Hot wires cannot measure negative velocities. This is a problem when the amplitude of velocity fluctuation exceeds the mean velocity, in which case the velocities are incorrectly acquired. The resulting FDF calculations using the velocity in such a situation will give a correct phase, but will result in an incorrect gain.

- The probe cannot be used in a combustion environment.

Considering these limitations, other velocity measurement techniques need to be implemented and are now described.

Multi-microphone method

A second velocity measurement technique used in this work relies on the multi-microphone method (Chung and Blaser 1980; Seybert and Ross 1977), which can also be used to determine various acoustical parameters such as velocity, acoustic intensity and flux, etc. In this technique, the velocity fluctuations are obtained from acoustic pressure measurements. The method is especially useful when the fluctuation amplitude is high, and the hot wire probes would not recognize the negative velocity fluctuations. Consider two microphones that are separated by a known distance Δx, and measuring 1D harmonic waves at a frequency f. Assuming that the mean flow velocity is small compared to the speed of sound, the acoustic velocity may be deduced from the pressure gradient, which, in turn, may be represented by a finite difference expression:

$$u' = \frac{1}{i\rho_0\omega}\frac{p'_2 - p'_1}{\Delta x} \tag{1.4}$$

Here, p'_1 and p'_2 are the pressures measured by the microphones at the frequency f and angular frequency $\omega = 2\pi f$. Δx is the distance between the two microphones, and ρ_0 is the local density. This method is precise only if the distance of separation is much smaller than the wavelength λ (i.e., $\Delta x << \lambda$). The previous expression is written in terms of complex numbers and requires that analytical signals be obtained from the pressure records. These complex signals are obtained using a Hilbert transform, and the resulting complex signals are used in Eq. 1.4. Further details of this method and its formulation are given by Tran (2009). The microphone sensors are those described in Section 1.6.1.1. This technique has been validated against hot wire anemometry through measurements in a Kundt's tube at low modulation levels to ensure that they produce the same amplitude and phase for the acoustic velocity. The multi-microphone technique overcomes some of the limitations of hot wire anemometry, but it only provides the acoustic velocity and cannot be used to determine the convective component associated with the flow. The method relies on the assumption that acoustic propagation is one-dimensional and that the velocity is constant throughout the measuring section. It cannot be used in situations where the velocity varies in the transverse direction, like, for example, near the chamber backplane, where the velocity fluctuation changes rapidly from the injector outlet to the side wall.

Laser Doppler anemometry and phase Doppler anemometry

Some of the above limitations may be overcome by using a third method relying on laser Doppler anemometry (LDA). This is a non-intrusive and direction-sensitive

measurement technique that can measure the velocity of a particle in the flow based on the light scattered by the particle. This frequency shift of the scattered signal is proportional to the local velocity component in the direction orthogonal to a set of interference fringes in the measurement volume formed by crossing two laser beams. In addition to being non-intrusive, this technique has a high spatial and temporal resolution, can be used to measure reverse flow velocities, does not require frequent calibration, and can be used in high-temperature environments. The LDA system used in this work is a *Dantec Dynamics* FlowExplorer two-component phase Doppler particle analyzer (PDPA) that can simultaneously measure two velocity components. The transmitting optics consists of two laser cavities for measuring the two velocity components. The laser beam from each laser cavity is split into two, one of which is shifted in frequency after passing through a Bragg cell, resulting in a total of four beams. This frequency shift in one of the laser beams allows for a moving interference field, which detects the particle's direction of motion. An optical system aligns the beams at a specific angle in the measurement zone, and their intersection results in the formation of interference patterns. The horizontal beams, initially formed by a $561\,\mathrm{nm}$ laser and later split into two beams, are used to measure radial or tangential velocity components, and the vertical beams, initially formed by a $532\,\mathrm{nm}$ laser and later split into two beams, are used to measure the axial velocity component. The transmitting optics of this system has a focal length of $500\,\mathrm{mm}$, and the receiving optics has a focal length of $310\,\mathrm{mm}$. The receiving optics is placed at $71.5°$ from the axis of the transmitting optics, an optimal position for the tracer droplets used in this study. The theoretical size of the laser beam intersection seen by the receiving optics is 0.14 $\times$ 0.14 $\times$ 0.23 mm. When a particle or a droplet passes through the measurement volume, it produces a burst of scattered signals, which are then captured by the receiving optics connected to a set of photomultipliers equipped with appropriate optical filters. The velocity U of the particle can be obtained as:

$$U = d_f f_d \tag{1.5}$$

where d_f is the fringe spacing, and f_d is the Doppler frequency. The inter-fringe spacing can, in turn, be obtained by knowing the wavelength of the laser beam and the angle between the two laser beams. When having a frequency shift for one of the laser beams, the signal from the emitted particle has a frequency of $\Delta f_{\mathrm{LDA}} = f_{\mathrm{shift}} + f_d$, where $f_d = U/d_f$. The measurement system comprises a *Dantec Burst Spectrum Analyser*, which conditions the scattered signals and processes them into velocity. While performing this experiment, it is necessary to ensure that the seeding in the measurement volume is sufficient to capture the fluctuating signals. It is also important to make sure that the tracer particles have a velocity that closely follows that of the gaseous stream.

The above principle can also be extended to obtain information on the size of spherical particles in the flow through phase Doppler anemometry (PDA). Two

detectors are employed for this purpose, and their location is carefully selected so that they have a phase shift in the received signals scattered by the particle. This phase difference is then used to determine the diameter of the particles based on whether the scattering is dominated by reflection or refraction. If only two detectors are used, then the diameter that can be unambiguously measured is restricted to a phase shift of 2π. Thus, a third detector is employed to remove ambiguity and increase the measurable size range as well as the measurement resolution. The PDPA system employed here can be operated in both PDA and LDA modes. Since a measurement under the PDA mode is carried out only when the particle is detected by all three detectors, the data acquisition rate under PDA mode of operation is lesser than when operating under the LDA mode. For measurements that only require the velocity information, the acquisition system is programmed to operate under LDA mode to improve the data rate. The reader is referred to Albrecht et al. (2013) for further details on the measurement principle and Vignat (2020) for further details on the measurement device used here. In LDA/PDA, a measurement is acquired only when a particle passes through the measurement volume, and hence the acquisition is non-uniformly sampled. It is pointed out that for the FDF determination in this thesis, the photomultiplier signal is acquired along with the velocity signals using the PDPA system. The non-uniformly acquired signals are later resampled to have a uniform sampling rate. It was verified that this could be achieved by simple linear interpolation.

1.6.2.2 Deployment in the test rigs

In both SICCA-Spray and TICCA-Spray, hot wire probes are mounted in the plenum (only for the central injector in the case of TICCA-Spray) at about $120\,\mathrm{mm}$ from the chamber backplane. The plenum is constricted just ahead of this section with a diameter of $32\,\mathrm{mm}$ to achieve a nearly flat velocity profile. In addition, acoustic velocity is also determined at this location using the multi-microphone method. In the chamber, velocities are measured using the PDPA system by operating in LDA mode or by operating in PDA mode when information on droplet diameter is simultaneously required. For these measurements, the spray of liquid fuel droplets itself acts as the tracer under hot-fire conditions, or the air flow is seeded with fine silicone oil droplets when the measurement is carried out under cold flow conditions. This is under the assumption that the fuel/oil droplets faithfully follow the flow and is valid if the droplets have a low Stokes number. In periodically modulated flows like the ones investigated here, this requires that the particle momentum relaxation time $\tau_m = \rho_p d_p^2/(18\mu_a)$ be much smaller than the oscillation period T or that the phase associated with this relaxation process $\varphi_m = \omega\tau_m$ be small. In the above equation, ρ_p and d_p are respectively the density and mean diameter of the particle, and μ_a is the viscosity of air. The measured mean droplet size is typically $d_p \approx 5\,\mu\mathrm{m}$ in the region of interest ($2.5\,\mathrm{mm}$ above the backplane at a radius of $4 \leq r \leq 3$ in the chamber). Considering the density of

heptane and viscosity of air at ambient temperature[1], one finds that $\tau_m \simeq 0.051\,\mathrm{ms}$, which is much smaller than the oscillation $T = 2\,\mathrm{ms}$ at $500\,\mathrm{Hz}$. The phase associated with the momentum relaxation process $\omega\tau_m$ would be $\varphi_m \simeq 0.051\pi$ at that frequency. This value is relatively small, and its impact on the measured velocities may be considered to be negligible. The oil seeding is usually achieved by an air nebulizer (Durox et al. 1999) which is designed to deliver only fine droplets of the order of $2.5\,\mu\mathrm{m}$ mean diameter. On the other hand, with the fuel spray delivered by the atomizer, the diameter of the droplets cannot be controlled, and it depends on the position in the chamber. Thus, it is necessary to ensure in advance that the location of velocity measurement for LDA is such that the fuel droplets are small enough. For certain measurements under cold flow conditions in the chamber, a hot wire probe also provides velocity signal records.

1.6.3 Flame chemiluminescence

The measurement of chemiluminescence from the flame is of central importance in the analysis presented in this thesis, as the flame chemiluminescence intensity is often considered to provide access to the heat release rate fluctuations. This quantity is usually deduced from the chemiluminescence emission intensity of excited radicals like OH^* or CH^*. The relation between this signal and the heat release rate is well established for lean premixed flames but is questionable in the case of spray flames. Chapter 2 deals with this issue and focuses on the chemiluminescence of spray flames. The light intensity measurements are generally carried out with photomultiplier (PM) tubes that have a high frequency response. The signal measured by the PM is the light intensity that is spatially integrated over the entire flame.

In MICCA-Spray, the flame chemiluminescence is captured by an array of eight *Hamamatsu* type H10722-110//001 photosensor modules (marked as PM1 to PM8 in Fig. 1.1 (d)) measuring the light intensity from one side of the annular chamber. Each sensor is fitted with an optical OH^* filter centered at $308\,\mathrm{nm}$ and a half-width of $10\,\mathrm{nm}$ to separate the emission of OH^* radicals from background radiation. As seen in Fig. 1.1, each PM is fitted with a mask in the front that acts as a spatial filter to capture the light emissions only from a single flame. In addition, a metal tube is placed inside the inner chamber wall so that the PMs do not see the light intensity from the flames on the opposite side. In SICCA-Spray, the flame emission is mainly captured by a *Thorn EMI Electron Tubes* type QL30F PM fitted with an OH^* filter centered at $308\,\mathrm{nm}$ with a half-width of $10\,\mathrm{nm}$. An additional PM of *Hamamatsu* make is also employed to capture CH^* ($430\,\mathrm{nm}$ with a width of $10\,\mathrm{nm}$) emissions from the flame. In TICCA-Spray, the chemiluminescence is captured by a *Hamamatsu* type H11902-110 PM fitted with an OH^* filter centered at $308\,\mathrm{nm}$. Like in MICCA-Spray, a mask is placed in front of the PM such that it

[1] $\rho_p = 684\,\mathrm{kg\,m^{-3}}$ for heptane and $\mu_a = 1.872 \times 10^{-5}\,\mathrm{kg\,m^{-1}\,s^{-1}}$.

only receives light emitted by the central flame (see Fig. 1.3).

1.6.4 Flame images

The chemiluminescence from the flame is also employed to obtain flame images using an intensified charge-coupled device (ICCD) camera. The camera used for this purpose is a PI-MAX 4® ICCD camera from *Teledyne Princeton Instruments*, having a resolution of 1024 $\times$ 1024 pixels. The camera is usually mounted with either OH^* ($310\,\mathrm{nm}$) or CH^* ($430\,\mathrm{nm}$) filters to capture the chemiluminescence from the respective radicals. This device is triggered internally when obtaining the steady flame images and externally using a microphone, PM, or a wave generator signal to obtain images at different phase instants in the acoustic cycle.

1.6.5 Temperature measurements

Temperature measurements are carried out at several locations on the test rigs either to determine wall temperatures or gas temperatures. Chamber wall temperature is measured in all three test rigs as a control sensor to ensure whether the system is thermally stabilized. This is accomplished by using a K-type thermocouple from *TC-direct*. In SICCA-Spray, the gas temperature is deduced from a double-bead R-type thermocouple (platinum-rhodium alloy) usually placed $25\,\mathrm{mm}$ below the chamber exit (for radiation correction, see Lemaire and Menanteau (2017)). Additionally, the chamber wall temperature profile in SICCA-Spray is measured using *TMC Hallcrest* MC153-14 thermal history paint, which undergoes permanent changes with thermal exposure. The paint is uniformly coated along a cylinder generatrix of the quartz tube on the inner side. The temperature profile can be determined after at least ten minutes of heating by visually comparing it with a color scale supplied by the manufacturer. This method does not provide a precise temperature estimate but can be used to quickly deduce the temperature without the need for complicated thermometry. The thermal paint can be used to determine the temperature in the range from $\leq 160\,^{\circ}\mathrm{C}$ to $1240\,^{\circ}\mathrm{C}$. Finally, the temperature of the backplane in SICCA-Spray is determined by applying a thermal crayon on the top surface of the injector terminal plate.

Chapter 2

Chemiluminescence interpretation

Contents

A few sections of this chapter have been included as a part of an article published in Combustion and Flame with the title "Swirler effects on combustion instabilities analyzed with measured FDFs, injector impedances and damping rates" by Preethi Rajendram Soundararajan, Daniel Durox, Antoine Renaud, Guillaume Vignat and Sébastien Candel, vol. 238, April 2022.

Determination of unsteady heat release rates from the flame is a central issue in combustion dynamics as it specifically intervenes in the determination of the flame describing functions. Heat release rate measurements have been traditionally obtained by estimating the light intensity of excited radicals (such as OH^* or CH^*) from the flame at a given equivalence ratio, exploiting the linear dependence of chemiluminescence with the heat release rate. This has been well established for perfectly premixed flames, but the validity of this assumption for technically premixed or spray flames is often questioned. This is because of spatial or temporal inhomogeneities in the mixture ratio or equivalence ratio that may be present in these flames, invalidating the linear assumption. The correlation is investigated in the present case by measuring the spatial and temporal equivalence ratio variations of the spray flames with liquid heptane and dodecane as fuels. This is performed by considering the ratio of light intensities of CH^* and OH^*, which has been proven to be linked to the equivalence ratio. A previous study (Vignat 2020) with the same type of injector producing similar spray flames under steady-state conditions revealed that the global OH^* chemiluminescence is better suited for heat release measurement than CH^* as it maintains the linear relation with heat release rate. An extension is now carried out in the present thesis using an intensified CCD camera to validate this relationship, first by identifying the presence of spatial inhomogeneities in the spray flames under steady conditions, followed by a scenario where the flame is modulated. The modulated case also allows investigating any significant temporal equivalence ratio fluctuations as only the air flow is modulated and the fuel flow remains unchanged. Subsequently, global chemiluminescence measurements using photomultipliers are also carried out to compare the spray flames with premixed propane-air flames. Results show that the particular spray flames considered here behave in a quasi-premixed fashion, with negligible equivalence ratio fluctuations due to the recessed position of the fuel atomizer inside the injector. Although chemiluminescence can be used as a heat release rate marker for the present case, its validity for technically premixed flames may not be generally applicable if they exhibit strong equivalence ratio variations.

2.1 Introduction

In combustion dynamics, the measurement of heat release rate (HRR) fluctuations in response to acoustic perturbations is vital if one wishes to determine flame transfer/describing functions (FTFs/FDFs) in a direct manner. One possibility of acquiring HRR from the flame is by measuring the chemiluminescence originating from excited radicals such as OH^* or CH^* that are present in the flame zone. This was demonstrated early on by Hurle et al. (1968) on open turbulent ethylene-air

premixed flames as a means to determine the source of combustion noise. The authors postulated that a measure of some species concentrated in the reaction zone could be used to determine the rate of consumption of combustible mixture. This led to the employment of C_2^* and CH^* light emissions from the flame, provided that they are present in sufficiently small quantities so that their emission intensity is not affected by self-absorption. Photomultipliers equipped with appropriate narrow-band filters were used to show that light emissions from these free radicals are proportional to the rate of consumption of the combustible gas mixture and, thus, to the HRR. The linearity between HRR and light intensity from the flames is only valid when the combustible mixture is burning at a constant equivalence ratio. This relationship was exploited to study several phenomena, such as the noise generated from turbulent flames (Hurle et al. 1968; Price et al. 1969), as an optical sensor for measuring equivalence ratio (Clark 1958; Muruganandam et al. 2005), and was further deployed as a means of a closed-loop diagnostic tool through equivalence ratio monitoring (Docquier et al. 2002) and as an active-feedback-control parameter (Higgins et al. 2001). Lawn (2000) successfully utilized the spatial cross-correlation of OH^* chemiluminescence emissions from two lines-of-sight photodiodes for a premixed swirling flame based on a novel approach of using root mean square intensity fluctuations to obtain mean HRR. In a study conducted by Hardalupas and Orain (2004) with premixed counter-flow flames fueled by natural gas, it was shown that the emissions from OH^*, CH^* and background intensity from CO_2^* could be considered a good indicator of HRR, whereas the chemiluminescence intensity from C_2^* was found to be inappropriate. While many works obtained chemiluminescence measurements integrated over the entire flame (Docquier et al. 2002; Ding et al. 2019), some have also obtained it using Cassegrain optics, where the signal is acquired from a small flame region (Kojima et al. 2000; Hardalupas and Orain 2004) and tomographic techniques (Obertacke et al. 1996; Anikin et al. 2010) to detect the two-dimensional distribution of excited radicals. Several of these efforts have been thoroughly reviewed by Docquier and Candel (2002) and Ballester and García-Armingol (2010). The specific case of chemiluminescence representing HRR of flames subjected to acoustic perturbations was considered, for example, by Balachandran et al. (2005) on a turbulent premixed bluff-body-stabilized flame. This reference contains a comparison between HRR measurements obtained from three different techniques, OH^* and CH^* chemiluminescence, OH planar laser-induced fluorescence (PLIF), and simultaneous OH and CH_2O PLIF measurements, and concluded that the global HRR obtained by chemiluminescence of excited radicals agreed well in both magnitude and phase for premixed flames. They also inferred from the OH PLIF measurements that the local effects of strain and curvature that are known to change the burning velocity might not majorly impact the global HRR variations. A contrary observation to the above conclusions was made by Najm et al. (1998), who indicated through numerical simulations and experiments that, for the specific case of premixed N_2-diluted methane-air flame at stoichiometry, the OH^*, CH^*, and C_2^*

are not reliable markers of HRR as their presence in the flame does not relate to the chemical pathway of carbon oxidation. It is shown that for the case of their highly curved flame, HCO PLIF directly correlates with the overall flame burning rate and heat release rate. Higgins et al. (2001) showed that for their studied case of a laminar counter-flow premixed flame, the CH^* chemiluminescence did not show any significant dependence on strain rate but indicated that for the case of a turbulent flame, a dependence on curvature could be expected. Thus, it is unclear whether the above conclusions are valid only for the considered configurations or applicable in general.

Although many works validate the adequacy of chemiluminescence to represent HRR for perfectly premixed flames, where fuel and air are mixed well ahead of the combustion chamber, the literature available for the case of spray flames that are only technically premixed is more limited. The mixing of fuel and air happens just ahead of combustion in the latter case, resulting in variations of equivalence ratio across the flame. As chemiluminescence only suitably represents HRR at a constant equivalence ratio, it is questionable to use it for the flames that might contain spatial stratification and where the linear relationship between light intensity and HRR will not be applicable. The case of a flame with mixture gradients was considered by Lauer and Sattelmayer (2010), who studied the applicability of spatially resolved HRR measurements based on chemiluminescence in turbulent swirled natural gas flames. The authors compare a technique of HRR measurement based on the first law of thermodynamics that involves the measurement of flow velocity, progress variable of combustion, and air excess ratio with chemiluminescence. Although the integral HRR and the integral chemiluminescence intensity show an identical monotonic behavior, the axial heat release rate distribution is not well captured by the light intensity measurements. This is attributed to the high turbulence intensity in the reaction zone, causing a shift in chemiluminescence distribution. The case of a swirling spray was evaluated by Mirat et al. (2014) for two flame types, one case where the flame is less sooty and visibly blue, and another case where the flame manifests a yellow sooty regime. Systematic measurements indicate that both OH^* and CH^* light intensities exhibit a linear behavior in the non-sooty regimes, whereas, in the sooty regimes, only OH^* can be used as a valid indicator of HRR. However, the authors also indicate that, for the case of a flame subjected to acoustic modulations, such a quasi-steady analysis is suitable only at low frequencies, and its appropriateness at higher frequencies needs validation. The same authors (Mirat et al. 2015) used the FDF obtained by measuring OH^* chemiluminescence in an acoustically coupled cavity model and retrieved most of the experimental observations on the thermoacoustic state of the system. This gives an indirect validation that OH^* chemiluminescence can indeed be used as a tracer of HRR fluctuations for spray flames at globally fuel-lean conditions. However, Nori and Seitzman (2009) showed through 1D simulations of the CH^* chemiluminescence mechanism incorporated into a flame

chemistry model that a small variation in equivalence ratio could lead to a much larger error in HRR determined using chemiluminescence due to its dependency on local equivalence ratio. The above inference was also made by Yi and Santavicca (2009), who found that on a liquid-fueled lean direct injection combustor, the difference between heat release rate and CH^* chemiluminescence can be more than 20% in gain and greater than 90 $^\circ$ in phase at frequencies greater than $400\,\mathrm{Hz}$. They also observed that the deviation is comparatively lower when there is a self-sustained combustion oscillation. This implies that chemiluminescence might not be a good indicator of HRR for flames with pronounced stratification. It is thus important to verify whether the technically premixed flames considered here manifest any spatial variations of equivalence ratio and ensure the linear relation of chemiluminescence with HRR. Quite often, for obtaining the FDF, only the air flow is modulated, and as the liquid fuel is injected under pressure, the fuel line is generally "stiff" and remains unresponsive to acoustics. This might also cause a wave of spatial and temporal equivalence ratio fluctuations at various instants of the acoustic cycle. In this case, the FDF cannot only be considered a function of velocity fluctuations or volumetric flow rate fluctuations but also as a function of equivalence ratio. The flame has to be treated as a multiple-input single-output (MISO) system defined by a heat release rate that depends on two inputs,

$$\dot{Q}'/\overline{\dot{Q}} = \mathcal{F}_\phi(\phi'/\overline{\phi}) + \mathcal{F}_v(\dot{q}_v'/\overline{\dot{q}_v}) \tag{2.1}$$

One of the means that can be employed to obtain the equivalence ratio in the flame relies on simultaneous measurements of the chemiluminescence of two radicals to determine ratios between two light intensities, such as CH^*/OH^* or $C2^*/OH^*$, etc. This was considered early on, for example, by Clark (1958), who found that C_2^* and CH^* ratios were an accurate index of equivalence ratio of combustible gases. Further studies have considered and validated this technique for different fuels and for both laminar and turbulent flames. This was used later by Kojima et al. (2000), who measured the light intensity of OH^*, CH^*, and C_2^* from a laminar premixed methane-air flame and found a strong correlation between the peak intensity ratios in the reaction zone to the equivalence ratio, indicating that these parameters could be used to investigate the local flame stoichiometry. It was also found that among the three ratios, C_2^*/CH^* was most sensitive to equivalence ratios greater than 0.9 and that OH^*/CH^* could be used for a wider range of equivalence ratios. The usage of emission intensity ratios of excited radicals was also investigated by Hardalupas and Orain (2004) on natural gas counter-flow flames, who found that the ratio OH^*/CH^* exhibited a monotonic dependence with equivalence ratio, while the ratio of C_2^*/CH^* could not be used as metric of equivalence ratio due to its strong dependence on strain rate. Chemiluminescence sensing to determine equivalence ratio was also validated by Muruganandam et al. (2005) for both natural gas and heptane-fired combustors at varying pressures. This technique is exploited in the present work to quantify the equivalence ratio variations.

It is also worth examining at this point whether any alternative techniques from the literature can be used to measure HRR. One such method was illustrated by Li et al. (2012) using ultrasonic waves in unconfined flames. This technique is based on measuring the travel time of ultrasonic waves when passing through flames. A relation was established by knowing the flame shape between low-frequency HRR disturbances generated by hydrodynamic instabilities driven by buoyancy forces. However, the extension of this technique to forced flame configurations is not straightforward, and in addition, it also requires prior knowledge of the flame shape. Another technique is the interferometric determination of HRR demonstrated by Leitgeb et al. (2013) and Li et al. (2015) on a pulsed premixed flame. A laser vibrometer was employed to measure the density fluctuations in the flame, which can, in turn, be related to HRR, assuming that the entropy fluctuations are mainly caused by variations in HRR. The HRR obtained by this technique was then validated with the chemiluminescence measurement of CH^* on a premixed flame. Laser interferometric vibrometry (LIV) measuring density fluctuations in flames was also used to obtain flame transfer functions (FTFs) of both perfectly and partially premixed flames, and a comparison with the classical chemiluminescence technique was presented by Peterleithner et al. (2016). The FTF deduced from LIV and chemiluminescence in the perfectly premixed cases matched well, as one would typically expect. For the case of technically or partially premixed flames, the overall trends in FTF were retrieved in terms of gain and phase, except for an overshoot at certain frequencies, which was later found to be due to the presence of equivalence ratio waves in the flame. However, this technique has only been demonstrated so far on unconfined premixed flames, and the presence of a spray of droplets would complicate the LIV measurement. The LIV technique also has other disadvantages, such as the sensitivity to temperature and Gladstone-Dale constant, which links the measured LIV voltage to density. Several researchers have also used laser-induced fluorescence to obtain HRR information from flames. This has been exemplified, for example, by Najm et al. (1998), who has shown that HCO PLIF gives a direct estimate of HRR from flames, by Ayoola et al. (2006) who obtained spatially resolved measurements using simultaneous OH and CH_2O PLIF, which is highly correlated with HRR. It has also been reported in the literature (see, for example, Paschereit et al. (2002), Schuermans et al. (2010)) that FTFs could be obtained indirectly by purely acoustic techniques, such as the flame transfer matrix (FTM) framework, by treating the flame as a black box and assuming that the flame response is only produced by the incident acoustic waves. This technique involves the usage of a multi-microphone method at two independent acoustic states of the system to determine the FTM from which the FTF can be synthesized without the need for measuring HRR fluctuations. This, however, requires an additional measurement of the injector transfer matrix and its inversion to extract the flame transfer matrix. The implementation of the above optical and acoustic techniques is not readily possible in the experimental arrangement of SICCA-Spray. PLIF, in addition to

being a technically demanding experimental technique, also poses the difficulty of requiring a 2D laser sheet which would be difficult to implement in SICCA-Spray because of its cylindrical geometry. It is also difficult to attain two independent acoustic states in the SICCA-Spray combustor, i.e., with acoustic modulation both upstream and downstream of the combustor. Although driver units are already present upstream in this setup, the presence of hot exhaust gases might potentially damage the driver units when placed downstream of the combustion chamber. The noise from combustion might hamper obtaining signals by a sufficient amount so that the coherence function between the microphone signals and the modulation takes low values. This only leaves the option of obtaining HRR measurements through chemiluminescence, but this first requires the verification of the level of stratification present in these flames.

This chapter begins with a brief description of the experimental setup in Section 2.2, followed by the assessment of the spray flames under steady and forced conditions in Section 2.3 at various instants of the acoustic cycle. Finally, in Section 2.4, the case of spray flames is compared with that where the flame is fully premixed.

2.2 Experimental setup

Experiments are carried out in the SICCA-Spray combustor equipped with a short combustion chamber of length $l_c = 150\,\mathrm{mm}$, whose generic experimental setup is described in Chapter 1. Under nominal operation, the atomizer is mounted at a distance of $6.75\,\mathrm{mm}$ from the combustor backplane. The measurements pertain to the operating point F1 ($\mathcal{P} = 6.4\,\mathrm{kW}$, $\phi = 0.85$ (global), and $\dot{m}_a = 2.6\,\mathrm{g\,s^{-1}}$) with swirlers 707 and 716, as these are widely used throughout this work. Liquid heptane and dodecane are delivered as hollow cone sprays into the combustion chamber by the fuel atomizer. When using premixed propane, the atomizer remains non-operational, and the fuel and air are mixed well ahead of the plenum. For the case of spray flames, any reference to equivalence ratio refers to the global equivalence ratio unless otherwise explicitly stated. Data are acquired in two steps —firstly, with an ICCD camera equipped with CH^* (centered at $434\,\mathrm{nm}$) and OH^* (centered at $310\,\mathrm{nm}$) interference filters. The measurements are carried out with the two filters, one after the other, while the camera takes images of the same region. One can then determine the ratio of the two light intensities and link this ratio to the equivalence ratio. The camera is equipped with a Nikon 105 UV lens and operates with a set gate width of $40\,\mu\mathrm{s}$ while permitting 1000 gates per exposure. Measurements are first carried out under steady state conditions after which the air flow is modulated at two frequencies, $500\,\mathrm{Hz}$ and $700\,\mathrm{Hz}$, using the driver units mounted at the bottom of the combustor (see Fig. 1.2). Flame images corresponding to the two radicals are obtained at different phase instants of the modulating signal. Since only the air flow rate is modulated and the fuel line

impedance is stiff, this measurement would help to determine the presence of any spatial/temporal inhomogeneities in the equivalence ratio that needs to be considered in the FDF estimation. A calibration measurement is also performed under steady conditions at different global equivalence ratios and fuel mass flow rates to represent the light intensity ratio in terms of equivalence ratio. These measurements are performed at five different fuel flow rates, and at each fuel flow rate, the air flow rate is varied to obtain different equivalence ratios. In the second step, photomultiplier tubes equipped with OH^* (centered at $308\,\mathrm{nm}$ with a half-width of $10\,\mathrm{nm}$) and CH^* (centered at $430\,\mathrm{nm}$ with a half-width of $10\,\mathrm{nm}$) filters are used to compare the fluctuations in light intensity ratio between cases of perfectly premixed propane-air flames and spray flames. The photomultipliers are placed side-by-side such that they both capture light intensity from the entire flame region. During these measurements, a signal generator connected to the driver units produces modulation signals at three frequencies 300, 500, and $700\,\mathrm{Hz}$, and at an amplifier voltage of $V_0 = 3\,\mathrm{V}$. The data are recorded over a period of $2\,\mathrm{s}$ at each frequency at the rate of 16,384 Hz. Mass flow rates of the three fuels are slightly adjusted such that the thermal power remains the same in all the cases.

2.3 Spatial and temporal equivalence ratio fluctuations

The presence of inhomogeneities in the equivalence ratio of the spray flames is here assessed with the ICCD camera equipped with CH^* and OH^* filters giving spatial information of the light intensity distribution. Results are first presented for the case of a steady flame, followed by the case where the flame is modulated at different frequencies. A calibration performed under steady conditions for representing the light intensity ratio in terms of equivalence ratio is also described in this section.

2.3.1 Assessment with steady flames

The specific case of spray flames considered in this study has already been thoroughly examined in a previous doctoral thesis (Vignat 2020) using a quasi-steady approach to verify the linear dependence of chemiluminescence with respect to HRR. The major findings from this work are briefly described to put the current work in perspective. In that work, OH^* and CH^* chemiluminescence was recorded with liquid heptane as fuel and compared with the case of premixed propane-air at different fuel mass flow rates. It was verified using a flue gas analyzer that the combustion efficiency of the combustor was close to unity and, thus, that the heat release rate from the flame could be considered to be proportional to the fuel mass flow rate. The measurements carried out with the two swirler configurations at different fuel mass flow rates indicate that the OH^* featured a lesser deviation

from linearity for the heptane spray flames and closely resembled the premixed propane flame. With CH*, the chemiluminescence signal was not quite proportional to HRR with both premixed as well liquid fuel injection. The nonlinearity of the CH* was attributed to the highly turbulent nature of the flame resulting in a possible overestimation by 20% to 40% in the fluctuating portion. However, a quadratic fitting method was established to apply a correction to the measured light intensities, which would then be representative of the HRR. Although from the study of Vignat (2020) it is seen that the linear relationship with respect to HRR is retained by the OH* chemiluminescence intensity, the measurements with PM give a measure of global chemiluminescence intensity, and it can be expected that for a spray flame, there might be some local variations of equivalence ratio in the flame. This is investigated in the present work, with the ICCD camera fitted with CH* and OH* filters by determining the ratio of the corresponding intensities. As already indicated, this ratio is a known measure of the equivalence ratio of hydrocarbon flames (for example, Hardalupas and Orain (2004)).

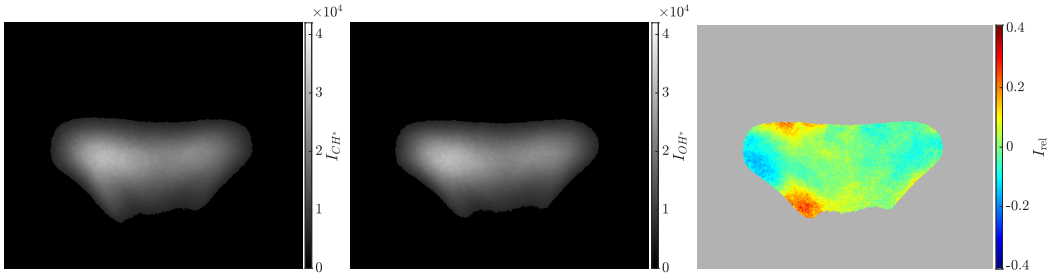

(a) CH intensity* *(b) OH* intensity* *(c) Rel. intensity deviation*

Figure 2.1. *(a-b) Flame images showing CH* and OH* chemiluminescence intensity obtained with the ICCD camera. (c) Relative intensity deviation obtained using Eq. 2.2. Flame images are captured with swirler 716 under steady conditions with liquid heptane as fuel.*

Figures 2.1 (a) & (b) show the CH* and OH* chemiluminescence intensity obtained with the ICCD camera under steady conditions. The images are obtained with swirler 716 while operating with liquid heptane as fuel. A filtering operation is applied to the flame images to only retain the portions that contain at least 20% of the maximum intensity. One observes that the intensity levels remain almost the same between the CH* and OH* images, possibly indicating that the spatial variation in equivalence ratio is negligible. To further confirm this, the relative intensity deviation is obtained between the CH* and OH* light intensity images as,

$$I_{\text{rel}} = \Big[\frac{I^{x,z}_{CH^*}}{I^{x,z}_{OH^*}} - \frac{\overline{I^{x,z}_{CH^*}}}{\overline{I^{x,z}_{OH^*}}}\Big] \Big/ \Big[\frac{\overline{I^{x,z}_{CH^*}}}{\overline{I^{x,z}_{OH^*}}}\Big] \tag{2.2}$$

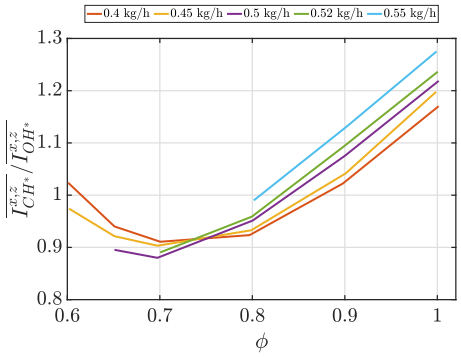

Figure 2.2. *Variation of the mean CH*/OH* ratio with respect to equivalence ratio ϕ at different levels of fuel flow rate determined under steady conditions. The spatially resolved images are recorded with an intensified CCD camera and the mean of the flame image at each operating point is calculated to obtain $\overline{I^{x,z}_{CH^*}}/\overline{I^{x,z}_{OH^*}}$. Measurements pertain to swirler 716.*

Here, $\overline{(.)}$ refers to the spatial averaging of a flame image. Figure 2.1(c) shows the relative deviation I_{rel}, which is only minor, mostly less than 10% in the flame zone. A higher level of deviation is observed in certain regions of the flame close to the periphery, where the data reliability is also low due to the reduced intensity signals obtained in these regions. Thus, one can consider that the spatial inhomogeneities in these spray flames are low.

2.3.2 Calibration curve for equivalence ratio

In order to represent the light intensity ratio in terms of equivalence ratio, a calibration is performed under steady conditions with swirler 716. For these experiments, the same camera equipped with CH* and OH* filters is used at different fuel flow rates, and at each fuel flow rate, the air flow rate is varied to obtain different equivalence ratios. Keeping the fuel flow rate constant at the different equivalence ratios ensures even atomization quality of the spray.

Figure 2.2 shows the variation of spatially averaged $\overline{I^{x,z}_{CH^*}}/\overline{I^{x,z}_{OH^*}}$ with ϕ at different levels of fuel flow rate. It is to be noted that, when operating at lower fuel flow rates, the flame is not well stabilized at $\phi < 0.7$, and the measurements are less reliable. However, in the present thesis, the combustor is operated at $0.85 \leq \phi < 1$ and mostly near $\dot{m}_f = 0.52\,\text{kg}\,\text{h}^{-1}$, where the data quality is adequate, and the slope is nearly linear between ϕ = 0.8 and 1. The relationship between the intensity ratio and equivalence ratio is obtained using this calibration curve and is found to be $\Delta\overline{I^{x,z}_{CH^*}}/\overline{I^{x,z}_{OH^*}} \approx 1.17\Delta\phi$ at $\dot{m}_f = 0.52\,\text{kg}\,\text{h}^{-1}$. This is used in the subsequent section to represent the light intensity ratio in terms of equivalence ratio and analyze the presence of equivalence ratio fluctuations when the system is modulated.

Table 2.1. *OH*, CH*, relative intensity deviation, and equivalence ratio deviation for heptane spray flame with swirler 716 measured when the flame is acoustically forced at* $500\,\mathrm{Hz}$ *and* $u'/\overline{u} \approx 0.22$ *at different phase instants* φ_g *of the reference generator signal. The fuel flow rate is* $0.52\,\mathrm{kg\,h^{-1}}$ *and the global equivalence ratio is 0.85.*

φ_g	I_{CH^*}	I_{OH^*}	I_{rel}	$\Delta\phi$
	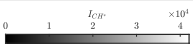		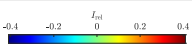	
0	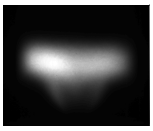	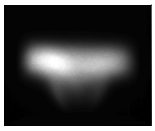	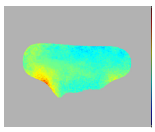	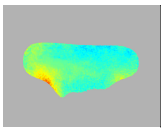
$\pi/4$	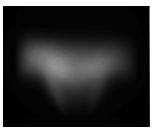	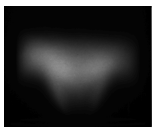	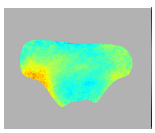	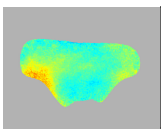
$\pi/2$			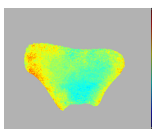	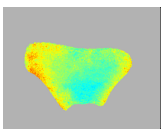
$3\pi/4$	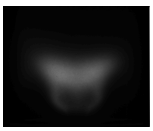	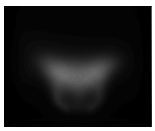	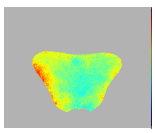	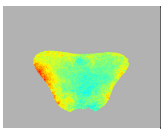
π	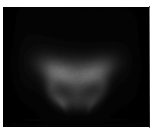		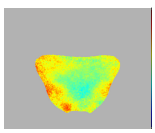	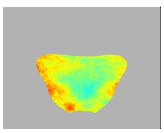
$5\pi/4$	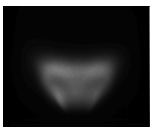	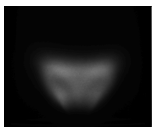	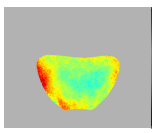	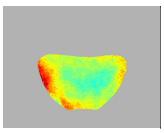
$3\pi/2$	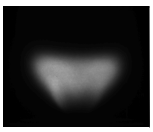	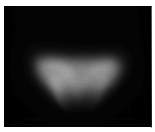	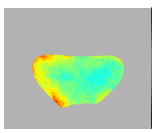	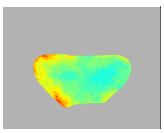
$7\pi/4$	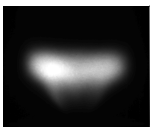	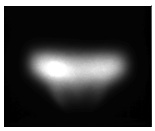	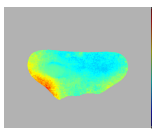	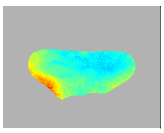

2.3.3 Assessment with modulated flames

As the fuel line is stiff, any modulation in air flow rate can possibly give rise to a wave of equivalence ratio fluctuations at various instants of the oscillation

cycle. This would mean that, in addition to the HRR variations caused by the velocity fluctuations at the flame base, one would also have to consider the flame response to equivalence ratio fluctuations as given by Eq. 2.1. To verify this, experiments are carried out at different phase instants of the generator signal while acoustically modulating the flame at two frequencies —500 Hz and 700 Hz. For these measurements, the amplifier voltage is fixed at its maximum allowable value of $V_0 = 3\,\mathrm{V}$ resulting in a velocity fluctuation level of $u'/\overline{u} \approx 22\%$ at 500 Hz and 17% at 700 Hz.

The first and second columns of Tab. 2.1 show the chemiluminescence intensity with CH^* and OH^* filters, respectively, for the heptane spray flame at 500 Hz. A filtering operation is performed on the raw images as in Section 2.3.1 to only retain the portions that contain at least 20% of the maximum intensity at each phase instant. As seen from the chemiluminescence images, the intensity distribution does not vary much between the two quantities. Next, the relative intensity deviation I_{rel} of the local to the mean intensity averaged over the oscillation cycle, calculated using Eq. 2.2, is presented in the third column of Tab. 2.1. For the pulsed flame images, the mean intensity ratio $\frac{\overline{I^{x,z}_{CH^*}}}{\overline{I^{x,z}_{OH^*}}}$ is a spatial average that is averaged over all phase instants (i.e., $\overline{\frac{I^{x,z}_{CH^*}}{I^{x,z}_{OH^*}}}^{\varphi_g}$). The deviation is minor, mostly less than 10% in the flame zone, except in small regions close to the periphery, where the deviation is slightly higher (the captured light intensity is also smaller in these regions). The calibration relation outlined in Section 2.3.2 is used to obtain the value of equivalence ratio ϕ from these flame images. The spatial evolution of the relative equivalence ratio deviation shown in the fourth column of Tab. 2.1 indicates that the spatial variation is small and that there is no visible stratification. Similar observations can also be made at 700 Hz, as shown in Fig. 2.3, where the spatial variation in equivalence ratio is minimal. The comparatively higher deviation in equivalence ratio observed near the periphery is attributed to the lower signal intensity in this region.

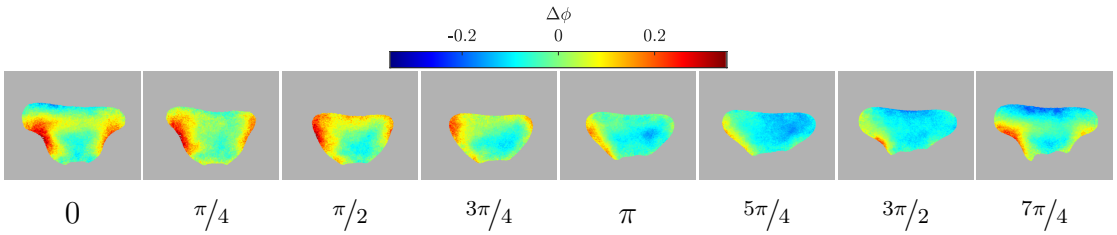

Figure 2.3. *Equivalence ratio deviation for heptane spray flame with swirler 716 measured when the flame is acoustically forced at* 700 Hz *with a measured* $u'/\overline{u} \approx 17\%$ *at the injector exit. The images are shown at different phase instants of the reference generator signal.*

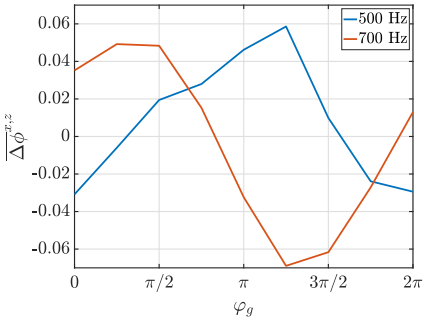

Figure 2.4. *Variation in spatially-averaged equivalence ratio with swirler 716 shown at different phase instants of the reference modulation signal at two frequencies.*

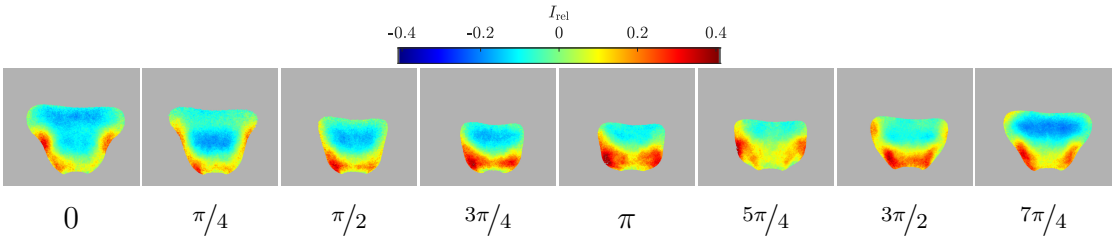

Figure 2.5. *Relative chemiluminescence intensity deviation for heptane spray flame with swirler 716 measured when the flame is acoustically modulated at* $500\,\mathrm{Hz}$ *and the atomizer is located at a distance of* $2.75\,\mathrm{mm}$ *from the backplane.*

Given that the spatial variation of equivalence ratio is not very significant for these spray flames, one can obtain the overall equivalence ratio of the flame at each instant of the oscillation cycle, as shown in Fig. 2.4 at the two frequencies considered. A minor variation can be observed with respect to the phase of the reference signal at the two modulation frequencies. From these results, a relative global equivalence ratio fluctuation $\dfrac{\Delta\phi_{gl}}{\overline{\phi}}$ (where $\overline{\phi} = 0.85$) can be obtained and is equal to 0.04 at $500\,\mathrm{Hz}$ and 0.05 at $700\,\mathrm{Hz}$, much lower than the relative velocity fluctuation of $u'/\overline{u} = 22\%$ at $500\,\mathrm{Hz}$ and $u'/\overline{u} = 17\%$ at $700\,\mathrm{Hz}$. This result is similar to the observation reported by Vogel et al. (2021) for a kerosene spray flame having negligible equivalence ratio fluctuations compared to velocity fluctuations. Although strong variations in equivalence ratio could normally be expected in a spray flame the reason for finding only minor fluctuations can be attributed to the recessed location of the fuel atomizer inside the injector (similar to Vogel et al. (2021)) and the high volatility of heptane. Because of the recessed atomizer position, a part of the fuel spray impinges on the convergent cone of the terminal plate (Fig. 1.4 left). The spray particles might form a liquid film that undergoes secondary atomization due to the shearing action of the air flow resulting in small droplets. The part of spray that interacts with the cone is then controlled by air

flow coming out of the injector, and the amount of fuel exiting into the chamber is then nearly proportional to the amount of air, as observed by Lo Schiavo et al. (2020) through LES simulations on a similar injector. The other possibility occurring due to a spray-wall interaction is that the particles might hit the wall and bounce back or slide along the conical wall and then get swept away by the air flow. The exact mechanism of the spray-wall interaction is unclear, but this interaction appears to reduce the fluctuation in equivalence ratio compared to a case where the fuel is conveyed directly into the chamber without any impact. The weak equivalence ratio fluctuation observed in the present case is also demonstrated through numerical simulations performed with a similar injector by Vignat et al. (2021). In the case where fuel is conveyed directly into the chamber without any wall interaction, any fluctuation in air flow rate would indeed change the equivalence ratio. This argument is validated by performing measurements at a smaller atomizer recess of $2.75\,\mathrm{mm}$ distance against the nominal recess distance of $6.75\,\mathrm{mm}$ from the backplane. This arrangement would prevent the fuel spray from impacting the convergent cone, and the spray is then directly delivered to the combustion chamber. The relative deviation in the chemiluminescence intensities is shown in Fig. 2.5 when the atomizer is located at a recess distance of $2.75\,\mathrm{mm}$ from the backplane. One observes in this case that the relative I_{CH^*}/I_{OH^*} ratio indeed exhibits a higher deviation than at the nominal recess distance of $6.75\,\mathrm{mm}$ (see Tab. 2.1, column 3), especially between $\varphi_g = {}^{3\pi}/_{4}$ and ${}^{7\pi}/_{4}$, substantiating the previous interpretation. A wave of negative relative intensity (seen as blue zones in Fig. 2.5) can also be seen originating near the upper flame region at $\varphi_g = {}^{7\pi}/_{4}$ and moving towards the flame center until $\varphi_g = {}^{\pi}/_{4}$, remaining at that location as the flame size shrinks until $\varphi_g = {}^{3\pi}/_{4}$. Additionally, a pattern of positive relative intensity (seen as red zones in Fig. 2.5) arises close to the flame base at $\varphi_g = {}^{\pi}/_{2}$, moving slightly up and towards the periphery until $\varphi_g = {}^{7\pi}/_{4}$. The slightly higher positive relative intensity regions observed close to the periphery at $\varphi_g = 0$ and ${}^{\pi}/_{4}$ cannot be sufficiently distinguished from noise to consider that they are significant. Further details on the spray and flame behavior with recess distance, along with their visualizations, are provided in Chapter 8.

2.4 Comparison of spray flames with a premixed flame

Although the spatial and temporal inhomogeneities in equivalence ratio are negligible in the present spray flames when the atomizer is at its nominal position of $6.75\,\mathrm{mm}$, this has been only verified with liquid heptane, and it still needs to be confirmed for the case of liquid dodecane. Having established in Section 2.3.3 that the spatial inhomogeneities are minor at the nominal atomizer position, it is possible to examine the global intensities from the flame using photomultipliers fitted with appropriate filters. In addition, it is also instructive to compare the case of spray flames with a premixed flame of propane and air, where the chemilumines-

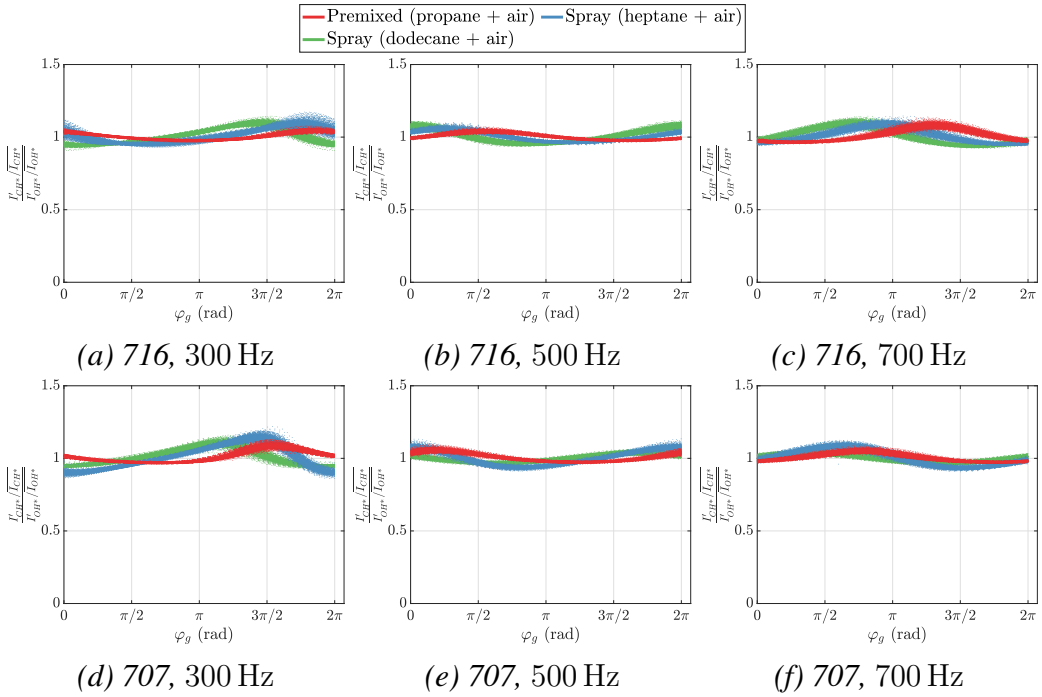

(a) 716, 300 Hz *(b) 716,* 500 Hz *(c) 716,* 700 Hz

(d) 707, 300 Hz *(e) 707,* 500 Hz *(f) 707,* 700 Hz

Figure 2.6. *Intensity ratio I_{CH^*}/I_{OH^*} (normalized by their respective mean) between perfectly premixed propane (red), heptane spray (blue), and dodecane spray (green) flames as a function of wave generator's phase φ_g. Results are shown in the top row for swirler 716 and in the bottom row for swirler 707 at three frequencies* 300 Hz, 500 Hz, *and* 700 Hz *and for an amplifier voltage of* $V_0 = 3\,\mathrm{V}$.

cence relation with HRR strongly holds. For this purpose, two photomultipliers equipped with OH^* and CH^* filters placed side by side capture the light emitted from the entire flame. The signal of the wave generator delivered to the driver units is also recorded simultaneously with the photomultiplier signals.

The top row of fig. 2.6 displays the ratio of light intensity normalized by mean intensities for 716 at select frequencies of 300 Hz, 500 Hz, and 700 Hz for an amplifier voltage of 3 V (peak-to-peak) as a function of the wave generator's phase φ_g. Since the instantaneous intensities are scaled by the ratio of mean intensities, the gains of the two photomultipliers do not intervene. A dispersion of the data points around an average value can be observed, but this is quite small. There is a ripple in the light intensity ratio during the oscillation cycle reaching about 10% of the average value with both heptane and dodecane. This variation during the cycle may reflect a variation in the equivalence ratio due to the air flow modulation, but it can also be linked to variations that are found in confined premixed flames when they are subjected to cyclic oscillations. This is because the fresh reactants entrain an amount of burnt gases from the outer recirculation zone. This is illustrated by examining the light intensity ratio of the fully premixed flame, which has a color and shape similar to the spray flame (images of premixed and spray flames are

shown in Chapter 9). A small variation in $(I(\mathrm{CH}^*)/I(\mathrm{OH}^*))/(\overline{I(\mathrm{CH}^*)}/\overline{I(\mathrm{OH}^*)})$ can be observed in the premixed case as well, at certain instants of the cycle. The ripple during the acoustic cycle is of the same order of magnitude as for the spray flame at the three frequencies considered. This confirms that the spray flames behave essentially like a premixed flame with a level of equivalence ratio variations that are small compared to the flow fluctuations. Similar features are also observed at lower amplifier voltages and other frequencies. The above measurement is also performed with swirler 707, which forms a “V"-shaped flame, which is different from that of the “M"-shaped flame corresponding to swirler 716 (flame images shown in Chapter 7). Results presented in Fig. 2.6 bottom row confirm that, for this swirler as well, the spray flames behave like premixed flames. They substantiate observations of Section 2.3.3, indicating that chemiluminescence can be used as a valid HRR marker for the specific spray flames considered here and that FDFs can be calculated by only considering velocity fluctuations as input.

2.5 Conclusions

The objective of this chapter is to see whether chemiluminescence constitutes a suitable marker for determining the heat release rate in the spray flames investigated in the present work. While this is well established in the literature for perfectly premixed flames, which operate at a constant equivalence ratio, one expects that spray flames might feature spatial equivalence ratio variations leading to errors in the determination of the heat release rate and subsequently of the flame describing functions. The verification is performed in the SICCA-Spray combustor with two swirlers, 716 and 707, producing two distinct flame shapes. In a previous work (Vignat 2020), a quasi-steady approach was used to verify the linearity of chemiluminescence intensity with heat release rate, and it was found that OH^* is a better marker for these spray flames than CH^*. This observation is further explored to see if spatial inhomogeneities in equivalence ratio arise when the flame is modulated. In the first step, an estimation of equivalence ratio is obtained by capturing flame images using an intensified CCD camera equipped with CH^* and OH^* filters, the ratio of which is a well-known measure of equivalence ratio for hydrocarbon flames. Results show that the light intensity ratio deviation is less than 10% in the flame zone for heptane spray flames, and a subsequent calibration to obtain the spatial equivalence ratio distribution reveals that both spatial and temporal inhomogeneities are negligible, and the fluctuations in equivalence ratio are much lower compared to the fluctuations in the flow velocity. This indicates that it is sufficient to just consider the relative velocity fluctuations as input to the flame describing functions. The reason for the current spray flames behaving in a quasi-premixed fashion is attributed to the recessed position of the atomizer inside the injector, which causes a part of the spray to hit the conical section of the convergent nozzle before exiting into the combustion chamber. This hypoth-

esis is confirmed by moving the atomizer further up and avoiding the impact of the fuel spray with the nozzle walls; the light intensity deviation, in this case, is much greater compared to the case with a higher recess. Finally, measurements performed at different frequencies with photomultipliers equipped with OH^* and CH^* show that a small ripple exists in the light intensity ratio of heptane and dodecane spray flames during the acoustic cycle but that it is of the same order of magnitude as the perfectly premixed propane-air flames. The findings of this chapter enable us to reasonably consider that the HRR fluctuations required for obtaining the flame describing function can be approximately obtained from the chemiluminescence intensity of OH^*. However, these results are only valid for the specific case of technically premixed flames considered here and cannot be generalized.

Chapter 3

Do flame describing functions represent combustion dynamics?

Contents

A part of this chapter corresponds to an article submitted for publication in the Journal of Sound and Vibration under the title "Do flame describing functions suitably represent combustion dynamics under self-sustained oscillation?" by Preethi Rajendram Soundararajan, Guillaume Vignat, Daniel Durox, Antoine Renaud, Sébastien Candel, and is under re-review. A preliminary version was also presented at the Colloque du réseau d'INitiative en Combustion Avancée (INCA) 2021 under the title "The flame describing function and flame dynamics under self-sustained oscillations" by Guillaume Vignat, Preethi Rajendram Soundararajan, Daniel Durox, Antoine Renaud, Sébastien Candel. The experimental setup of the SICCA-Spray combustor is briefly recalled in Section 3.2, and familiar readers can skip this part.

Transfer function concepts that appear in many areas and most notably in control systems have been extensively used to represent the flame response in low-order models of combustion instability. Much of the theoretical work is based on flame transfer functions (FTF). In recent years, its nonlinear extension, namely the flame describing function (FDF), has been used to get a more accurate representation of the flame response when the level of oscillation becomes large, and the system reaches a limit cycle. Despite their wide and reasonably successful use in predicting instabilities, the direct validity of using FTF/FDFs to represent the flame response still remains to be experimentally substantiated. This chapter is aimed at providing a direct assessment of the capacity of the FDF to suitably describe the flame behavior under self-sustained oscillations (SSOs) for a spray-swirl flame anchored by an injector that is weakly transparent to acoustic waves. This is accomplished by using an experimental combustion configuration that not only exhibits unstable oscillations but also features a set of driver units to modulate the flame (namely stable flame modulation or SFM). The flame is modulated at the frequency of SSO, and the amplitude of incident velocity modulations is then progressively varied until it coincides with that found under SSO. The injector dynamics is shown to be different between SSO and SFM for an injector that is weakly transparent to acoustic waves and imposes a certain degree of decoupling between plenum and chamber. For such injectors, the FDF built with the upstream velocity would not suitably represent SSO, as this lumps the injector and flame dynamics together. It is then important to use velocity measurements at the injector outlet, at a point where the relative velocity fluctuation matches the relative volumetric flow rate fluctuation. The describing function with velocity reference at the injector outlet is determined for various input levels and found to approximately match those measured under SSO. The best match is obtained when the amplitude of external modulation induces a level of velocity oscillations that comes closest to that prevailing under SSO. This demonstrates that the FDF may suitably capture the nonlinearity of the flame response, at least in the configuration investigated in this research.

3.1 Introduction

Among the many questions raised by the phenomenon of thermoacoustic instability, that of modeling occupies a central position. Much effort has been devoted to deriving models that could guide the analysis of combustion dynamics phenomena and be used as predictive tools. This effort was initiated during the early days of rocket engine development, where the instability problems were encountered, inducing some spectacular failures. More recently, many experiments in active control of combustion indicated that progress could be achieved by developing

modeling methods (McManus et al. 1993; Annaswamy et al. 1997; Candel 2002; Dowling and Morgans 2005; Morgans and Stow 2007), and this gave rise to a considerable research effort that was aimed at representing the combustion system and controller in the framework of control systems theory. The central idea was to describe the combustion response in terms of transfer functions and use closed-loop representations of the coupling that was achieved by acoustic modes and controller actions. Much effort has been devoted to deriving models that could guide the analysis of combustion dynamics phenomena and may then be used as predictive tools. This modeling effort was begun to gain some understanding of processes leading to unstable oscillations in rocket engines (Crocco 1951; Crocco 1952; Tsien 1952; Marble and Cox Jr. 1953; Crocco and Cheng 1956; Harrje and Reardon 1972; Yang and Anderson 1995). More recently, attention has been focused on dynamical phenomena in gas turbine combustors operating in the premixed mode and using swirling flows to anchor the flames at a distance from the injection units (Richards and Janus 1998; Lieuwen and Zinn 1998; Lieuwen et al. 2001; Hubbard and Dowling 2001; Candel 2002; Paschereit et al. 2002; Lieuwen and Yang 2005a; Schildmacher et al. 2006; Huang and Yang 2009; Krebs et al. 2013; Candel et al. 2014; Poinsot 2017). The present chapter addresses a central modeling issue in the context of swirl stabilized flames. Is it possible to suitably describe the combustion response in terms of transfer functions or their nonlinear extension, describing functions? In other words, can one model a complex multi-dimensional flow characterized by the presence of multiple scales, those of turbulence and combustion, and the fast kinetics of strongly exothermic reactions in terms of low-order dynamical tools relying on transfer or describing functions? Do these reduced descriptions capture the three-dimensional flame dynamics that are involved in the process? This analysis aims at providing direct experimental proof that transfer functions and their describing functions extensions represent the flame behavior and that the reduced-order model suitably describes the multi-dimensional reality. It is not our intention to give a general answer to the questions raised previously, and the analysis is restricted to a case that has much practical importance, that of swirling flames that are compact with respect to the acoustic wavelength of the coupling modes. This case will be investigated experimentally to highlight the difficulties and limitations of this kind of representation and provide some insight on issues of low-order modeling of combustion instabilities.

At this point, it is worth briefly reviewing the state of art in low-order modeling to place the present investigation in perspective. The early analysis of combustion instability relied on the sensitive time lag (STL) theory. The flame response was represented in terms of an interaction index n and a time lag τ that was assumed to be a function of the state variables in the combustion region (Crocco 1951; Tsien 1952; Marble and Cox Jr. 1953). In general, these two terms were considered to be parameters that could be varied to determine instability regions. This kind of model assumed, in essence, that a transfer function existed between

the state variable disturbances and combustion disturbances such as those of the heat release rate. The gain of this transfer function was a constant proportional to the interaction index n, while the phase was a linear function of the angular frequency $\varphi_F = \omega\tau$. More recently, considerable effort was expended to understand mechanisms controlling instabilities and represent the flame dynamics in terms of transfer functions. This effort is reviewed, for example, in (Huang and Yang 2009; Candel 2002; Polifke 2020; Schuller et al. 2020). The transfer function was introduced to link relative fluctuations of heat release rate in the flame, treated as an output, to the relative fluctuations in volume flow rate. When the relative velocity fluctuation and the mean velocity at the input are uniform, it is possible to consider that the relative volume flow rate fluctuation is equal to the relative velocity fluctuation. For experimental convenience, velocity fluctuation is then considered as the input instead of volume flow rate fluctuation. The transfer function may have multiple inputs, and in the present case, one other input could be the perturbations in equivalence ratio. For the case considered in this chapter, the mode of combustion is quasi-premixed, as shown in Chapter 2, and the primary input is the disturbance in velocity (representing the disturbance in volume flow rate). The transfer function is given by

$$\mathcal{F}_0(\omega) = \frac{\dot{Q}'(\omega)/\overline{\dot{Q}}}{u'/\overline{u}} = G_F(\omega)e^{i\varphi_F(\omega)} \tag{3.1}$$

Transfer functions were introduced, in particular, to derive active control methods and help interpret their experimental demonstrations. Transfer function expressions were obtained for many simple flames like premixed conical and "V" flames and for swirling premixed flames (Matsui 1981; Fleifil et al. 1996; Ducruix et al. 2000; Schuller et al. 2002; Schuller et al. 2003; Lieuwen 2003; Preetham et al. 2006; Preetham et al. 2008; Palies et al. 2011; Kim and Santavicca 2013; Kornilov et al. 2009) and were compared in some cases with experimental data. It was then recognized that the flame response depended not only on frequency but also on the oscillation amplitude. This led to the replacement of the FTF by a describing function, i.e., a family of transfer functions with each of these functions depending on the amplitude of the input.

$$\mathcal{F}(\omega, u') = \frac{\dot{Q}'(\omega, u')/\overline{\dot{Q}}}{u'/\overline{u}} = G_F(\omega, u')e^{i\varphi_F(\omega,u')} \tag{3.2}$$

This was employed, for example, in a theoretical analysis of the dynamics of a ducted flame by Dowling (1997), which indicated only a gain saturation with the velocity fluctuation amplitude. The concept of flame describing function (FDF) was generalized by Noiray et al. (2008) to also consider phase dependence with respect to the amplitude of perturbations. The FDF was shown to provide an understanding of many nonlinear features observed experimentally, like frequency

shifting during oscillation growth, mode switching (frequency jumping during oscillation), instability triggering, and hysteresis, and more generally represent the dynamics of finite-amplitude oscillations (Durox et al. 2009). This has been a notable advance because the describing function allowed to retrieve nonlinear dynamical features (Noiray et al. 2009b; Boudy et al. 2011; Boudy et al. 2011; Palies et al. 2011; Heckl 2013; Silva et al. 2013; Han and Morgans 2015; Han et al. 2015; Heckl 2015; Gopinathan et al. 2018; Ghirardo et al. 2016; Laera et al. 2017; Haeringer et al. 2019; Rajendram Soundararajan et al. 2021). Models using the FDF yield amplitude-dependent results that allow direct comparisons with experimental data since most instability experiments are carried out when the oscillations are established and have reached a finite value. It was, however, found that the FDF has limitations and cannot easily handle situations where the limit cycle amplitude evolves as a function of time and the amplitude becomes irregular giving rise to "galloping" limit cycles (GLCs), or modulated in a more regular fashion when the oscillation is sustained by two modes. These cases require extensions of the FDF in the form of multiple-input describing functions (Moeck and Paschereit 2012; Orchini and Juniper 2016; Haeringer et al. 2019). A practical difficulty encountered while obtaining the FDF is the need to measure the heat release rate fluctuations $\dot{Q}/\overline{\dot{Q}}$ from the flame. This is often deduced from the fluctuations of light intensity originating from excited radicals such as OH^* or CH^* present in the reaction zone and considering that these intensities are monotonically related to the heat release rate fluctuations. This is well validated for fully premixed flames (Hurle et al. 1968) but might not be fully applicable to the case of non-premixed or technically premixed systems. In such cases and in configurations where optical access to the flame is not available, an alternative purely acoustic method consists in determining the flame transfer matrix (FTM) (Paschereit et al. 2002; Schuermans et al. 2004). In this framework, the flame is represented by a 2×2 transfer matrix $\boldsymbol{T}$, and the acoustic states upstream and downstream of the flame are obtained using multiple microphones. This method has been widely adopted for modeling industrial gas turbines which do not have optical access to the flame. It is also useful for technically premixed flames where the quantitative estimate of heat release rate using chemiluminescence is not well validated. However, being a purely acoustic method, FTM does not account for the convective disturbances that result from interactions between acoustic waves and flow singularities, like those associated with swirlers and injection units (Noiray et al. 2009c). In practice, the method yields a transfer matrix $\boldsymbol{T}$ corresponding to the combination of a flame transfer matrix $\boldsymbol{F}$ and injector transfer matrix $\boldsymbol{B}$, and the flame transfer matrix is deduced from $\boldsymbol{F} = \boldsymbol{T}\boldsymbol{B}^{-1}$. It requires a separate measurement of the injector matrix $\boldsymbol{B}$ obtained under cold flow conditions and the inversion of this matrix. One assumes that $\boldsymbol{B}$ does not change under hot fire conditions. Uncertainties also arise from practical application in a highly noisy background in which the coherence between the forcing and microphone signals may not be very high (Paschereit et al. 2002; Gaudron et al. 2019b). The FTM is also experimentally

complex as it requires measurements at two independent acoustic states of the system, which imply modulation and signal acquisition on the upstream and downstream sides of the injector unit. Independent acoustic states of the system can also be achieved either by increasing the combustion chamber length or changing the impedance at the outlet. While the former has the disadvantage of triggering self-sustained modes, the latter can be difficult to achieve. These techniques are not always feasible, and in such cases, one may prefer direct FDF measurements.

Whatever the framework (FDF or FTM), it is worth asking whether the low-order models in which the flame response is treated as a black box can suitably represent the fluid and combustion dynamics that determine thermoacoustic instabilities. In the present study, the FDF framework is chosen for use in low-order models as the test rig is better suited for carrying out optical measurements and studying flame response by modulating the system from upstream. The test setup is also not equipped to perform purely acoustic measurements at two independent acoustic states of the system. Although many previous studies in the literature (including Noiray et al. (2008) and, more recently, Rajendram Soundararajan et al. (2022)) have demonstrated the capability of FDFs in instability prediction, thus constituting an indirect validation of the methodology, no direct experimental proof is available to verify if the FDF suitably renders the combustion dynamics under self-sustained oscillations (SSO). This question is represented schematically in Fig. 3.1 (a) and (b). This diagram shows on the left a representation of the sys-

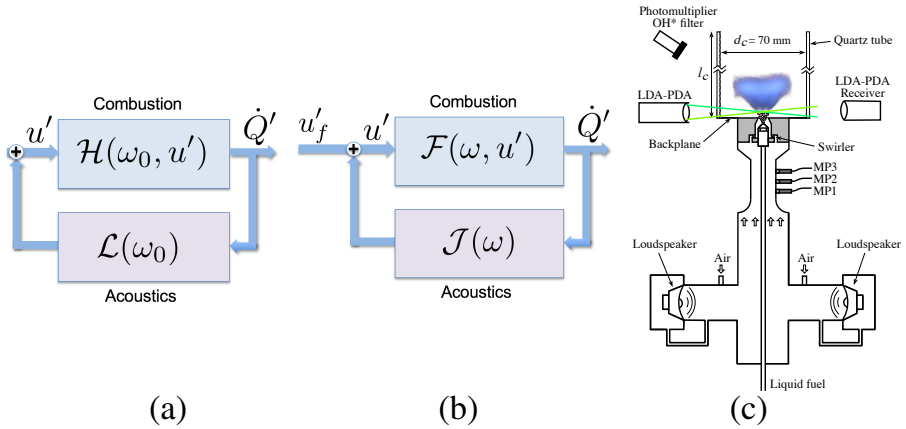

Figure 3.1. *(a) Closed-loop representation of a self-sustained instability at an angular frequency ω_0 and an amplitude of oscillation u'. The function $\mathcal{H}$ represents the flame response in the self-sustained oscillation. (b) Stable flame operation obtained by changing the acoustic coupling. This is used to allow external modulation and the determination of the flame describing function $\mathcal{F}(\omega, u')$ by imposing $u'_f = v_0 e^{-i\omega t}$. (c) Schematic of the experimental setup SICCA-Spray.*

tem when it is executing SSO and features a limit cycle at an angular frequency ω_0. The flame dynamical response is $\mathcal{H}(\omega_0, u')$. The inclusion of u' in this expression is to indicate that the flame behavior is also controlled by the level of

incident disturbances. In the center, the diagram shows the combustor operating in a stable manner and being modulated externally to measure the FDF designated as $\mathcal{F}(\omega, u')$. Of course, this cannot be done if the system features a self-sustained oscillation. The harmonic modulation can be applied when the flame is stable. It can be argued that one cannot separate the flame from its environment so that an acoustic coupling is always present. However, this coupling may be reduced by shifting the roots of the dispersion relation that give rise to unstable oscillations. The method is explained with a model problem treated in Appendix 1. It is shown there that the flame may be made to operate in a stable regime by changing the acoustic feedback. This is represented in Fig. 3.1 by replacing $\mathcal{L}$ with $\mathcal{J}$ and achieved in practice by changing the combustion chamber size to remove the resonant frequencies out of the range of interest manifested under SSO. One may then see if $\mathcal{F}$ and $\mathcal{H}$ coincide or, more precisely, if

$$\mathcal{F}(\omega_0, u') \simeq \mathcal{H}(\omega_0, u') \tag{3.3}$$

It is worth underlining that the flame dynamics under SSO represented by $\mathcal{H}$ cannot be a priori considered to coincide with the FDF $\mathcal{F}$ determined under stable flame modulation (SFM) because (1) these descriptions are only a reduced model of reality, and (2) the FDF is determined in an environment that differs from the one considered under SSO. A good match between these two functions will indicate that a low-order model using a measured FDF may suitably represent the real system and will provide reasonable predictions of SSO. However, one cannot be certain that the flame behavior has not been modified when the loop is closed and when a strong acoustic coupling occurs. A modification of this type is not considered in control systems where the transfer function or describing function of the "plant" does not depend on the feedback path. Here, the situation is different because the flame is a result of a complex multidimensional flow where exothermic reactions take place, and one cannot be certain that the low-order modeling based on the FDF suitably represents the flame dynamics under SSO.

This chapter begins with a presentation of the experimental setup (Section 3.2). Flame dynamics are then examined using OH^* chemiluminescence images in Section 3.3 under SSO and compared to those corresponding to external modulation (referred to as stable flame modulation or SFM). A comparison between the flame response $\mathcal{H}$ and the FDF $\mathcal{F}$ is then carried out in Section 3.4. This is followed by Section 3.5, which is focused on the injector dynamics under SSO and SFM. It is shown in that section that the injector operates in a different manner when the system is modulated from upstream and when the system executes self-sustained oscillations. This has consequences in terms of low-order modeling that are also briefly examined. In addition, an appendix provided at the end serves to explain the meaning of what is being measured under the stable operation schematically presented in Fig. 3.1 (b).

3.2 Experimental setup

Experiments are carried out in a generic single injector setup (SICCA-Spray), whose generic experimental setup is discussed in Chapter 1. Only the essential details of the setup are recalled in this section. The swirler for the present investigation is 716, and the experiments are carried out at the operating point F2, which corresponds to a global equivalence ratio of $\phi = 0.95$, which corresponds to an air flow rate of $2.3\,\mathrm{g\,s^{-1}}$ and a fuel flow rate of $520\,\mathrm{g\,h^{-1}}$. Liquid heptane fuel is delivered as a hollow cone spray by a simplex atomizer producing a dispersion of fine fuel droplets. The atomizer is recessed at a distance of $6.75\,\mathrm{mm}$ with respect to the chamber backplane. The combustion chamber is formed by a fully transparent cylindrical quartz tube providing complete optical access to the combustion zone. Self-sustained oscillations of the system are obtained by varying the chamber length l_c. One finds, in this way, different resonant frequencies and amplitudes of longitudinal limit cycle instabilities. During the measurement of FDFs under SFM, a chamber length of $l_c = 150\,\mathrm{mm}$ is chosen to operate the system under stable conditions. For these measurements, two driver units located at the bottom of SICCA-Spray are excited to achieve different levels of fluctuations. These driver units are modulated at the same frequencies as SSO and at an amplifier voltage close to the level of relative fluctuations observed under SSO. When the system is operating under SSO, the driver units are left inactive.

The three microphones (marked MPx in Fig. 3.1) plugged onto the plenum are used for measuring pressure signals and also to determine the acoustic velocity fluctuations with the multi-microphone method. The velocity measurement for the determination of FDF (defined by Eq. 3.2) is obtained at the injector outlet using laser Doppler anemometry (LDA). When using a swirling injector, the velocity profile at the exit of the injector is nonuniform, and this raises the question of choosing an optimal position for the measurement. This point is chosen at a location where the relative velocity fluctuation coincides with the relative volumetric flow rate fluctuation. For the swirler 716, the reference position for the velocity measurement is located at a distance of $r = 4\,\mathrm{mm}$ from the center of the injector and at a height of $h = 2.5\,\mathrm{mm}$ from the backplane. Further details on the determination of this point are provided in Chapter 4. The measured axial velocity at the exit of the injector is henceforth referred to as $u_{c,r}$.

An estimate of heat release rate (HRR) integrated over the flame volume is obtained by measuring the OH^* chemiluminescence (with a 10 nm filter centered at $308\,\mathrm{nm}$) from the flame using a photomultiplier tube. The validity of using OH^* chemiluminescence as an HRR indicator has been systematically validated in the current configuration in Chapter 2. The spray flame considered in this study is found to operate in a quasi-premixed fashion due to the recessed position of the atomizer inside the injector. It is found that the equivalence ratio fluctuations remain low at the injector outlet compared to the velocity fluctuations, and there is

no significant spatial stratification in the flame zone. The readers are also referred to Chapter 2 for a detailed analysis of this point. Additionally, an ICCD camera from Princeton Instruments is used to obtain the flame images. The signals from the plenum microphones and photomultiplier are sampled simultaneously during the velocity measurements by the LDA system for a period of $10\,\mathrm{s}$ and at a data rate of roughly 25,000 Hz.

3.3 Flame dynamics

Before examining the FDF and the flame response in terms of gain and phase, it is logical to compare the flame dynamics under SSO and SFM using OH^* chemiluminescence images as presented in Fig. 3.2. The images are captured by a PI-MAX intensified camera equipped with a Nikon 105 mm UV lens and an Asahi optical bandpass filter ($10\,\mathrm{nm}$ half-width centered at $310\,\mathrm{nm}$ corresponding to emission bands of OH* radicals in the flame). The camera is triggered with respect to the instability using the photomultiplier signal, which is low-pass filtered with a cut-off frequency of $800\,\mathrm{Hz}$ using an analog filter. This improves triggering by reducing the jitter present in the photomultiplier signal. A Tektronix TBS 2000 oscilloscope provides a trigger signal when the filtered photomultiplier signal reaches its mean value and is at its rising edge. This setup is used to obtain the phase averaged flame images shown in Fig. 3.2. The exposure is $40\,\mu\mathrm{s}$ long. The images appearing in Fig. 3.2 are averaged over 1000 individual samples and processed with an Abel inversion algorithm.

For the measurements, the quartz tube for the unstable case is $265\,\mathrm{mm}$ long, and the limit cycle features a frequency of $533\,\mathrm{Hz}$. The amplitude of velocity oscillation at $(r, z) = (4.0, 2.5)\ \mathrm{mm}$ measured using LDA is $u'_{c,r}/\overline{u}_{c,r} = 9\%$, and that of the chemiluminescence signal is $I'_{\mathrm{OH}^*}/\overline{I_{\mathrm{OH}^*}} = 28.9\%$. Here and henceforth, the notation $(\cdot)$' refers to the root mean square (RMS) fluctuations, and $\overline{(\cdot)}$ refers to the mean of a quantity. The flame dynamics under SSO is shown in Fig. 3.2 (a), and stable flame modulation is examined in Fig. 3.2 (b-d). In Fig. 3.2 (b), directly underneath the SSO images, the forcing level is set to match the conditions encountered under SSO. In Fig. 3.2 (c), the forcing level is significantly lower, while in Fig. 3.2 (d), it is significantly higher.

The set of images in (a) and (b) indicate that the flame shapes and intensity corresponding to SSO agree with those of SFM at $3.5\,\mathrm{V}$, i.e. when the velocity fluctuation levels match. On comparing SSO with SFM at other amplifier voltages where the velocity fluctuations do not match, some minor differences can be observed in the flame shapes and intensity levels. A periodic elongation and widening are visible in all the cases starting from $\Phi = 3\pi/2$ and extending till $\pi/2$, the latter corresponding to the broadest flame during the cycle. To further understand the similarities and differences between SSO and SFM, the flame front

Figure 3.2. *(a-d) Phase-averaged, Abel-transformed flame images shown in false colors. Light intensity of OH* chemiluminescence is obtained at different phase instants of the acoustic cycle using an intensified camera. (a) Images obtained under SSO at a frequency* $f_0 = 533$ Hz. $I'_{OH^*}/\overline{I_{OH^*}} = 28.9\%$. *(b-d) Images corresponding to SFM at the frequency of SSO. (b) The forcing amplitude matches that observed during SSO (*$I'_{OH^*}/\overline{I_{OH^*}} = 30.4\%$*). (c) The forcing amplitude is lower than that observed during SSO (*$I'_{OH^*}/\overline{I_{OH^*}} = 14.2\%$*). (d) The forcing amplitude exceeds that observed during SSO (*$I'_{OH^*}/\overline{I_{OH^*}} = 37.8\%$*). (e-g) Flame isocontours determined by Otsu thresholding method for SSO (solid black line in (e-g)) and three levels of SFM (same—red dotted line in (e), lower—magenta dotted line in (f), and higher—blue dotted line in (g) fluctuation level compared to SSO).*

location is identified by applying the so-called Otsu thresholding method to the OH* images, as demonstrated by Degenève et al. (2019), and is shown in Fig. 3.2 (e-g) when the flame is under SSO (in solid black) and for the four cases of SFM: same (dotted red), lower (dotted magenta), and higher (dotted blue) relative in-

tensity fluctuation compared to SSO. The extracted flame contour data evidently show a close match between the SSO and SFM flame shapes when the forcing level of SFM (i.e., at $V_0 = 3.5\,\mathrm{V}$) matches the oscillation level of SSO. At the other two SFM levels, visible differences can be observed in the flame contour shape at certain parts of the cycle. For instance, this difference is more pronounced for the higher fluctuation level between the phase instants $\Phi = \pi/4$ and $3\pi/4$. For the remaining part of the cycle, the difference is minor, with only some observable deviation close to the base of the flame. The difference in the flame contour position between SSO and SFM is more prominent for the lower amplitude case at all the phase instants, except at $\Phi = 7\pi/4$, where the contours corresponding to all four cases nearly collapse.

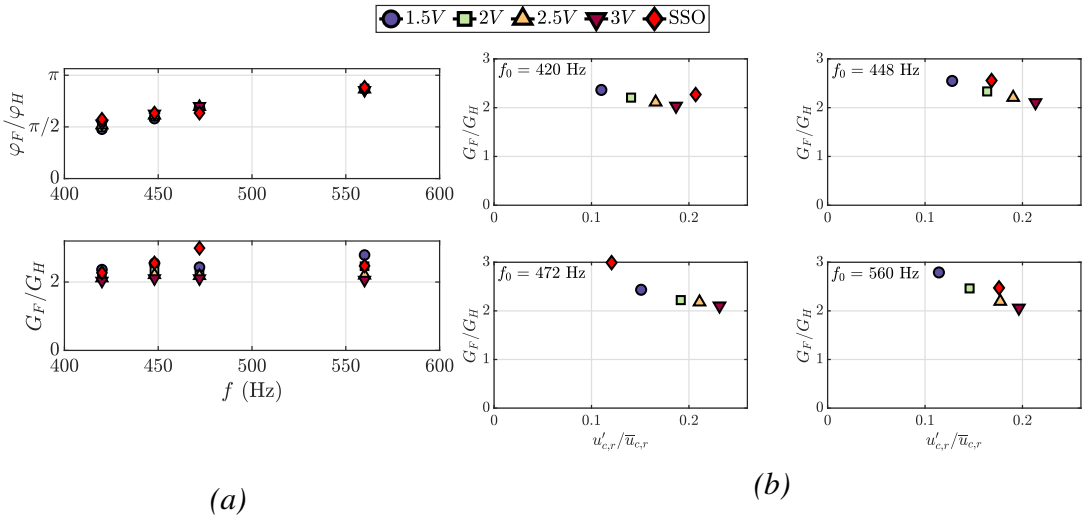

Figure 3.3. *Comparison between the stable flame describing function $\mathcal{F}$ and the combustion response under SSO, $\mathcal{H}$. (a) Phases φ_F and φ_H and gains G_F and G_H plotted at the four resonance frequencies and at different amplitude levels for SFM. The relative velocity fluctuation for obtaining $\mathcal{F}$ and $\mathcal{H}$ is measured in the chamber. The red diamonds represent phases and gains of $\mathcal{H}$ during SSOs for different chamber lengths. The other colors and symbols correspond to the measured $\mathcal{F}$ during SFM obtained while modulating the flame at the SSO frequencies and at four different levels of amplifier voltages (1.5, 2, 2.5, and $3\,\mathrm{V}$). (b) Gain of $\mathcal{F}$ and modulus of $\mathcal{H}$ plotted as a function of the relative velocity fluctuation in the chamber. The velocity is measured at the reference position $(r, z) = (4.0, 2.5)$ mm. The representation in terms of amplifier voltages shown in (a) is expressed in terms of velocity fluctuation levels in (b).*

3.4 Comparison of FDF and flame response under limit cycle oscillations

The comparison between FDF $\mathcal{F}$ and the flame response $\mathcal{H}$ is shown in Fig. 3.3 (a) in terms of gain and phase at different frequencies. For the measurements under SSO, the chamber length l_c is varied to obtain self-sustained oscillations at different frequencies. Chamber lengths of 250, 300, 315, and $350\,\mathrm{mm}$ are used to attain the oscillations at frequencies 560, 472, 448, and $420\,\mathrm{Hz}$, respectively. The measurement under SFM is performed by modulating the flame using the two driver units mounted upstream of the injectors at the frequencies of SSO and at four different levels of amplifier voltages (1.5, 2, 2.5, and $3\,\mathrm{V}$) fed to the driver units. Although a representation based on amplifier voltage is not physically relevant, it is provided here as a common ground for SFM between flame image measurement (shown in Fig. 3.2) and the measurements carried out to obtain the describing functions shown in Fig. 3.3. A representation based on amplifier voltage can alternatively be indicated in terms of relative velocity fluctuations in the chamber $u'_{c,r}/\overline{u}_{c,r}$, as shown in Fig. 3.3 (b).

On comparing the phase of $\mathcal{F}$ at different fluctuation levels (Fig. 3.3(a) top), it can be seen that there is no discernible nonlinearity with respect to the level of fluctuation and the phases of $\mathcal{F}$ and $\mathcal{H}$ match quite well. The role of phase on stability analyses (see, for example, Noiray et al. (2008), Schuller et al. (2020)) is critical, and the experimentally observed match validates the usage of FTF/FDF in reduced-order models. Contrary to the phase observation, one may notice the presence of nonlinearity in the gain of SFM (Fig. 3.3 (a) bottom) with respect to the fluctuation level at all the frequencies. Figure 3.3 (b) shows the gain G_F as a function of velocity fluctuation levels at the four frequencies considered in this study along with G_H. At $f_0 = 448\,\mathrm{Hz}$ and $560\,\mathrm{Hz}$, the fluctuation levels match between SSO and SFM at an amplifier voltage of $2\,\mathrm{V}$ and $2.5\,\mathrm{V}$, respectively, where one may also notice that the gains G_F and G_H match in these two cases. Whereas, at $f_0 = 420\,\mathrm{Hz}$ and $472\,\mathrm{Hz}$, none of the SFM cases matches with the fluctuation level of SSO. Hence, a match of gain between SFM and SSO is not attained, but the respective values are close. These results and the flame images shown in Fig. 3.2 clearly indicate the importance of utilizing a version of $\mathcal{F}$ that matches with the velocity fluctuation level of $\mathcal{H}$ in the low-order models to have a good prediction of instabilities. If the low-order model uses an $\mathcal{F}$ that does not match the level of SSO, one might still be able to potentially predict whether or not the system will be unstable purely based on the phase information from the FDF. But the prediction of limit cycle amplitude would potentially be erroneous due to the mismatch in gain.

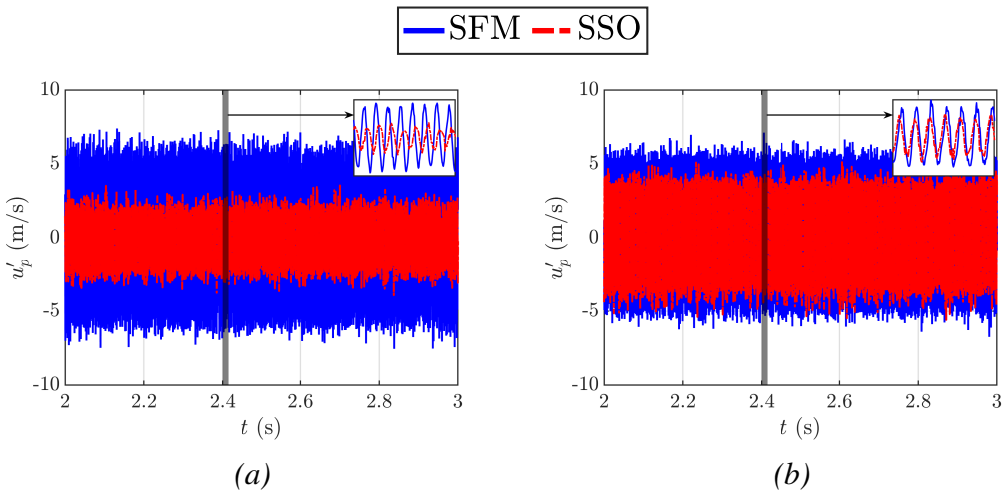

Figure 3.4. *Comparison of time evolution of the plenum velocity between an SFM and SSO shown for a period of* 1 s. *Results are plotted when the chamber velocity fluctuation level of SFM matches with that of SSO. (a) SFM:* $V_0 = 2.5\,\mathrm{V}$*; SSO:* $l_c = 250\,\mathrm{mm}$, $f_0 = 560\,\mathrm{Hz}$ *and (b) SFM:* $V_0 = 2\,\mathrm{V}$*; SSO:* $l_c = 315\,\mathrm{mm}$, $f_0 = 448\,\mathrm{Hz}$.

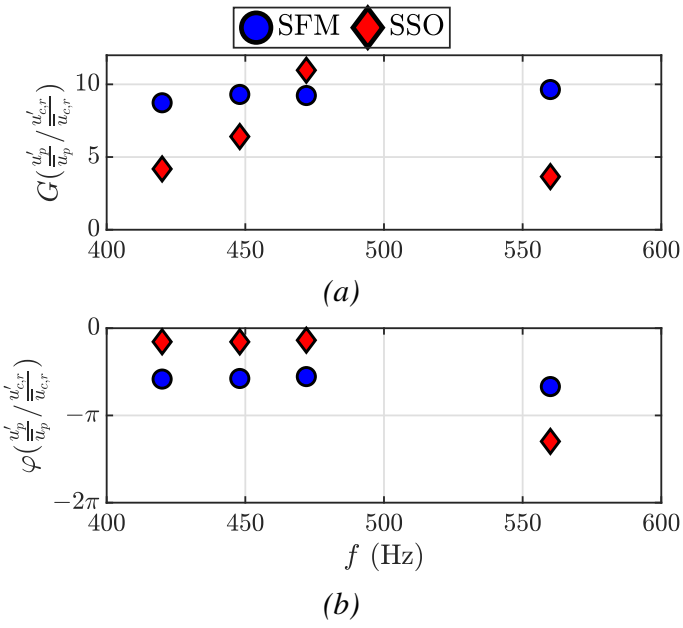

Figure 3.5. *The gain (a) and phase (b) of relative plenum velocity fluctuations to relative chamber velocity fluctuations. At* $f_0 = 448\,\mathrm{Hz}$ *(*$l_c = 315\,\mathrm{mm}$*) and* $560\,\mathrm{Hz}$ *(*$l_c = 250\,\mathrm{mm}$*), the results are shown when the chamber velocity fluctuations of SFM coincide with those of SSO. At* $f_0 = 420\,\mathrm{Hz}$ *(*$l_c = 350\,\mathrm{mm}$*) and* $472\,\mathrm{Hz}$ *(*$l_c = 300\,\mathrm{mm}$*), the results are shown when the chamber velocity fluctuations of SFM are closest to SSO.*

3.5 Injector dynamics during SSO and SFM

Although the FTF/FDF framework, by definition, considers the reference velocity at the base of the flame, it is a common practice to use a velocity reference for the transfer function in the plenum, upstream of the injection unit (this is exemplified in Palies et al. (2011), and more recently by Gatti et al. (2019), Wang et al. (2021)). This choice is made because of the practical difficulties associated with the measurement of velocity at the base of the flame, which would mandate some form of optical measurement technique to access the flame zone. For an acoustically transparent injector that is compact compared to the acoustic wavelength, the velocity upstream and downstream of the injector would remain the same as it stays passive to the acoustic waves. In such a case, the FDF, considering upstream velocity as the reference, would still be valid as the injector dynamics would be the same between SSO, where there is strong pressure oscillation downstream, and during modulation of the flame from upstream. However, the injector considered in the present work is only weakly transparent to acoustic waves due to the high pressure drop and abrupt area changes in the swirler channels. Such injectors act as a loss element by converting some of the incoming acoustic waves into convective waves at the injector outlet. This raises the question of whether the FDF measured with a reference velocity in the plenum and an upstream acoustic modulation would suitably represent the flame dynamics during SSO. Figure 3.4 shows the time evolution of plenum velocity between SFM and SSO when the chamber velocity $u'_{c,r}$ coincides in two of the investigated cases. The plenum velocity is obtained by the two-microphone method from the microphones MP1 and MP3 (refer to Fig. 3.1(c)). Chamber velocity is measured by LDA as described in Section 3.2. Figure 3.4 left shows the plenum velocity during an SSO at $l_c = 250\,\mathrm{mm}$ and SFM at $V_0 = 2.5\,\mathrm{V}$, and on the right is the SSO at $l_c = 315\,\mathrm{mm}$ and SFM at $V_0 = 2\,\mathrm{V}$. It can be seen that for the same level of velocity fluctuations in the chamber, SFM always yields a higher level of plenum velocity u'_p than SSO. This means that the amplitude of the relative velocity fluctuation in the plenum is not preserved between SSO and SFM. Figure 3.5 shows the gain and phase of relative velocity fluctuations in the plenum to the relative velocity fluctuations in the chamber at different frequencies considered in this study. Here, $\overline{u}_p$ is the bulk velocity in the plenum, while $\overline{u}_c$ is the mean velocity at the exit of the injector measured at $r = 4\,\mathrm{mm}$ and $h = 2.5\,\mathrm{mm}$. The data plotted at $f_0 = 448\,\mathrm{Hz}$ and $560\,\mathrm{Hz}$ correspond to a situation where the chamber velocity fluctuations nearly coincide for SSO and SFM. At $f_0 = 420\,\mathrm{Hz}$ and $472\,\mathrm{Hz}$, the data points pertain to a situation where the velocity fluctuations in the chamber of SFM are closest to the SSO case but do not quite match. Significant differences can be observed between SSO and SFM with regard to the velocity fluctuation ratio, with the gain during SFM being twice as high as that corresponding to SSO for most frequencies, except at $472\,\mathrm{Hz}$, where this difference is minor. It is also found that under SFM, the phase between plenum and chamber velocity fluctuations remains the

same at all frequencies and is slightly higher than $-\pi/2$. However, when the system is under SSO, the phase is rather close to 0 at lower frequencies and close to $-\pi$ at $560\,\mathrm{Hz}$. Differences in the dynamical state of a swirling injector system submitted to upstream and downstream modulation observed in Gaudron et al. (2019a) are analogous to those found in the present investigation if one considers that the downstream modulation state is similar to SSO, where pressure oscillations originate from downstream combustion processes. A velocity measurement performed upstream of the injector would, in fact, lump the injector and flame dynamics together and will not suitably represent the flame dynamics under SSO. Thus, for an injector that is weakly transparent to acoustic waves, the velocity measurement for FDF determination should be positioned at the injector outlet. Alternatively, one might consider measuring the injector transfer function under cold flow conditions and extracting it from the lumped injector and flame transfer function in a way similar to that used in the FTM framework (Schuermans et al. 2004). There are, however, differences in the injector transfer function gain with and without flame, as shown in Chapter 4, thus emphasizing the need for directly obtaining the flame transfer/describing function. This direct determination requires that the incident fluctuations be measured at a point where the relative velocity fluctuations coincide with the relative volumetric fluctuations to be suitably used in the FDF framework. Alternatively, the behavior of the injector might be represented by the injector transfer matrix model described in Paschereit et al. (2002) and Bellucci et al. (2005) and designated as the $L-\zeta$ model. In this model, the injector transfer matrix $\boldsymbol{B}$ features elements $B_{21} = 0$ (the element in row 2, column 1) and $B_{22} = 1$ (Bellucci et al. 2005) or $B_{22} = A_u/A_d$ (the element in row 2, column 2 and where A_u and A_d are the upstream and downstream cross-sectional areas in Paschereit et al. (2002)). A rapid inspection indicates that this might not account for the large drop in fluctuation level and shift in phase observed between the upstream and downstream velocity fluctuation levels under SFM. In addition, as indicated by Gaudron et al. (2019b), the L-ζ model is only linear, and such a model is not suitable if the injector exhibits a nonlinear response to acoustics, such as the ones considered in this thesis. Further details on the injector behavior and its describing function are discussed in Chapter 4.

Although in the present work, the FDF framework is adopted instead of the FTM framework to represent the flame dynamics, the accurate measurement of FDFs for acoustically weakly transparent injector raises a difficulty as it requires precise positioning of the measurement probe in the chamber to obtain relative velocity fluctuations. Even a small deviation from this position can notably change the measured FDF, which will then not suitably represent the flame dynamics in a low-order model, thereby leading to erroneous instability prediction. Also, the velocity measurement in the chamber mandates some form of optical measurement technique, in addition to requiring the heat release rate fluctuations from the flame, which is difficult to obtain for technically premixed flames. This might not

be possible in the case of industrial combustors where optical access to the flame zone is generally not available. The other possibility is to reconstruct the FTF/FDF with purely acoustic measurements using the FTM framework. However, it was shown by Gaudron et al. (2019b), who compared the FDF determined with both optical (heat release rate approximately represented by flame chemiluminescence) and purely acoustical technique (with the FTM framework), that the FDF obtained with the two techniques do not exactly match in their turbulent premixed swirling flame case. The FDF phase is captured reasonably well, but the reconstruction of the FDF gain from the purely acoustic method deviates from the one obtained with the optical method. The FDF gain mismatch was also observed by Schuermans et al. (2010) for a technically premixed flame, but it is not clear from which method the error is arising. One reason for such a mismatch could be attributed to the fact that the disturbances just at the outlet of the injector are generally convective in nature (Noiray et al. 2009c), and this might not be captured by purely acoustic methods. In addition, the requirement of two independent acoustic states of the system presents problems in obtaining noise-free measurements, especially when modulating the system from the downstream side of the flame (Gaudron et al. 2019b), leading to incorrect results. A note on an alternate FDF determination technique using the velocity measured at the injector outlet and acoustic velocity measured downstream of the flame is discussed in the appendix.

3.6 Conclusions

Although many theoretical models in combustion instability rely on transfer functions or describing functions, it was essential to see if these concepts are effectively applicable, particularly, if they can be used in the case of complex multi-dimensional turbulent spray flames formed by swirling injectors. This central question is investigated by comparing two situations: the first corresponding to a well-established limit cycle self-sustained oscillation (SSO), while the second may be assimilated to a stable flame modulation (SFM) in which the acoustic coupling is minimized, and the flame is externally modulated. Three levels of external modulation are chosen—same, lower, and higher levels than the SSO fluctuations. It is shown that the flame dynamics observed using Abel-transformed OH^* light intensity images matches best when the level of acoustic oscillation in the two situations is equal. It is also found that the gain of the flame describing function (FDF) is close to that of the flame response measured under SSO when the level of oscillation in the externally modulated flame (SFM) equals that found under SSO. The level of fluctuation does not affect the phase, and all the phase values under SFM cases match those found under SSO tests. These elements confirm that the FDF framework is applicable and that it is crucial to consider the dependence of flame response on the level of incident perturbations. Additionally, it is shown that the injector dynamics during SFM and SSO are not the same in the case of an

injector that is weakly transparent to acoustic waves. It is advisable to calculate the FDF with respect to relative velocity fluctuations in the chamber since the use of plenum velocity would lump the dynamics of injector and flame together and may fail to represent the flame dynamics under SSO in the absence of a suitable description of the injector's frequency response. The FDF obtained with plenum velocity would neither have the correct gain nor the correct phase evolution, and it will not be possible to predict the unstable operating points with the corresponding low-order model. The present experiments, although restricted to a specific case, provide a direct validation of the FDF concept in the analysis of combustion instabilities leading to limit cycle oscillations.

Appendix 1: A model problem featuring self-sustained oscillations and allowing stable flame modulation

We consider, in this appendix, a model problem in which a flame placed in a duct may become unstable and leads to an oscillation, and in which it is also possible to apply an external modulation to determine the flame describing function (FDF). The objective is to show in an idealized case what distinguishes the situation where the flame executes a self-sustained oscillation (SSO) from that where the system is stable and modulated externally to determine the FDF (referred to as stable flame modulation or SFM). The geometry of the problem shown in Fig. 3.6 features a driver unit on the left that may be passive i.e. $u'_f = 0$, or may impose a velocity perturbation $u'_f = v_0 e^{-i\omega t}$. The flame is located at a distance a from the upstream end of the duct. The downstream end is open, and its length l already includes the so-called "end correction", so that one may write $p'(l) = 0$. Regions 1 and 2 respectively correspond to upstream $0 \leq x \leq a$ and to downstream $b \leq x \leq l$ of the flame. For simplicity, one assumes that the temperatures on the two sides of the flame are the same so that the densities, sound velocities, and wave numbers are the same in the two regions. The jump conditions at the flame express pressure continuity such that $p'_1(x = a) = p'_2(x = a)$, and the acoustic volume flow rate is defined by the heat release rate fluctuation of the flame:

$$Su'_2 - Su'_1 = \frac{\gamma - 1}{\rho_0 c^2}\dot{Q}' \tag{3.4}$$

It is possible to express the heat release rate in the flame by making use of the flame describing function $\mathcal{F}$. One obtains after standard calculations,

$$u'_2 - u'_1 = \widehat{\mathcal{F}} u'_1 \tag{3.5}$$

where $\widehat{\mathcal{F}} = \Theta\mathcal{F}$ with $\Theta = (T_2/T_1) - 1$. With a set of standard calculations, one may obtain the various field constants $A...D$ and express the velocity disturbance on the upstream side of the flame in the form:

$$u'_1(x = a) = \frac{v_0}{\mathcal{D}(\omega)}[ie^{-ikl}\sin ka + e^{-ika}\cos kl] \tag{3.6}$$

where $\mathcal{D}(\omega) = \cos kl - \widehat{\mathcal{F}}\sin ka \sin kb$ designates the dispersion relation of the system. It is then easy to deduce the heat release rate fluctuation induced by this velocity fluctuation as,

$$\dot{Q}' = \overline{\dot{Q}}\mathcal{F}\frac{u'_1}{\overline{u}} = \overline{\dot{Q}}\mathcal{F}(\omega, u')\frac{v_0}{\overline{u}}\frac{1}{\mathcal{D}(\omega)}[ie^{-ikl}\sin ka + e^{-ika}\cos kl] \tag{3.7}$$

These expressions give rise to two different situations. In the first, designated in this article as SSO, the dispersion relation $\mathcal{D}(\omega) = 0$ has complex roots, and one of these roots has a positive imaginary part. This may give rise to unstable

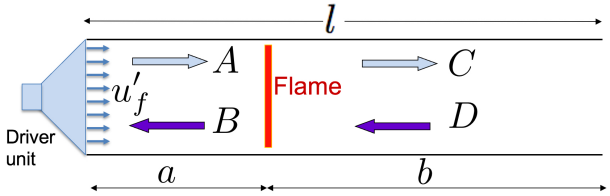

Figure 3.6. *Model problem. The combustion system comprises a driver unit on the upstream side, an open end downstream. A compact flame is located at a distance $x = a$ from the inlet. The driver unit modulates the flame with a velocity $u'_f = v_0 e^{-i\omega t}$.*

oscillations that will eventually lead to a limit cycle because of nonlinear mechanisms represented by the describing function. The second possibility is to avoid having an oscillatory operating regime by moving the complex roots of the dispersion relation and shifting them in the high frequency range where the describing function features low gain values. We know that combustion oscillations generally occur at a frequency corresponding to one of the natural resonant modes of the system. These eigenfrequencies are given by the dispersion relation in the absence of a flame, i.e., $\cos kl = 0$. The first of these eigenfrequencies corresponds to the 1L (quarter-wave) mode and is given by $\omega_0^1 = (\pi/2)(c/l)$. If l is made sufficiently short, this eigenfrequency takes large values, and one may expect that the FDF gain corresponding to this eigenfrequency will be small: $|\widehat{\mathcal{F}}(\omega_0^1)| << 1$. For the range of angular frequencies that is well below ω_0^1, ka will take small values $ka << 1$, since a is a fraction of l. One then finds that $\mathcal{D}(\omega) \simeq \cos kl$. The velocity fluctuation on the upstream side of the flame given by expression (Eq. 3.6) then becomes:

$$u'_1(x = a) \simeq \frac{v_0}{\mathcal{D}(\omega)}(\cos kl) \tag{3.8}$$

Using the approximate expression of $\mathcal{D}(\omega)$, one arrives at the result that $u'_1(x = a) \simeq v_0$. The velocity fluctuation on the upstream side of the flame is nearly identical to the velocity modulation imposed on the system u'_f. In essence, the flame has been stabilized by reducing the feedback contribution to the velocity disturbance that is incident to the flame. The feedback is present, but its contribution has been made negligible. One may then measure $u'_1(x = a)$, determine $\dot{Q}'$, and deduce $\mathcal{F}$ from these measurements. This second situation is designated in this article as SFM. It clearly allows the determination of the FDF using harmonic forcing.

Chapter 4

Guide for measuring FDFs of weakly transparent injectors

Contents

This chapter contains a detailed discussion on the determination of the flame describing functions (FDFs). The case of injectors that are weakly transparent to acoustic waves is specifically considered. These injectors act as dissipative elements due to their large area changes and high pressure drops, and in this sense, they differ from the traditional acoustically-transparent elements, which only weakly influence the acoustic propagation. The velocity reference generally considered in the plenum for acoustically transparent injectors can only capture the FDF phase at the base of the flame, whereas the FDF gain differs substantially between plenum and chamber velocity measurements. In this case, if the velocity reference is considered in the plenum, the obtained describing function would represent the response of both the injector and flame to incoming acoustic perturbations. It is then advisable to consider the velocity reference directly at the base of the flame according to the primary definition of the FDF. A criterion is discussed for determining the relative velocity fluctuations at the injector exit by considering its equality with the relative volumetric flow rate fluctuations. The deduced location is found to be close to the position of the maximum of mean axial velocity for the type of injectors studied. Both the gain and the phase of the FDF are found to be sensitive to the velocity measurement location in the chamber, indicating that this has to be correctly determined. A brief note on the injector's frequency response is provided in terms of an injector describing function, which varies nonlinearly depending on the amplitude of incident perturbations. Finally, the low frequency behavior of the FDFs is discussed in the case of premixed propane/air and in that of heptane spray flames. While the low frequency limits of the premixed propane flame match the analytically-derived low frequency limit from the literature, the behavior of heptane spray flames is different, which could be attributed to the quasi-premixed behavior of these spray flames under certain operating conditions, as discussed in Chapter 1.

4.1 Introduction

The flame transfer function (FTF) is a widely used concept for characterizing the flame response to incident acoustic perturbations and is extensively exploited in low-order models. Since the FTF is linear, it cannot describe nonlinear phenomena such as limit cycle amplitude saturation, mode switching, or triggering. To account for nonlinearity in the flame response to incident perturbations, the flame describing function (FDF) framework was introduced, which considers the dependence of flame response on the amplitude of the incoming perturbations. This was exemplified by Dowling (1997) in a theoretical investigation of a ducted flame, and the effectiveness of this framework was demonstrated by Noiray et al. (2008), who showed that it allowed retrieving many of the nonlinear features observed

experimentally. The FTF/FDF framework has been successfully used in capturing the flame dynamics and in low-order predictive tools of instabilities (see, for example, Schuller et al. (2020)). Several extensions to the FTF/FDF framework have also been proposed to account for other phenomena such as the consideration of harmonics (Haeringer et al. 2019), the existence of multiple modes (Boudy et al. 2013; Moeck and Paschereit 2012; Orchini and Juniper 2016) and varying-amplitude limit cycles (Kabiraj and Sujith 2011; Kabiraj et al. 2011).

In general, the heat release rate fluctuations ($\dot{Q}'/\overline{\dot{Q}}$) from flames are known to depend on equivalence ratio fluctuations ($\phi'/\overline{\phi}$) together with volumetric flow rate fluctuations ($\dot{q}_v'/\overline{\dot{q}_v}$). and one would have to determine two describing functions such that:

$$\dot{Q}'/\overline{\dot{Q}} = \mathcal{F}_\phi(\phi'/\overline{\phi}) + \mathcal{F}_v(\dot{q}_v'/\overline{\dot{q}_v}) \tag{4.1}$$

where $\mathcal{F}_\phi$ is the describing function pertaining to the equivalence ratio fluctuations and $\mathcal{F}_v$ is the describing function corresponding to the volumetric flow rate fluctuations. In the case of perfectly premixed flames, it is natural to eliminate the dependence with respect to equivalence ratio fluctuations, but this need not be true for the case of technically premixed flames, such as the spray flames studied here. It is indicated, however, in Chapter 2 that these flames behave in a quasi-premixed fashion, and further details on this consideration are provided in the respective chapters of this thesis dealing with the FDFs. Thus, in the following discussions, only the describing function accounting for the volumetric flow rate fluctuations at the flame base is examined according to the equation:

$$\mathcal{F} = \frac{\dot{Q}'/\overline{\dot{Q}}}{\dot{q}_v'/\overline{\dot{q}_v}} \tag{4.2}$$

It is generally not easy to measure volumetric flow rate fluctuations experimentally, and the denominator is usually replaced by velocity fluctuations ($u'/\overline{u}$) by assuming that,

$$\dot{q}_v'/\overline{\dot{q}_v} = u'/\overline{u} \tag{4.3}$$

By definition, the velocity must be measured at the base of the flame. However, for practical reasons, velocity measurements are often carried out upstream of the injector in the plenum, where the flow is nearly uniform in the measuring section, and simpler techniques can be used. In the case of injectors that are acoustically transparent, the length of the injector is usually much smaller than the acoustic wavelength, and the velocity change across the injector is negligible. The injector essentially transmits the acoustic waves, and the reference velocity can be measured before or after the injector for FDF determination. This has been verified, for example, by Palies et al. (2011), Palies et al. (2009), and Kim et al.

(2009), who have measured the velocity fluctuations in the plenum and chamber with acoustically transparent injectors and have found the two to be equivalent. Even though the injectors studied here are acoustically compact, they impose a strong variation in the velocity fluctuation level between the plenum and the chamber, and the FDF is then less easily obtained. This chapter thus deals with the general questions arising in the FDF determination when the injection unit is weakly transparent to acoustic waves. It begins with a brief description of the experimental setup (Section 4.2). It is next useful to examine the nature of injectors that are weakly transparent to acoustic waves (Section 4.3). It is then shown how to select a suitable location for measuring relative velocity fluctuations (Section 4.4) and the sensitivity of the FDF to the measurement location is analyzed in Section 4.5. The importance of considering the injector frequency response is examined in Section 4.6. This is followed by a discussion of the low frequency limits of the FDF (Section 4.7). Finally, an appendix discusses a specific point of the present FDF experimental setup, where sometimes a metal ring is mounted at the bottom of the chamber to hold a microphone. The bottom metal ring changes the thermal environment compared to a case where the chamber is completely made of a quartz tube, and the idea is to verify whether this influences the flame response measurement. This chapter serves as a guide for determining FDFs for injectors that are weakly transparent to acoustic waves, a class of injection units analyzed throughout this thesis.

4.2 Experimental setup

The SICCA-Spray combustor shown in Fig. 4.1 (a) is used in the present set of experiments. Only the essential information of the experimental setup is recalled here, and the readers are referred to Chapter 1 for more details. This system comprises two driver units plugged onto the upstream manifold. The wave generator excites the driver units through a power amplifier to modulate the air flow at different frequencies and amplitudes. The amplitude of the reference signal is controlled by specifying an amplifier voltage V_0 in the wave generator, which, in turn, results in a particular level of velocity fluctuation in the system depending on the frequency of the modulating signal. The length of the chamber is chosen between $100\,\mathrm{mm}$ to $165\,\mathrm{mm}$ to avoid any possible self-sustained oscillations. Acoustic pressures in the plenum are measured with three microphones marked as MP1, MP2, and MP3 in Fig. 4.1. These are also used to obtain the acoustic velocity at this section using the multi-microphone method as discussed in Chapter 1. In addition, a hot wire anemometer marked as HW1 is placed in the same section as MP2 to measure the velocity. Velocity measurements in the chamber are delivered by a phase Doppler particle analyzer (PDPA) operating in laser Doppler anemometry (LDA) mode to augment the data rate. For velocity measurements under cold conditions, the flow is seeded with fine oil droplets, whereas the mea-

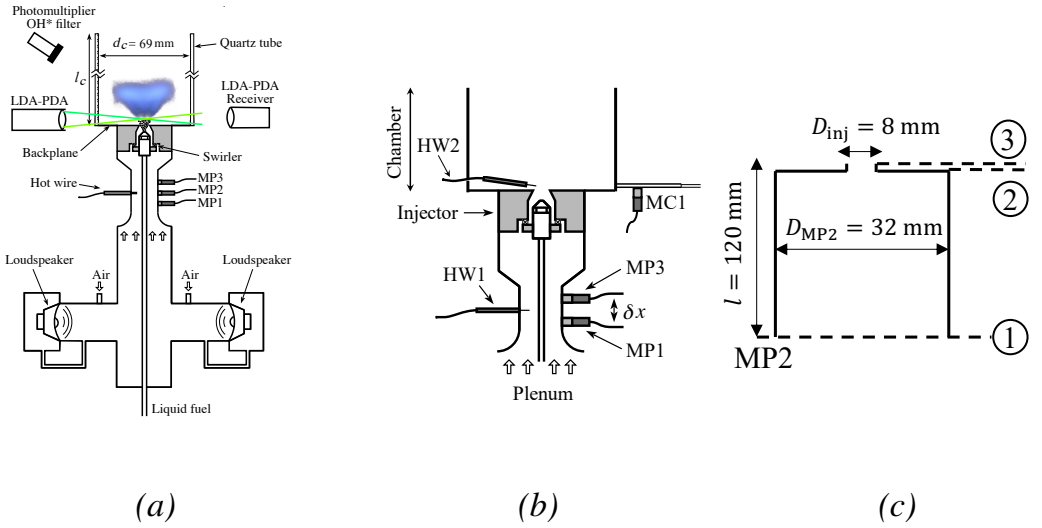

(a) *(b)* *(c)*

Figure 4.1. *(a) Schematic of SICCA-Spray experimental setup (reproduced from Chapter 1). (b) The experimental setup of SICCA-Spray featuring a hot wire anemometer and microphone in the chamber. The bottom portion of the plenum is not shown. (c) Idealized representation of the plenum from the location of MP2 to the injector outlet.*

surements are carried out directly on the heptane droplets in the presence of flame. The velocity measurements in cold conditions are also carried out using a second hot wire anemometer placed in the chamber designated as HW2, as shown in Fig. 4.1 (b). These measurements are useful in situations where flow seeding is not possible. Light emission is measured using a photomultiplier fitted with an OH^* filter centered at $308\,\mathrm{mm}$. These signals are considered to approximately represent the heat release rate fluctuations from the flame, as discussed in Chapter 2. All the measurements reported in this chapter are carried out at an air mass flow rate of $\dot{m}_a = 2.6\,\mathrm{g\,s^{-1}}$, and when a flame is present, the fuel mass flow rate is maintained at $\dot{m}_f = 520\,\mathrm{g\,h^{-1}}$, corresponding to the operating point F1.

4.3 Injectors that are weakly transparent to acoustic waves

As already indicated, the measurement of velocity for FDF determination, although by definition needs to be considered at the base of the flame, is generally carried out upstream of the injector in the plenum considering ease of measurements. While this is suitable for the case of acoustically transparent injectors, it is not so for the injectors considered in this study that are only weakly transparent to acoustic waves. Figure 4.2 shows the evolution of magnitude and phase of the normalized velocity fluctuations $u'/\overline{u}$ with frequency in the plenum and chamber for swirler 716. While bulk velocity is used for normalizing the plenum velocity,

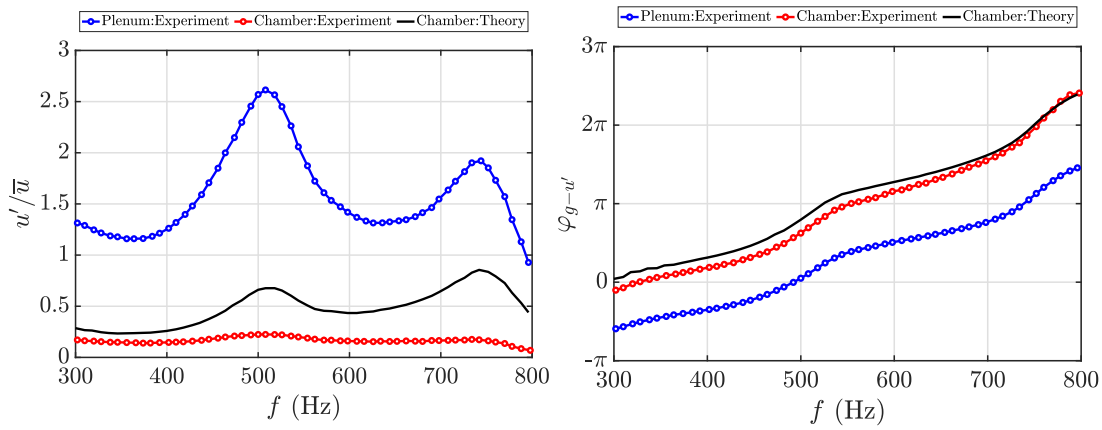

Figure 4.2. *Left: RMS of relative velocity evolution measured in the plenum and chamber close to the injector exit along with a comparison of the theoretically deduced chamber relative velocity fluctuations at different frequencies. Right: Phase between velocity and reference generator signal for velocity measured in the plenum, chamber and theoretically deduced chamber velocity at different frequencies. Swirler: 716*

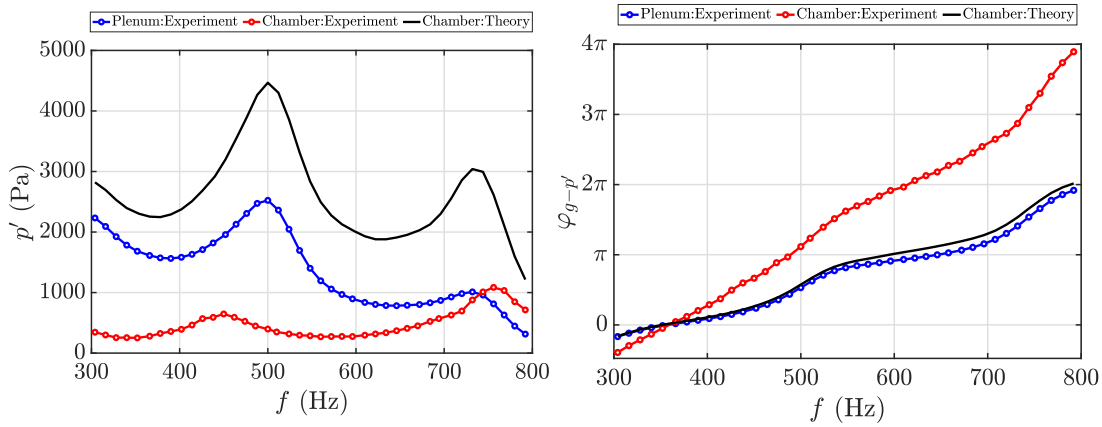

Figure 4.3. *Left: RMS pressure evolution measured in the plenum and chamber close to the injector exit along with a comparison of the theoretically deduced chamber pressure at different frequencies. Right: Phase between pressure and reference generator signal for pressure measured in the plenum, chamber and theoretically deduced chamber pressure at different frequencies. Swirler: 716*

mean velocity is used for the chamber measurements, and the reason for this is discussed in the following section. The phase of velocities is obtained by considering the reference signal produced by the wave generator. The air flow is modulated at the maximum possible amplifier voltage ($V_0 = 3\,\mathrm{V}$), thus ensuring the highest velocity fluctuation levels in the system. The acoustic velocity in the plenum is obtained by multi-microphone method described in Chapter 1 at the section where MP2 is mounted (see Fig. 4.1 (a)). $\overline{u}$ is the bulk velocity in the measurement section of the plenum. The velocity fluctuations in the chamber close to the injector exit are obtained at a radius $r = 4\,\mathrm{mm}$ from the injector axis and at a height of $h = 2.5\,\mathrm{mm}$ above the backplane using LDA. It is worth noting at this stage that the velocity at the exit of a swirling injector is highly nonuniform and one has to select a particular point to measure the velocity mean value and its fluctuations. The reason for the selection of this point for velocity measurement is elaborated in Section 4.4. The relative root mean square (RMS) velocity fluctuation amplitude strongly diminishes from the plenum to the chamber for the class of injectors considered in the present investigation. Additionally, the phase of the velocity with respect to the reference generator signal 'g' also differs between the two measurements. It is then useful to verify if the variation in the velocity fluctuation level can be depicted by a simple model considering the section change from the plenum to the chamber. For this, it is sufficient to only consider the area change from the MP2 section of the plenum having a diameter of $D_{\mathrm{MP2}} = 32\,\mathrm{mm}$ to the injector exit diameter of $D_{\mathrm{inj}} = 8\,\mathrm{mm}$, as the other area changes in between them would eventually be canceled out in transfer matrix multiplications. The idealized representation between plenum and chamber is shown by the schematic diagram shown in Fig. 4.1 (c). Using $e^{-i\omega t}$ convention to represent the time harmonic dependence of the acoustic waves in the system and adopting a transfer matrix representation, the relation between pressure and velocity in the straight tube between sections 1 and 2 can be written as (Fischer et al. 2006)

$$\begin{bmatrix} \dfrac{p_2'}{\rho c} \\ u_2' \end{bmatrix} = \begin{bmatrix} \cos(kl) & i\sin(kl) \\ i\sin(kl) & \cos(kl) \end{bmatrix} \begin{bmatrix} \dfrac{p_1'}{\rho c} \\ u_1' \end{bmatrix} \tag{4.4}$$

where p' and u' represent the pressure and velocity in the respective sections, and ρ and c represents the density and speed of sound. The area change between sections 2 and 3 can be represented as,

$$\begin{bmatrix} \dfrac{p_3'}{\rho c} \\ u_3' \end{bmatrix} = \begin{bmatrix} 1 & 0 \\ 0 & \dfrac{S_1}{S_2} \end{bmatrix} \begin{bmatrix} \dfrac{p_2'}{\rho c} \\ u_2' \end{bmatrix} \tag{4.5}$$

where S_1 and S_2 represents the cross-sectional area in the plenum (indicated with the subscript '1') and injector exit (indicated with the subscript '2'), respectively. By combining Eqs. 4.4 and 4.5, the pressure and velocity at the injector exit can

be written in terms of pressure and velocity at section 1 as,

$$u'_3 = i\frac{S_1}{S_2}\frac{p'_1}{\rho c}\sin(kl) + \frac{S_1}{S_2}u'_1\cos(kl) \tag{4.6}$$

$$\frac{p'_3}{\rho c} = \cos(kl)\frac{p'_1}{\rho c} + i\sin(kl)u'_1 \tag{4.7}$$

Using the above equation, one obtains the velocity at the injector exit shown in Fig. 4.2 (black curve) after normalizing with the bulk velocity. It can be seen that the phase of the velocity in the chamber at the exit of the injector is retrieved by making use of this formulation. However, the magnitude of velocity fluctuations notably differs from the measurements. Although this difference is minor at frequencies below $400\,\mathrm{Hz}$, there is a factor of five between theoretical estimates and measured values at higher frequencies, implying that velocities at the injector exit cannot be reproduced by a purely acoustic representation of the system. Even if one considers a normalization of the measured velocities at the injector exit with bulk velocity, the match can still not be obtained using the representation of Eq. 4.6. In addition to velocity, the evolution of measured pressure in the plenum and chamber along with the chamber pressure deduced using Eq. 4.7 is shown in Fig. 4.3. The phase of the pressure signals is obtained by comparing it against the reference generator signal. The pressure phase is nearly the same between the plenum measurement and the theoretically determined chamber pressure. Simple calculations from Eq. 4.7 also reveal that the model would give nearly the same phase in the chamber as in the plenum if one considers that a standing wave is established in the plenum. The experimentally determined phase in the chamber, however, notably differs from the phase deduced from the theory considering a network formed by a straight tube and an area change between plenum and injector exit. One can also see that the theory over-predicts the chamber pressure compared to the experimentally determined value.

An alternate way to account for this variation in pressure and velocity is to consider the representation of the injector from the literature. This was, for example, considered by Paschereit et al. (2002), Bellucci et al. (2005), and Fischer et al. (2006) and validated through experiments. Other works have also reported such models with a similar basis, and as an example, only these three representations are considered in a simplified fashion to see if they represent the present injectors. It is important here to note that the references Paschereit et al. (2002), Bellucci et al. (2005) use the convention $e^{+i\omega t}$ convention so that $+i$ has to be replaced by $-i$ to be consistent with our own convention. This is done in what follows. It is also worth noting that Fischer et al. (2006) use the more standard $e^{-i\omega t}$ convention, but the matrices quoted in one of their tables are not consistent with that convention.

The model for the injector given by Paschereit et al. (2002) accounting for the

area jump and the pressure drop can be written as,

$$\boldsymbol{B} = \begin{bmatrix} 1 & \rho c M \left[\left(1 - \sigma - \left(\dfrac{S_1}{S_2} \right)^2 \right) + i \dfrac{\omega}{c} L_{\text{eff}} \right] \\ 0 & \dfrac{S_1}{S_2} \end{bmatrix} \tag{4.8}$$

where M is the Mach number, σ is the pressure loss coefficient, and L_{eff} is the reduced effective length of the injector which relates the upstream and downstream area of the injector. Note that we use σ instead of ζ to designate the pressure loss coefficient and that $+i$ replaces the $-i$ of the original article Paschereit et al. (2002). The model proposed by Bellucci et al. (2005) and designated as the L-ζ model is given in its original form,

$$\boldsymbol{B} = \begin{bmatrix} 1 & i\rho\omega L_{\text{eff}} + \rho\zeta u \\ 0 & 1 \end{bmatrix} \tag{4.9}$$

However, one notes that the off-diagonal coefficient in the matrix should be dimensionless and the sign of the second term should probably be negative to be consistent with the model of Paschereit et al. (2002). It is then necessary to correct for these various items and one gets :

$$\boldsymbol{B} = \begin{bmatrix} 1 & -\sigma u/c + i\omega L_{\text{eff}}/c \\ 0 & 1 \end{bmatrix} \tag{4.10}$$

Another model given by Fischer et al. (2006) to account for the injector pressure loss is with our own notations,

$$\boldsymbol{B} = \begin{bmatrix} 1 & -\sigma M \sqrt{\dfrac{\omega D_{\text{H}}}{c}} \\ 0 & 1 \end{bmatrix} \tag{4.11}$$

where D_H is the hydraulic diameter. It is unusual to see a dependence with respect to the square root of ω which is relatively non-standard and also to note that this last model would in the zero frequency limit correspond to an identity matrix inducing no pressure loss at all.

Combining the injector models in Eqns. 4.8, 4.9, and 4.11 with the straight section and area change between plenum and injector exit might account for the change in pressure, but will result in the same form for u_3' as Eq. 4.6, which does not reflect for the magnitude change in velocity. Further considerations on whether these models capture the variation in pressure need to be analyzed and are not pursued in this thesis. The injectors studied here do not conform to the traditional

representation valid for injectors that are transparent to acoustic waves as they notably reduce the acoustic energy between the upstream and downstream sections, as shown by the significant reduction in pressure and velocity fluctuation levels in Figs. 4.2 and 4.3. Even though the injectors are compact compared to the acoustic wavelength, they feature high pressure drop and abrupt area changes resulting in dissipation of the acoustic energy, making them only weakly transparent to acoustic waves. In addition, considering a purely acoustic formulation might not be able to capture the convective vorticity mode that is known to be generated when acoustic waves impinge on a flow singularity like an orifice in a baffle (Noiray et al. 2009c), on a blade row, or on a swirler. The behavior of injectors that are weakly transparent to acoustic waves is investigated further in Section 4.6. Considering reference velocity measurement location in the plenum, in fact, couples the injector and flame response to acoustics, giving rise to an injector + flame describing function $\mathcal{F}_{IF}$. Although a correction can be applied to obtain the phase of the flame describing function, the gain would still not be right. This necessitates the measurement of velocity fluctuation in the chamber for the class of injectors considered in this study to directly obtain the flame describing function $\mathcal{F}_F$. The other possibility is to use a frequency-dependent factor in the injector model accounting for the reduction in relative velocity fluctuations. This is not considered in the present study and is left as future work. However, the velocity determination in the chamber raises additional questions on the measurement location as the velocity at the exit of a swirling injector is nonuniform. This is explained in further detail in the following section.

4.4 Reference velocity determination

This section discusses the selection of a location for the measurement of velocity that can be used to determine the describing function of flames established by injectors that are weakly transparent to acoustic disturbances. This location is deduced from detailed measurements of axial velocity profiles.

4.4.1 Axial velocity profiles

This subsection gives information about the spray and velocity profile of swirler 716 and 712, both under cold flow and reacting conditions.

Figure 4.4 (a) shows the axial velocity profiles (mean and RMS) of 716 in the chamber when the cold flow is modulated at $700\,\mathrm{Hz}$ with an amplifier voltage of $V_0 = 3\,\mathrm{V}$ (peak to peak) applied to the SICCA-Spray driver units. The measured velocity is henceforth attached with the subscripts ‘c’ referring to chamber and ‘r’ referring to the radial location. Although the cold flow velocity profiles with different swirlers were already discussed in Chapter 1, it is necessary to examine the results obtained when the air flow is modulated. For these measurements, the

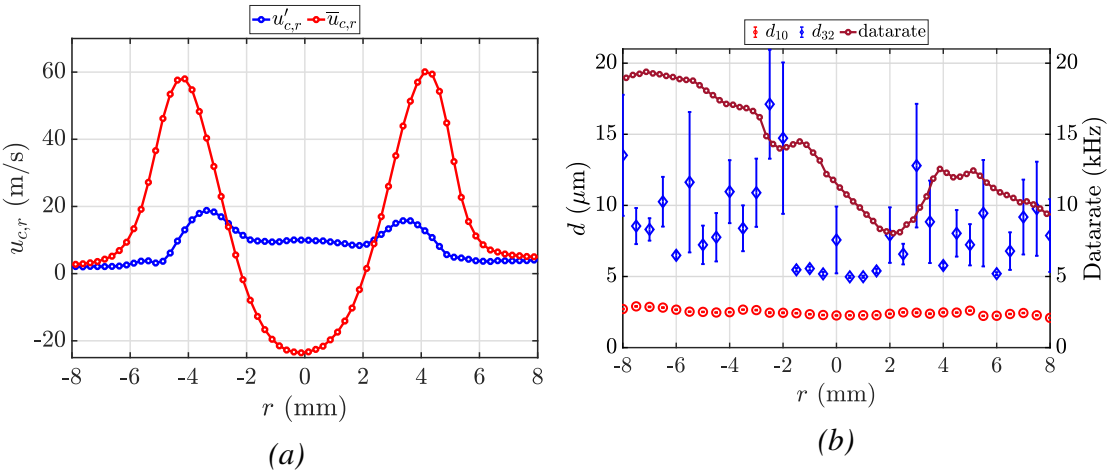

Figure 4.4. *(a) Axial velocity profile measured in cold conditions showing mean (red) and RMS (blue) velocity fluctuations for swirler 716. The flow is seeded with small oil droplets and the system is pulsed at* $700\,\mathrm{Hz}$ *with an amplifier voltage* $V_0 = 3\,\mathrm{V}$. *(b) Mean* (d_{10}) *and Sauter mean diameter* (d_{32}) *of the oil droplets measured in PDA mode and the data rate of the measurement when operated under LDA mode. Error bars on the diameters indicate the 95% statistical confidence interval computed using bootstrapping method. All measurements are performed at a height of* $h = 2.5\,\mathrm{mm}$ *above the chamber backplane.*

air flow is seeded with oil droplets dispensed by an air nebulizer (Durox et al. 1999). The presence of a strong recirculation zone can be seen near the injector centerline, down to $-20\,\mathrm{m\,s^{-1}}$. The mean velocity reaches a maximum of $60\,\mathrm{m\,s^{-1}}$ at $r = 4\,\mathrm{mm}$. It is worth noting that the velocity fluctuation profile is not flat and that the maximum velocity fluctuation does not occur at the same radius as the maximum of mean velocity. The data acquisition rate profiles and the mean diameter d_{10} and Sauter mean diameter d_{32} of the oil droplets are shown in Fig. 4.4 (b) for swirler 716. The data rate quoted is for operation in the LDA mode, while droplet sizes are obtained in PDA mode. The large data rate allows reconstruction of the velocity signals up to $1000\,\mathrm{Hz}$ (more than 10,000 counts per second). Furthermore, d_{10} is small enough, of the order of $2.5\,\mu\mathrm{m}$, for the oil droplets to follow the air flow well. The velocity profile for the other swirlers of the T2 category can be reasonably expected to evolve similar to that of 716 based on the steady velocity profiles shown in Chapter 1, and hence are not explored separately. The measurements are also performed with swirler 712 belonging to the T1 category, and the velocity profile is displayed in Fig. 4.5. Swirler 712 has comparatively a slightly lower negative peak velocity of $-12\,\mathrm{m\,s^{-1}}$ at the center, with the maximum mean velocity also being smaller at roughly $50\,\mathrm{m\,s^{-1}}$. The location of the maximum mean axial velocity occurs at a radius of $3.5\,\mathrm{mm}$, identical to the steady state velocity profile reported in Chapter 1. Since the size of the oil droplets will not change with the swirler, only the distribution corresponding to heptane spray

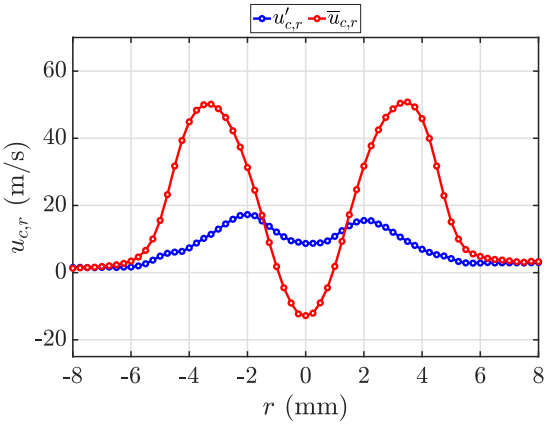

Figure 4.5. *Axial velocity profile measured in cold conditions showing mean (red) and RMS (blue) velocity fluctuations for swirler 712. The flow is seeded with small oil droplets and the system is pulsed at* $700\,\mathrm{Hz}$ *with an amplifier voltage* $V_0 = 3\,\mathrm{V}$*. The measurements are performed at a height of* $h = 2.5\,\mathrm{mm}$ *above the chamber backplane.*

under hot conditions is reported in Fig. 4.7.

Under reactive conditions, the velocity measurements are made directly on the spray of heptane droplets. The mean and RMS velocity profile for 716 are shown in Fig. 4.6 (a) when the flame is modulated at $700\,\mathrm{Hz}$ with an amplifier voltage of $3\,\mathrm{V}$ (peak to peak). The maximum velocity is slightly higher than under cold flow conditions ($69\,\mathrm{m\,s^{-1}}$) and occurs at $r = 4\,\mathrm{mm}$. The recirculation zone around the injector axis is less pronounced than in the cold flow velocity profile (shown in Fig. 4.4 (a)). This is because of fewer droplets in this region resulting in less precise velocity estimates. The data acquisition rate and diameter profiles shown in Fig. 4.6 (b), indicate that beyond $r = 7\,\mathrm{mm}$ there are practically no droplets due to the presence of the flame in this zone. The data rate is high between $r = 3\,\mathrm{mm}$ to $r = 6\,\mathrm{mm}$ (more than 20,000 counts per second), making it possible to temporally reconstruct the droplet dynamics. The particle sizes d_{10} and d_{32} change substantially depending on the position relative to the injector outlet ($8\,\mathrm{mm}$ diameter). Close to the center, only a small amount of large droplets get trapped in the stagnation zone. As the atomizer produces a hollow cone, the fine droplets are ejected away from the axis. Outside the recirculation zone, from $r = 2.5\,\mathrm{mm}$, the droplet size is reduced, and the droplet number increases, resulting in a higher counting rate. Beyond the injector outlet radius, the particle size is slightly augmented. Just ahead of the injector outlet lip ($r = 4\,\mathrm{mm}$), the spray features very fine droplets ($d_{10} = 5\,\mu\mathrm{m}$), which can follow the air flow well even in the presence of strong velocity gradients. An estimate of the flow tracking by the $5\,\mu\mathrm{m}$ droplets can be done by looking at how they behave in a flow that is harmonically modulated. A classical calculation makes it possible to show that, with an oscillation at $500\,\mathrm{Hz}$, the amplitude of the droplet velocity fluctuation is 95% compared to the ampli-

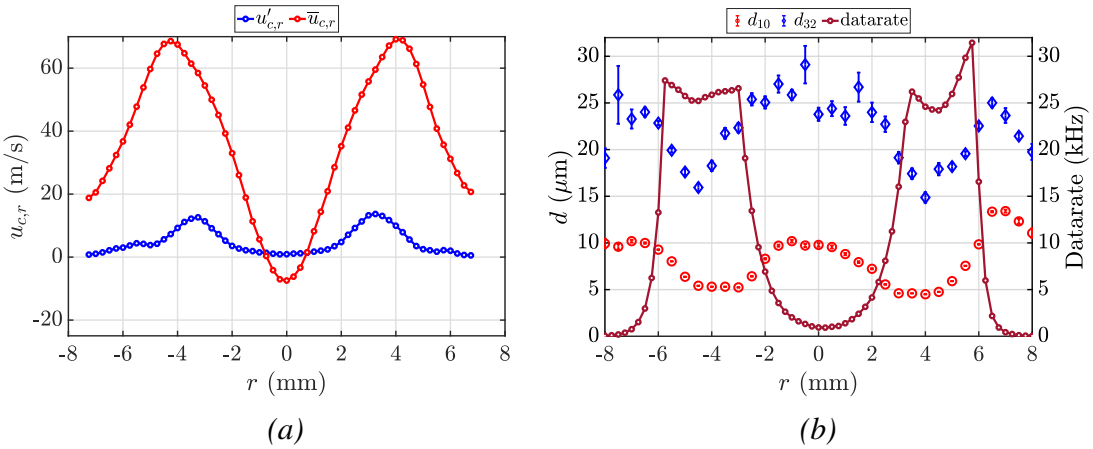

Figure 4.6. *(a) Axial velocity profile measured in reactive conditions showing mean (red) and RMS (blue) velocity fluctuations for swirler 716. The system is pulsed at* 700 Hz *with an amplifier voltage* $V_0 = 3\,\mathrm{V}$. *(b) Mean (*d_{10} *in red) and Sauter mean diameter (*d_{32} *in blue) of the heptane droplets measured in PDA mode and the data rate of the measurement when operated under LDA mode. Error bars on the diameters indicate the 95% statistical confidence interval computed using bootstrapping method. All measurements are performed at a height of* $h = 2.5\,\mathrm{mm}$ *above the chamber backplane.*

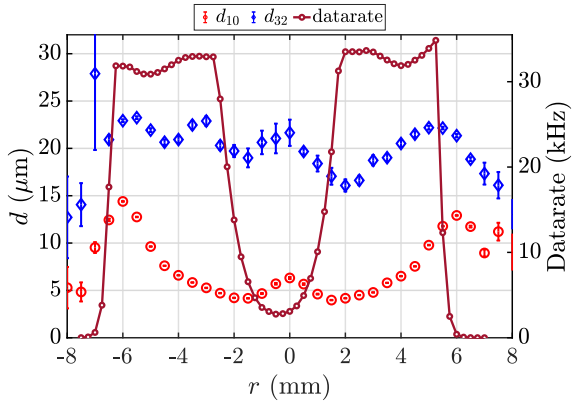

Figure 4.7. *(a) Mean (*d_{10} *in red) and Sauter mean (*d_{32} *in blue) diameter of the heptane droplets measured in PDA mode and the data rate of the measurement when operated under LDA mode for swirler 712. This acquisition is carried out in the presence of flame at* 700 Hz *with an amplifier voltage* $V_0 = 3\,\mathrm{V}$. *Error bars on the diameters indicate the 95% statistical confidence interval computed using bootstrapping method. The measurements are performed at a height of* $h = 2.5\,\mathrm{mm}$ *above the chamber backplane.*

tude of the gas flow. The phase delay remains small, of the order of $\pi/20$ for this droplet size and frequency. It is, therefore, possible to measure the relative velocity fluctuations that are needed to determine the FDF under reactive conditions by deducing the air velocity from the velocity measurement carried out on the fuel droplets in the region where the diameter d_{10} is small. The size distributions for 712 reported in Fig. 4.7 under hot conditions indicate that the droplet diameters take values similar to those found for 716, and d_{10} is mostly less than $10\,\mu\mathrm{m}$ in the regions where the droplet availability is sufficient. It is pointed out in advance that the measurements made with the two swirlers under the same flow rate conditions give the values d_{10} of $5.8\,\mu\mathrm{m}$ at $r = 3.5\,\mathrm{mm}$ for swirler 712 and $4.5\,\mu\mathrm{m}$ at $r = 4\,\mathrm{mm}$ for swirler 716. The reason why the droplet sizes are indicated at these radial positions is given in the following section.

4.4.2 Velocity measurement location

Profiles shown in the previous section indicate that the velocity at the injector outlet is nonuniform, and this raises a question on the location to be chosen for measuring the reference velocity fluctuations that can be used to determine the FDF. As already mentioned, the FDF, by definition, considers volume flow rate fluctuations at the base of the flame. One may then find a point at the flame base where the relative volumetric flow rate fluctuations can be replaced by the relative velocity fluctuations, i.e., where Eq. 4.3 is satisfied. To find where this equality is verified, one has to first determine mean $\overline{\dot{q}_v}$ and RMS $\dot{q}'_v$ of volume flow rate at the modulation frequency by integrating the measured velocity profiles (from LDA) obtained under cold flow conditions at $h = 2.5\,\mathrm{mm}$ for 716 and 712 (shown in Fig. 4.4 and 4.5). The velocity is measured under cold flow conditions as the data rate under reactive conditions is too low in the central injection region, thus reducing the accuracy here. In addition to the velocity amplitude shown in Fig. 4.4 and 4.5, it is also interesting to see how the phase of velocity disturbances evolves as a function of the radial position. This is accomplished by acquiring the velocity signal delivered by the LDA system together with a reference signal constituted by the generator waveform delivered to the power amplifier. The phase between these two signals plotted as a function of the radial distance to the injector axis appears in Fig. 4.8 for swirler 716. This figure also shows the mean flow velocity measured under cold flow conditions (the corresponding profile is the same as that appearing in Fig. 4.4 (a) $\overline{u}_{c,r}$). The air flow is modulated at $700\,\mathrm{Hz}$ and at an amplifier voltage of $3\,\mathrm{V}$. It can be seen that the phase is only roughly constant between $3\,\mathrm{mm}$ and $4\,\mathrm{mm}$ and features rapid changes outside this region. This makes it necessary to account for this phase shift as a function of the radius in calculating the volumetric flow rate fluctuation. Figure 4.9 shows the radial evolution of $u'_{c,r}/\overline{u}_{c,r}$ for swirler 716 and 712, along with the calculated $\dot{q}'_v/\overline{\dot{q}_v}$. For 716, the curve of $u'_{c,r}/\overline{u}_{c,r}$ intersects the line of $\dot{q}'_v/\overline{\dot{q}_v}$ at four points: close to $\pm 4\,\mathrm{mm}$ and $\pm 5\,\mathrm{mm}$. It was previously shown that the diameter d_{10} of the spray droplets becomes larger

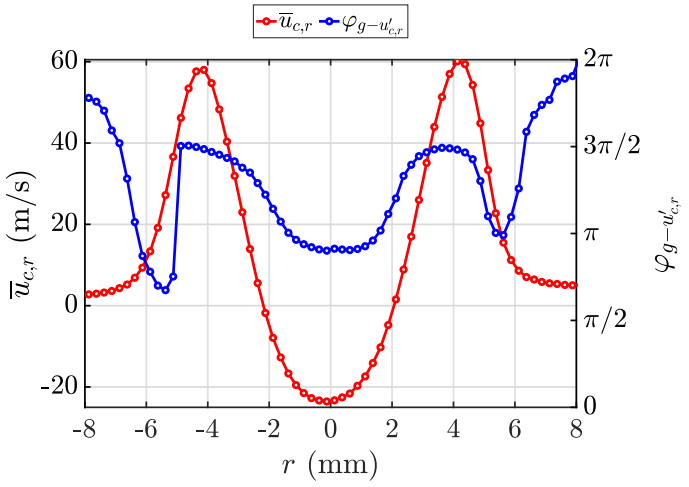

Figure 4.8. *Mean velocity profile (red) and phase between generator signal and velocity fluctuations (blue) for swirler 716. These measurements are made under cold conditions with oil seeding and by modulating the system at* 700 Hz *and* $V_0 = 3\,\mathrm{V}$. *The measurements are performed at a height of* $h = 2.5\,\mathrm{mm}$ *above the chamber backplane.*

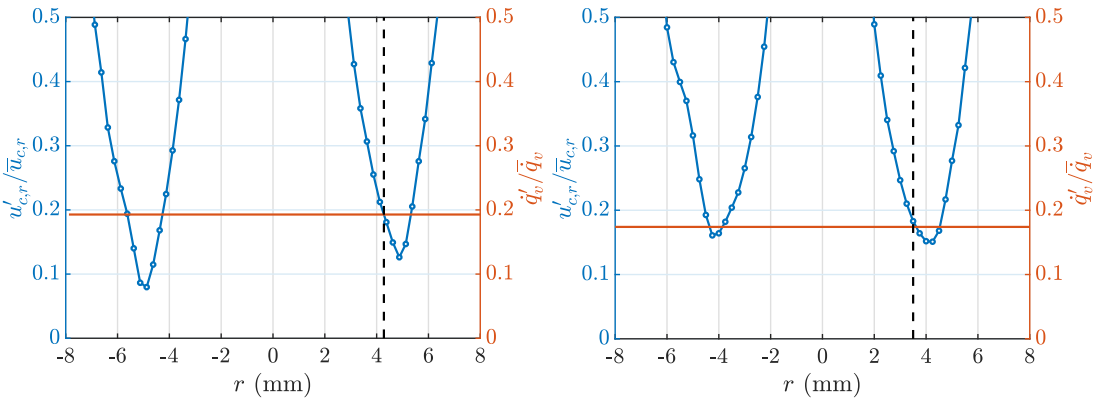

(a) 716 *(b) 712*

Figure 4.9. *Ratio of RMS to mean velocity at different radii and the calculated volume flow rate for swirlers 716 and 712. The vertical dotted line in black shows the location where relative velocity fluctuations coincide with the relative volume flow rate fluctuations. These measurements are made under cold conditions with oil seeding and by pulsing the system at* 700 Hz *and* $V_0 = 3\,\mathrm{V}$. *The measurements are performed at a height of* $h = 2.5\,\mathrm{mm}$ *above the chamber backplane. The results close to the center of the injector are not shown as the* $u'_{c,r}/\overline{u}_{c,r}$ *values are high due to the low value of* $\overline{u}_{c,r}$ *and also as the region of interest for this figure lies close to the injector outlet radius.*

beyond the injector outlet radius (shown in Fig. 4.6 (b)). It is, therefore, suitable to choose the point $r = \pm 4\,\mathrm{mm}$ and $h = 2.5\,\mathrm{mm}$ for the relative velocity fluctuation

measurement to use in the FDF determination as it satisfies the equality in Eq. 4.3. The location of r for FDF determination plays a crucial role as even a $1\,\mathrm{mm}$ shift from the optimal position will result in a larger difference (nearly a factor of 2 in this case) between the relative rates of velocity and volumetric flow fluctuations, with an error of the order of $\pi/10$ for the phase. For example, a measurement carried out in the middle of the outlet radius at $r = 2\,\mathrm{mm}$ and $h = 2.5\,\mathrm{mm}$ would have dramatic consequences on the FDF estimation, both on the gain and on the phase. It can also be seen from Fig. 4.4 (a) that nominal location ($r = 4\,\mathrm{mm}$ and $h = 2.5\,\mathrm{mm}$) essentially corresponds to the maximum of the mean axial velocity. Although these measurements were performed under cold flow conditions, on comparing the velocity profile with flame in Fig. 4.6 (a), one finds that the maximum of mean axial velocity still occurs at $r = \pm 4\,\mathrm{mm}$, validating the usage of cold flow conditions for selecting the measurement location of the relative velocity fluctuation used in the FDF. Similarly, for swirler 712 (Fig. 4.9 (b)), the point where Eq. 4.3 is verified occurs close to $r = 3.5\,\mathrm{mm}$, also the point corresponding to the maximum of mean axial velocity. From this analysis, it appears that the nominal velocity measurement point for FDF determination corresponds to the location of the maximum of mean axial velocity. Thus, as seen from the steady velocity profiles in Chapter 1, the suitable point for measuring relative velocity fluctuations is at $r = 3.5\,\mathrm{mm}$ for all the swirlers of T1 group and swirler 713 and 714 of T2 group, and $r = 4\,\mathrm{mm}$ for the rest of T2 group and swirler T. Measurements at other frequencies and amplitudes lead to similar conclusions.

4.5 Sensitivity of FDF to velocity measurement location

As seen in the previous section, the relative velocity fluctuation changes as a function of the radial distance from the injector axis, and a nominal point is chosen that verifies the equality in Eq. 4.3. This section discusses the possible deviation that could occur in the FDF if the reference velocity is measured away from the nominal location. For these measurements, the wave generator supplies a frequency ramp of $250\,\mathrm{Hz}$ to $850\,\mathrm{Hz}$ in $133\,\mathrm{s}$ to the driver units at an amplifier voltage of $V_0 = 3\,\mathrm{V}$. Figure 4.10 shows the FDF evolution for swirler 716 at different radial locations between $2.5\,\mathrm{mm}$ to $4.5\,\mathrm{mm}$. It is recalled here that the nominal velocity measurement location is at $r = 4\,\mathrm{mm}$. In order to ensure a good signal-to-noise ratio, the coherence function $\gamma^2 = |S_{\dot{Q}'u'}|^2/(S_{\dot{Q}'\dot{Q}'}S_{u'u'})$ is calculated at each frequency and the data is retained only if this value exceeds 0.9, ensuring a signal-to-noise ratio of at least $9.5\,\mathrm{dB}$. This procedure is adopted for all the transfer function measurements reported in this thesis. The heat release rate fluctuations for these measurements remain the same, and the variation occurs only in the velocity fluctuation levels. The phase φ_F evolves in a similar fashion for these radii except when $r > R_{\mathrm{inj}}$. Thus the sensitivity of the FDF phase to velocity location

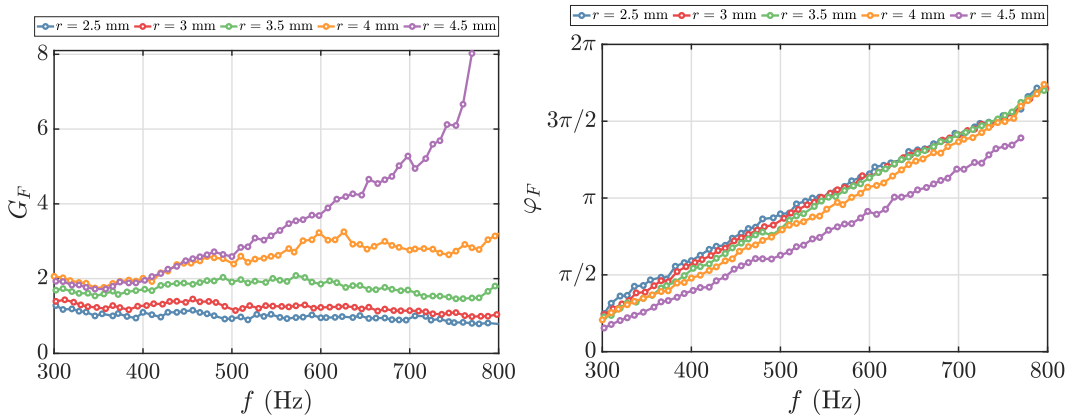

Figure 4.10. *Gain G_F and phase φ_F of the FDF $\mathcal{F}_F$ at different radial locations for swirler 716.*

is low as long as the measurements are carried out at a distance from the axis that is less than the outlet radius. The gain G_F, however, is sensitive to the radial position where velocity is recorded, underlining the necessity of using the nominal location.

4.6 Injector describing function

As discussed previously, the class of injectors considered in this study requires that the reference velocity measurement be performed at the exit of the injector at a nominal position where the relative velocity fluctuations match the relative volume flow rate fluctuations. One would then directly obtain the flame describing function $\mathcal{F}_F$. A reference velocity measurement in the plenum would result in a combined injector and flame transfer function $\mathcal{F}_{IF}$. Figure 4.11 shows the two describing functions $\mathcal{F}_{IF}$ and $\mathcal{F}_F$ for swirler 716 at different amplifier voltages V_0 delivered to the driver units. It is recalled here that the representation in terms of amplifier voltages can, in turn, be related to velocity fluctuations at the different frequencies. The displayed data is also smoothed using a five-point moving average. From the figure, it can be seen that the $\mathcal{F}_{IF}$ and $\mathcal{F}_F$ are notably different. This is distinct from the case of injectors that are transparent to acoustic waves, as, for example in Palies (2010), where the two describing functions were found to match at comparatively lower frequencies (wavelengths much larger than the distance between the plenum and the combustion chamber). Thus, one needs to either directly obtain the flame describing function by measuring the reference velocity in the chamber or account for the injector describing function if the reference velocity is measured in the plenum.

The optimum strategy is probably to do a direct measurement of velocity fluctuations in the chamber at the base of the flame, but it mandates some form of

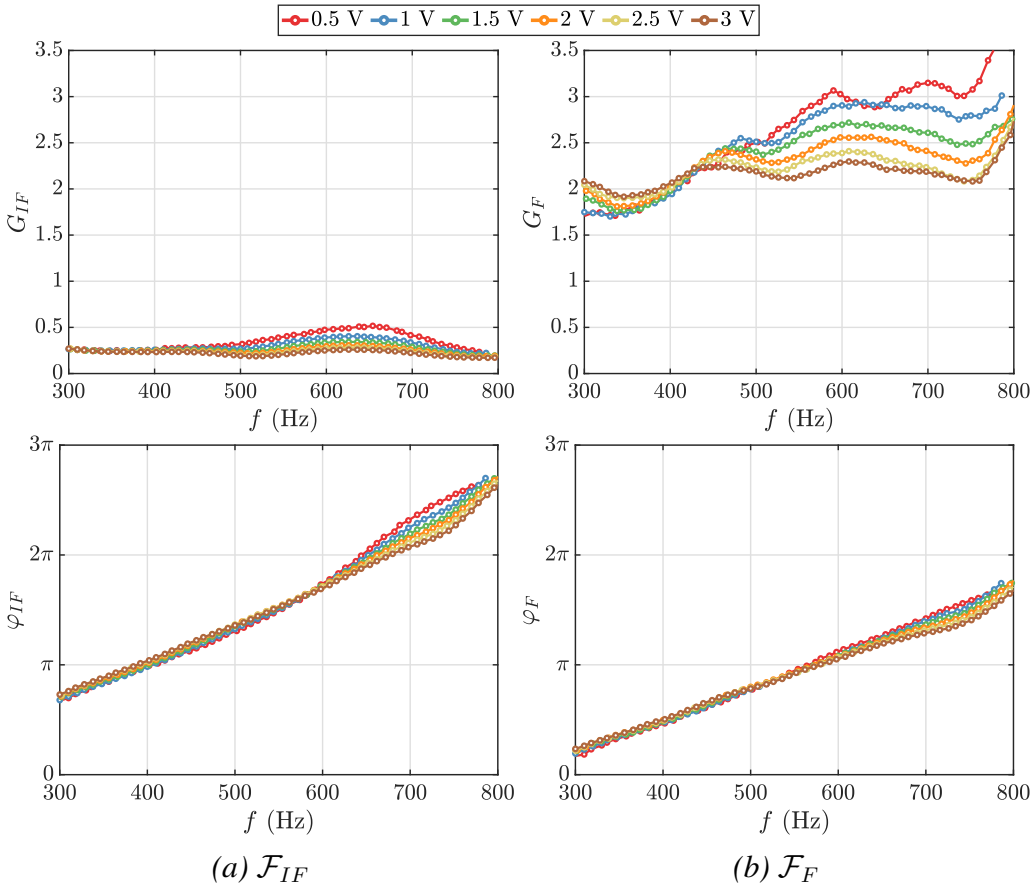

Figure 4.11. *Coupled injector and flame describing function $\mathcal{F}_{IF}$ and flame describing function $\mathcal{F}_F$ for swirler 716 at different amplifier voltages V_0 given to the driver units.*

optical measurement technique such as LDA or particle image velocimetry. However, such a measurement is not always feasible, especially in the case of industrial combustors where optical access to the flame zone is not available. Even though in the present work LDA is adopted, it is not suitable for all the configurations considered; for the spray flames, the small fuel droplets are themselves used as seeders, but for the case of premixed propane, such a flow seeding is not available. An oil seeding as in the cold flow measurements could be considered, but it was found with the heptane spray flame that the addition of oil droplets changes the equivalence ratio. Another possibility is to use particle seeding, but this was not adopted owing to certain difficulties with practical implementation. One way to overcome this problem for the case of premixed propane and for a more general scenario where optical access to the flame zone is not feasible is by performing the measurements under cold flow conditions with a hot wire anemometer placed at the nominal position in the chamber to obtain the injector describing function (IDF) $\mathcal{F}_I$. The flame describing function $\mathcal{F}_F$ can then be obtained by extracting out $\mathcal{F}_I$ from $\mathcal{F}_{IF}$. For these measurements, a 1D-hot wire probe (HW2 shown

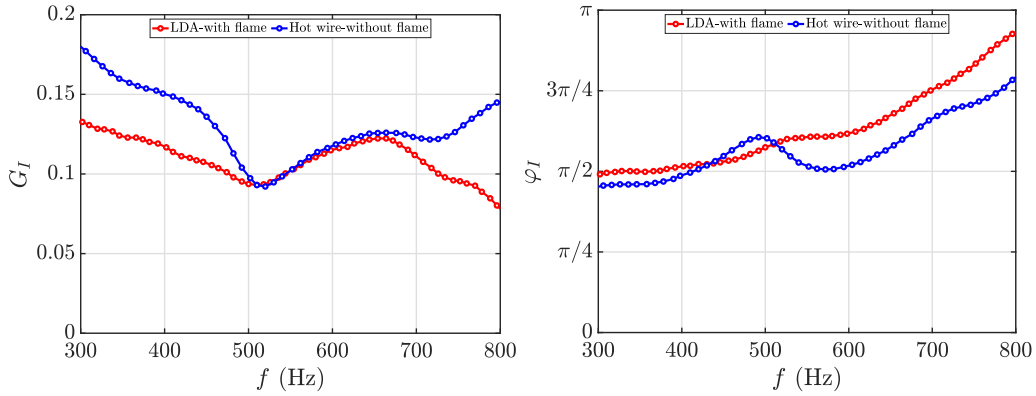

Figure 4.12. *Gain G_I and phase φ_I of the injector transfer function $\mathcal{F}_I$ for swirler 716 at an amplifier voltage of $V_0 = 3\,\mathrm{V}$ measured with the hot wire anemometer under cold conditions and the PDPA system in the presence of flame.*

in Fig. 4.1 (b)) is placed at the nominal reference location in the chamber. The injector describing function is obtained between the relative velocity fluctuations measured in the plenum using the multi-microphone method and the relative velocity fluctuations measured at the injector outlet by the hot wire probe as:

$$\mathcal{F}_I = \frac{u'_{c,r}/\overline{u}_{c,r}}{u'_p/\overline{u}_p} \tag{4.12}$$

where $u'_{c,r}/\overline{u}_{c,r}$ refers to the relative velocity fluctuations measured in the chamber at the nominal position, and $u'_p/\overline{u}_p$ refers to the relative velocity fluctuations measured in the plenum at the MP2 section (see Fig. 4.1 (a)). It is necessary to see if the IDF obtained without the flame using a hot wire probe and an IDF obtained directly at the flame base using LDA are similar or if there is a difference that should be quantified. It is also necessary to recall that the velocity fluctuations in the chamber are sensitive to the location, and that the hot wire probe itself being $1.25\,\mathrm{mm}$-wide might add to uncertainties in the measurements. Figure 4.12 shows the gain and phase of the injector describing function comparing the measurements made in the absence of flame using the hot wire anemometer and with flame using LDA at the injector outlet. A prior measurement (not shown here) is carried out to verify that the measurement under cold conditions with a hot wire in the chamber and LDA (with oil seeding) gives nearly the same injector transfer function. The gains in the lower frequency range differ until $500\,\mathrm{Hz}$, after which the evolution is identical until about $700\,\mathrm{Hz}$. Beyond this frequency, the two values begin to diverge. The phase functions match quite well at lower frequencies, but a difference of approximately $\pi/8$ exists beyond $500\,\mathrm{Hz}$. This variation in phase is, however, minor compared to the gain. The phase plays an important role in the stability analysis using FDFs (Chapter 5), and as will be seen later, even the approximate injector phase response can be used to obtain an FDF that can reasonably predict the stability behavior. As other alternatives are not feasible for

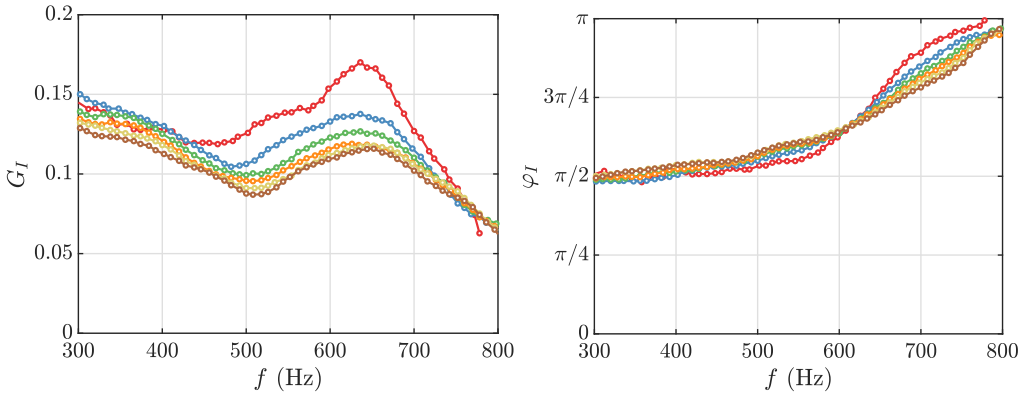

Figure 4.13. *Gain G_I and phase φ_I of direct IDF $\mathcal{F}_I$ for swirler 716 when operated at F1 and different amplifier voltage levels. The IDF is determined using Eq. 4.12, where the plenum velocity fluctuations are obtained using multi-microphone method at the MP2 section (see Fig. 4.1 (a)) and the velocity fluctuations in the chamber close to the injector exit are obtained using LDA in the presence of flame at the nominal measurement location.*

the case of premixed propane, the injector describing function obtained with the hot wire probe located in the chamber is used with a subsequent correction to determine an approximate FDF, henceforth referred to as an indirect FDF. The FDF determined directly in the presence of flame using LDA is referred to as the direct FDF. In the rest of the thesis, simply specifying 'FDF' refers to the direct FDF, and an explicit reference is made if the FDF is determined indirectly. The injector describing function obtained between the acoustic velocity determined with the microphones in the plenum and the velocity measured in the presence of flame with LDA in the chamber is shown in Fig. 4.13 at different amplifier voltage levels for swirler 716. Each amplifier voltage imposes a particular level of relative velocity fluctuations in the plenum and in the chamber close to the injector outlet. It can be seen from the figure that the injector response is a function of the modulation amplitude, mainly in the gain and also in the phase in the higher frequency range.

One might attempt to extract the injector response using one of the models shown previously, like the L-ζ model discussed in Section 4.3. But our previous analysis indicates that they do not suitably represent the observed injector behavior. In addition to these models the mode conversion from acoustics to convective dissipation across the swirler based on Howe's model (Howe 1979) is considered, for example, by Schuermans et al. (2003) and Gaudron et al. (2019b). In the form given in Schuermans et al. (2003), this dissipation is accounted for as a time delay that is independent of the frequency, while in Gaudron et al. (2019b), it was found sufficient to just consider the area jump for the specific injectors. Since the above injector descriptions are linear, they cannot account for nonlinearity with respect to the forcing amplitude (Gaudron et al. 2019b) shown in Fig. 4.13. These

formulations would not suitably model the present injectors, and a more comprehensive modeling framework needs to be developed with subsequent experimental validation. This is not considered in the present thesis, and the FDF with reference velocity at the injector exit is directly obtained using LDA measurement. An alternate way for obtaining the FDF in the literature is using the transfer matrix methodology. It is pointed out here that this involves measuring the burner transfer matrix under cold flow conditions and separating it out from the burner + flame transfer matrix with the assumption that the former does not change due to the combustion process. On the contrary, as shown in Fig. 4.12, this assumption would lead to uncertainties that need to be accounted for in the final flame transfer matrix or the flame transfer function determined from the transfer matrix.

4.7 Low frequency FDFs

It is next interesting to examine the evolution of FDFs in the low frequency range to determine their limiting behavior. The case of both fully premixed flames and combustion systems where equivalence ratio perturbations are prevalent was considered by Polifke and Lawn (2007), who have analytically derived low frequency limits from first principles. They found that for a fully premixed flame, the FTF tends towards unity, and for a practically premixed system with stiff fuel injection, the FTF would tend towards zero as the frequency tends to zero. The authors also compared their findings with experimental FTFs reported by other teams as a validation. It is then instructive to verify if the low frequency behavior of the complex spray flames produced by the injectors considered here matches the low frequency limits derived by Polifke and Lawn (2007). As the driver units can be damaged by low frequency modulations, only a few experiments are carried out at frequencies below $300\,\mathrm{Hz}$ until $50\,\mathrm{Hz}$. Measurements at the highest amplifier voltage of $V_0 = 3\,\mathrm{V}$ are also avoided in the low frequency range to prevent possible damage to the driver units.

Figure 4.14 shows the FDF of swirler 716 measured at different amplifier voltages. The FDF results in the low frequency region between $50\,\mathrm{Hz}$ and $300\,\mathrm{Hz}$ are shown here for the first time, and the results for frequencies greater than $300\,\mathrm{Hz}$ are reproduced from Fig. 4.11. The results are first shown with premixed propane by seeding the flow with oil droplets in order to verify the low frequency limits in the case of premixed flames. The addition of oil droplets slightly changes the operating condition, and the equivalence ratio for this case is expected to be higher than 0.85. However, the injected quantity of oil seeding is much smaller compared to the propane flow rate, and since the low frequency limits will not be affected by the operating point, it is acceptable to carry out the measurements with oil seeding. One finds that the gain tends to 1, and the phase tends to 0 for the fully premixed case, matching the low frequency asymptotics of Polifke and Lawn (2007). It is also useful to note that both the gain and the phase curve change slope in the low

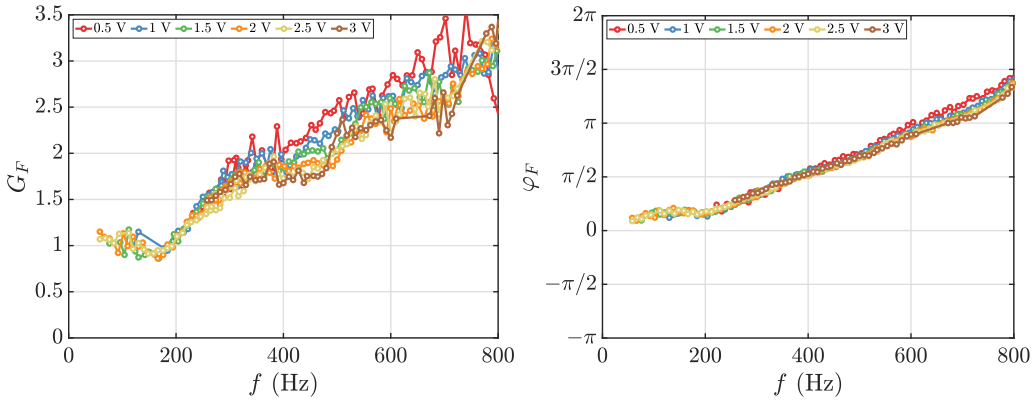

(a) Propane (fully premixed)

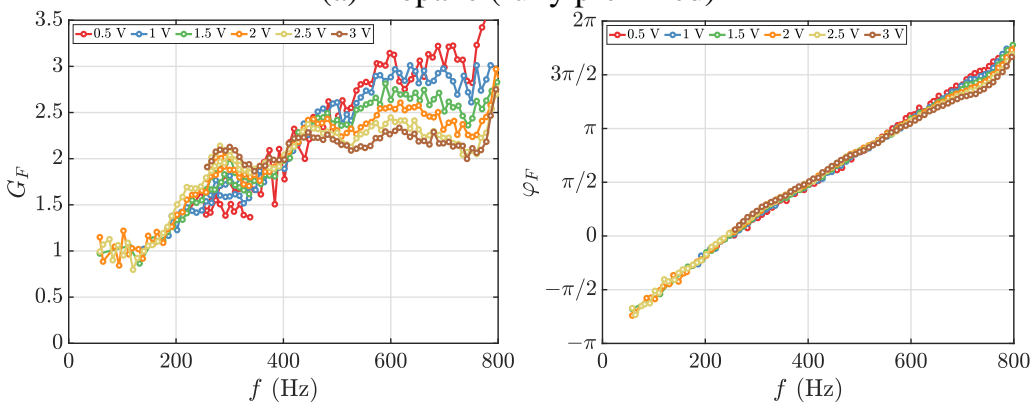

(b) Heptane (spray)

Figure 4.14. *Gain G_F and phase φ_F of FDF $\mathcal{F}_F$ for swirler 716 at different amplifier voltage levels. These measurements are carried out in the low frequency range between* 50 Hz *and* 300 Hz*, and the result of Fig. 4.11 at frequencies above* 300 Hz *is reproduced. Measurements at lower frequencies are not performed at the highest amplifier voltage of $V_0 = 3$ V in order to prevent damage to the driver units.*

frequency region, and a linear extrapolation of $\mathcal{F}_F$ shown in Fig. 4.11 (second column) would result in an erroneous low frequency limit prediction (also observed by Polifke (2020)). The case of heptane spray flames features a gain of 1 and a phase of $-\pi$ in the vicinity of vanishing frequency. Although the fuel injection can be considered stiff in this case, these flames behave in a quasi-premixed fashion, as described in Chapter 2 when the fuel atomizer is recessed inside the injector. This is possibly why the gain of the FDF tends to 1, like in the premixed propane case. The negative phase evolution below 200 Hz presents a peculiar scenario, and the question of the meaning of the $-\pi$ phase between velocity perturbation at the injector outlet and heat release rate is not easily resolved. It is perhaps the result of a mechanism where the velocity perturbations that are being observed at the injector outlet are not the original velocities that gave rise to the heat release rate disturbance but correspond to velocity perturbations that are caused by the heat re-

lease rate disturbances themselves in the downstream flow. In other words, what is observed is essentially the result of the heat release rate disturbances in the flame that induce pressure perturbations which reach the injector outlet and, in turn, induce an opposite velocity fluctuation. When the pressure is positive, the velocity disturbance is negative.

Consider $\dot{Q}'_1(t)$, a heat release rate disturbance in the downstream flow. This gives rise to a pressure disturbance which propagates to the injector outlet $p'_1(t)$ such that $p'_1(t) = A\dot{Q}'_1(t-\tau_a)$. In turn, this pressure disturbance produces a velocity disturbance at the injector outlet $v'_1(t) = -Bp'_1(t)$ or $v'_1(t) = -AB\dot{Q}'_1(t-\tau_a)$. Now, this velocity disturbance is out of phase by $-\pi$ with respect to the heat release rate. Thus, in the low frequency range, it appears that the disturbances that are fed back from the combustion process dominate the velocity fluctuations at the injector outlet, and as they result from the heat release rate perturbations, they are out of phase by $-\pi$ with respect to the heat release rate disturbances.

One may immediately wonder why this mechanism does not intervene in the case where the system operates in the fully premixed mode but only occurs when the fuel is delivered as a spray. This may be due to the difference in the non-steady combustion process. When the fuel is injected as a spray, and the air flow is pulsated, the droplet spray might pile up in successive regions of higher fuel concentrations that may give rise to the kind of disturbances described previously. This will not happen in the premixed mode where the non-steady combustion is governed by the creation and destruction of flame surface area that does not give rise to the pulse-like combustion described previously.

4.8 Conclusions

This chapter focuses on issues raised by the describing function determination for flames formed by the specific class of injectors considered in this work. These injectors act as a loss element in the acoustic pathway caused by the small swirler channels, abrupt area changes, and relatively high pressure drop. These injectors are thus only weakly transparent to acoustic waves and feature their own nonlinear frequency response to incoming disturbances. It is found that for this family of injectors, the traditional way of measuring reference velocity fluctuations in the plenum raises issues that are not easily resolved, and one needs to carry out these measurements directly at the base of the flame. An alternate route consisting in calculating the describing function using velocity measurements in the plenum gives a coupled injector and flame describing function, which substantially differs in both gain and phase from the flame describing function. Although the phase of the FDF may be reconstructed from measurements in the plenum using a simple network model accounting for the plenum and the injector geometries, this modeling would not provide a suitable estimate of the FDF gain. The direct measurement

of velocity at the injector outlet raises other problems because the velocity profile is highly nonuniform. It is shown that this can be resolved by recording the velocity at a location where the relative volumetric flow rate fluctuations equal the relative velocity fluctuations. It is found that this position corresponds to the location of the maximum of mean axial velocity for the family of injectors considered here. The FDF is highly sensitive to the velocity measurement location, and it is found that even a $0.5\,\mathrm{mm}$ variation in this position notably affects the FDF gain and, to a lesser extent, the phase function. For carrying out velocity measurement with the presence of flame in the chamber, some form of optical measurement technique is needed, but this might not be possible with systems where optical access is limited. One would then have to use the alternate possibility of determining an injector describing function under cold conditions, which can then be used to extract the FDF from the coupled injector and flame describing function. It is found, however, that measurements of the injector describing function under cold conditions introduces a new uncertainty because the response of this component depends on the flow conditions (cold or hot-fire). This will affect the FDF gain and, to a lesser extent, its phase. The last part of this chapter is dedicated to the low frequency FDF asymptotic. Analytically-derived limiting values of the gain and phase are known for premixed flames from Polifke and Lawn (2007). The FDF measurements obtained by considering the reference velocity at the injector exit are in agreement with the theoretical results (unity gain and zero phase) when the flame is formed by premixed propane and air. For heptane spray injection, the gain also tends to one in the low frequency limit, indicating a possible quasi-premixed behavior, further supporting the observations discussed in Chapter 2. The phase tends in this limit to $-\pi$, which is less easy to interpret. The methodology derived in this chapter is used to measure most of the FDFs used in this thesis and might guide other experiments where injectors are weakly transparent to acoustic disturbances.

Appendix 1: FDF measurement with and without chamber metal ring

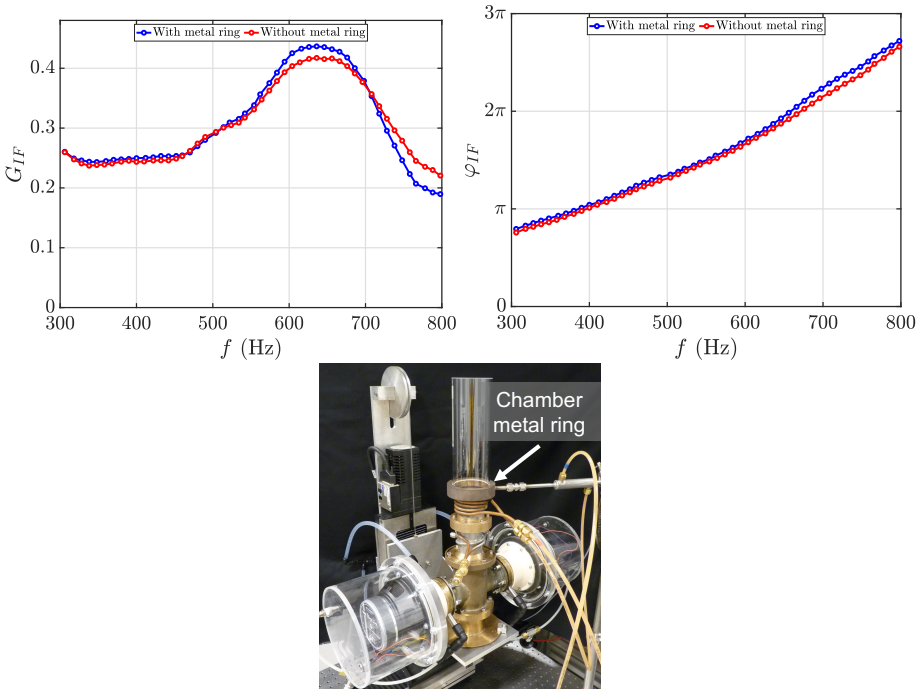

Figure 4.15. *Top: Gain G_{IF} and phase φ_{IF} of injector + flame transfer function $\mathcal{F}_{IF}$ with and without the metal ring fitted at the bottom of the chamber for holding the waveguide of chamber microphone (MC1 in Fig. 4.1 (b)). Swirler: 716; $V_0 = 1300\,\mathrm{mV}$. Bottom: Photograph of SICCA-Spray experimental setup with chamber metal ring.*

This section concerns a specific question raised by the experimental setup where a metal ring of $15\,\mathrm{mm}$ height is sometimes placed at the bottom of the chamber for pressure acquisition. This metal ring is mainly used when performing measurements under self-sustained oscillations where the chamber pressure is measured by the microphone mounted on this ring. But the FDF measurements are carried out without the metal ring to have optical access to the base of the flame. As the measured FDFs are used in a low-order model for predicting the SSOs, it is necessary to see if there is any effect due to the variation of the thermal environment at the bottom of the chamber. Since the direct FDF measurement with the bottom metal ring is not possible, this comparison is only based on the coupled injector and flame describing functions. Figure 4.8 shows the gain G_{IF} and phase φ_{IF} of the coupled injector and flame transfer function with and without the metal ring mounted at the bottom of the chamber. A small deviation at certain frequencies in the gain and beyond $650\,\mathrm{Hz}$ in the phase is observed, but this variation is only minor (less than 5%). This analysis indicates that the slight change in thermal environment at the bottom of the chamber does not influence the heat release rate and that the FDFs obtained without the bottom metal ring

are suitable for predicting the behavior during an SSO, where the bottom ring is generally mounted.

Chapter 5

Theoretical framework

Contents

The theoretical model presented in this chapter has been previously published as a part of the full-length article titled "Swirler effects on combustion instabilities analyzed with measured FDFs, injector impedances and damping rates" authored by Preethi Rajendram Soundararajan, Daniel Durox, Antoine Renaud, Guillaume Vignat and Sébastien Candel in Combustion and Flame, vol. 238, April 2022.

The present chapter discusses a theoretical framework for the instability prediction of a system comprising an injector that is weakly transparent to acoustic waves. The traditional three-cavity acoustic network model, discussed, for example, by Palies et al. (2011), comprising simple cavities with section changes between plenum, injector, and chamber, will not entirely work for such injectors because these units dissipate acoustic energy and by imposing a large head loss, they essentially decouple the upstream manifold from the combustor. It is then more appropriate to derive a modified framework to carry out a stability analysis of the system and eventually predict the growth rate and frequency of oscillation. This is achieved in the present work by introducing an impedance imposed by the injector at its outlet and considering only the cavities corresponding to the injector outlet and the chamber, with the flame response represented using an FDF. A dispersion relation is derived on these grounds, which can be solved to obtain the growth rate and frequency. In addition, the limits of unstable bands encompassing the regions of positive growth rate can also be determined and traced in the FDF phase curve to identify the stability domains of the system. A sensitivity analysis is subsequently carried out to identify the dependence of the solution on different parameters considered in the model. It is seen that the magnitude and phase of the injector impedance have the strongest influence on the results and that this impedance needs to be carefully determined. Validation of this theoretical analysis is provided in the following chapter discussing the experimentally-observed instability behavior with different swirling injectors. This model also serves as a useful tool throughout this thesis for understanding the self-sustained instability behavior of both the single-injector combustor as well as the annular combustor.

5.1 Introduction

Assuming that the flame response to the incoming acoustic perturbation is known, the corresponding flame describing function can be used in a low-order stability analysis framework for instability prediction. This framework can then be used to control instabilities by tailoring the flame transfer/describing functions. A detailed discussion on approaches based on FTFs and FDFs was recently proposed by Schuller et al. (2020), in the case of premixed combustion systems. As demonstrated in Chapter 3, the FDF suitably represents the complex spray flames considered in this work while undergoing self-sustained oscillations, and this framework can be exploited in a low-order model to depict the flame response. The demonstrated capability of FTF/FDF combined with 1D network models (Kim and Santavicca 2009; Palies et al. 2011; Li and Morgans 2016) has made it a valuable technique for predicting instabilities. This was exemplified by Palies et al. (2011) with a three-cavity model, where the different cavities of the system (the plenum,

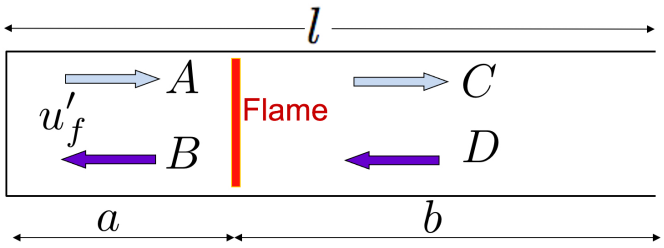

Figure 5.1. *A simplified combustion system comprising a rigid backplane at $x = 0$, an open end at $x = l$ and a compact flame located at $x = a$.*

injector and chamber) are represented in a simplified fashion accounting for variations in sectional area of the system and changes in density and sound velocity associated with the flow temperature. The flame was represented by an FDF, and the dispersion relation was subsequently solved to determine the frequency and growth rate of oscillations. Predictions were then compared with experimentally-observed instabilities to validate the low-order approach. A recently developed open-source low-order network model tool named OSCILOS that uses a somewhat similar approach has also been shown to predict the oscillations of several systems (Han et al. 2015; Xia et al. 2019; Kim et al. 2022). The dispersion relation obtained using the network models can also be solved to obtain limits of unstable bands that correspond to the regions of positive growth rate. The unstable band can then be traced on the FDF phase diagram, and based on whether or not the FDF phase falls inside this band, the stability of the system can be identified. In addition, one also considers the gain of the FDF at the frequency of instability to determine the growth rate of oscillation. This, for example, was shown in Prieur (2017) and Schuller et al. (2020).

To be more concrete, consider a simple channel (Fig. 5.1) with a rigid termination on the upstream side $u'(x = 0) = 0$ and an open-to-atmosphere outlet with $p'(x = l) = 0$. It is convenient to consider that the length l contains the end-correction so that one may assume that the pressure perturbation vanishes at $x = l$. A flame is located at a distance a from the backplane. Considering this simple system with an FTF $\mathcal{F}$ characterized by a gain G_F and a phase φ_F, a linear stability analysis can be carried out. One obtains, after some standard calculations, the unstable bands corresponding to the first 1L mode as $\pi < \varphi_F(\omega_0) < 2\pi \bmod 2\pi$, where ω_0 is the eigenfrequency of the 1L mode. If the phase φ_F falls outside this band, the system can be deemed to be stable. This is further explained by Schuller et al. (2020), who have also demonstrated that the derived unstable bands can be drawn in the FDF phase curves to predict the instabilities from a simple Rijke tube to the MICCA annular combustor equipped with multiple matrix injectors (Bourgouin et al. 2015a). Although the above description works well for acoustically transparent injectors, as outlined in Chapter 4, there is an underlying issue in

rightly capturing the variation in the acoustic state across injectors that are weakly transparent to acoustic waves. Even though a standing wave is established in the plenum, the phase between pressure and velocity at the exit of the injector does not correspond to $3\pi/2$ (or $\pi/2$, if one considers pressure to be ahead of velocity), as will be seen in Chapter 6. One can then not simply consider that the unstable band corresponds to [π,2π], and one has to account for the variation in the impedance phase at the injector exit. A modified approach is then used with only two cavities, representing the injector geometry and chamber and imposing an impedance close to the injector outlet to represent the acoustic state upstream. The possibility of using an inlet impedance or admittance has been previously explored Krebs et al. (2013) and Schuller et al. (2020). While Krebs et al. (2013) used an experimentally determined impedance at the inlet of the flame tube, Schuller et al. (2020) have listed analytical expressions of admittance for common boundary conditions. The present chapter describes a theoretical analysis carried out in this general framework to represent the SICCA-Spray combustor dynamics. The description of the model is given in Section 5.2, followed by a sensitivity analysis shown in Section 5.3. An appendix is also provided, which considers an approach based on the modal expansion method to further validate the method derived in Section 5.2.

5.2 Model description

In the following theoretical model, one considers that the injector acoustic response may be expressed in terms of an impedance at its outlet. The system now comprises two cavities, one representing the injector outlet and the other representing the combustion chamber open to the atmosphere. This modeling effort relies on a compact flame description, with the flame represented as a plane discontinuity in combination with a one dimensional acoustic model of wave propagation, an open end boundary condition at the combustor exhaust, and an effective specific impedance ζ at the injector outlet. The single-injector SICCA-Spray combustor is first considered for developing this model, although this approach could also be extended to a multiple-injector combustor, as shown in Chapter 7. The SICCA-Spray system is sketched in an idealized manner in Fig. 5.2. Here, the injector is represented by a short cylindrical tube of length $1\,\mathrm{mm}$ and an experimentally measured impedance at the injector outlet representing the upstream manifold. The short length of the injector corresponds to the straight cylindrical section of the terminal plate, just after the conical convergent nozzle (highlighted by the red ellipse in Fig. 5.2 (a)), and does not play a role in the final results. This short section has an outlet diameter of $d_1 = 8\,\mathrm{mm}$ leading to the combustion chamber, which has an internal diameter of $d_2 = 69\,\mathrm{mm}$. The flame is located at a distance of a_b from the chamber backplane, which corresponds to the location of the heat release rate barycenter. The jump conditions relating pressure and velocity at the different

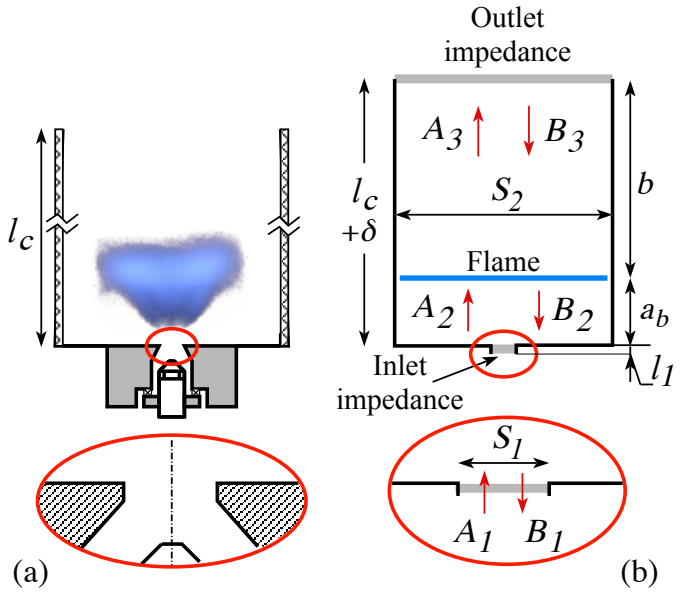

Figure 5.2. *Model representation of the injector exit section and combustion chamber. (a) Real configuration, (b) Idealized model. The injector and upstream manifold are replaced by an effective impedance at the injector outlet. An end correction δ is used to account for acoustic radiation from the combustor outlet.*

sections of this idealized configuration are derived using the standard convention, where the time harmonic term in all waves is $\exp(-i\omega t)$. The acoustic pressure and velocity can be represented as follows:

$$p'_j(x,t) = A_j \exp(ik_j x - i\omega t) + B_j \exp(-ik_j x - i\omega t) \tag{5.1}$$

$$u'_j(x,t) = \frac{1}{\rho_j c_j}[A_j \exp(ik_j x - i\omega t) - B_j \exp(-ik_j x - i\omega t)] \tag{5.2}$$

A_j and B_j correspond to the amplitudes of the waves, $k_j = \omega/c_j$ is the acoustic wavenumber, ρ_j and c_j are respectively the density and speed of sound in the j^{th} section and ω designates the angular frequency. Considering the specific impedance $\zeta = p_1/\rho_1 c_1 u_1$ at the injector exit portion, one obtains

$$A_1 e^{ik_1 l_1}(1-\zeta) + B_1 e^{-ik_1 l_1}(1+\zeta) = 0 \tag{5.3}$$

Now, the jump condition for the pressure and volumetric flow rate perturbations in section 1 give

$$A_1 e^{ik_1 l_1} + B_1 e^{-ik_1 l_1} - A_2 - B_2 = 0 \tag{5.4}$$

$$A_1 \frac{S_1}{\rho_1 c_1} e^{ik_1 l_1} - B_1 \frac{S_1}{\rho_1 c_1} e^{-ik_1 l_1} - A_2 \frac{S_2}{\rho_2 c_2} + B_2 \frac{S_2}{\rho_2 c_2} = 0 \tag{5.5}$$

The jump condition across the flame deduced from the linearized Rankine-Hugoniot relation yields (Schuller et al. 2020),

$$S_2 u_3' - S_2 u_2' = \frac{\gamma - 1}{\rho_0 c_0^2} \dot{Q}' \tag{5.6}$$

Here, S_2 is the cross-sectional area at the flame location, which is the same upstream and downstream of the flame. $\dot{Q}'$ is the heat release rate and can be represented by the FDF. As discussed in Chapter 4, the velocity reference for the FDF measurement is that existing at the injector outlet and using the general definition of FDF relating heat release rate fluctuations and relative velocity fluctuations, one finds,

$$S_2 u_3' - S_2 u_2' = \frac{\gamma - 1}{\rho_0 c_0^2} G_F e^{i\varphi_F} \overline{\dot{Q}} \frac{u_1'}{\overline{u}_1} \tag{5.7}$$

Here, u_1' is the velocity measured in section 1, and G_F and φ_F represent the gain and phase of FDF, respectively. The mean heat release rate from the flame can be represented in terms of burnt products and incoming fresh reactants temperatures (T_b and T_u, respectively) and is given by $\overline{\dot{Q}} = \dot{m}\overline{c_p}(T_b - T_u)$. $\dot{m} = \rho_1 S_1 u_b$ is the total mass flow rate and u_b is the bulk velocity at the injector outlet. The specific heat coefficient is $\overline{c_p} = \dfrac{1}{T_b - T_u} \displaystyle\int_{T_u}^{T_b} c_p dT = \frac{\dot{m}_f}{\dot{m}} \frac{\Delta h}{T_b - T_u}$, where $\dot{m}_f$ represents the mass flow rate of heptane and Δh is the lower calorific value of heptane equal to $44.6\,\mathrm{MJ\,kg^{-1}}$. $\rho_0 c_0^2 = \gamma \overline{p}$ is nearly constant across the flame region. Here, $\overline{p}$ represents the mean pressure, and it is suitable to consider that $\rho_0 c_0^2 = \rho_1 c_1^2 = \rho_1 \gamma r T_1$. Simplifying $(\gamma - 1)/\gamma r$ gives $1/c_p$. Then Eq. 5.6 can be further simplified as,

$$S_2 u_3' - S_2 u_2' = \Theta \mathcal{F} \Gamma S_1 u_1' \tag{5.8}$$

Here $\Theta = (T_b/T_u) - 1$ is the volumetric expansion parameter and Γ is $\overline{c_p}/c_p$. It is next convenient to replace $\Theta\mathcal{F}$ with $\widehat{\mathcal{F}}$. In this simplified 1D case, u_b and $\overline{u}_1$ cannot be differentiated, although they are different, and hence replaced by $\overline{u}_1$.

Now, imposing a continuity condition for the pressure fluctuations across the flame yields,

$$A_2 e^{ik_2 a_b} + B_2 e^{-ik_2 a_b} - A_3 - B_3 = 0 \tag{5.9}$$

Considering an open end at section 3,

$$A_3 e^{ik_3 b} + B_3 e^{-ik_3 b} = 0 \tag{5.10}$$

Here $b = l_c + \delta_e - a_b$ where l_c is the chamber length and $\delta_e \approx 0.4 \times d_2$ is the acoustic end correction (Rienstra and Hierschberg 2004; Bourgouin 2014). Eqns. 5.3, 5.4, 5.5, 5.8, 5.9 and 5.10 are combined to obtain a set of linear equations in the form $M \times X = 0$, where $X = [A_1\ B_1\ A_2\ B_2\ A_3\ B_3]^T$ and M is

$$\begin{bmatrix}
e^{ik_1 l_1}(1-\zeta) & e^{-ik_1 l_1}(1+\zeta) & 0 & 0 & 0 & 0 \\
e^{ik_1 l_1} & e^{-ik_1 l_1} & -1 & -1 & 0 & 0 \\
\frac{S_1}{\rho_1 c_1} e^{ik_1 l_1} & \frac{-S_1}{\rho_1 c_1} e^{-ik_1 l_1} & \frac{-S_2}{\rho_2 c_2} & \frac{S_2}{\rho_2 c_2} & 0 & 0 \\
\frac{\widehat{\mathcal{F}} \Gamma S_1}{\rho_1 c_1} & \frac{-\widehat{\mathcal{F}} \Gamma S_1}{\rho_1 c_1} & \frac{S_2}{\rho_2 c_2} e^{ik_2 a_b} & \frac{-S_2}{\rho_2 c_2} e^{-ik_2 a_b} & \frac{-S_2}{\rho_3 c_3} & \frac{S_2}{\rho_3 c_3} \\
0 & 0 & e^{ik_2 a_b} & e^{-ik_2 a_b} & -1 & -1 \\
0 & 0 & 0 & 0 & e^{ik_3 b} & e^{-ik_3 b}
\end{bmatrix}$$

On solving for the nontrivial solution of M which requires that $\det[M] = 0$, one obtains the dispersion relation of this system:

$$\begin{aligned}
\frac{S_1}{\rho_1 c_1 \rho_3 c_3} \cos(k_3 b) \sin(k_2 a_b) + \frac{\widehat{\mathcal{F}} \Gamma S_1}{\rho_1 c_1 \rho_2 c_2} \sin(k_3 b) + \frac{S_1}{\rho_1 c_1 \rho_2 c_2} \cos(k_2 a_b) \sin(k_3 b) \\
- \frac{i\zeta S_2}{\rho_2 c_2 \rho_3 c_3} \cos(k_2 a_b) \cos(k_3 b) + \frac{i\zeta S_2}{\rho_2^2 c_2^2} \sin(k_2 a_b) \sin(k_3 b) = 0
\end{aligned} \tag{5.11}$$

The complex roots of this expression $\omega = \omega_r + i\omega_i$ can be obtained by numerically solving the dispersion relation. The frequency of oscillation is deduced from $\omega_r = 2\pi f$ while ω_i provides the growth rate. The regions of positive growth rate determine the limits of the unstable bands that can be traced in the FDF phase curve to predict the stability regimes of the system.

5.3 Model results and sensitivity analysis

It is now interesting to examine some model results and consider their sensitivity to the impedance values at the injector outlet. Calculations are based on the dispersion relation (Eq. 5.11). This can be written in the following form:

$$\mathcal{D}(\omega; G_F, \varphi_F, G_\zeta, \varphi_\zeta) = 0 \tag{5.12}$$

where the describing function is represented in terms of its gain and phase as $\mathcal{F} = G_F e^{i\varphi_F}$ and the impedance is defined in terms of its absolute value and phase

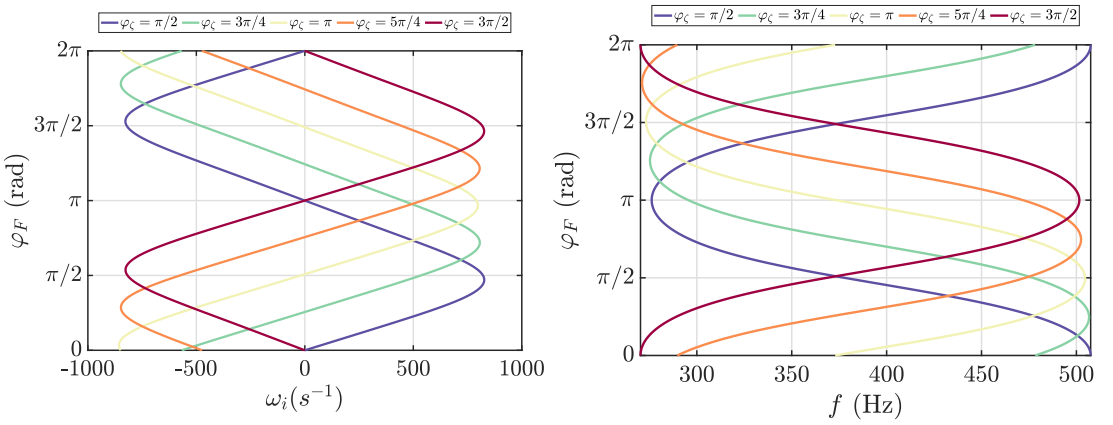

Figure 5.3. *Sensitivity of the growth rate ω_i and frequency f to the phase φ_ζ of injector impedance.*

as $\zeta = G_\zeta e^{i\varphi_\zeta}$. The geometrical parameters of the system are fixed. The flame barycenter a_b is the only parameter that is not listed but may be varied (to a small extent). In a first stage it is natural to fix all geometrical parameters, including a_b, and to determine the roots of the dispersion relation by fixing the impedance ζ and using G_F and φ_F as parameters. One obtains in this way $\omega = \omega(G_F, \varphi_F; G_\zeta, \varphi_\zeta)$ which may be decomposed into an imaginary and a real part:

$$\omega_i = \omega(G_F, \varphi_F; G_\zeta, \varphi_\zeta) \tag{5.13}$$
$$f = f(G_F, \varphi_F; G_\zeta, \varphi_\zeta) \tag{5.14}$$

It is convenient to plot a family of ω_i and f isocontours by fixing the FDF gain value G_F and using φ_F as a variable. This is done in Fig. 5.3, where G_F has a fixed value for a fixed impedance modulus G_ζ, but different values of φ_ζ. The calculations correspond to the dispersion relation root pertaining to the 1L mode.

Similarly, Fig. 5.4 shows the growth rate and frequency variation with the magnitude of the injector impedance at a fixed transfer function gain G_F and phase of injector impedance φ_ζ. These figures feature variations in the positive growth rate zones in Fig. 5.3 (left), which correspond to the location of the unstable bands. For example, an impedance phase of $\varphi_\zeta = 3\pi/2$ results in an unstable band between π and 2π, whereas modifying the impedance phase to π moves the unstable band between $\pi/2$ and $3\pi/2$. Figure 5.4 shows that the magnitude of the injector impedance does not modify the boundaries of the unstable band, and this parameter mainly influences the value of the predicted growth rate and frequency at a given FDF phase. A higher impedance would result in a lower growth rate from the model within the limits of the unstable band. Finally, Fig. 5.5 shows the variation of the growth rate and frequency deduced from the model when the flame barycenter location a_b is changed. It can be seen from the figure that neither the predicted frequency nor the growth rate or the unstable band depends much on

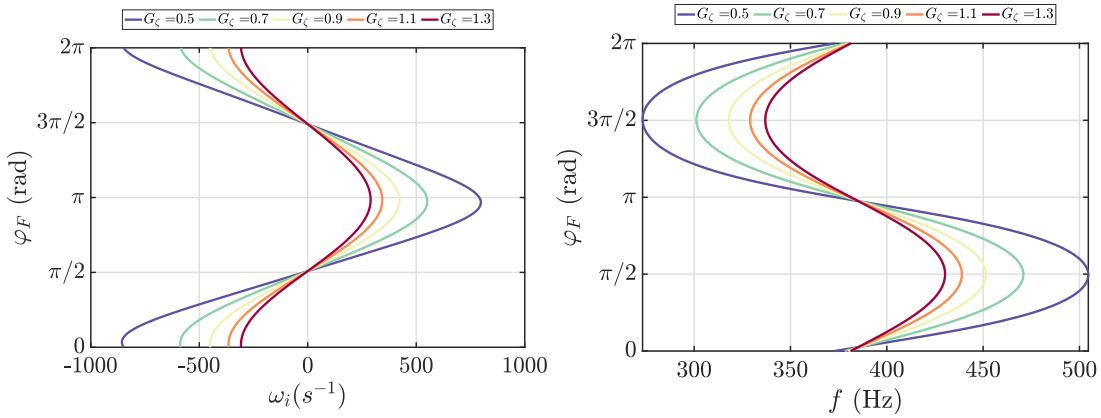

Figure 5.4. *Sensitivity of the growth rate ω_i and frequency f to the magnitude G_ζ of injector impedance.*

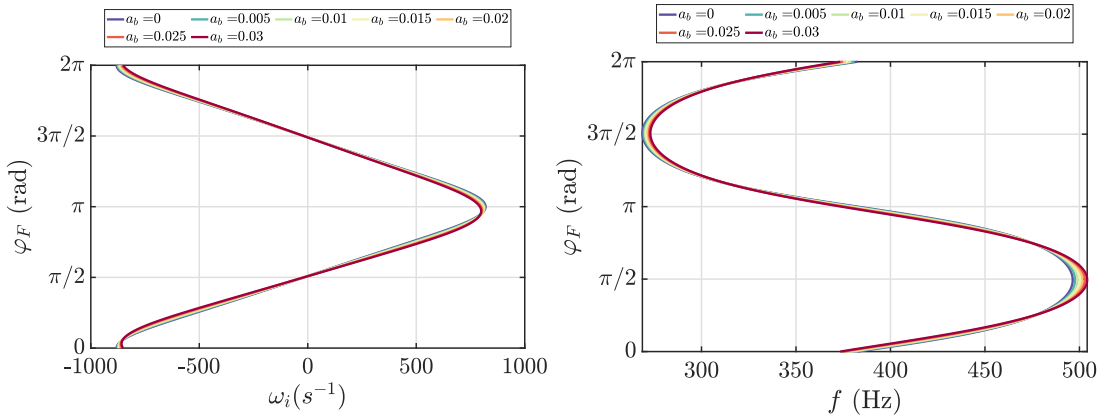

Figure 5.5. *Sensitivity of the growth rate ω_i and frequency f to the flame barycenter location a_b.*

the barycenter location. In addition to the above parameters, the temperatures in the different sections also play a role in the solution to the dispersion relation. The value for T_1 of the fresh gases is well known, but the temperatures T_2 at the base of the flame and T_3 in the chamber downstream of the flame still need to be determined. A rapid analysis indicates that T_2 has only a negligible impact on the growth rate or frequency. The temperature T_3 downstream of the flame does not alter the growth rate but plays a significant role in deciding the value of the predicted frequency. Determining this temperature is quite difficult and is only approximately obtained by coating the inner walls of the chamber using thermal paint. Further details are provided in Chapter 6.

The above analysis shows that the solution of the dispersion relation is notably influenced by the magnitude and phase of the impedance imposed by the injector and that it is crucial to obtain this value correctly for the stability analysis. Although a variation with the inlet impedance can be obvious, this analysis indicates

the sensitivity to this parameter and quantifies the extent of this variation. As will be seen later, this knowledge will be useful in the next chapter, which deals with the variation in the instability behavior with different swirling injectors. A small variation, especially in the phase of the impedance, can shift the unstable bands in the FDF phase curves,ß thus modifying the predicted stability domains. This model is applied in the following chapter and used to interpret the experimental observations of self-sustained instability carried out with different swirling injectors.

5.4 Conclusions

This chapter contains a description of the theoretical framework that can be used to analyze the linear stability of a combustor system equipped with an injector that is weakly transparent to acoustic waves. A traditional acoustic network model accounting for the plenum, injector and chamber cavities adopted in several other studies ceases to work and is replaced here by a model where the injector is represented by its specific impedance. This is found to better describe a situation where the injector dissipates a large amount of acoustic energy and attenuates incident disturbances, a situation that is not well represented by a purely acoustic description of the upstream and downstream states. The low-order model derived in this chapter takes into account the impedance imposed at the injector outlet by considering only two cavities —one corresponding to the injector outlet and the other to the chamber. The measured FDF can then be used in the dispersion relation to predict the growth rate and frequency of oscillations. The predicted growth rates can also be used to derive the limits of the unstable bands, which correspond to the region of positive growth rate. A sensitivity analysis is carried out to examine the variability of the predicted growth rate and frequency with respect to the various model parameters. It is shown that the solution of the dispersion relation is most sensitive to the gain and phase of impedance. Although such an effect on the predicted values is expected, the extent of this sensitivity is quantified through this analysis. Further considerations and experimental validation of this framework are discussed in Chapter 6.

Appendix 1: Instability analysis using modal expansion

To complement the theoretical analysis of Section 5.2, the description of the system is now carried out by making use of a relatively different theoretical framework. The derivation now relies on a modal expansion starting from the wave equation. A part of the description given in Schuller et al. (2020) is used while adapting the problem specifically for the injectors considered here.

Consider the wave equation written as,

$$\frac{\partial^2 p'}{\partial t^2} + 2\alpha\frac{\partial p'}{\partial t} - \rho c^2 \nabla \cdot \frac{1}{\rho}\nabla p' = (\gamma - 1)\frac{\partial \dot{q}'}{\partial t} \tag{5.15}$$

where α is the damping rate. Note that the previous expression allows for changes in the sound velocity and density induced by variations in temperature.

The modes of this equations must satisfy,

$$\rho c^2 \nabla \cdot \frac{1}{\rho}\nabla \psi_n + \omega_n^2 \psi_n = 0 \tag{5.16}$$

subject to some homogeneous boundary conditions. These modes are normal and this can be represented as,

$$\int_V \psi_n \psi_m \mathrm{d}V = \Lambda_n \delta_{mn} \tag{5.17}$$

where Λ_n is the energy of the n$^{\text{th}}$ mode and $\delta_{mn} = 0$ is the Kronecker delta function which is unity only when $m = n$ and 0 elsewhere. The pressure field can now be expanded in terms of these modes as,

$$p' = \sum_n \eta_n(t)\psi_n(\boldsymbol{x}) \tag{5.18}$$

where $\eta_n(t)$ are the modal amplitudes. Inserting the above expression in the wave equation Eq. 5.15 and projecting on one of the modes, one obtains a set of differential equations.

$$\frac{d^2\eta_n}{dt^2} + 2\alpha\frac{d\eta_n}{dt} + \omega_n^2\eta_n = \frac{1}{\Lambda_n}(\gamma - 1)\int_V \frac{\partial \dot{q}'}{\partial t}\psi_n \mathrm{d}V \tag{5.19}$$

If one assumes that the heat release rate is concentrated at a point $\boldsymbol{x}_j$ then $\dot{q}' = \dot{Q}'\delta(\boldsymbol{x} - \boldsymbol{x}_j)$. Substituting this on the right-hand side of Eq. 5.19,

$$\frac{1}{\Lambda_n}(\gamma - 1)\int_V \frac{\partial \dot{q}'}{\partial t}\psi_n \mathrm{d}V = \frac{1}{\Lambda_n}(\gamma - 1)\frac{d\dot{Q}'}{dt}\psi_n(\boldsymbol{x}_j) \tag{5.20}$$

The modal amplitude equation now writes:

$$\frac{d^2\eta_n}{dt^2} + 2\alpha\frac{d\eta_n}{dt} + \omega_n^2\eta_n = \frac{1}{\Lambda_n}(\gamma-1)\frac{d\dot{Q}'}{dt}\psi_n(\boldsymbol{x}_j) \tag{5.21}$$

This can be written in the frequency domain as,

$$(-\omega^2 - 2i\alpha\omega + \omega_n^2)\widetilde{\eta_n} = \frac{1}{\Lambda_n}(\gamma-1)(-i\omega)\widetilde{\dot{Q}'}\psi_n(\boldsymbol{x}_j) \tag{5.22}$$

The above equation is similar to what is derived in Schuller et al. (2020). The unsteady heat release rate can be expressed in terms of the FDF as,

$$\widetilde{\dot{Q}'} = \overline{\dot{Q}}\mathcal{F}(\omega, u_1')\frac{u_1'}{\overline{u}_1} \tag{5.23}$$

The fluctuation velocity u_1' can be written in terms of the specific impedance ζ at the injector outlet measured at, say $\boldsymbol{x}_i$, as,

$$u_1'(\boldsymbol{x}_i) = \frac{1}{\zeta}\frac{p_1'(\boldsymbol{x}_i)}{\rho_1 c_1} \tag{5.24}$$

where $p_1'(\boldsymbol{x}_i) = \sum_m \eta_m\psi_m(\boldsymbol{x}_i)$. Equation 5.22 becomes,

$$(\omega^2 + 2i\alpha\omega - \omega_n^2)\widetilde{\eta_n} = i\omega\frac{1}{\Lambda_n}(\gamma-1)\frac{\overline{\dot{Q}}}{\overline{u}_1}\frac{1}{\rho_1 c_1}\frac{\mathcal{F}}{\zeta}\sum_m \eta_m\psi_m(\boldsymbol{x}_i)\psi_n(\boldsymbol{x}_j) \tag{5.25}$$

Considering an open end at a distance of $l = l_c + \delta$ from the injection plane, then $\psi_n = \cos(k_n x)$ such that $k_n l = (2n-1)\frac{\pi}{2}$ and $\int_V \psi_m\psi_n dV = \delta_{mn}\frac{1}{2}S_2 l$. After some calculations (similar to Section 5.2), it can be shown that:

$$\frac{1}{\Lambda_n}(\gamma-1)\frac{\overline{\dot{Q}}}{\overline{u}_1}\frac{1}{\rho_1 c_1} = 2\frac{c_1}{l}\Gamma\Theta\frac{S_1}{S_2} \tag{5.26}$$

and,

$$(\omega^2 + 2i\alpha\omega - \omega_n^2)\widetilde{\eta_n} = i\omega\Theta\frac{\mathcal{F}}{\zeta}\frac{S_1}{S_2}\frac{2c_1}{l}\Gamma\sum_m \eta_m\psi_m(\boldsymbol{x}_i)\psi_n(\boldsymbol{x}_j) \tag{5.27}$$

Now, considering the first 1L mode with $n = 1$, the above equation becomes,

$$(\omega^2 + 2i\alpha\omega - \omega_1^2)\eta_1 = 2i\omega\Gamma\frac{S_1}{S_2}\frac{c_1}{l}\frac{\widehat{\mathcal{F}}}{\zeta}\eta_1\psi_1(0)\psi_1(a_b) \tag{5.28}$$

as $\boldsymbol{x}_i = l_1$ and $\boldsymbol{x}_j = a_b$, then $\psi_1(l_1) = \cos(k_1 l_1)$ and $\psi_1(a_b) = \cos(k_2 a_b)$. Further,

$$\omega^2 + 2i\left[\alpha - \Gamma\frac{S_1}{S_2}\frac{c_1}{l}\frac{\widehat{\mathcal{F}}}{\zeta}\cos(k_1 l_1)\cos(k_2 a_b)\right]\omega\eta - \omega_1^2 = 0 \tag{5.29}$$

The roots for the above equation can be found by linearizing around ω_1 such that $\omega = \omega_1 + \Omega_1$.

$$\omega^2 \approx \omega_1^2 + 2\Omega_1\omega_1 \tag{5.30}$$

Substituting Eq. 5.29 in the above equation, one obtains:

$$\Omega_1 = -i\left[\alpha - \Gamma\frac{S_1}{S_2}\frac{c_1}{l}\frac{\widehat{\mathcal{F}}}{\zeta}\cos(k_1 l_1)\cos(k_2 a_b)\right] \tag{5.31}$$

The length l_1 is small and hence $\cos(k_1 l_1) \approx 1$ in the frequency range of interest. Considering a simpler case of a flame located at $a_b = 0$ and ignoring the damping term, the growth rate and change in frequency can be written as,

$$\Omega_{1i} = \Gamma\frac{S_1}{S_2}\frac{c_1}{l}\mathrm{Re}\left\{\frac{\widehat{\mathcal{F}}}{\zeta}\right\} \tag{5.32}$$

$$\Omega_{1r} = \Gamma\frac{S_1}{S_2}\frac{c_1}{l}\mathrm{Im}\left\{\frac{\widehat{\mathcal{F}}}{\zeta}\right\} \tag{5.33}$$

Given that $\zeta = G_\zeta e^{i\varphi_\zeta}$, the growth rate will be positive if,

$$\Gamma\frac{S_1}{S_2}\frac{c_1}{l}\left|\frac{\widehat{\mathcal{F}}}{\zeta}\right|\cos(\varphi_F - \varphi_\zeta) > 0 \tag{5.34}$$

In other words, the first unstable band would be such that $-\pi/2 + \varphi_\zeta < \varphi_F < \pi/2 + \varphi_\zeta$. Considering $\varphi_\zeta = 3\pi/2$ would result in the unstable band falling in the range [π,2π] and $\varphi_\zeta = \pi$ would result in [$\pi/2$,$3\pi/2$] as the unstable bands that can be traced on the FDF phase curve. Figure 5.6 shows the variation of the growth rate Ω_{1i} (same as ω_i) and frequency $2\pi f = \omega_1 + \Omega_{1r}$ with respect to φ_F at a fixed G_F and G_ζ but at different values of φ_ζ. This is identical to the results obtained by solving Eq. 5.11 shown in Fig. 5.3. It is interesting to note that the growth rate and frequency are deduced here from a notably different framework.

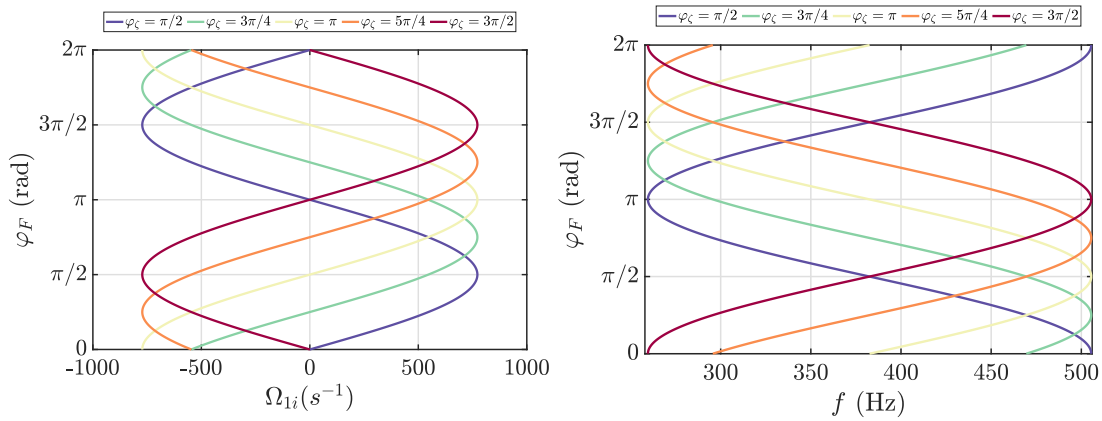

Figure 5.6. *Sensitivity of the growth rate Ω_{1i} and frequency f to the phase φ_ζ of injector impedance.*

Part II

Injector and fuel impact on combustion dynamics

Chapter 6

Influence of injectors on self-sustained oscillations: SICCA-Spray

Contents

A part of this chapter is published as a full-length article with the same title, "Swirler effects on combustion instabilities analyzed with measured FDFs, injector impedances and damping rates" by Preethi Rajendram Soundararajan, Daniel Durox, Antoine Renaud, Guillaume Vignat and Sébastien Candel in Combustion and Flame, vol. 238, April 2022. The experimental setup of the SICCA-Spray test rig comprehensively described in Chapter 1 is briefly recalled in Section 6.2, and familiar readers can skip this part.

The influence of the injection system on combustion instabilities is investigated on a laboratory-scale combustor equipped with a single injector that is weakly transparent to acoustic waves. The combustor is fed with liquid heptane delivered as a spray by a hollow cone atomizer. Experiments are carried out with three swirlers having similar geometries but different pressure losses and swirl numbers. Self-sustained oscillations (SSOs) corresponding to these swirlers feature differences in oscillation frequency and amplitude for a given chamber length. These observations do not match with standard modeling predictions. Therefore, the low-order analytical model derived in Chapter 5 is used, where the effect of the injection system is represented using an impedance at the injector outlet. This quantity and the flame describing function (FDF), both determined experimentally, are used together with damping rate estimates as model inputs. The FDFs are obtained at the suitable measurement location for the incident velocity disturbances at the injector outlet based on the discussions in Chapter 4. It is also indicated earlier that OH-chemiluminescence intensity can be used as a proxy for the heat release rate as the equivalence ratio modulations are relatively weak for the particular spray flames considered in this study (Chapter 2). Results from the model indicate that the injector impedance (that depends on the swirler characteristics) shifts the classical bands of instability and modifies the growth rate magnitude compared to a generic combustor with an acoustically transparent injector. Using the proposed model, the stability of the system can be rated along with a prediction for growth rate and frequency of oscillation. Predictions generally agree with experimental observations with some limitations. The model combined with damping rate estimates is finally used to predict limit cycle oscillation amplitudes with the aid of the FDF framework.*

6.1 Introduction

Combustion instabilities often raise serious issues in the development and operation of high-performance devices such as liquid propellant rockets, aircraft engines, and gas turbines. Early work on rocket thrust chambers provided fun-

damental insights on the mechanisms driving and coupling combustion instabilities, emphasizing effects associated with the delay inherent to the combustion process and its sensitivity to the state variables (Harrje and Reardon 1972; Yang and Anderson 1995). Considerable research carried out more recently in relation with novel combustor architectures for gas turbines has focused on the underlying mechanisms and control techniques, an effort reviewed, for example, by Candel (2002), Huang and Yang (2009), and Poinsot (2017). In aeronautical engines and gas turbines for energy production, much of the research has been focused on configurations operating in a nearly premixed mode, in which a swirling injector stabilizes the flame at a distance from the combustor backplane. These swirled injectors produce relatively compact flames, featuring a large volumetric power in an environment characterized by a reduced level of damping, thus making the system more susceptible to instabilities (Poinsot 2017; Méry 2018). The flow generated by such injectors exhibits complex fluid mechanics such as vortex breakdown, presence of precessing vortex core, etc., raising additional challenges in understanding the instabilities of such configurations (as discussed, for example, in Steinberg et al. (2010), Steinberg et al. (2013) and in reviews by Huang and Yang (2009), Syred (2006), Candel et al. (2014)). Some of these investigations indicate that the injection unit plays a vital role in determining the dynamics of the system and its propensity to instability. In the wide variety of injection configurations, one may try to distinguish swirling units in terms of characteristic parameters, the most obvious being the swirl number S_N and the pressure drop Δp or the pressure drop coefficient $\sigma = 2\Delta p/\rho_0 u_b^2$ (where ρ_0 is the density and u_b is the injector bulk velocity), in addition to other parameters like the Reynolds number or the turbulence intensity at the injector outlet. By comparing injectors featuring different swirl numbers and pressure losses, the present investigation intends to underline the role of the swirler in the process leading to self-sustained oscillations (SSOs).

At this stage, it is worth reviewing some previous investigations that specifically examine the effects of swirling injector parameters on combustion dynamics. One indication of the key role of the swirl number is provided by the large eddy simulation (LES) of a swirl-stabilized, lean premixed combustor reported by Stone and Menon (2002). An increase in this number (achieved by changing the premixer vane angle) from 0.56 to 0.84 results in a 50% reduction in the amplitude of acoustic pressure oscillations. Another LES study by Huang and Yang (2005), focused on the effect of swirl on flame dynamics in a lean premixed swirl combustor, indicates that high swirl numbers lead preferentially to transverse acoustic oscillations, whereas longitudinal oscillations prevail at weak swirl levels. Swirl number effects are also illustrated in a study by Durox et al. (2013), where an injector with continuously variable swirl numbers was used. Different flame topologies are observed and two types of instabilities are identified, a higher frequency instability—occurring for larger values of the swirl number featuring the highest acoustic pressure amplitudes and another instability coupled with the plenum at

lower values of the swirl number. A more recent investigation by Kim (2016) considers the instability mechanism in an industrial-scale lean premixed gas turbine combustor with a swirling injector. Two swirlers with swirl numbers 0.4 and 0.8 were tested at different chamber lengths. The normalized pressure amplitude, as well as the heat release rate fluctuations, were more intense in the higher swirl number case than at the low swirl number situation. These experimental results are somewhat at variance with those described by Stone and Menon (2002). The fact that these investigations arrive at opposing conclusions may be interpreted as an indication that the instability mainly depends on the flame dynamics and its coupling with acoustics but not directly on the swirl number value.

The effect of injector head loss is comparatively less well documented. In general, the injector unit introduces a large change in the passage area, and this causes a notable decoupling of the upstream manifold, as shown by Schuller et al. (2012). This is characterized by an acoustic coupling index Ξ, based on the expansion ratio between the chamber and injection unit cross-sections and on the fresh and burned gas temperature ratio. A large expansion ratio is often caused by a small passage area inside the injector, inducing a high pressure drop. However, it is not easy to distinguish the direct effect of the index Ξ from that associated with head loss. Recent work by Vignat et al. (2019) considers the effects of injector pressure loss on self-sustained oscillations (SSOs) using a set of swirling spray injectors. These injectors have the same swirl number, ensuring nearly identical flame structures but different head losses. The instability map is derived over a wide range of operating conditions, and it is found that instability regimes change when the operating conditions are varied. This reveals the notable influence of the pressure drop on the system stability and on the oscillation intensity and nature. In another study, Polifke et al. (2003) investigated a pressure loss instability mechanism in a swirl-stabilized premixed burner. Experiments indicated that the onset of instability corresponded to a negative slope of pressure drop characteristics with respect to the mass flow rate. The experimental observations were supported by an analytical representation based on a network model using acoustic transfer matrices leading to an instability criterion. Indications of the notable influence of the injection parameters are also derived from recent experiments on annular combustors, which are reviewed by Vignat et al. (2020). The potential of using low-order models in representing complicated swirler geometries was explored, for instance, by Fischer et al. (2006) using transfer matrices that were experimentally validated under cold flow conditions in a combustor equipped with a variable swirl number injector. The pressure loss coefficient was also modified by variably blocking the swirl generator. These investigations naturally encourage one to look for the applicability of low-order models even in complicated swirling geometries.

From this review, it appears that in swirl-stabilized flames, the injector defines the combustion dynamics of the system to a large extent. Changes in injector char-

acteristics that vary the swirl number could alter the flow behavior resulting in a different flame shape. Variations in the pressure drop across the injector (leading to a change in the injector impedance) may alter the coupling between plenum and chamber, thus modifying the instability behavior. This forms the motivation for the present investigation. A single-injector system is employed to understand the injector effect on combustion instabilities under longitudinal SSOs. The flame describing functions (FDFs) (Dowling 1997; Noiray et al. 2008) of the various units are determined and used in combination with a stability analysis framework that employs a measured impedance at the injector outlet to interpret the experimental data.

The present chapter is organized as follows. Section 6.2 describes the SICCA-Spray setup. Experimental data gathered in Section 6.3 illustrate differences in SSOs that may be observed in this combustor with the different swirlers. Section 6.4 highlights the issue of finding an optimal position for measuring the input velocity fluctuations at the swirling injector outlet and reports the FDF measurements. Sections 6.5 and 6.6 describe the impedance measurements at the injector outlet and the damping rate estimation respectively. These data are combined with a theoretical model developed in Chapter 5 to predict the occurrence of instabilities. Comparison of the model predictions with experimental data discussed in Section 6.7 underlines the importance of including injector dynamics in the theoretical model for instability analysis.

6.2 Experimental setup

6.2.1 The SICCA-Spray test rig

Experiments reported in this chapter are carried out in the single-injector combustor SICCA-Spray described in Chapter 1 and only a few essential details of the setup are recalled here. The schematic of the experimental setup and the exploded view of the injector are reproduced in Fig. 6.1. For the current study, three swirlers, designated as 707, 712, and 716 imparting clockwise rotating to the incoming air flow are used, and their characteristics are gathered in Tab. 6.1. It is reminded that the swirlers 707 and 712 have nearly the same swirl number and velocity profile at the outlet, but 712 has a higher pressure drop. The swirler 716 features a higher value for both swirl number and pressure drop. In the present study, the system is operated at a global equivalence ratio of $\phi = 0.85$ and thermal power of $6.4\,\mathrm{kW}$, which corresponds to the operating point F1 having an air flow rate of $2.6\,\mathrm{g\,s^{-1}}$ and a fuel flow rate of $520\,\mathrm{g\,h^{-1}}$.

Two kinds of combustion chambers are used depending on the measurement type. In the configuration of Fig. 6.1 (b), velocity measurements near the injector outlet, flame visualization, and chemiluminescence intensity detection are

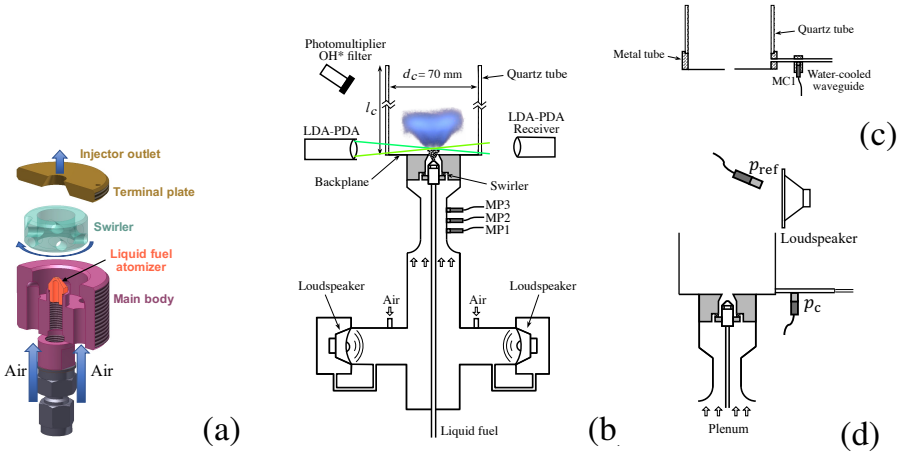

Figure 6.1. *(a) Exploded view of the swirling injector showing its various components. (b) Schematic of the experimental setup of SICCA-Spray reproduced from Chapter 1. The combustion chamber is configured for laser Doppler anemometry measurements. (c) Combustion chamber setup for pressure measurements during an SSO. (d) Schematic diagram of the experimental setup used for damping measurements under cold flow conditions. The bottom portion of the plenum is not shown.*

Table 6.1. *Injector characteristics measured in an unconfined configuration (in cold flow) with a mass flow rate of* $\dot{m}_{air} = 2.6\,\mathrm{g\,s^{-1}}$. *The swirl number* S_N *is measured at a height* $h = 2.5\,\mathrm{mm}$ *above the outlet. The head loss coefficient is calculated using the equation* $\Delta p = \frac{1}{2}\sigma\rho_0 u_b^2$ *where* u_b *is the bulk velocity given by* $\dot{m}_{air}/\pi\rho_0 R_{inj}^2$ *and is approximately equal to* $43\,\mathrm{m\,s^{-1}}$. *Here* $R_{inj} = 4\,\mathrm{mm}$ *is the radius of the injector outlet,* d_{sc} *is the diameter of the swirler channels and* $2R_{0,sc}$ *is the distance separating the axis of two opposing channels. Reproduced from Chapter 1.*

Swirler	S_N (-)	Δp (kPa)	σ (-)	d_{sc} (mm)	$R_{0,sc}$ (mm)
707	0.60	3.65	3.33	4.0	4.6
712	0.59	4.50	4.10	3.0	2.3
716	0.70	5.74	5.23	3.5	4.7

carried out with a transparent quartz tube with an internal diameter of $70\,\mathrm{mm}$ and a length of $100\,\mathrm{mm}$ or $150\,\mathrm{mm}$, depending on the experiment. More details of the experimental conditions are given in Tab. 6.2. In a slightly different configuration, illustrated in Fig. 6.1 (c), a $15\,\mathrm{mm}$-high metal ring is placed at the chamber bot-

tom, on top of which quartz tubes of different lengths are placed to complete the combustion chamber. The length of the chamber can thus be varied from 115 to $365\,\mathrm{mm}$ in steps of $50\,\mathrm{mm}$, with an additional longest chamber of $465\,\mathrm{mm}$. The bottom metal ring supports the water-cooled waveguide microphone MC1 (shown in Fig. 6.1 (c)) that records the acoustic pressure close to the backplane. Two driver units mounted at the bottom of the plenum subject the system to external acoustic modulations for determining the flame response to incident velocity fluctuations at different perturbation amplitudes.

6.2.2 Diagnostics

In the plenum, three microphones (designated as MP1, MP2, MP3 in Fig. 6.1 (b)) measure the pressure fluctuations, the signals from which are also used to calculate the acoustic velocity. For the chamber pressure measurement close to the backplane, the microphone MC1 is fixed on a water-cooled waveguide mounted on the bottom metal ring (Fig. 6.1 (c)). The pressure sensor element is placed on the waveguide at a distance of $276\,\mathrm{mm}$, resulting in a propagation delay of $0.79\,\mathrm{ms}$ in the acoustic pressure record. A photomultiplier fitted with an OH* filter detects the flame chemiluminescence $I(\mathrm{OH}^*)$ emitted by OH* radicals. Additionally, an intensified CCD camera comprising 1024 $\times$ 1024 pixels is used to visualize the flame shapes formed by each injection system by recording OH* light emission. The velocity in the chamber is measured with a Dantec FlowExplorer 2-component phase Doppler anemometry (PDA) system, while configured exclusively for anemometric measurements (laser Doppler anemometry—LDA). Table 6.2 gives a synthesis of the diagnostics used in the experiments presented in this chapter.

Table 6.2. *Summary of the different experimental procedures described in this chapter. LDA: laser Doppler anemometry, SSO: self-sustained oscillation, FDF: flame describing function.*

Experiment	Operation	Total chamber length	Measurement	Procedure	Section
Flame images	With flame Stable	$100\,\mathrm{mm}$	ICCD camera OH* chemiluminescence	Single image obtained by averaging 30 frames Abel deconvolution	6.3
SSO	With flame Stable/unstable	115, 165, 215, 265, 315, 365, $465\,\mathrm{mm}$	Microphone MC1 in chamber Mounted on bottom metal ring	Vary chamber length to obtain different SSO	6.3
FDF: Velocity	With flame	$150\,\mathrm{mm}$	LDA Measurement of $u'_{c,r}/\overline{u}_{c,r}$	Upstream modulation: $300\,\mathrm{Hz}$ to $800\,\mathrm{Hz}$	6.4.1
FDF: Heat release rate	Stable Acoustic forcing		Photomultiplier OH* chemiluminescence	$V_0 = 0.5\,\mathrm{V}$ to $3\,\mathrm{V}$ $u'_{c,r}/\overline{u}_{c,r}$ = 0 to 0.35	
Impedance under SSO	With flame Unstable	265, 315, $365\,\mathrm{mm}$	Step 1: LDA - measurement of $u'_{c,r}/\overline{u}_{c,r}$ Step 2: Microphone MC1 for chamber pressure	Chamber length varied to obtain SSO	6.5
Cold flow damping rate	Cold flow Stable; acoustic forcing	165 and $315\,\mathrm{mm}$	Microphone MC1 in chamber Measurement of frequency response	Downstream modulation: $300\,\mathrm{Hz}$ to $1000\,\mathrm{Hz}$ $V_0 = 5\,\mathrm{V}$	6.6.1

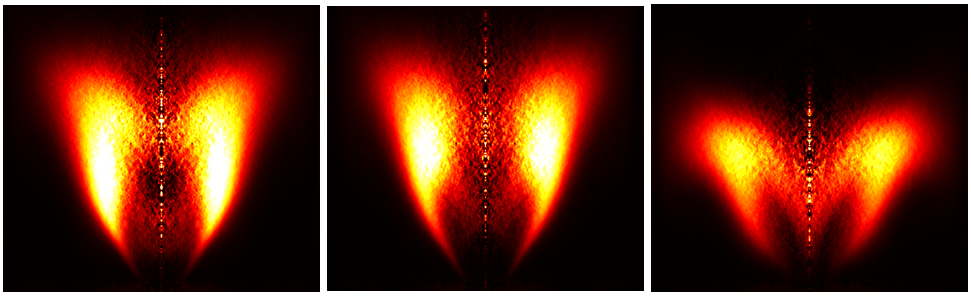

(a) 707 (b) 712 (c) 716

Figure 6.2. *OH* images in SICCA-Spray for the three swirlers showing the flame chemiluminescence captured using an intensified CCD camera. The images are captured when SICCA-Spray is stable. An Abel deconvolution is applied to the average image recorded by the camera and is shown in false colors.*

6.3 Self-sustained oscillations (SSOs)

Before describing the unstable operation, it is first interesting to examine flame images obtained under stable conditions with a chamber length of $l_c = 100\,\mathrm{mm}$. Figure 6.2 shows the OH* chemiluminescence images for the three different swirlers. A single image is obtained by averaging 30 frames and applying an Abel deconvolution. The flame shapes corresponding to the various swirler units are notably different, especially near the central axis. For swirler 707, the flame is relatively narrow and takes a “V" shape. For swirler 712, the “V” shape opens up slightly, while for swirler 716, the flame spreads out and takes the form of a hollow “M” with a central trough, which may be attributed to the higher swirl induced by this swirler. From the flame images, the axial location a_b of the heat release rate barycenter is estimated, and it takes a value of $37\,\mathrm{mm}$ above the backplane for swirler 707, $38\,\mathrm{mm}$ for swirler 712, and $32\,\mathrm{mm}$ for swirler 716.

Instability characteristics are now examined during longitudinal self-sustained oscillations by varying the total chamber length l_c. This changes the eigenfrequency of the quarter-wave chamber mode and allows to investigate the influence of this parameter. Seven different chamber lengths are considered: 115, 165, 215, 265, 315, 365, and $465\,\mathrm{mm}$, and the pressure signals measured by MC1 are recorded at a sampling rate of $f_s = 16{,}384\,\mathrm{Hz}$ for a total acquisition time of at least $8\,\mathrm{s}$.

The pressure power spectrum of the signal from the chamber microphone MC1 is calculated using Welch’s periodogram method, considering 32 Hamming windows with a 50% overlap between windows resulting in a frequency resolution of $\Delta f \approx 2\,\mathrm{Hz}$. The root mean square (RMS) of chamber pressure p_rms representing the instability amplitude (measured by MC1) and the peak frequency f_peak obtained from the frequency spectrum together characterize the self-sustained oscillations of SICCA-Spray. Figure 6.3 shows the power spectra plotted in terms of

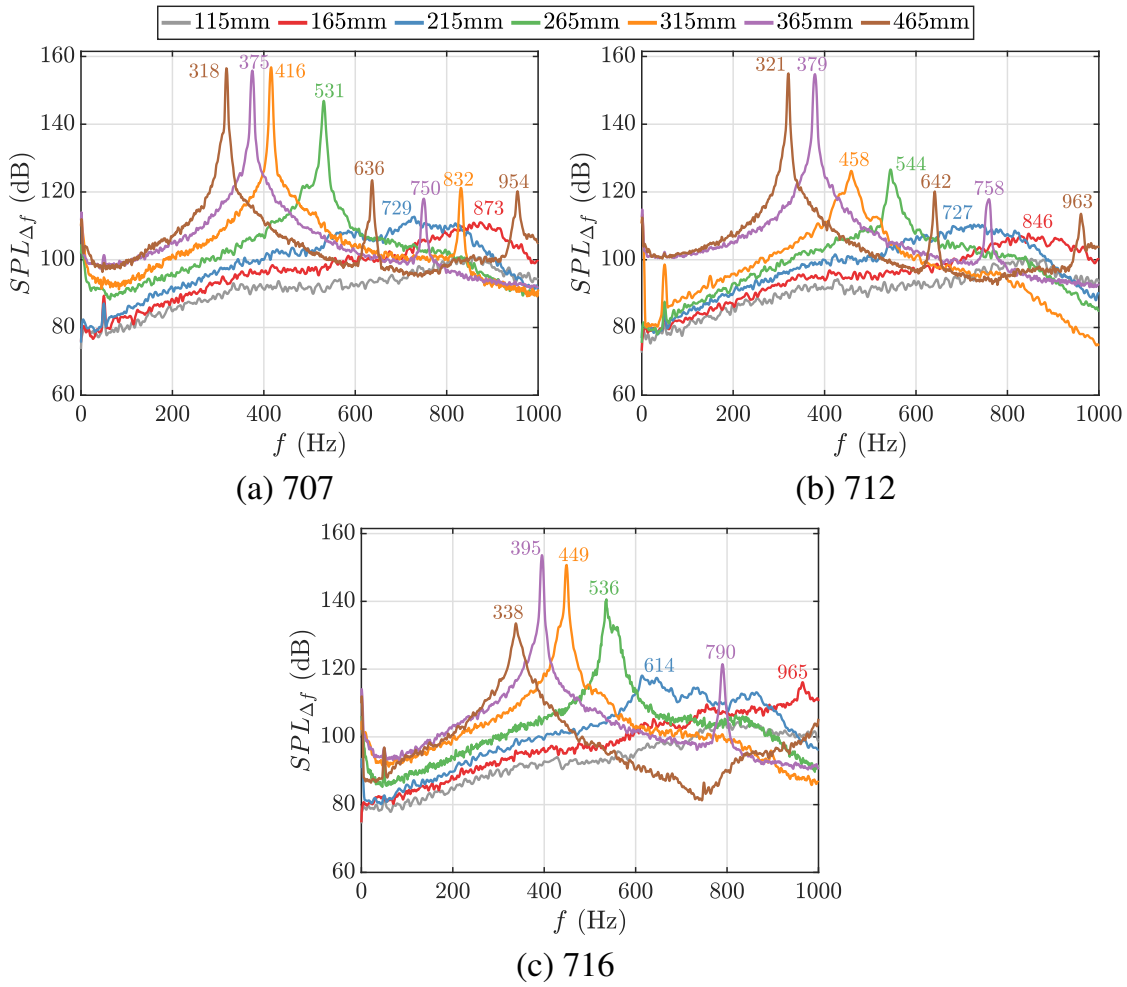

(a) 707 (b) 712

(c) 716

Figure 6.3. *Frequency spectra showing the sound pressure level ($SPL_{\Delta f}$) measured by microphone MC1 near the combustor backplane for the three swirlers at different combustion chamber lengths l_c.*

sound pressure level $SPL_{\Delta f}$ in the frequency band Δf and given in dB at different chamber lengths (the reference pressure being $p_{\text{ref}} = 2 \times 10^{-5}$ Pa). In the figure, the frequency corresponding to each peak is also marked.

At $l_c = 115\,\text{mm}$, the spectra exhibit a relatively broadband shape without any prominent peak. The measured chamber pressure fluctuations are relatively low at this length, with a value of $p_{\text{rms}} = 67\,\text{Pa}$ for swirler 716, the maximum among the three swirlers at this length. SICCA-Spray is therefore considered to be stable at this length, and $p^{bl}_{\text{rms}} = 67\,\text{Pa}$ is associated to background combustion and flow noise. This length with swirler 716 is considered as a baseline (*bl*) configuration for comparing the instabilities at other chamber lengths.

To determine whether the system can be considered stable or unstable, two criteria are used. A first condition to identify an unstable regime is that the pressure RMS value be at least twice that recorded in the baseline configuration

$p'^{bl}_{\text{rms}} = 67\,\text{Pa}$, i.e., $p_{\text{rms}} > 2\,p'^{bl}_{\text{rms}}$. In the second condition, the maximum $\text{SPL}_{\Delta f}$ in the spectrum (Fig. 6.3) is compared with the maximum $\text{SPL}^{bl}_{\Delta f}$ ($\approx 100\,\text{dB}$) recorded in the baseline configuration, and one requires that the maximum peak level exceeds the baseline level by a predetermined amount, typically $\Delta S = 30\,\text{dB}$. This condition maybe written as $\text{SPL}_{\Delta f}(peak) > \text{SPL}^{bl}_{\Delta f}(peak) + \Delta S$. This criterion considers whether the system features a well-defined pure frequency tone. If the two conditions are met, one may say that the system is unstable, but when only one condition is met, the system is considered to be marginally unstable. An alternate criterion employed by Ebi et al. (2018) was also examined for distinguishing stable and unstable points based on the probability density function (PDF) of time records of the pressure signal. Although this criterion results in an equivalent categorization for unstable and stable points, it classifies some marginally unstable points as stable even though a short but distinguishable peak is seen in the spectrum (*e.g.,* 712 at $l_{\text{c}} = 265\,\text{mm}$ in Fig. 6.3).

Figure 6.4 shows the stability map of SICCA-Spray for the different chamber lengths based on the previous criteria. The peak frequency f_{peak} and pressure amplitude p_{rms} for the different chamber lengths are also shown in this figure. For swirler 707, at $l_{\text{c}} = 165$ and $215\,\text{mm}$, the system is stable as there is no peak in the frequency spectrum and p_{rms} is low. These points are represented as gray circles in Fig. 6.4. At the other lengths, SICCA-Spray with swirler 707 is unstable, marked by a prominent frequency peak and significantly higher values of pressure amplitude. This is denoted in the figure by red diamonds. With swirler 712, the system is stable at $l_c = 165$ and $215\,\text{mm}$, which can be seen from the lack of a peak in the frequency spectrum of Fig. 6.3b, and it exhibits a behavior similar to that of swirler 707 at this length. However, at $l_c = 265$ and $315\,\text{mm}$, SICCA-Spray is only marginally unstable, a behavior that differs from that of swirler 707 at these lengths. At $l_c = 365$ and $465\,\text{mm}$, the instability reaches a level similar but slightly lower to that of swirler 707. The instability frequency does not change between the swirlers 707 and 712 except during marginally unstable operation.

For swirler 716, the only stable configuration is found at $165\,\text{mm}$ apart from the baseline at $l_c = 115\,\text{mm}$. At $l_{\text{c}} = 215\,\text{mm}$, the system features a small peak in the frequency spectrum, and the pressure amplitude p_{rms} is moderate. Consequently, SICCA-Spray is mildly unstable at this point—represented by a black star symbol in Fig. 6.4. At the lengths $l_{\text{c}} = 265, 315$ and $365\,\text{mm}$, SICCA-Spray is unstable with high chamber pressure amplitudes. However, when the length is increased further, 716 starts to enter the stable zone and exhibits only a marginal instability at $l_c = 465\,\text{mm}$. In general, swirler 716 has a lower oscillation amplitude during instability and also exhibits a difference in the oscillation frequency compared to the two other swirlers.

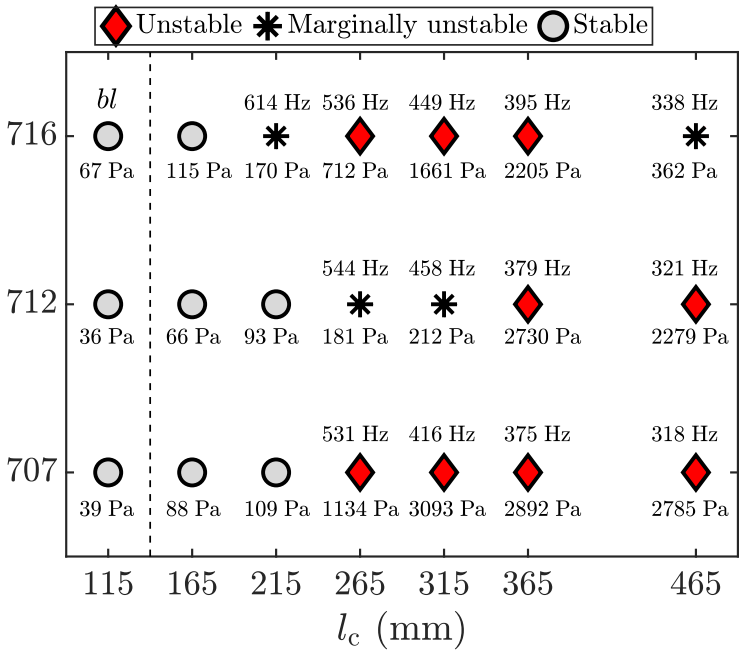

Figure 6.4. *Experimentally determined stability map of SICCA-Spray under self-sustained oscillations at different chamber lengths l_c for the three swirlers. The peak frequency f_{peak} (Hz) from the frequency spectrum and RMS chamber pressure p_{rms} (Pa) measured by MC1 are indicated for each configuration. Gray circles correspond to stable points, black stars represent points that are marginally unstable, and red diamonds designate unstable points. The baseline level measured at $l_c = 115\,\mathrm{mm}$ with swirler 716 is designated as bl.*

6.4 Flame describing functions (FDFs)

FDF measurements are performed by submitting the flame to different levels of acoustic velocity fluctuations induced by the loudspeakers located at the bottom of the plenum. The wave generator produces sinusoidal waves with an amplitude V_0 (peak to peak) of $0.5\,\mathrm{V}$ to $3\,\mathrm{V}$ in steps of $0.5\,\mathrm{V}$, and a linear frequency sweep is performed from $250\,\mathrm{Hz}$ to $850\,\mathrm{Hz}$ for a time duration of $133\,\mathrm{s}$ at each level. This procedure subjects the flame to different levels of velocity modulation. The amplifier voltages given to the driver units are selected to produce a velocity fluctuation similar to the SSO measurements whenever possible. For the FDF measurements, it is necessary to ensure that SSOs are absent and that the system is stable. This is achieved by setting the chamber length at $150\,\mathrm{mm}$.

It is here convenient to recall the FDF definition from Chapter 4,

$$\mathcal{F}(\omega, |u'_{c,r}|) = \frac{\dot{Q}'/\overline{\dot{Q}}}{u'_{c,r}/\overline{u}_{c,r}} = G_F(\omega, |u'_{c,r}|)e^{i\varphi_F(\omega,|u'_{c,r}|)} \tag{6.1}$$

Here, $G_F = |\mathcal{F}|$ and $\varphi_F = \arg(\mathcal{F})$ are the gain and phase of the FDF; $u'_{c,r}$ is the

acoustic velocity fluctuation determined at the base of the flame (subscript 'c' referring to the measurement in the chamber) at a certain distance r from the center of the injector and at a particular height h from the chamber backplane. Equation 6.1 is such that the relative velocity fluctuations equal the relative volumetric flow rate fluctuations, and it was shown in Chapter 4 that the appropriate point that satisfies this equality is at $r = 3.5\,\mathrm{mm}$ for 707 & 712, and $r = 4\,\mathrm{mm}$ for 716, all at a height of $h = 2.5\,\mathrm{mm}$. In the above equation, $\dot{Q}'$ represents the fluctuation in heat release rate and $\overline{\dot{Q}}$ is the mean heat release rate[3], both deduced from the light intensity of OH*. It is assumed that the equivalence ratio fluctuations are negligible based on the analysis of Chapter 2, and hence the OH* light intensity fluctuations are used as an approximate indicator of heat release rate, *i.e.*, $I(\mathrm{OH})^*/\overline{I(\mathrm{OH})^*} \approx \dot{Q}'/\overline{\dot{Q}}$.

6.4.1 Results

It is now worth examining the FDF corresponding to the three swirlers operating under the same conditions ($\mathcal{P} = 6.4\,\mathrm{kW}$ & $\phi = 0.85$) as the self-sustained instabilities. The FDFs shown in Fig. 6.5 represent the variation of gain G_F and phase φ_F with frequency for different values of velocity fluctuation level in the chamber, $u'_{c,r}/\overline{u}_{c,r}$. For the FDF calculation, the signals recorded from the photomultiplier (representing the heat release rate) and the velocity signals delivered by LDA are filtered $\pm 5\%$ around the signal generator frequency. The velocity RMS is determined by integrating the power spectral density of the filtered signal. The transfer function between the filtered heat release rate and velocity fluctuations is obtained by dividing the cross power spectral density of these two signals by the spectral density of the relative velocity signal. The spectral densities are estimated using Welch's periodogram method. Each frequency block of two seconds in the ramp is divided into 8 Hamming windows with a 50% overlap between windows. The measurements are performed in the frequency range between $300\,\mathrm{Hz}$ and $800\,\mathrm{Hz}$. The low frequency range below $300\,\mathrm{Hz}$ is not covered because of the limitations of the modulation system of driver units. This situation is often found in similar investigations (see, for example, Bade et al. (2013)). Additionally, FDF measurements below $300\,\mathrm{Hz}$ are outside the range of interest for the current study.

In general, the three FDFs have similar shapes, but one also notices significant variations. This is particularly the case for the gain curves (Fig. 6.5 left). The position of the maximum gain is around 520 Hz for swirler 712 and around 600 Hz for swirler 716. For swirler 707, the gain is nearly flat up to $600\,\mathrm{Hz}$, after which it begins to fall. The gain only weakly changes with the input level for swirlers 707 and 712, while it is more sensitive to this level for swirler 716. Thus, swirlers 707 and 712 are still in the linear regime with respect to the input, while the behavior of the flame formed by swirler 716 is nonlinear in the vicinity of

[3]Here and henceforth the notation $(\cdot)'$ refers to fluctuations and $\overline{(\cdot)}$ refers to mean of a quantity.

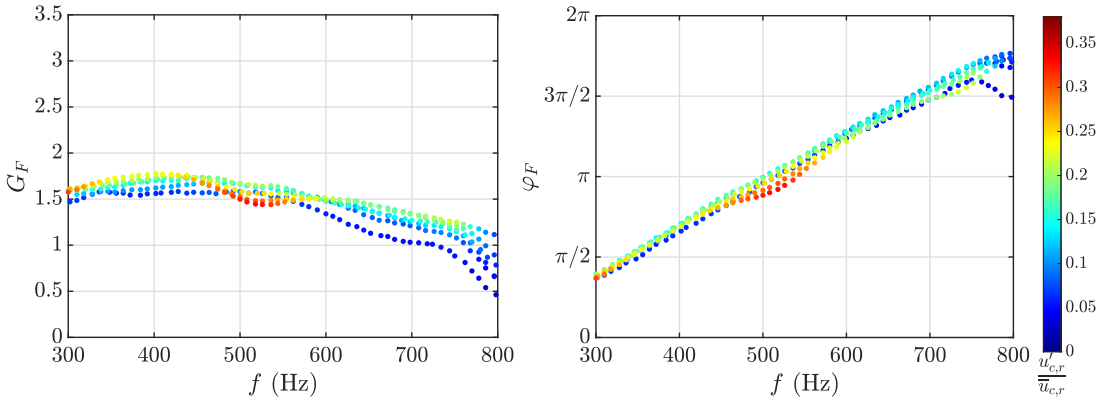

(a) 707

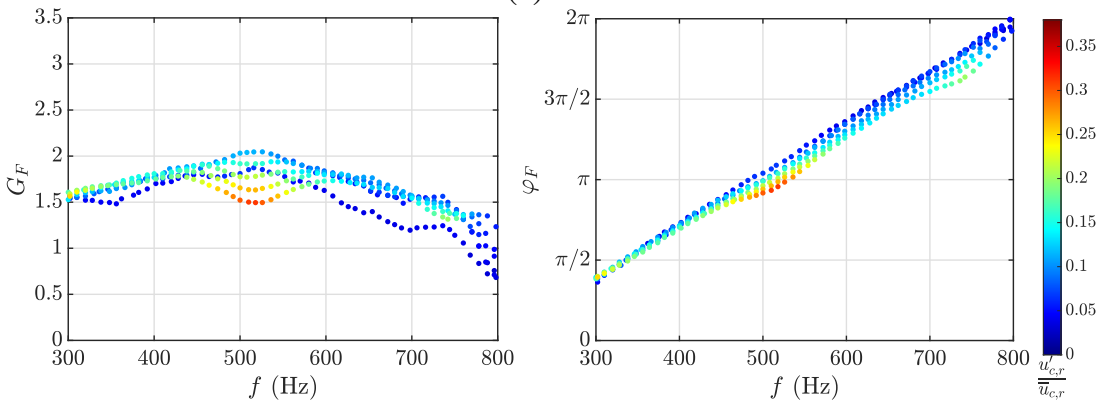

(b) 712

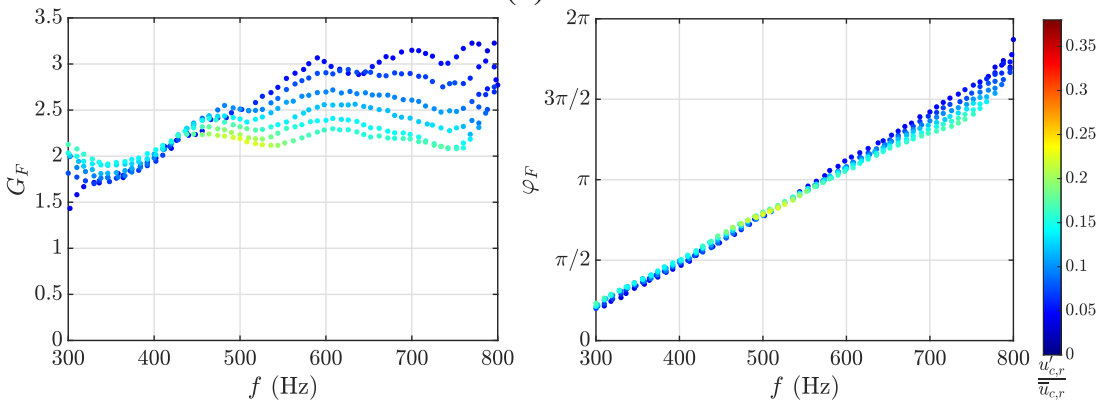

(c) 716

Figure 6.5. *Flame describing function gain G_F (left) and phase φ_F (right) for the three swirlers. From top to bottom: swirlers 707, 712, and 716. The color scale represents the level of velocity fluctuations measured at $r = 3.5\,\mathrm{mm}$ for swirlers 707 and 712, and $r = 4\,\mathrm{mm}$ for swirler 716, at a height of $h = 2.5\,\mathrm{mm}$ from the backplane. Here, $u'_{c,r}$ and $\overline{u}_{c,r}$ are respectively the RMS velocity fluctuations and mean velocity fluctuations ('c' refers to measurements made in the chamber and 'r' refers to the radius at which the velocity fluctuations are measured). The data are smoothed using a five-point moving average.*

the gain maximum, i.e., around $f = 600\,\mathrm{Hz}$. The phase evolution (Fig. 6.5 right) is quasi-linear with frequency. The slopes corresponding to the different swirlers are of the same order of magnitude but with some variations in the delays that may be deduced from these slopes. These delays are 1.35, 1.46 and $1.33\,\mathrm{ms}$ for swirlers 707, 712 and 716, respectively. Assuming that the delay is essentially controlled by convection, one may deduce from these data the length scale a from the injector outlet where the heat release fluctuations take place. Considering that the perturbations travel at half the maximum of the mean velocity on the axial velocity profile (Durox et al. 2005) (maximum velocity is around $69\,\mathrm{m\,s^{-1}}$ for swirler 716 shown in Chapter 4, $58\,\mathrm{m\,s^{-1}}$ for swirler 707 and $56\,\mathrm{m\,s^{-1}}$ for swirler 712—not shown), one obtains for a: 3.9, 4.1 and $4.6\,\mathrm{cm}$ respectively for swirlers 707, 712 and 716. This distance is slightly longer than the axial distance of the heat release rate barycenter a_b determined in Section 3.2 under stable conditions but is only approximate. Even if the delay is relatively precise, the estimate of the mean convection velocity is less accurate. As the distance a_b is known more precisely, it will be used in the theoretical analysis described in Section 6.7. It is worth noting that this distance has only a minor impact on the results, as seen in Chapter 5.

6.5 Impedance at the injector outlet during a self-sustained oscillation

Changing the injector not only changes the dynamic behavior of the flame, as indicated in the previous section but also modifies the acoustic response of this unit. For low-order modeling of situations where the injector is weakly transparent to acoustic waves, it is suitable to consider only the chamber with an impedance at the inlet representing the combined response of the injection unit and upstream manifold, as indicated in Chapter 5. It is observed with these injectors that, for the same amplitude of velocity fluctuation downstream of the injector, the velocity fluctuations upstream of the swirler in the plenum are completely different between SSO and forcing (shown in Chapter 3). This was also confirmed in a previous numerical study (Prieur (2017), pp. 144-158), where it was found that the injector dynamics is not the same during an upstream acoustic modulation and under SSO. Such behavior could be attributed to the strong pressure drop created by the small air channels in the swirler, resulting in strong acoustic decoupling of the upstream (plenum) and downstream (combustion chamber) cavities. To assign an impedance that is representative of the injector and the upstream cavity during an SSO, it is, therefore, necessary to modulate the system from downstream (unlike the FDF measurement in Section 6.4 where the system is modulated from upstream). Even though such a downstream modulation is carried out for damping measurements described in the next section, it is not possible to do this with flame in the SICCA-Spray test rig. However, the impedance may be directly measured

during an SSO, where there is a strong pressure oscillation downstream, and this is done in two steps here. Firstly, during an SSO, the velocity fluctuation $u_{c,r}$ at the injector outlet is measured with LDA. Next, the pressure fluctuation p'_c close to the backplane is recorded with the waveguide microphone MC1. The two measurements cannot be performed simultaneously because MC1 is supported on a metal ring comprising the water-cooled waveguide, and this blocks the optical access required for the LDA measurements. From the pressure and velocity measurements, the specific impedance $\zeta = p'_c/(\rho_u c_u u'_{c,r})$ at the outlet of the injector is calculated for the three swirlers. The density ρ_u and the sound velocity c_u are considered at the temperature of the fresh stream of air ($T_u = 293\,\mathrm{K}$). It is verified that the OH^* signal is the same between the two measurements, and this serves as a phase reference to deduce the phase difference between pressure and velocity.

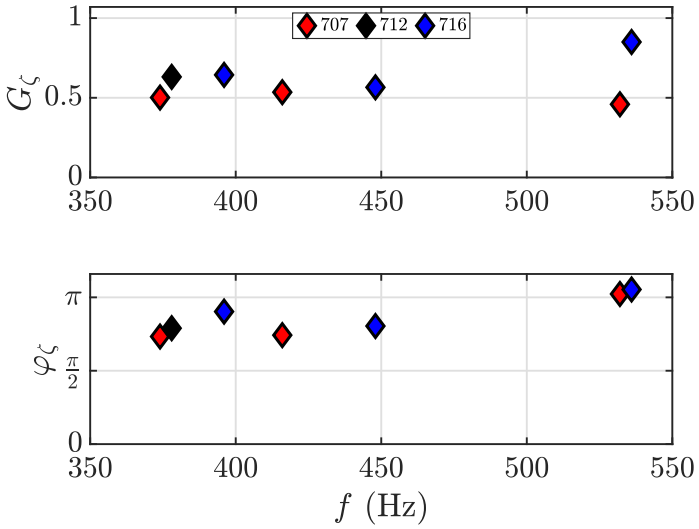

Figure 6.6. *The modulus G_ζ and phase φ_ζ of the injector impedance for the three swirlers. The measurements are reported only under limit cycle self-sustained oscillations at different frequencies.*

Figure 6.6 shows the specific impedance for the three swirlers at different instability frequencies—in other words, for different combustion chamber lengths. Only the impedance corresponding to a limit cycle oscillation with sufficient amplitude is shown in the figure. The phase of this specific impedance takes similar values for the swirlers 707 and 712, and its value is close to $3\pi/4$, especially when the instability is high (i.e., for longer chamber lengths and therefore for lower frequencies). For swirler 716, this phase is closer to π when the instability amplitude is highest (i.e., at the chamber length $l_c = 365\,\mathrm{mm}$ and for a frequency of $395\,\mathrm{Hz}$). A quasi-phase opposition between pressure and velocity at the injector outlet has also been observed previously in LES calculations by Staffelbach et al. (2009) of an annular system exhibiting combustion oscillations and more recently by Patat et al. (2021) under a downstream transverse acoustic field with similar type of

injector as those in the present work. This effect arises when the acoustic pressure amplitude downstream of the injector exceeds the mean dynamic pressure of the flow (Baillot and Lespinasse 2014; O'Connor et al. 2015) and is analogous to the injection-coupling analyzed in the domain of combustion instabilities in rocket engines (Hutt and Rocker 1995). The impedance values reported here will be used in the theoretical framework from Chapter 5. Growth rates obtained from this theoretical model will be compared to damping rates determined in the following section.

6.6 Damping rate estimate

To determine the stability of the system, it is essential to know the damping rate induced by each swirler. Two methods for the experimental determination of the damping rate are exploited in this section. In the first, one assumes that the system behaves like a second-order linear system, and the damping rate is deduced from the half-power bandwidth Δf_r of the resonance curve. This measurement can, however, only be performed in cold flow conditions. In the second method, the damping rate is estimated from an energy balance during a limit cycle oscillation.

6.6.1 Cold flow damping rate estimation using the resonance curve method

Performing this measurement in cold flow conditions is admittedly a limitation of this procedure, but it is still instructive to estimate the changes in damping rate that may be linked with the different swirlers.

The experimental setup for this measurement is shown in Fig. 6.1 (d). A driver unit placed near the top of the combustor excites the system, and the pressure response (p_c) is measured with microphone MC1. During this measurement, the two bottom loudspeakers are left electrically open, as they are during the self-sustained instability experiments. A microphone located in front of the driver unit serves as a reference and measures the frequency response p_ref of this device. The combustor surroundings are covered with an acoustic liner to reduce unwanted reflections. The damping measurement is performed at two chamber lengths in cold condition (with $\dot{m}_\mathrm{air} = 2.6\,\mathrm{g\,s^{-1}}$), $l_\mathrm{c} = 165\,\mathrm{mm}$ and $l_\mathrm{c} = 315\,\mathrm{mm}$, such that the resonance response occurs around the frequency of SSO in SICCA-Spray. At $l_\mathrm{c} = 165\,\mathrm{mm}$, the chamber resonates at a frequency $f_\mathrm{chamber} \approx 460\,\mathrm{Hz}$ corresponding to a quarter wave mode while at $l_\mathrm{c} = 315\,\mathrm{mm}$ it resonates at $f_\mathrm{chamber} \approx 760\,\mathrm{Hz}$, corresponding to a three quarter wave mode of the chamber. A frequency sweep is performed around the resonance frequencies at a ramp rate of $1\,\mathrm{Hz\,s^{-1}}$. The measurements are sampled at a frequency of $f_s = 16{,}384$ Hz and measured in blocks that are $2\,\mathrm{s}$ long. Damping is deduced from $\alpha = \pi\Delta f_r$, where Δf_r is the width of the resonance curve at half power. The calculation of frequency response

is performed using Welch's periodogram technique by averaging two Hamming windows at each 1 s block with 50% overlap. This results in a frequency resolution of ± 1 Hz, which in turn corresponds to a damping uncertainty of $\pm 3.14\,\mathrm{s}^{-1}$. The calculated damping values are indicated in the top row of Fig. 6.7 (b) at 460 Hz and in the bottom row for 760 Hz. The damping rate is found to be about $90\,\mathrm{s}^{-1}$ at 460 Hz and $120\,\mathrm{s}^{-1}$ at 760 Hz, with some variation between the swirlers. The lowest value corresponds to the swirler 712 at both frequencies. It is interesting to note that the swirler geometry influences this damping rate and that the variation in damping is of about 20% of the mean level at 460 Hz, whereas such a difference between swirlers is less evident at 760 Hz. However, these measurements do not quite represent the level of damping corresponding to the system under hot-fire conditions. In particular, there is no temperature evolution between the upstream manifold, injector, and chamber. This will modify the resonance conditions and the mode shape. The cold flow measurements only provide an estimate of the level of damping that may be expected for this system and to distinguish the swirlers in terms of their damping rate.

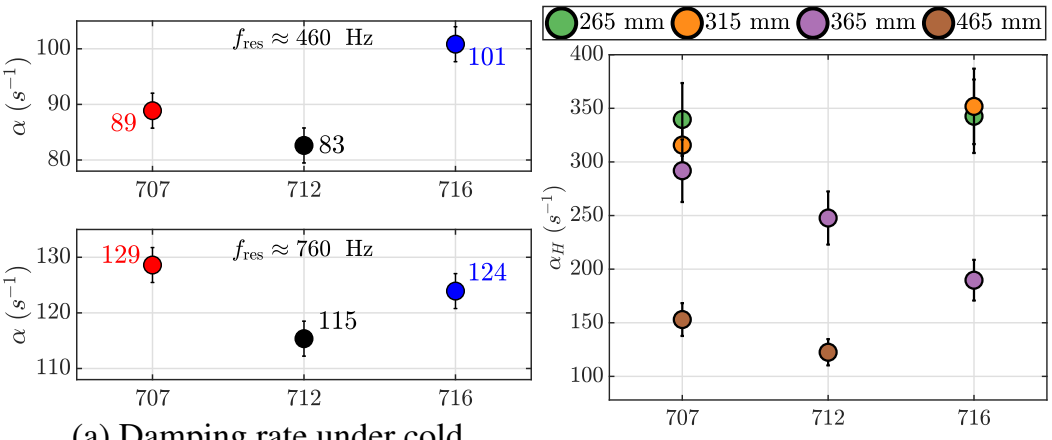

(a) Damping rate under cold conditions

(b) Damping rate under hot-fire conditions

Figure 6.7. *(a) The top row shows the damping ($\alpha = \pi \Delta f_r$) for the three swirlers at a frequency of* 460 Hz *with a chamber length of* 165 mm. *The bottom row shows damping at* 760 Hz *measured with a chamber length of* 315 mm. *The error bars indicate the uncertainty in damping determined from the frequency resolution in Welch's periodogram calculation and is equal to* ± 1 Hz. *(b) Damping rate under hot-fire conditions deduced using energy balance method. The error bars represent an approximate uncertainty which is considered to be about 10%. The damping rate estimate is obtained only from measurements corresponding to a well-established limit cycle oscillation.*

6.6.2 Hot-fire damping rate estimation using energy balance method

It is not easy to obtain a direct measurement of the damping rate when there is a flame. For example, it is not possible to perform a downstream modulation as the hot gases might damage the driver unit located close to the chamber exit, and the combustion noise will hamper obtaining a noise-free resonance curve. Furthermore, it is difficult to cover the surroundings with liner material because of the hot exhaust stream. One may instead use a system identification method or an acoustic energy balance. These two methods were exploited by Vignat (2020) (pp.245-255) in the case of axial coupling in the annular configuration MICCA-Spray equipped with the same swirling injectors (of the 716 type). It was found that the damping coefficient was $\xi \simeq 6 \times 10^{-2}$ giving a damping rate under hot-fire conditions $\alpha_H = \xi\omega_0 \simeq 170\,\mathrm{s}^{-1}$.

The acoustic energy balance method is used in the present configuration, and the damping rate obtained with this method is given by:

$$\alpha_H = \frac{\langle S \rangle}{2\langle E \rangle} \tag{6.2}$$

where α_H refers to the damping rate under hot-fire conditions, $\langle S \rangle$ is the volume integrated Rayleigh source term, $\langle E \rangle$ is the acoustic energy density integrated over the volume. This equation is valid only when the oscillations have reached a limit cycle. The individual expressions for $\langle S \rangle$ and $\langle E \rangle$, along with their derivation, are given in Vignat (2020) & Durox et al. (2009) and are not provided here. After a few calculations one may finally express the damping rate in terms of spectral densities as:

$$\alpha_H = (\gamma - 1)\frac{\mathrm{Re}(S_{p'\dot{Q}'})}{S_{p'p'}V} \tag{6.3}$$

where $S_{p'\dot{Q}'}$ is the cross power spectral density between chamber pressure and heat release rate, $S_{p'p'}$ is the power spectral density of the chamber pressure, both obtained at the fundamental frequency of a limit cycle oscillation, and V is the chamber volume. This expression is employed to obtain the damping rate using the experimentally determined SSO described in Section 6.3. Results are shown in Fig. 6.7 (b) for the different swirlers at various lengths. The uncertainty in this damping estimate is not well known but is approximately considered to be about 10% (indicated by error bars). This does not preclude the analysis that will be carried out in the upcoming section, and it may be treated as a means to incorporate the variability that characterizes the experimental measurements of damping rates. The damping rate under hot conditions is two to three times larger than the damping rate under cold flow operation. The changes observed are partially linked to the variations in the resonance frequency. As this method

is valid only for a limit cycle oscillation, the damping rate cannot be obtained for oscillations corresponding to a marginal instability (for example, at $l_c = 265$ and $365\,\mathrm{mm}$ for swirler 712 and at $l_c = 215$ and $465\,\mathrm{mm}$ for swirler 716).

6.7 Low-order theoretical analysis

A simplified theoretical analysis is now carried out to help understand the self-sustained instability observations. This can be done, for instance, by defining unstable bands in the FDF phase diagram using linear stability analysis. One may do this by employing the traditional three-cavity analysis considering closed-open boundary conditions with an acoustically-transparent injector. This will result in an unstable band of $\pi < \varphi_F < 2\pi$, mod$[2\pi]$ (Schuller et al. 2020) for the first axial mode. If the first of these bands is considered with swirler 716, for example (see Fig. 6.5c right), then the possible unstable frequencies would only lie between $580\,\mathrm{Hz}$ and $880\,\mathrm{Hz}$, and this is at variance with the observed oscillation frequencies, which are much lower ($400\,\mathrm{Hz}$ to $530\,\mathrm{Hz}$, as shown in Fig. 6.4). It is then natural to use the theoretical formulation, described in Chapter 5 in which the injector is explicitely represented by its impedance. The model uses two cavities—one representing the injector outlet with an impedance boundary condition defining the injector's acoustic response, and the other representing the combustion chamber open to the atmosphere. The dispersion relation derived in the previous chapter is:

$$\frac{S_1}{\rho_1 c_1 \rho_3 c_3}\cos(k_3 b)\sin(k_2 a_b) + \frac{\widehat{\mathcal{F}}\Gamma S_1}{\rho_1 c_1 \rho_2 c_2}\sin(k_3 b) + \frac{S_1}{\rho_1 c_1 \rho_2 c_2}\cos(k_2 a_b)\sin(k_3 b) - \frac{i\zeta S_2}{\rho_2 c_2 \rho_3 c_3}\cos(k_2 a_b)\cos(k_3 b) + \frac{i\zeta S_2}{\rho_2^2 c_2^2}\sin(k_2 a_b)\sin(k_3 b) = 0 \tag{5.11 Rep.}$$

The above equation is numerically solved to determine the growth rates and oscillation frequency in the following section. The values of ρ and c in each section correspond to the following temperatures $T_1 = 293\,\mathrm{K}$, $T_2 = 573\,\mathrm{K}$, and $T_3 = 900\,\mathrm{K}$. The value of T_3 here is much lower than the burnt gas temperature $T_b = 2100\,\mathrm{K}$, as the former value is an estimation of mean temperature in the chamber. This was approximately determined in a steady state experiment by coating the inner wall of the quartz tube with a thermochromic paint (MC153-14 from *TMCHallcrest* adapted to a temperature range of 160 to $1240\,^\circ\mathrm{C}$).

6.7.1 Model predictions

A necessary condition for instability is that the growth rate be positive, i.e., $\omega_i > 0$. This defines an instability band that is shown as a band in gray in Figs. 6.8 and 6.9. In addition to this, it is also necessary that the growth rate exceeds the

damping rate to sustain instability. Solving the dispersion relation (Eq. 5.11) provides this growth rate and the expected oscillation frequency, but it requires two parameters as input, the gain and phase of the FDF, which depend on frequency. Therefore an iterative process is used to solve the dispersion relation until convergence is reached on the predicted frequency. The experimentally measured FDFs shown in Section 6.4 display a dependence on the velocity fluctuation level $u'_{c,r}/\overline{u}_{c,r}$ in addition to the frequency, which adds more complexity to obtaining the solution. Hence for simplicity, the dispersion relation is solved using a flame transfer function framework (without taking the fluctuation level into account) as a first step. For this purpose, FDF gain and phase values shown in Fig. 6.5 are averaged over the fluctuation level at each frequency (obtaining $G_{F,\text{avg}}$ and $\varphi_{F,\text{avg}}$).

Figure 6.8 shows the roots of the dispersion relation when gain G and phase φ are taken as independent parameters (not measured) for a chamber length $l_c = 365\,\text{mm}$ for the three swirlers. It also graphically illustrates the procedure to solve the dispersion relation. Firstly, one chooses an arbitrary value for the gain, say $G = 1$ (green curves on the top row of Fig. 6.8), and plots the roots of the dispersion relation as a function of an arbitrary phase φ. The intersection with the curve $\varphi_{F,\text{avg}}(f_r)$ (blue curve in the top row of Fig. 6.8) then gives an initial value of oscillation frequency f_r (represented by the downward arrow in Fig. 6.8). This frequency is then used to obtain a new gain from the transfer function (averaged FDFs), and the dispersion relation is solved to obtain a new oscillation frequency. The above process is repeated until convergence is reached with respect to the oscillation frequency . The final gain (dotted black curve in Fig. 6.8) and phase at this converged frequency is used to obtain the growth rate (bottom row in Fig. 6.8 indicated with a downward arrow).

One may now compare the model predictions with the observations of SSOs. This is done in Figs. 6.9 and 6.10. Two conditions need to be satisfied for instability to occur. In the first, the predicted point should fall inside the instability band. The growth rate then is positive so that the system will be potentially unstable. In addition, the predicted growth rate must exceed the damping rate. Figure 6.9 compares the calculated instability bands with results from experiments to verify the first condition. The symbols represent experimental SSO data from Section 6.3. The frequencies correspond to the peaks of the spectra in Fig. 6.3 and the phase $\varphi_{F,\text{avg}}$ is obtained using an average of the FDF phase plots from Fig. 6.5, shown as blue dotted lines. For each of these experimental data points, the instability band for the corresponding length and swirler is obtained by solving the dispersion relation and shown in gray. The position of the unstable band notably depends on the injector impedance and, more specifically, on its phase φ_ζ. The band location substantially differs from the standard position corresponding to a quarter wave mode coupling $[\pi, 2\pi]$ (Schuller et al. 2020; Poinsot and Veynante 2012). When the experimental data point falls within the instability band (as is the case for the

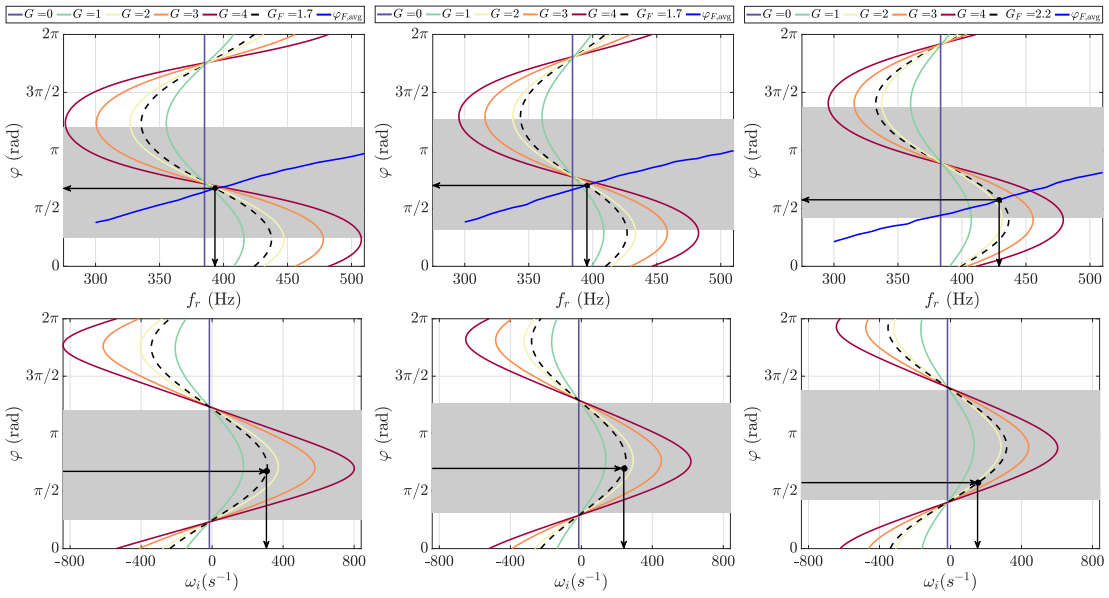

(a) 707 (b) 712 (c) 716

Figure 6.8. *Frequency and growth rate prediction from the model for different gains and phases at* $l_c = 365\,\mathrm{mm}$. *The unstable band is defined when* $\omega_i > 0$ *and indicated by the gray bands. The dotted black curve corresponds to the final gain of FDF* G_F *and the black dot is the point where it intersects the final phase* ($\varphi_{F,avg}$). *The converged frequency and growth rate prediction are obtained at this point. The arrows show the direction of obtaining a value from the graphical solution.*

three swirlers at $l_c = 365$ mm), the model predicts a positive growth rate, and the system is potentially unstable. Conversely, when the point falls outside the instability band, the model predicts a negative growth rate, and the system will be stable. It can be seen that the predictions are mostly confirmed by experiments since all unstable points fall well within the predicted instability bands. It is also instructive to compare the instability bands with the evolution of the phase curve. For example, the model predicts that swirler 716 is unconditionally stable for any frequency below $375\,\mathrm{Hz}$ and that swirler 712 is also unconditionally stable above $600\,\mathrm{Hz}$. In Fig. 6.9, the dark gray bands with black outlines represent the points where the impedance is experimentally measured (definite prediction). For the points where the impedance is not measured, the nearest neighbor value is used to obtain the solution, and the predicted unstable band is shown with a lighter shade of gray (approximate prediction). This procedure is admittedly a limitation, but if the frequency is close enough, the impedance might be expected not to vary much.

As mentioned earlier, a positive growth rate only indicates potential instability but is not enough to predict whether the system is effectively unstable. For this purpose, one must check if the predicted growth rate is higher than the damping rates determined in Section 6.6. Figure 6.10 reports the predicted instability

frequencies and growth rates for all investigated cases. Points that fall outside the instability bands are marked as stable. Points that fall within the instability band but for which the damping rate is unavailable or is higher than the predicted growth rate are dubbed “potentially unstable". The former ones are the points that correspond to a marginal instability in SSO (refer Fig. 6.4) and where the hot-fire damping rate cannot be obtained. Points that fall inside the band and for which the growth rate exceeds the estimated damping rate are unstable. Note that in Fig. 6.9, the symbols correspond to the experiments, whereas in Fig. 6.10, they correspond to the prediction from the model. On comparing the predicted stability map with the experimental stability map (Fig. 6.4), one can see that the model predicts all the stable and most of the unstable operations. It can be seen from Fig. 6.10 that the growth rate exceeds the damping rate (typically of the order of 150 to $350\,\mathrm{s}^{-1}$), indicating the growth of oscillations at most unstable points, except two (712 at $465\,\mathrm{mm}$ and 716 at $365\,\mathrm{mm}$). However, the growth rate at these points is still fairly close to the lower limit of the damping rate. The marginally unstable points from the experiments cannot be predicted accurately, and only a potential instability can be speculated. The lack of experimental impedance and definite damping rate estimate and analysis based on a linear approach can contribute to the inexact prediction of such points. At the two smaller lengths ($115\,\mathrm{mm}$ and $165\,\mathrm{mm}$), experimental FDF data are not available beyond $800\,\mathrm{Hz}$ to make an exact prediction. However, if one linearly extrapolates the phase, the resonant frequencies that can

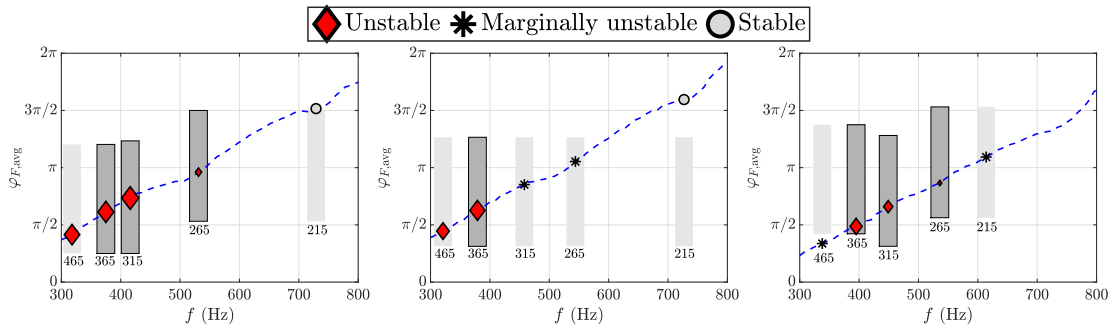

(a) 707 *(b) 712* *(c) 716*

Figure 6.9. *Instability bands (marked in gray) predicted by the model are shown at self-sustained oscillation (SSO) frequency for the three swirlers. The combustion chamber length l_c is quoted under each band in* mm. *The dark gray bands with black outlines correspond to a definite prediction and the light gray bands refer to an approximate prediction. For the unstable points (black diamonds with red shading), the size of the marker is proportional to the RMS chamber pressure p_{rms}. The blue dotted line represents the phase of the FDF averaged over the fluctuation level $\varphi_{F,avg}$. The theoretical model provides unstable bands while the FDF phase and the stability of the system are obtained from experiments (also shown in Fig. 6.4).*

be expected for these two lengths in hot conditions would lie outside the band giving a stable prediction. The frequency predicted by the model is close but almost always has a difference of $\pm 20\,\mathrm{Hz}$ compared to the experimental measurement of SSO.

In the method described here, an average gain and phase of FDF are considered to remove the dependence on the fluctuation level. This iterative process can also be extended to deal with the dependence of FDF on the input level $u'_{c,r}/\overline{u}_{c,r}$ and is exemplified in Section 6.7.2 for swirler 716.

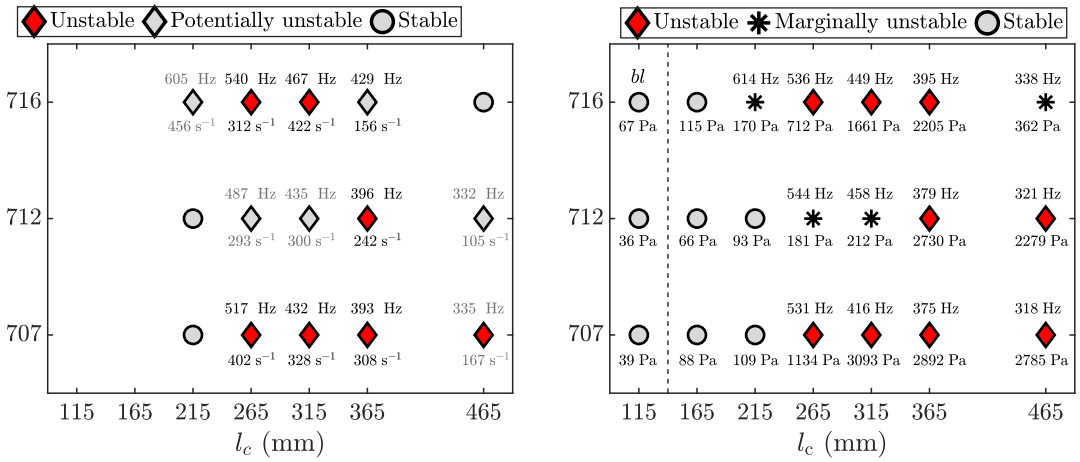

(a) Prediction *(b) Experiment*

Figure 6.10. *(a) Prediction obtained from the model at different chamber lengths l_c. The predicted frequency and growth rate are indicated when the prediction points to an unstable operation. Black font colors are marked to show a definite prediction from the model, whereas gray font colors show only an approximate prediction. The gray circles represent the stable points, gray diamonds represent the potentially unstable points, and red diamonds represent the unstable points. (b) Experimentally obtained stability map duplicated from Fig. 6.4.*

6.7.2 Model prediction at different $u'/\overline{u}$

The theoretical model to consider the measured FDF at different $u'/\overline{u}$ (same as $u'_{c,r}/\overline{u}_{c,r}$ in Section 6.4) for limit cycle prediction is demonstrated here. The process involves applying the iteration procedure presented in Section 6.7.1 for every input level $u'/\overline{u}$ of the FDF. One can then predict the growth rate and frequency of oscillation as a function of the input level. These two quantities are plotted in Fig. 6.11 for the swirler 716 at two chamber lengths $l_c = 265$ and $315\,\mathrm{mm}$. Swirler 716 is chosen as its FDF exhibits sufficient difference with respect to the input level, whereas, for swirlers 707 and 712, considering an average FDF is still reasonable as the FDFs do not vary much with respect to the input level in the available data range. Figure 6.11 shows the changes in growth rate ω_i in the

top row as the relative velocity fluctuation level is augmented. These figures also indicate the level of damping α_H (shown as a band to represent uncertainties) under hot-fire conditions estimated in Section 6.6. A limit cycle oscillation may be expected when $\omega_i \simeq \alpha_H$. For a chamber length $l_c = 265$ mm, the limit cycle corresponding to this condition implies a level of velocity fluctuation $u'/\overline{u}$ that is of the order of 0.1. On comparing with the experimental measurement at this length, $(u'/\overline{u})_{SSO} \approx 0.06$ which is close to the predicted oscillation level. For $l_c = 315$ mm, the crossing point between ω_i and α_H is slightly outside the range where the FDF was measured, but the value of $u'/\overline{u}$ may be extrapolated and is 0.32. In comparison with the measurements, the fluctuation level is $(u'/\overline{u})_{SSO} \approx 0.14$, which is much lower than the prediction. While the predicted frequency is close to that found experimentally, the predicted level of velocity oscillation is twice that observed during SSO. This discrepancy could be attributed to the linear extrapolation of $u'/\overline{u}$, which might not be adequate.

Using the predicted fluctuation level, one may try to estimate the frequency at limit cycle, the evolution of which is shown in the bottom row of Fig. 6.11. The frequencies at limit cycle are predicted to be $f_{LC} = 540$ and 453 Hz, respectively, at $l_c = 265$ and 315 mm, which agree with the experimental values of 536 and 449 Hz (refer to Fig. 6.4 or Fig. 6.10 (b)).

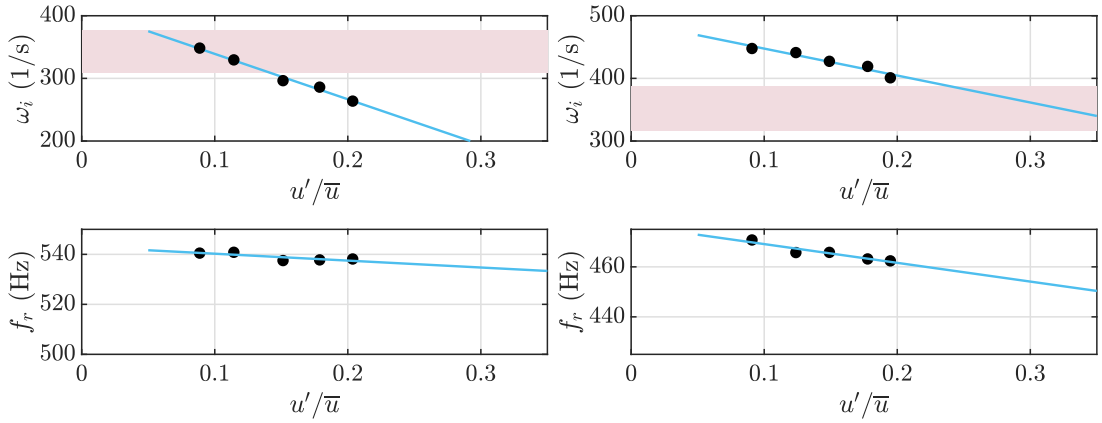

(a) $l_c = 265\,\mathrm{mm}$ (b) $l_c = 315\,\mathrm{mm}$

Figure 6.11. *Prediction of growth rate and frequency at different $u'/\overline{u}$ for swirler 716. The red band shows the calculated damping under hot-fire conditions α_H described in Section 6.6 with an uncertainty of 10%. The black circles indicate the prediction by the model at different $u'/\overline{u}$, while the solid blue line shows a linear fit applied to these points.*

6.7.3 Model implications

Figure 6.9 reveals that the position of the unstable band changes with the swirler and with the combustion chamber length (in other words, with the instability frequency). This is because the unstable bands are solely determined by

the phase φ_ζ imposed by the injector impedance at the entrance of the combustion chamber and this changes with the swirler and frequency. The impedance modulus G_ζ determines the growth rate magnitude. A smaller impedance modulus results in a broader evolution of growth rate and frequency with respect to the phase of the FDF. On revisiting the question raised at the beginning of the section on why the standard instability band of $\pi < \varphi_F < 2\pi$ does not work for the instability prediction in the present case, it can be seen that this is due to the changes in phase imposed by the injector unit between the pressure and local velocity disturbances. The instability band of $\pi < \varphi_F < 2\pi$ works if the velocity is in quadrature with respect to the pressure i.e., $\varphi(u', p') = 3\pi/2$ as considered by Noiray et al. (2009b) & Schuller et al. (2020). Such a band cannot be used for modeling the injectors considered in the present study because these elements define impedance at the combustion chamber inlet that does not correspond to such a quadrature. It is then important to have a good model for the injector impedance or to use an experimentally determined impedance. The injectors employed in this study are not acoustically transparent, resulting in a certain degree of decoupling between plenum and chamber. Such a decoupling has been observed in a previous study with these injectors on the annular test rig MICCA-Spray (Prieur et al. 2018), where the observed instability is mainly a chamber mode decoupled from the plenum.

The injector outlet impedance is deduced from measurements during SSO in this work. This is not completely satisfactory since, logically, it would be necessary to use a measurement that is independent of the SSO. In addition, the impedance is only obtained at discrete frequencies where limit cycle oscillations exist, hampering predictions over the entire frequency range of interest. One could use a downstream modulation of the flame in the frequency band of interest by measuring pressure near the chamber backplane and velocity fluctuations at the outlet. This kind of modulation was, however, not feasible in the present experimental setup. Despite this limitation in the experimentation, the knowledge of impedance derived from SSO, even at discrete frequencies, allows a good prediction of the instability bands and, therefore, validates the modeling strategy. The impedance does not significantly vary with the type of swirler and the oscillation frequency, but these changes are sufficient to move the unstable band. For all the tests carried out in this study, the modulus of the impedance is of the order of 0.5, and the phase is between $3\pi/4$ and π. With an injector roughly identical to those in the present study and with a downstream modulation by acoustic waves transverse to the flame, Patat et al. (2021) obtain similar phase shift values. Alternatively, a simple theoretical analysis of the behavior of injectors with significant pressure drops can be done to estimate the impedance phase. It is possible to consider that the injector operates in a quasi-steady regime. The calculations show that the real part of the impedance is negative and generally larger than the imaginary part.

One may then express $\zeta = \zeta_r + i\zeta_i$ with

$$\zeta_r = -\kappa \overline{u} \sigma / c \tag{6.4}$$

In this expression, σ designates the head loss parameter, and κ is a coefficient of the order of one. It is less easy to obtain an expression for ζ_i, but it is possible to infer from the data that $|\zeta_i| << |\zeta_r|$ so that the phase angle φ_ζ is generally close to π.

The experimental measurements presented here and the subsequent modeling approach feature certain limitations. For example, the impedance measurement is performed in two steps: one with a metal ring to measure pressure signals and the other with a quartz chamber to obtain velocity fluctuations. This sort of approach might change the thermal environment at the flame base, resulting in a small error in the measured impedance. Although this variation is expected to be minor, as shown in Appendix 1 of Chapter 4, this could induce some uncertainties, especially near the limits of the unstable band. The model also uses a linear approach that cannot distinguish marginally unstable points. The other limitation is in the prediction of limit cycle amplitude. Even though an estimate of hot-fire damping was obtained with the energy balance method, there exists an uncertainty in this estimation, making it difficult to predict the oscillation amplitude at the limit cycle. There is also a limitation of the modulation system to reach a fluctuation level $(u'/\overline{u})$ similar to those found at the limit cycle. As a consequence, the FDF data do not cover the full range of relative velocity fluctuations that may arise in the system. Although the present modeling has limitations, it nevertheless highlights the importance of injector impedance on the instability of the system calling for further studies aimed at identifying the role of injector dynamics and modeling injector impedance, which is planned in the future work following this thesis.

6.8 Conclusions

Experiments and theoretical modeling reported in this article underline the importance of the injection unit in combustion instability analysis. The present investigation considers seven combustion chamber lengths and three different swirlers with a fixed geometry of the upstream manifold and the injector unit. Experiments are conducted under the same operating conditions with liquid heptane as fuel delivered as a spray by a hollow cone atomizer. The major findings from this chapter are as follows.

(1) Systematic experiments indicate that the regimes of instability for the three swirlers do not occur for the same chamber length and that they also differ in peak frequency and limit cycle amplitude levels.

(2) Results show that the phase of the FDF is relatively insensitive to the ampli-

tude level but that the phase curves corresponding to the three swirlers are distinct. The gain of FDF remains in the linear regime even up to a fluctuation level of 35% for two of the swirlers having the same swirl number and different pressure losses. For the swirler with the highest value of swirl number and pressure drop, the gain changes substantially with the fluctuation level beyond $500\,\mathrm{Hz}$ but remains in the linear regime in the low frequency range.

(3) It is next indicated that the standard modeling approach that uses acoustically coupled cavities in closed-open conditions cannot explain the observed instability regimes. In the case of injection units that have a significant pressure drop and are therefore acoustically weakly transparent, it is necessary to represent the injector outlet with a specific impedance. A low-order modeling approach combining the measured injector impedances and flame describing functions (FDFs) developed in Chapter 5 can then be used to explain the experimentally observed behavior, and obtain an estimate for the growth rate and frequency of instability. The instability bands deduced from this model markedly differ from the classical ranges $[\pi,\, 2\pi]$ mod 2π by an offset of more than $\pi/2$. By further combining the model with damping rate estimates, predictions can also be derived for limit cycle amplitudes.

In summary:

- The injector imposes a specific impedance at the chamber inlet, which displaces the bands of instability in a way that depends on the swirler characteristics.
- It defines the flame geometry and its dynamics, and this is reflected in changes in the FDF gain and phase functions. These changes, together with those observed in the injector impedance, determine whether an operating point belongs to a band of instability.
- It contributes to the damping rate. The levels induced by the different swirlers and deduced from resonance experiments under cold flow conditions change, and the relative difference between injectors may reach up to 20%. The cold flow damping rates are, however, found to be a fraction of those estimated under hot-fire conditions using an energy balance method.

The admittedly simplified modeling approach highlights the importance of injector impedance on stability and allows to retrieve most but not all of the instability features observed in the systematic experiments described in this chapter.

Chapter 7

Influence of injectors on annular combustion dynamics: MICCA-Spray

Contents

This chapter is accepted for publication as a full-length article at the ASME Turbo Expo 2022 after peer-review with the title "Azimuthal instabilities of an annular combustor with different swirling injectors" by Preethi Rajendram Soundararajan, Daniel Durox, Antoine Renaud, Sébastien Candel and recommended for publication in the Journal of Engineering for Gas Turbines and Power. It includes additional appendices with supplementary data. The experimental setup described in Section 7.2 is already discussed in Chapter 1 and familiar readers can skip this part.

Experiments are carried out on the laboratory-scale MICCA-Spray annular combustor to examine the effects of swirlers on combustion instabilities. This system comprises sixteen spray-swirl injectors and gives rise to instabilities coupled by azimuthal modes. Five swirlers producing clockwise rotation and varying in swirl numbers and pressure drops are considered. These swirlers can be broadly categorized into two groups, lower-swirl, and higher-swirl groups, based on their swirl numbers. An arrangement where clockwise and counterclockwise swirlers alternate is also studied. Experiments are performed systematically with liquid heptane at five levels of thermal power and six equivalence ratios. Results reveal that none of the swirlers in the lower-swirl category exhibit instability in the operating region considered, whereas the higher-swirl units feature strong azimuthal instabilities that trace an overall limit cycle envelope with a few short and random bursts. Among the higher-swirl group, a higher pressure drop swirler is associated with a broader instability map. This shows that the transition to instability mainly depends on the swirl number through its effect on the flame structure, and the pressure drop adds to further variations in amplitude and frequency of oscillation. The spin ratio time series indicate that the modes are of mixed type and that its distribution depends on the operating condition. On specifically comparing the spin ratio distribution between a full set of clockwise rotating (CR) swirlers and a configuration where clockwise and counterclockwise rotating (CCR) swirlers are alternatively placed, it is found that there is no definite statistical preference for spin ratio linked to the effect of bulk swirl. In some cases, however, the CCR configuration promotes a broader distribution of spin ratios centered around the standing mode ($s = 0$), while the CR setup favors azimuthal modes spinning in the counterclockwise direction. An attempt is made to interpret the occurrence of instabilities by making use of flame describing functions (FDFs) measured in a single-injector combustor. It is found that the FDFs corresponding to the two swirler categories (lower-swirl and higher-swirl) are relatively distinct. The observed behavior is tentatively interpreted using an instability analysis in which the injector and upstream plenum are represented by an impedance that shifts the band of instability. The unstable behavior is then linked to the relative position of the FDF phase with respect to the instability band in the frequency range corresponding to the expected azimuthal mode frequency. The phase and gain of the FDF notably depend on the swirl number, and it is possible to distinguish, for the present configuration, a category of low swirl number injectors inducing stable operation and another category of high swirl number units leading to oscillations.

7.1 Introduction

Combustion instabilities have been the subject of an intense research effort (Mongia et al. 2003; Lieuwen and Yang 2005b), with much of the more recent work focused on gas turbine applications. In these systems, the combustor geometry is mostly annular, and the coupling modes are predominantly azimuthal (Poinsot 2017). It is generally considered that these modes are the most dangerous because they are less well-damped and also because they correspond to the lowest eigenfrequencies where flames are most sensitive to disturbances. These azimuthal modes, in turn, induce axial velocity fluctuations in each injector (Staffelbach et al. 2009), a process that dominantly leads to heat release rate fluctuations. Experiments carried out on lab-scale and industrial annular combustors (Worth and Dawson 2013a; Prieur et al. 2017; Rajendram Soundararajan et al. 2021; Aguilar et al. 2021), numerical simulations (Pankiewitz and Sattelmayer 2003; Staffelbach et al. 2009; Wolf et al. 2012; Wolf et al. 2012; Laera et al. 2017), and theoretical analysis (Parmentier et al. 2012; Ghirardo and Juniper 2013) have provided a wealth of information on azimuthal coupling. Other investigations aim to develop active and passive control techniques (Steele et al. 2000; Annaswamy and Ghoniem 2002; Noiray et al. 2009a; Krishnan et al. 2021) to reduce such instabilities. This article is specifically concerned with effects related to the swirling injector. The injector unit (Huang and Yang 2009; Candel et al. 2014) is known to determine the flame structure and dynamical characteristics, and it is important to document its influence on azimuthal combustion instabilities. This could help unravel the mechanisms of instabilities associated with swirling injectors and might, in turn, help identify injector architectures that are less sensitive to disturbances and less prone to instabilities.

Before moving further, it is worth considering some of the past research efforts carried out on annular combustors and the influence of swirler on acoustic instabilities to give a context for the present work and identify the existing knowledge gap. A large eddy simulation (LES) of a full aeronautical combustor was carried out by Wolf et al. (2012) to capture the azimuthal modes of this combustor. Results revealed that the amplitude of azimuthal modes varies with time, resulting in pressure fluctuations changing between purely standing and spinning modes. It was also found that the presence of a bulk swirling convection velocity resulted in slow rotation of the standing mode. The effect of injector spacing on instabilities was analyzed by Worth and Dawson (2013a) and Worth and Dawson (2013b) on an annular combustor with flames stabilized by a bluff body. The time evolution of the pressure variations indicated repeated switching between standing and spinning modes, similar to Wolf et al. (2012). It was found that for larger separation distances between injectors, each flame unit behaved independently and adopted a helical structure of heat release rate. The effect of bulk swirl motion on instabilities was investigated in Worth and Dawson (2013a). The configuration with al-

ternating swirl directions resulted in statistically preferred standing modes, while for the arrangement where all swirlers rotated in the same direction, the statistical preference depended on the operating conditions considered and the direction of spin dominantly depended on the bulk swirl direction. Early studies were carried out with matrix burners in the lab-scale annular combustor MICCA. Several pure azimuthal modes, such as standing, spinning (Bourgouin et al. 2015a), and slanted (Bourgouin et al. 2015b) modes, were observed in this system. Experiments were also carried out on this combustor to identify the effect of symmetry breaking by partially blocking the injectors or changing their geometry (Aguilar et al. 2021).

At this point, it is also useful to identify the role of the injection units in the mechanism leading to combustion instabilities. Several studies indicate the presence of a strong interaction between the flow behavior in a swirl combustor and combustion instability (for example, Steinberg et al. (2012)). This reveals a possibility of developing control techniques by altering the flow structures (Paschereit et al. 2000) through modification of the swirler geometry. Few researchers have pursued this, but such studies are limited only to simplified single burner test rigs. For example, the effect of inlet swirl number was studied by Huang and Yang (2005) using LES, and it was observed that strong swirling flows resulted in transverse acoustic oscillations, whereas with weak swirl, longitudinal instabilities prevailed. Komarek and Polifke (2010) attempted to identify the effect of swirl number fluctuations by varying the axial position of the swirl generator. Through the combination of experiments and numerical simulations, it was observed that the position of the swirl generator has a strong impact on the flame's dynamical response. Another study that considered the effect of swirl number was reported by Kim (2016). Experiments with two different swirl numbers indicated that the normalized pressure and heat release rate oscillations were more intense in the stronger swirl number case than in the weaker swirl configuration. Recently, Zhang et al. (2021) performed LES on a premixed swirl-stabilized combustor and found changes in the regions of instability depending on the swirl number value. It was noted that the corner recirculation zones played a major role in inducing heat release rate fluctuations compared to the central recirculation zone. Apart from the dependence on swirl number, the work carried out by Vignat et al. (2019) revealed the effect of swirler pressure drop on combustion instabilities. A recent study by Rajendram Soundararajan et al. (2022) in a single-injector combustor shows that the longitudinal self-sustained instabilities strongly depended on the swirler type used. A low-order model based on injector impedance using flame describing function (FDFs) was also shown to predict these instabilities. FDFs from single-injector systems have also been used to successfully predict the instabilities of annular combustors equipped with matrix burners featuring laminar flames (Laera et al. 2017).

The above review shows that the swirler effect on instabilities has been inves-

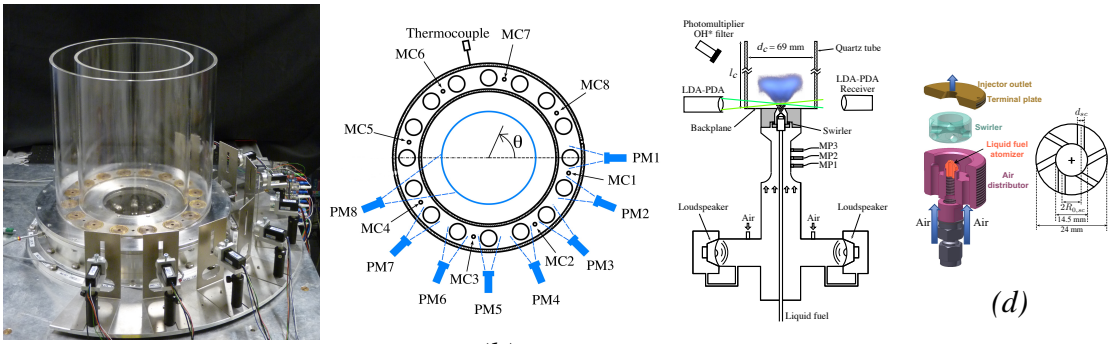

(a) (b) (c) (d)

Figure 7.1. *(a) Photograph of the MICCA-Spray setup. The height of the combustion chamber is maintained at* 400 mm *for both the inner and the outer chamber walls. (b) Schematic top view of the combustion chamber showing the locations of chamber microphones (MCx) and photomultipliers (PMx). The azimuthal angle* θ *is positive along the counterclockwise direction, and its baseline is taken along the centerline of injector 1. (c) Schematic diagram of complementary single-injector setup SICCA-Spray. (d) An exploded view of the injector unit with its various components together with a schematic drawing of the swirler.*

tigated in single-injector combustors, but to our knowledge, such studies have not been carried out in annular combustors. The current investigation would thus help in bridging several knowledge gaps. (1) What happens when the swirl number and pressure drop of the injector unit are systematically varied in an annular combustor? Such knowledge would help develop swirlers that are less susceptible to instabilities. (2) What happens to the modal structure in a configuration where co- and counter-rotating swirlers are alternating compared to a configuration where all the swirlers are co-rotating? (3) Can a simplified single-injector setup capture some of the features exhibited by the multi-flame annular combustor where there are flame-flame interactions?

Experiments reported in this chapter address the above questions by systematically documenting instabilities in the lab-scale MICCA-Spray annular combustor. The setup is presented in Section 7.2. Stability maps of the annular combustor with the various swirler configurations are presented in Section 7.3, followed by a discussion of the modal structure between a fully co-rotating configuration and an alternate co- and counter-rotating configuration (Section 7.4). Results from a complementary single-injector setup, SICCA-Spray, with the various swirlers are finally presented in Section 7.5, along with a discussion on how they can help analyze the instabilities observed in the annular system. Two appendices are included at the end of this chapter. Appendix 1 is concerned with the FDF phase evolution at a higher equivalence ratio, and Appendix 2 proposes a detailed comparison of spin ratio distributions between co- and counter-rotating swirlers when operating with premixed propane and air or with liquid dodecane delivered as a spray.

7.2 Experimental setup of MICCA-Spray

The experimental setup of the lab-scale annular combustor MICCA-Spray is shown in Fig. 7.1 (a) & (b). Only the main features of the test rig are described here, and the readers are referred to Chapter 1 for a more detailed description. The test rig consists of an annular plenum connected to the annular combustion chamber through sixteen swirling injectors (exploded view shown in Fig. 7.1 (d)). In the present study, liquid heptane is used as fuel and is delivered into the chamber through a simplex atomizer mounted on the injector. The atomizer is mounted inside the injector at the nominal distance of $6.75\,\mathrm{mm}$ from the backplane and disperses finely atomized fuel droplets as a hollow cone spray in the presence of air flow. The MICCA-Spray chamber consists of two concentric, cylindrical quartz tubes of height $400\,\mathrm{mm}$. Eight Brüel & Kjær microphones are mounted on the chamber (marked as MCx in Fig. 7.1 (b)). These microphones are placed on waveguides whose ports are flush-mounted on the chamber backplane to prevent direct contact of the microphones with the hot chamber environment. The microphone signals are acquired at a sampling frequency of $f_s = 32,768\mathrm{Hz}$ for a total time period of $T_0 = 16\,\mathrm{s}$.

For the present study, five different radial swirlers featuring six tangential channels are tested. The swirlers are named 707, 712, 716, 726, and 727, and their characteristics are recalled in Tab. 7.1. The swirlers can be grouped into two categories based on their swirl number: the lower-swirl category comprising swirlers 707 and 712, and the higher-swirl category comprising the rest of the swirlers. Each group also includes swirlers with the same swirl number values, but different pressure drops. The swirlers 707 and 712 have nearly the same swirl number, but their pressure drop values are not identical. Among the higher-swirl category, the swirlers 726 and 727 have the same swirl numbers but a slightly different pressure drop, while the swirlers 716 and 727 have almost the same pressure drop, but 727 has a slightly higher swirl number. In addition to the five swirling injectors, a combination of clockwise rotating (716-type) and counterclockwise rotating (namely, 816) swirlers are placed alternatively to understand the effect of overall bulk swirl on instabilities. Swirler 816 is completely identical to swirler 716 except in the swirl direction.

7.3 Stability map of MICCA-Spray annular combustor

The stability map of the MICCA-Spray annular combustor is obtained by considering five levels of thermal power $\mathcal{P}$ and, at each level, operating at six different equivalence ratios ϕ, resulting in a total of thirty data points per swirler. At each operating point, the fuel flow rate is fixed, and the air flow rate is systematically

Table 7.1. *Swirler characteristics measured under cold flow at an air flow rate of $\dot{m}_{air} = 2.6\,\mathrm{g\,s^{-1}}$ and $2.5\,\mathrm{mm}$ above chamber backplane. S_N represents the experimentally obtained swirl number and Δp represents the pressure drop of the injector. σ is the head loss coefficient defined by $\Delta p = \frac{1}{2}\sigma\rho_0 u_b^2$, where u_b is the bulk velocity at the injector exit and ρ_0 is the density. d_{sc} is the diameter of the swirler channels, and $R_{0,sc}$ is the distance between the axis of a channel and the axis of the swirler.*

Category	Swirler (-)	S_N (-)	Δp (kPa)	σ (-)	d_{sc} (mm)	$R_{0,sc}$ (mm)
Lower-swirl	707	0.60	3.65	3.33	4.0	4.6
	712	0.59	4.50	4.10	3.0	2.3
Higher-swirl	716/816	0.70	5.74	5.23	3.5	4.7
	726	0.74	6.00	5.47	3.5	5.5
	727	0.74	5.70	5.20	3.5	5.1

varied to obtain different equivalence ratios. The stability map of MICCA-Spray is represented in terms of two parameters, amplitude and frequency of instability, to suitably represent the first azimuthal-first longitudinal 1A1L modes exhibited in the assessed operating points. Considering a $e^{-i\omega t}$ time harmonic convention for the acoustic waves, at any instant t, the acoustic pressure measured by the chamber microphones can be represented as:

$$p'_c(\theta, t) = A^+ \exp(\mathrm{i}\theta - \mathrm{i}\omega t) + A^- \exp(-\mathrm{i}\theta - \mathrm{i}\omega t) \tag{7.1}$$

In this expression, p'_c represents the instantaneous pressure measured by the microphones, A^+ and A^- designate counterclockwise and clockwise spinning waves respectively of the 1A1L mode, $\omega = 2\pi f_i$ is the angular frequency, and θ is the azimuthal angle, which is considered positive in the counterclockwise direction. The instantaneous signals recorded by the eight chamber microphones can be used to determine the wave amplitudes A^+ and A^- and deduce an indicator of instability that is spatially averaged over the annulus and temporally averaged over the duration of acquisition (Rajendram Soundararajan et al. 2021). This amplitude, proportional to the root mean square (RMS) amplitude and independent of the structure of the unstable mode, is given by

$$\mathcal{A} = (|A^+|^2 + |A^-|^2)^{1/2} \tag{7.2}$$

$\mathcal{A}$ is used to compare the instability between the different swirlers along with the instability frequency f_i, which is the peak frequency from the power spectrum of

the microphone signals. The power spectral densities are obtained using Welch's periodogram method by considering 64 windows with 50% overlap between windows, resulting in a frequency resolution of $\Delta f \approx 2\,\mathrm{Hz}$. The microphone signals are bandpass-filtered between $500\,\mathrm{Hz}$ and $1100\,\mathrm{Hz}$, and the time-resolved analytical signals are obtained through the Hilbert transform. The wave amplitudes are then reconstructed up to the third order in azimuthal harmonics (Vignat et al. 2020).

In addition to comparing the amplitude and frequency of instability, the spin ratio s_r is calculated to identify the structure of the azimuthal instabilities and is given by,

$$s_r = \frac{|A^+| - |A^-|}{|A^+| + |A^-|} \tag{7.3}$$

A value $s_r = 1$ corresponds to a counterclockwise spinning wave, $s_r = -1$ represents a clockwise spinning wave, and $s_r = 0$ pertains to a standing azimuthal wave.

The behavior of the swirlers in the lower-swirl category (707 and 712) is special as they do not exhibit any azimuthal instability in the domain of interest ($\mathcal{P}$: 93-$118\,\mathrm{kW}$ and ϕ: 0.75-1.05), and the fluctuating pressure amplitude remains below $50\,\mathrm{Pa}$. On the contrary, all the swirlers in the higher-swirl category exhibit unstable behavior. Although the various swirlers have similar geometries, a minor change resulting in the reduction of swirl number improves the stability of the annular combustor. This study indicates that a critical value exists $0.6 < S_{Ncrit} < 0.7$ such that injectors with low swirl $S_N < S_{Ncrit}$ yield stable operation, while units with swirl numbers exceeding this critical value $S_{Ncrit} < S_N$ lead to oscillations in certain ranges of operating parameters. It is worth noting, however, that this categorization is specific to the present configuration and may not be generally applicable. For the different swirlers in the higher swirl category, stability maps representing the amplitude and frequency of instability are displayed in Fig. 7.2. The data obtained at the thirty operating points are interpolated to derive the stability maps plotted in this figure.

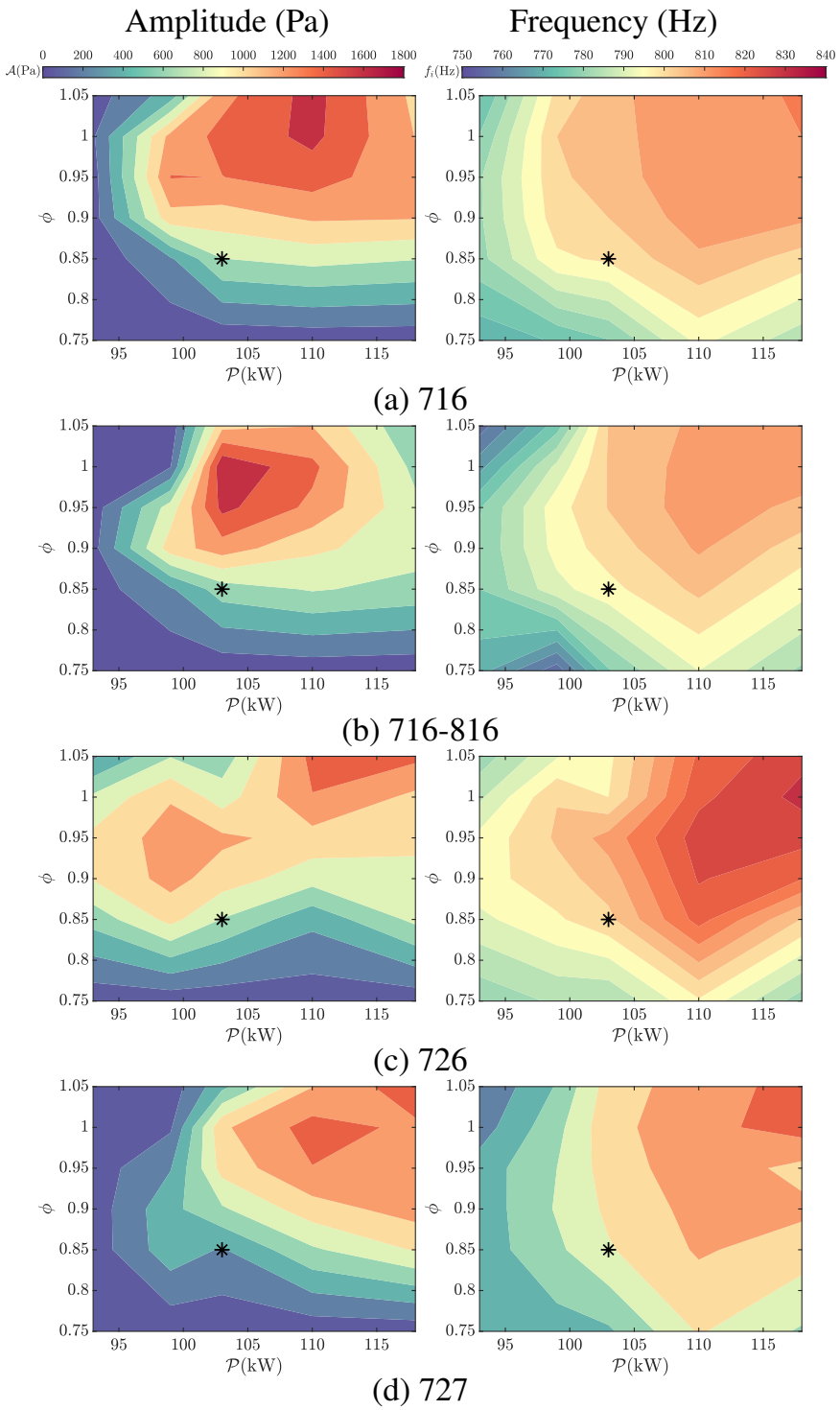

Figure 7.2. *Amplitude (left) and frequency (right) stability map of MICCA-Spray for the different swirlers in the higher-swirl category. The swirlers in the lower-swirl category (707 and 712) are always stable in the assessed operating zone and hence are not shown here. The black star on the stability map refers to the operating conditions of the complementary single-injector combustor described in Section 7.5.*

The measurements reported here were also repeated, and it was found that the stability contour shapes and their location were reproducible but with some differences in the amplitude levels caused by variations in the nature of the modes sustaining the instability. Overall, the swirlers exhibit gradual changes from stable to unstable states as the operating points are varied. On comparing the three swirlers in the higher-swirl category (716, 726, 727), minor variations in amplitude can be observed; the highest amplitude of instability is exhibited by swirler 716 ($\mathcal{A}_{\text{max}} \approx 1673\,\text{Pa}$) at $\mathcal{P} = 110\,\text{kW}$ and at slightly fuel-rich conditions ($\phi = 1.05$). This is followed by swirler 727, which exhibits a maximum amplitude of $\mathcal{A}_{\text{max}} \approx 1540\,\text{Pa}$ at $\mathcal{P} = 118\,\text{kW}$, also under slightly rich conditions, and then swirler 726, which reaches the maximum amplitude of $\mathcal{A}_{\text{max}} \approx 1460\,\text{Pa}$ at both $\mathcal{P} = 118$ and $110\,\text{kW}$ for slightly rich conditions. The amplitude stability map of 727 evolves like that of 716 (Fig. 7.2 (a) & (d) left), while it differs from the map of 726, which has the broadest instability region among the three swirlers, exhibiting instability even at the lowest power. The swirlers 727 and 716 possess the same pressure drop, which is slightly lower than the pressure drop of 726. This observation points to the dependence of instability amplitude on the pressure drop; a higher pressure drop for the same swirl number appears to widen the region of instability. The amplitude map of 726 contains two discrete high-instability zones (red zones in Fig. 7.2 (c) left), one occurring at higher power and slightly richer conditions and the other occurring at lower power and leaner equivalence ratio. Swirlers 716 and 727, however, exhibit continuous high-instability regions at higher equivalence ratios and are always stable at the lowest power. All the swirlers are stable at the lowest equivalence ratio of $\phi = 0.75$, irrespective of the thermal power.

On comparing the frequency maps, swirlers 716 and 727 feature similar values. But with 726, the frequencies are nearly $15\,\text{Hz}$ higher than those of the other two swirlers. The operating point where the instability frequency is highest occurs at $\mathcal{P} = 118\,\text{kW}$ and close to stoichiometry, a set of conditions yielding the highest adiabatic flame temperature and correspondingly the highest frequency of oscillation. It is indicated here that the results corresponding to swirler 716 are also reported in Chapter 9, where a comparison of instabilities with different fuels is presented.

It is also interesting to examine oscillations at some points in the unstable range to compare features exhibited by the different swirlers. A first point is characterized by $\{\mathcal{P} = 110\,\text{kW}\ \&\ \phi = 1.0\}$ while the second corresponds to $\{\mathcal{P} = 103\,\text{kW}\ \&\ \phi = 0.95\}$. The pressure-time traces recorded by four chamber microphones are shown in the top rows of Fig. 7.3, whereas the spin ratio evolutions are plotted in the bottom rows of this figure. The pressure signals feature an overall limit cycle envelope with small, random bursts. The spin ratio randomly switches between standing and spinning modes. Such a modal behavior was previously observed in large eddy simulations (Wolf et al. 2012) and in annular combustor experi-

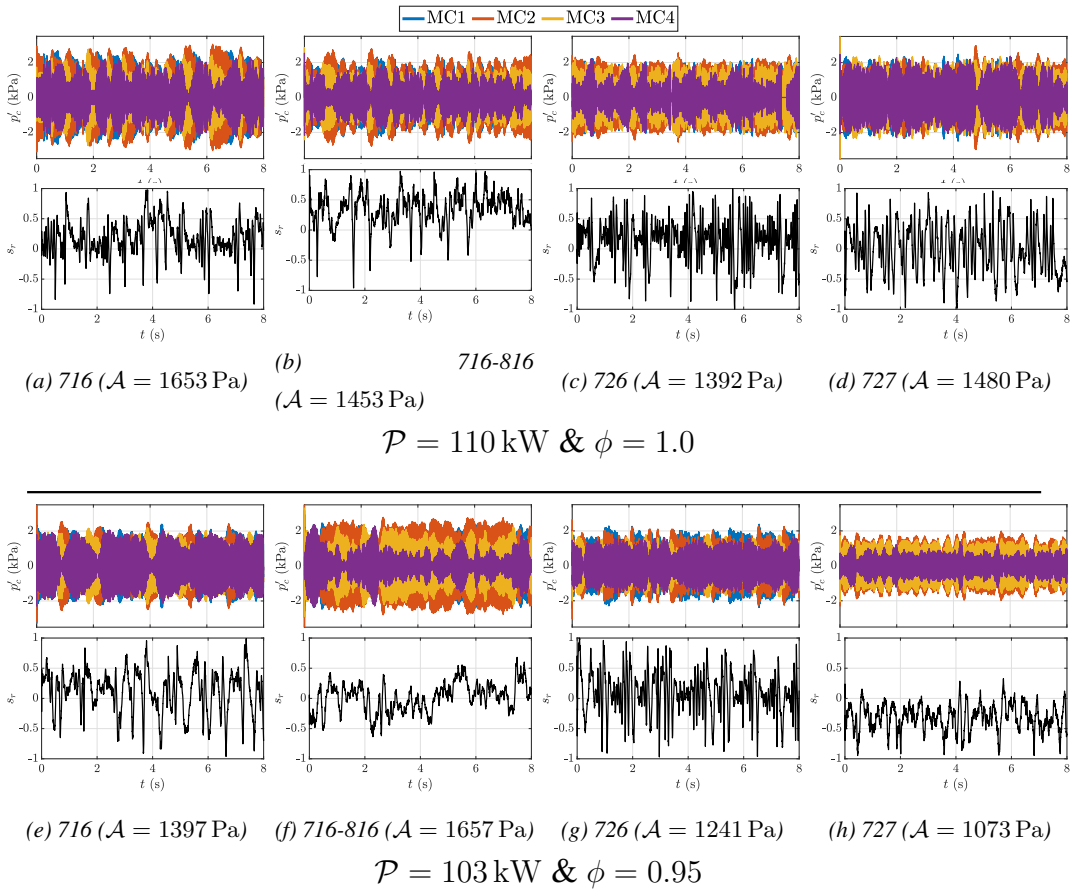

(a) 716 ($\mathcal{A} = 1653\,\mathrm{Pa}$) *(b) 716-816 ($\mathcal{A} = 1453\,\mathrm{Pa}$)* *(c) 726 ($\mathcal{A} = 1392\,\mathrm{Pa}$)* *(d) 727 ($\mathcal{A} = 1480\,\mathrm{Pa}$)*

$\mathcal{P} = 110\,\mathrm{kW}$ & $\phi = 1.0$

(e) 716 ($\mathcal{A} = 1397\,\mathrm{Pa}$) *(f) 716-816 ($\mathcal{A} = 1657\,\mathrm{Pa}$)* *(g) 726 ($\mathcal{A} = 1241\,\mathrm{Pa}$)* *(h) 727 ($\mathcal{A} = 1073\,\mathrm{Pa}$)*

$\mathcal{P} = 103\,\mathrm{kW}$ & $\phi = 0.95$

Figure 7.3. *Time evolution of chamber pressure p_c' (MC1 to MC4) and spin ratio s_r for 716, the alternate arrangement of 716-816, 726, and 727. Two operating points are chosen from the instability map, where strong instability is exhibited by the four swirler configurations. The pressure-spin ratio set at the top corresponds to $\{\mathcal{P} = 110\,\mathrm{kW}$ & $\phi = 1.0\}$, and the bottom set corresponds to $\{\mathcal{P} = 103\,\mathrm{kW}$ & $\phi = 0.95\}$.*

ments (Worth and Dawson 2013a; Bourgouin et al. 2013). At the two operating points, swirler 716 is characterized by similar spin ratio fluctuations between standing $s_r = 0$ and the two spinning modes $s_r = -1$ and +1. The spin ratio traces corresponding to 726 are also quite similar with rapid fluctuations between the different modes but centered around the standing mode $s_r = 0$. However, these traces are notably different for swirler 727. For this swirler, at $\{\mathcal{P} = 110\,\mathrm{kW}$ & $\phi = 1.0\}$, s_r rapidly oscillates between the standing and spinning modes, whereas, at $\{\mathcal{P} = 110\,\mathrm{kW}$ & $\phi = 0.95\}$, it mostly oscillates between standing and clockwise spinning mode and spends almost no time in the $s_r > 0$ (counterclockwise) region.

7.4 Instability with co- and counter-rotating swirlers

It is now worth comparing the combustion dynamics in a configuration where all the swirlers impart clockwise rotation (all are of 716-type, referred to as CR: clockwise rotating) and a configuration where clockwise and counterclockwise rotating swirlers are alternatively placed (716-816, designated as CCR: clockwise-counterclockwise rotating). Our goal is to check whether the bulk swirl induced in the annular chamber when all swirlers rotate in the same direction influences the modal dynamics. A study of this type was already carried out by Worth and Dawson (2013a) in an annular system using a different class of injectors comprising a central bluff-body stabilizer and featuring a lower swirl number. As indicated by Worth and Dawson (2013a), the bulk rotation in the CR arrangement can be expected to be in the clockwise direction along the outer wall of the annulus and in the anticlockwise direction along the inner wall. The CR arrangement would also form a shear velocity layer between two adjacent injectors due to the opposite direction of the swirling velocity. The bulk motion would be canceled out in the CCR configuration, where co- and counter-rotating swirlers are alternatively placed.

The stability maps in Fig. 7.2 (a) & (b) right show that the instability frequency is the same for the two cases. This is expected since changing the swirl direction does not change the overall temperature distribution in the chamber, which, in turn, is reflected in the instability frequency. On the other hand, some changes appear in the location of the unstable domain (Fig. 7.2 (a) & (b) left), which is shifted towards lower thermal powers and equivalence ratios for the CCR arrangement compared to the CR arrangement. This can be better appreciated by probing the point where the maximum amplitude of oscillation occurs in these two cases. In the CR arrangement, one finds $\mathcal{A}_{\text{max}} = 1673\,\text{Pa}$ at $\mathcal{P} = 110\,\text{kW}$ and $\phi = 1.05$, while in the CCR configuration $\mathcal{A}_{\text{max}} = 1775\,\text{Pa}$ occurs at a lower thermal power of $\mathcal{P} = 103\,\text{kW}$ and a lower equivalence ratio of $\phi = 1.0$. The pressure signals plotted in Fig. 7.3 (a-b) & (e-f), corresponding to CR and CCR arrangements, are fairly similar with intermittent bursts along with rapid changes in the modal composition as indicated by the spin ratio evolution in the same figures.

Previous studies on annular combustors (Wolf et al. 2012; Worth and Dawson 2013a) indicate that when all the swirlers impart rotation in the same direction, the bulk swirl imposes a slow rotational motion of the nodal line of the $s_r = 0$ standing mode. Worth and Dawson (2013a) indicate that in the alternate anticlockwise and clockwise swirler arrangement (i.e., CCR configuration), a statistical preference towards a standing mode appears compared to the case where all swirlers induce a rotation in the same direction (i.e., all are co-rotating as in the CR configuration). To see if this is verified in the present configuration, one may examine the spin ratio statistical distributions plotted in Fig. 7.4 for the CR and CCR configurations corresponding to four thermal powers ($\mathcal{P}$: 118, 110, 103, $99\,\text{kW}$) and a single

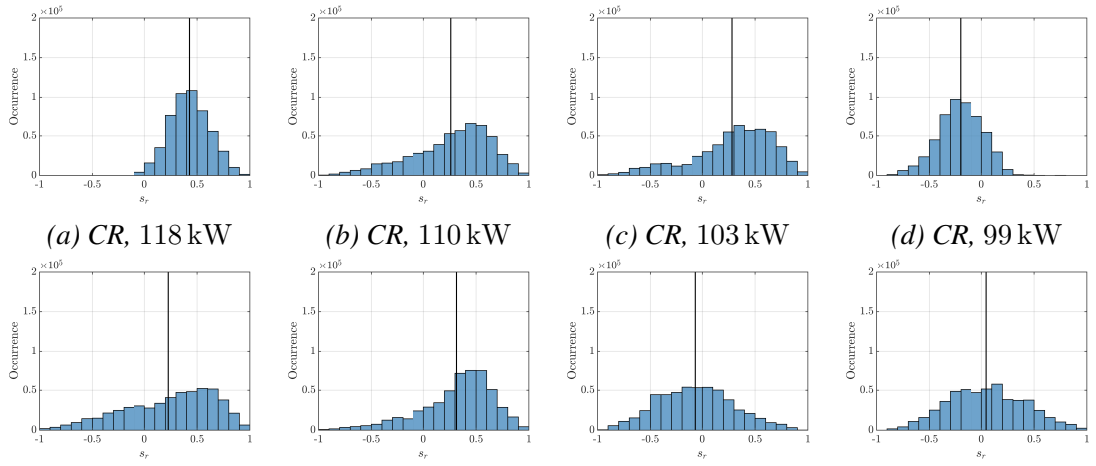

(a) CR, 118 kW *(b) CR,* 110 kW *(c) CR,* 103 kW *(d) CR,* 99 kW

(e) CCR, 118 kW *(f) CCR,* 110 kW *(g) CCR,* 103 kW *(h) CCR,* 99 kW

Figure 7.4. *Histogram of spin ratio occurrence comparing a configuration where all the swirlers impact clockwise rotation (CR) and a configuration where clockwise and counterclockwise rotating (CCR) swirlers are alternatively placed. The black vertical line corresponds to the mean spin ratio $\overline{s_r}$. The results are presented at four thermal powers and $\phi = 0.9$.*

equivalence ratio $\phi = 0.9$. The lowest thermal power of $93\,\mathrm{kW}$ is not considered as the system is always stable at this power when $\phi = 0.9$. In these diagrams, most of the spin ratio distributions resemble a Gaussian random process with a mean and standard deviation that depend on the operating point. The preferred operating mode can be roughly deduced from the mean spin ratio $\overline{s_r}$, shown as a vertical black line. The statistical preference is mostly either a standing mode or an anticlockwise spinning mode but not a clockwise spinning mode except for the CR configuration at $99\,\mathrm{kW}$, where the distribution inclines towards clockwise spinning wave mixtures. The CCR combination has a wider distribution spanning the full range of spin ratios at most operating points. This may be attributed to an effect of the bulk swirl, but one observes that, at certain operating points, the CR configuration as well features a relatively broad distribution (see Fig. 7.4(b) & (c)). Therefore, in contrast with Worth and Dawson (2013a), the present data indicate that there is no statistical preference for a particular mode. Similar data at other operating points confirm this finding, so one cannot generally infer that the presence of a bulk swirl determines the nature of the coupling mode.

7.5 Flame describing functions and their impact

It is natural to ask whether flame describing functions (FDFs) can be used to analyze the differences in unstable behavior observed in MICCA-Spray with the various swirler units. The FDFs are determined in the single-injector combustor, namely SICCA-Spray, which represents one sector of the MICCA-Spray annular

combustor. This analysis is carried out at one operating point selected from the MICCA-Spray stability map, which is marked as a black star in Fig. 7.2. The annular combustor operates at a thermal power of $\mathcal{P} = 103\,\mathrm{kW}$ and an equivalence ratio of $\phi = 0.85$. The corresponding thermal power of SICCA-Spray is $\mathcal{P}_{\mathrm{sicca}} = 6.4\,\mathrm{kW}$. The experimental setup shown in Fig. 7.1(c) is described in Chapter 1. The rig comprises a cylindrical quartz chamber with an inner diameter of $69\,\mathrm{mm}$, allowing optical access to the flame region, and is operated with the same injectors as MICCA-Spray. Although the wall-bounded flames in SICCA-Spray do not exactly represent the flames of MICCA-Spray, where each flame is surrounded by other flames, it is concluded in a later investigation that they approximately represent the flame dynamics in MICCA-Spray. Further details are provided in Chapter 10. This conclusion relies on a comparison between the single-injector configuration and a newly developed three-injector linear test rig TICCA-Spray, where the central flame is surrounded by two side flames and more closely resembles the MICCA-Spray environment. In these three configurations, the injection-to-backplane surface area ratio is kept constant. It is found that the FDFs measured in the single-injector rig do not coincide but are generally close to those found in the multiple injector array. Since the FDF data from the single-injector configuration (SICCA-Spray) is thoroughly determined, it is used in what follows to interpret observations made in the annular system. Before discussing the flame response in terms of FDFs, it is logical to first examine flame shapes under steady conditions.

7.5.1 Flame shapes formed by the different swirlers

Flame images displayed in Fig. 7.5 are recorded when the SICCA-Spray combustor is in a steady state stable operation. Each image is obtained by averaging 30 frames recorded by an intensified CCD camera fitted with an OH* filter and applying an Abel inversion to the average image.

The overall flame shapes corresponding to the lower-swirl injectors notably differ from those formed by the higher-swirl units. The lower-swirl devices (707 and 712) establish “V" flames that are narrower and longer. Such flames would result in reduced interactions with the neighboring flames in MICCA-Spray. Between 707 and 712, the flames differ in the distribution of chemiluminescence intensity; while 707 has a relatively uniform distribution in the flame wings, 712 features a more concentrated chemiluminescence intensity close to the tip. The higher-swirl units form “M" flames that are generally wider, resulting in augmented flame-flame interactions in MICCA-Spray. The flame wing angle is lower for 716 compared to the other two swirlers (726 and 727), probably because this unit has a lower swirl number. A modest difference exists between 726 and 727 in the two central branches, which are seen to merge at a greater distance from the outlet for 727 compared to 726. This could possibly be linked to the difference in

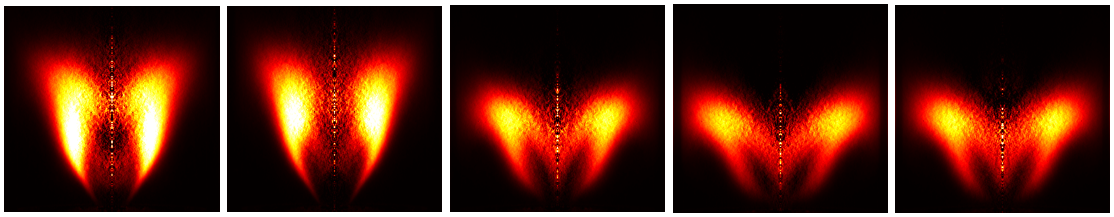

(a) 707 *(b) 712* *(c) 716* *(d) 726* *(e) 727*

Figure 7.5. *Flame images showing OH* chemiluminescence captured in SICCA-Spray under stable conditions. An Abel inversion is applied to the averaged images captured by the camera and are displayed in false colors.* $\mathcal{P}_{sicca} = 6.4\,\mathrm{kW}$ *and* $\phi = 0.85$*. The swirlers 707 and 712 belong to the lower-swirl category, while the other three swirlers (716, 726, 727) belong to the higher-swirl category.*

pressure drop values, as other parameters remain the same for these two swirlers. Differences in mean flame shapes can be expected to influence the flame response to incoming disturbances, as confirmed in what follows.

7.5.2 Measurement of flame describing function

The flame response to external acoustic modulations is obtained in the SICCA-Spray combustor in terms of a flame describing function (FDF). In the absence of equivalence ratio fluctuations, the FDF is given by:

$$\mathcal{F} = (\dot{Q}'/\overline{\dot{Q}})/(\dot{q}_v'/\overline{\dot{q}_v}) \qquad \text{(4.2 Rep.)}$$

where $\dot{Q}'/\overline{\dot{Q}}$ designates the relative fluctuations in heat release rate, and $\dot{q}_v'/\overline{\dot{q}_v}$ represent the relative fluctuations in volume flow rate. The assumption that equivalence ratio fluctuations are negligible is verified in Chapter 2 for the injectors considered in the present study. Further, it is observed that these injectors behave in a quasi-premixed fashion due to the recessed position of the atomizer. Thus, for the present spray flames, chemiluminescence intensity can be used as an indicator of heat release rate. A photomultiplier fitted with an OH* filter centered at 308 nm records the mean and fluctuating light intensities $I'(\mathrm{OH^*})/\overline{I(\mathrm{OH^*})}$ from the flame, which approximately represents the relative heat release rate fluctuations $\dot{Q}'/\overline{\dot{Q}}$.

The relative fluctuations in volume flow rate $\dot{q}_v'/\overline{\dot{q}_v}$ are often replaced by the relative velocity fluctuations for ease of measurement. Such a substitution is valid as long as the measurement is carried out in a region where the relative velocity fluctuations match the relative volumetric flow rate fluctuations. This was reported in Chapter 4, and it was found that the suitable measurement position is close to the location of maximum mean axial velocity. This location is at $r = 3.5\,\mathrm{mm}$ for the swirlers in the lower-swirl category (707 and 712) and at $r = 4\,\mathrm{mm}$ from the

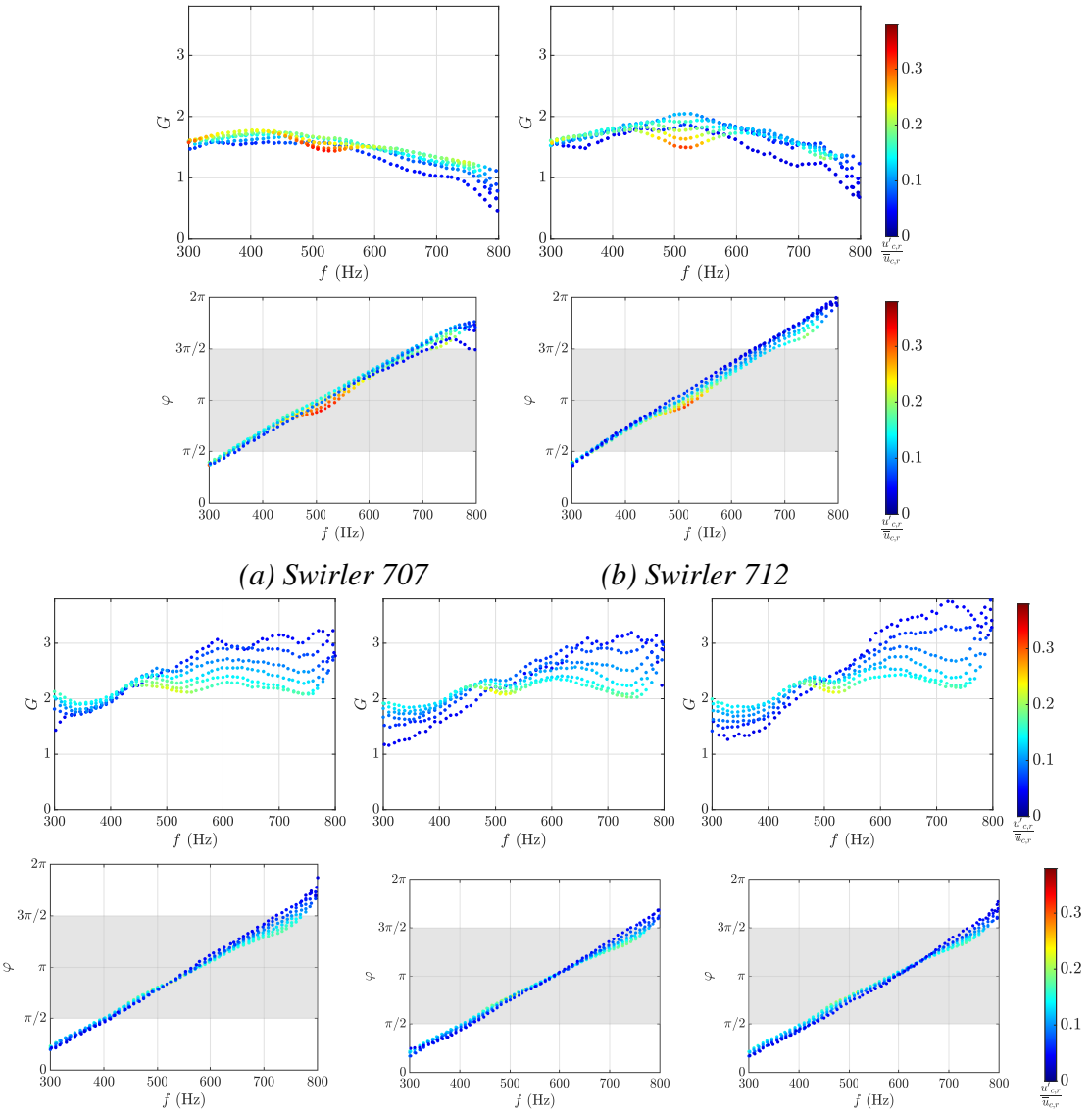

(a) Swirler 707 *(b) Swirler 712*

(c) Swirler 716 *(d) Swirler 726* *(e) Swirler 727*

Figure 7.6. *Flame describing function represented in terms of gain G_F and phase φ_F at different levels of relative velocity fluctuation $u'_{c,r}/\overline{u}_{c,r}$ and shown for the five swirlers considered. The gray bands in the phase diagrams indicate the tentative unstable bands. It is recalled here that swirlers 707 and 712 belong to the lower-swirl category, while the other three swirlers (716, 726, 727) belong to the higher-swirl category.*

center of the injector for the swirlers in the higher-swirl category (716, 726, 727) and at a height of $h = 2.5\,\mathrm{mm}$ above the backplane. The axial velocity fluctuations are measured with a 2-component phase Doppler particle analyzer (PDPA) system operating in laser Doppler anemometry mode and making use of the heptane droplets in the spray. This is adequate because the droplet size at the measurement point does not exceed a mean diameter of $8\,\mu\mathrm{m}$, and the droplets, therefore, follow the air flow well in the frequency range of interest. Henceforth, the relative velocity fluctuations measured at the injector exit are represented by $u'_{c,r}/\overline{u}_{c,r}$, where '$c$' refers to measurement carried out in the chamber and 'r' refers to the radial measurement location.

The two driver units mounted at the bottom of SICCA-Spray are modulated at different frequencies and amplitudes, resulting in different levels of relative velocity fluctuations $u'_{c,r}/\overline{u}_{c,r}$ at the injector outlet to obtain the FDF gain G_F and phase φ_F. The FDFs are shown in Fig. 7.6 for the five swirling injectors considered in this study. The FDFs for the lower-swirl category (Fig. 7.6 (a) & (b)) notably differ in both gain and phase from the FDFs of the higher-swirl category (Fig. 7.6 (c), (d), & (e)). However, the FDFs are quite similar when the swirlers belong to the same category. On comparing the swirlers 707 and 712 (Fig. 7.6 (a) & (b) top), one observes that the overall trend in gain is preserved with some minor differences. While the gain of 707 evolves almost linearly with the velocity fluctuation levels, 712 exhibits mild variations with respect to the velocity fluctuation level close to $500\,\mathrm{Hz}$ in the tested amplitude range. The gain for swirler 707 features a plateau until $600\,\mathrm{Hz}$, beyond which there is a steady drop. For swirler 712, the gain mildly increases in the low frequency range ($< 600\,\mathrm{Hz}$) and falls beyond that frequency. Similarly, the gains of the swirlers 716, 726, and 727 exhibit the same overall behavior, rising until around $550\,\mathrm{Hz}$ and then reaching a plateau, especially at the higher velocity fluctuation levels. In the low frequency range, the 716 gain is nearly independent of the velocity fluctuation level but then exhibits substantial sensitivity to the excitation level beyond $500\,\mathrm{Hz}$. The other two swirlers (726 and 727) feature a weak nonlinearity, first at the lower velocity fluctuation amplitudes and below $500\,\mathrm{Hz}$, but this becomes more pronounced beyond this limit, similar to the 716 case. For the same level of amplifier input voltages delivered to the driver units of SICCA-Spray, 707 reaches the highest level of velocity fluctuations, with $u'_{c,r}/\overline{u}_{c,r} \approx 37\%$ at a frequency of around $500\,\mathrm{Hz}$. This level is slightly lower for 712 at 31%, whereas the swirlers in the higher-swirl category feature a maximum level of about 23%. These limitations in relative modulation levels may be linked to the pressure drop. The swirlers in the higher-swirl category also feature the highest pressure drop values offering higher resistance to the incoming acoustic disturbances.

The phase of the FDF is almost linear for all of the swirlers in the amplitude range tested. A mild nonlinearity is observed around $500\,\mathrm{Hz}$ for 707, beyond

500 Hz for 712, and beyond 700 Hz for the higher-swirl units. The phase of the FDF essentially depends on the swirler category. In general, the higher-swirl units have similar phase functions, whereas the lower-swirl devices differ in their phase characteristics beyond 630 Hz.

7.5.3 Instability analysis using FDFs

The FDF framework allows for a reasonable prediction of instabilities observed in MICCA-Spray, as demonstrated in Laera et al. (2017). For injectors that are weakly transparent to acoustic waves, like the ones considered here, it was shown in Chapter 6 that a low-order model might be used to predict instabilities of SICCA-Spray. The model consists of imposing an impedance ζ at the injector outlet, the phase of which determines the unstable bands, and an experimentally determined FDF $\mathcal{F}$ to represent the flame dynamics. One may infer, from this model, a qualitative interpretation of observations made in the annular system.

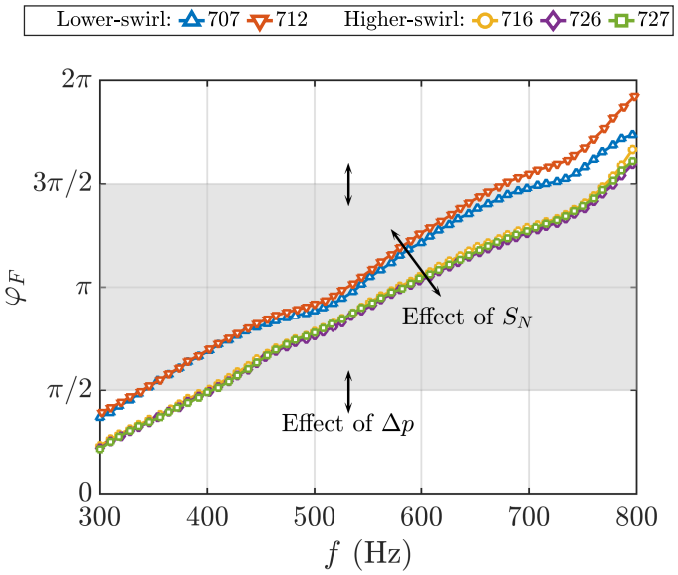

Figure 7.7. *FDF phase φ_F for the different swirlers considered in this study. Only the phase evolution of Fig. 7.6 corresponding to maximum attainable relative velocity fluctuations are shown. The swirlers 707 and 712 belong to the lower-swirl category while the swirlers 716, 726, and 727 belong to the higher-swirl category.*

The model yields unstable bands, which can be plotted in the FDF phase diagram. If the phase of the FDF at a particular frequency falls within this band, then one can predict a “potential instability" at this frequency. The location of this unstable band is predominantly decided by the phase of the impedance φ_ζ at the injector outlet, which, in turn, could be linked to the injector pressure drop, as seen in Chapter 6. In addition, one also obtains a growth rate for the instability, which

directly depends on the FDF gain. If this growth rate is greater than the damping imposed by the system, then it can be concluded that a particular operating point will be “definitely unstable" in MICCA-Spray. Using this simplified injector representation and FDF, an attempt is made to understand the instabilities of the MICCA-Spray combustor. It has been shown in Chapter 6 that for an acoustically weakly transparent injector, the impedance measured at the injector outlet takes a phase φ_ζ in the range $[3\pi/4, \pi]$ for frequencies lying between 300 and $600\,\mathrm{Hz}$. It is, however, not possible to obtain the injector impedance in SICCA-Spray as the measurements can be obtained only when there is a self-sustained oscillation and the system is stable beyond $600\,\mathrm{Hz}$ (discussed in Chapter 6). A similar result is also obtained by Patat et al. (2021) using an equivalent injector placed in a linear multi-injector test rig and submitted to transverse acoustic perturbations around $750\,\mathrm{Hz}$. In the absence of information on the definite injector impedance in the annular configuration, one may tentatively assume that $\varphi_\zeta = \pi$. The corresponding unstable band lies in the range between $[\pi/2, 3\pi/2]$, and this band can be placed in the phase diagrams shown in Fig. 7.6 & 7.7 (marked as a gray region). As seen from the images in Fig. 7.5, the flames are longer for the lower-swirl group, whereas they are shorter and broader for the higher-swirl group. From these images, the axial location of the heat release rate barycenter a_b can be calculated and is found to be approximately at a height of $36\,\mathrm{mm}$ for the lower-swirl category and $30\,\mathrm{mm}$ for the higher-swirl category. Given that the higher-swirl group has a slightly higher maximum mean axial velocity between the different swirlers (seen in Chapter 1 under cold conditions and shown in Chapter 4 under hot conditions, where the maximum mean axial velocity is $69\,\mathrm{m\,s^{-1}}$ for 716 and $58\,\mathrm{m\,s^{-1}}$ for 707, measured $2.5\,\mathrm{mm}$ above chamber backplane), and assuming that disturbances travel at half the maximum mean velocity (Durox et al. 2005), one can expect the lower-swirl group to have a higher time delay. This is then reflected as a comparatively higher FDF phase for the lower-swirl category, which is seen in Fig. 7.7, where two distinct groups of FDF phase functions can be distinguished depending on the swirler category. This figure shows the FDF phase for all the swirlers to facilitate comparison. Only the phase curves of Fig. 7.6 corresponding to the maximum of relative velocity fluctuations at all frequencies are shown in Fig. 7.7. Noting that the instabilities in MICCA-Spray coupled with the 1A1L mode have oscillation eigenfrequencies lying between 750 and $832\,\mathrm{Hz}$, one can see that the phases for 707 and 712 cross the $3\pi/2$ upper limit of the unstable band at $700\,\mathrm{Hz}$ and $650\,\mathrm{Hz}$ respectively. This clearly indicates that the two lower-swirl units will not give rise to 1A1L instability in MICCA-Spray. For the three swirlers in the higher-swirl group, the phase of the FDF crosses the $3\pi/2$ limit of the instability band at $\approx 790\,\mathrm{Hz}$ at the highest level of velocity fluctuations ($u'_{c,r}/\overline{u}_{c,r} \approx 15\%$ in Fig. 7.6 (c-e) (bottom row). This crossing frequency is close to the 1A1L eigenfrequency, which is around $800\,\mathrm{Hz}$ for the three swirlers (marked in Fig. 7.2 right), thus providing a positive growth rate. This means that these swirlers might give rise to instability and that their crossing frequency would then increase as the am-

plitude grows, while the phase would continue to be reduced and stay within the unstable band in Fig. 7.2 so that the oscillation corresponding to 726 would finally reach a limit cycle at a frequency of $832\,\mathrm{Hz}$. Of course, this is only a tentative scenario since there is no information beyond 800 Hz and also because the unstable band has been placed in the range $[\pi/2, 3\pi/2]$. Thus, as a general guideline, one may say that the pressure drop defines the position of the unstable band, whereas the swirl number controls the location of the FDF phase with respect to the unstable band, consequently deciding the stability of the system.

One other condition for instability is to have a growth rate level that is sufficiently high to overcome the system damping rate. The growth rate increases with the FDF gain. From the gain plots in Fig. 7.6, a significant difference is observed between the two swirl categories. For the lower-swirl group, the gain decreases between 750 and $832\,\mathrm{Hz}$ and drops below one. Whereas, for the higher-swirl category, the gain increases in this range and is about two times higher than that of the lower-swirl category. The three swirlers in the higher-swirl category feature similar FDF gain values ($G_{\text{average}} \approx 2.8$), thus promoting the occurrence of instabilities in the annular combustor at this operating point and partially explaining why the swirlers in the higher-swirl category become unstable in MICCA-Spray, whereas units in the lower-swirl category are always stable.

It is also possible to infer why swirlers 716 and 727 have similar stability maps, as indicated in Section 7.3. These two swirlers have the same pressure drops, their FDF phase functions are identical, and their gains are roughly similar. The unstable bands will have the same location, and one may expect a common instability behavior. In contrast, the relatively high pressure drop induced by swirler 726 might shift the tentative unstable band towards higher phase values. Thus, for an FDF phase that is slightly above the upper limit of the unstable band corresponding to 716 and 727, the swirler 726 might still show an unstable operation (refer to Fig. 7.7). Therefore, in the frequency range between 750 to $832\,\mathrm{Hz}$, one can expect that 726 will feature a broader instability range, which is also confirmed by the results shown in Section 7.3 (Fig. 7.2 (c) left). In addition, the FDF phase corresponding to slightly higher frequencies would be inside the unstable band for 726. This potentially explains the comparatively higher instability frequencies in MICCA-Spray with this swirler (see Fig. 7.2 (c) right).

7.6 Conclusions

Systematic experiments carried out on a lab-scale annular combustor equipped with sixteen injectors are used to identify swirler effects on azimuthal combustion instabilities. The present investigation reports results obtained with five different swirlers that may be qualified as weakly transparent to acoustic waves. Their swirl numbers range from 0.59 to 0.74 with relatively high pressure drop coefficients.

The swirlers are categorized based on the swirl number values into lower-swirl (swirlers 707 and 712) and higher-swirl (swirlers 716, 726, 727) groups with variations in pressure drops within each category. The swirlers in the lower-swirl group also have comparatively lower pressure drops. Experiments are carried out with liquid heptane at five thermal power and six global equivalence ratio levels (30 operating points) for each swirler. The data are then used to plot stability maps which indicate that the swirler type has a notable influence on the stability characteristics of the system. One observes that:

- None of the swirlers in the lower-swirl category feature instability at any of the thirty operating points tested. In contrast, all the swirlers in the higher-swirl category give rise to azimuthal instabilities.
- The transition to an unstable mode is mostly determined by the swirl number through its effect on flame structure. The pressure drop contributes to further variations in amplitude and frequency of oscillation.
- On comparing the swirlers in the higher-swirl category, a higher pressure loss value appears to be associated with wider instability regions and higher oscillation frequencies in the tested range of operating conditions.
- The evolution of the spin ratio reveals that the modes are of mixed type and constantly switch between standing and spinning modes, an observation similar to Worth and Dawson (2013a) and Wolf et al. (2012).

An additional case of alternatively-placed clockwise and counterclockwise rotating (CCR) swirlers is compared with the standard arrangement where all the swirlers are clockwise rotating (CR), to reveal possible effects of mean bulk swirl on instabilities. It is found that:

- Compared to the CR arrangement, the stability map for the CCR arrangement is shifted towards lower thermal powers and lower equivalence ratios.
- When the mean bulk swirl is absent, the spin ratio distribution features no statistical preference to standing or spinning mode.
- In some cases, the CCR configuration promotes a broader distribution of spin ratios centered around the standing mode ($s_r = 0$), while the CR arrangement appears to favor counterclockwise spinning modes.

Flame shapes and flame describing functions (FDFs) measured in a single-injector combustor, namely SICCA-Spray, representing one sector of MICCA-Spray, are employed to interpret the differences in behavior observed in the annular system at one operating point. Results show that:

- The flame shapes obtained under stable conditions are distinct for each swirler category. Swirlers in the lower-swirl category generally take a “V" shape, whereas the swirlers in the higher-swirl category take an “M” shape.
- The dynamical response of the flames represented in terms of an FDF also distinctly depends on the swirler category.

An attempt is made to qualitatively interpret instability observations in the annular combustor by making use of a simplified instability analysis combining the FDFs and impedance at the swirler outlet. A tentative instability band is defined (Rajendram Soundararajan et al. 2022), the position of which depends on the impedance, which, in turn, is expected to depend on the pressure drop of the injector. For the lower-swirl injector, one finds that the FDF phase lies outside the instability band in the frequency range of the 1A1L mode of MICCA-Spray. In the higher-swirl case, the phase is near the band upper boundary in the frequency range of the 1A1L mode, and the gain takes larger values that are about twice those of the lower-swirl units. These two features may then promote the growth of instability. As the gain decreases with the amplitude of velocity oscillations, this will lead to a limit cycle. As a general rule, one may say that the pressure drop decides the position of the unstable band, whereas the location of the FDF phase with respect to the unstable band is controlled by the swirl number, consequently deciding the stability of the system.

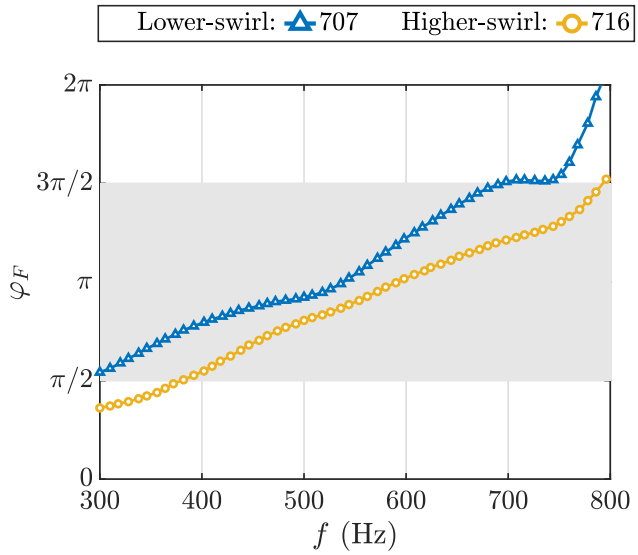

Figure 7.8. *FDF phase φ_F for swirlers 707 and 716 at $\phi = 0.95$ (operating point F2) in SICCA-Spray. Only the phase evolution with the maximum attainable relative velocity fluctuations at all frequencies are shown.*

Appendix 1: FDF phase evolution at a higher equivalence ratio

It is interesting to see whether the instability analysis developed in Section 7.5.3 can be used to explain observations made at a higher equivalence ratio of $\phi = 0.95$ but at the same thermal power of $\mathcal{P} = 103\,\mathrm{kW}$ in MICCA-Spray corresponding to a thermal power $\mathcal{P}_{\mathrm{sicca}} = 6.4\,\mathrm{kW}$ in SICCA-Spray. One may only consider two swirlers, 707 and 716, one from each category, which typify the trends observed for the two swirler groups. It is also sufficient to examine the FDF phase corresponding to the highest level of relative velocity fluctuations plotted in Fig. 7.8 together with the tentative unstable band between $[\pi/2, 3\pi/2]$ marked in gray. The phase of 707 leaves the unstable band at $700\,\mathrm{Hz}$. Since the instability frequency in MICCA-Spray corresponding to the 1A1L mode lies between 750 and $832\,\mathrm{Hz}$, one can conclude that this swirler will lead to a stable operation of the annular combustor. In contrast, the phase of 716 falls within the unstable band between 380 and $800\,\mathrm{Hz}$, which comprises a part of the eigenfrequencies of MICCA-Spray. When MICCA-Spray is equipped with this swirler, it may potentially become unstable. The regime will be unstable if, in addition, the gain of the FDF is sufficiently high and such that the growth rate may overcome the damping rate in the system. The present results obtained at a higher equivalence ratio substantiate the discussion in Section 7.5.3.

Appendix 2: Spin ratio comparison between co- & counter-rotating swirlers

In Section 7.4, it was observed with heptane that the CR and CCR configurations did not exhibit any statistical preference for a particular azimuthal mode. This analysis is now extended to the other two fuels —premixed propane and liquid dodecane.

With premixed propane, the mean spin ratio of the CR configuration indicates a standing mode at the highest thermal power ($118\,\mathrm{kW}$), but there is an inclination towards counterclockwise spinning mode at the other powers. With CCR configuration, the mode is nearly standing at the two higher powers. However, at the two lower powers, the CCR configuration peculiarly exhibits a double peak favoring both spinning modes. With dodecane, the CR configuration mostly features a preference for the standing mode, and the CCR configuration mainly prefers clockwise spinning, except at $103\,\mathrm{kW}$, where the preference is close to a standing mode. The spin ratio distribution is not shown for the CCR configuration at $99\,\mathrm{kW}$, as the system is almost stable ($\mathcal{A} = 260\,\mathrm{Pa}$) at this operating point. From the 24 distributions shown for the two configurations with three fuels and four operating points, one can say there is no conclusive statistical preference exhibited, unlike in Worth and Dawson (2013a).

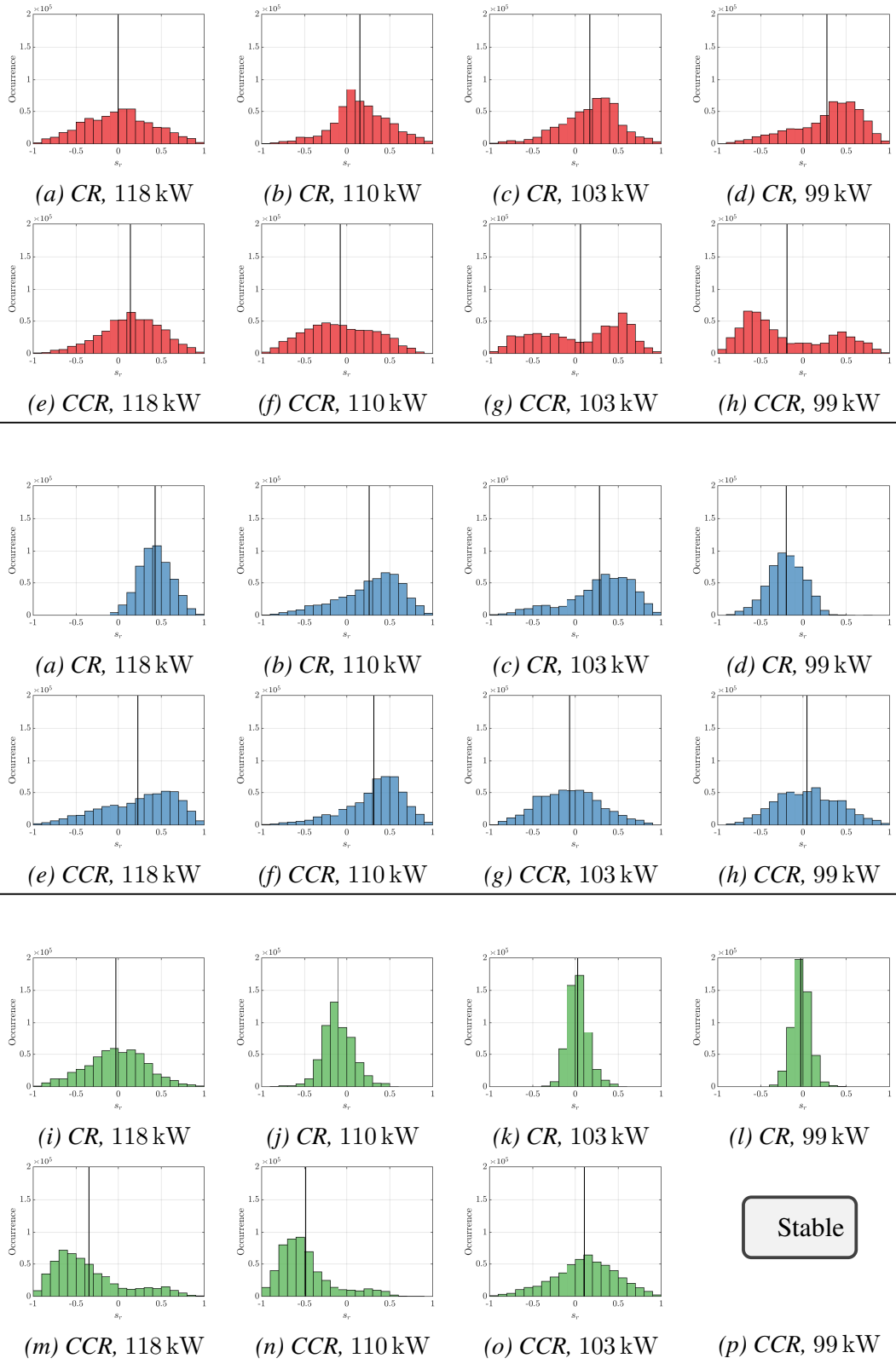

(a) CR, 118 kW *(b) CR,* 110 kW *(c) CR,* 103 kW *(d) CR,* 99 kW

(e) CCR, 118 kW *(f) CCR,* 110 kW *(g) CCR,* 103 kW *(h) CCR,* 99 kW

(a) CR, 118 kW *(b) CR,* 110 kW *(c) CR,* 103 kW *(d) CR,* 99 kW

(e) CCR, 118 kW *(f) CCR,* 110 kW *(g) CCR,* 103 kW *(h) CCR,* 99 kW

(i) CR, 118 kW *(j) CR,* 110 kW *(k) CR,* 103 kW *(l) CR,* 99 kW

(m) CCR, 118 kW *(n) CCR,* 110 kW *(o) CCR,* 103 kW *(p) CCR,* 99 kW

Figure 7.9. *Histogram of spin ratio occurrence comparing a configuration where all the swirlers impact clockwise rotation (CR) and a configuration where clockwise and counterclockwise rotating (CCR) swirlers are alternatively placed. The black vertical line corresponds to the mean spin ratio $\overline{s_r}$. Top set: Propane, middle set: heptane, bottom set: dodecane. The results are presented at four thermal powers and $\phi = 0.9$, except for CCR configuration with dodecane at $\mathcal{P} = 99\,\mathrm{kW}$ as MICCA-Spray is almost stable at this operating point.*

Chapter 8

Effect of fuel atomizer location: SICCA-Spray

Contents

This chapter reports experiments aimed at identifying the effect of fuel atomizer location on combustion instabilities. Results obtained in this study might serve to guide design that will reduce injector sensitivity to disturbances and instabilities. Experiments are carried out on a single-injector combustor comprising a swirler with high swirl number and pressure drop, and a pressure atomizer that delivers liquid heptane fuel in the form of a fine spray. In the first set of experiments, longitudinal self-sustained oscillations (SSOs) are studied by systematically varying the atomizer recess distance and making use of three combustion chamber lengths. Three distinct instability zones characterized by jumps in amplitude and frequency are observed as a function of the atomizer recess. At lower SSO frequencies, the pressure fluctuation amplitude in the chamber decreases as the atomizer recess distance is diminished, tending towards a stable operation. This behavior is reversed at higher SSO frequencies, where the system becomes less unstable at higher atomizer recess distances. The oscillation frequency is also found to change and increases as the recess distance is reduced. Three recess distances corresponding to each zone of operation are selected to further analyze the flow structure and flame behavior. The mean velocity profiles only reveal moderate differences in the flow field, but the liquid droplet spray geometry and size distribution feature significant differences in the neighborhood of the injector axis. Laser sheet images of the fuel spray showing the spatial distribution of droplets reveal two patterns —one where the spray predominantly interacts with the conical exit nozzle unit when the atomizer is recessed, and the other where this interaction is minimal. In the latter case, the fuel spray exits directly into the chamber, and this happens when the atomizer recess is small. The spray distribution, in turn, affects the flame shapes resulting in two distinct configurations. Finally, the flame response to external disturbances is studied to obtain the flame describing function. The gain and phase at the three recess positions vary quite substantially, changing the instability behavior of the system.

8.1 Introduction

Combustion instabilities characterized by high-amplitude pressure fluctuations are extensively investigated because of their detrimental effects (Lieuwen and Yang 2005b; Poinsot 2017). The case of liquid fuels is of particular interest to the aviation industry and many investigations on combustion instabilities in lab-scale combustors specifically operated with liquid spray flames have provided useful insights (Wolf et al. 2012; Vignat et al. 2020). The presence of liquid spray adds additional complexity to the mechanism leading to these instabilities as time lags associated with vaporization and mixing may alter the stability domains of the combustors (Rajendram Soundararajan et al. 2021).

At this stage it is worth considering some of the previous works that investigated the effect of spray dynamics on instabilities. Giuliani et al. (2002) performed measurements on an air-blast atomizer and showed that the spray number density and droplet size distribution fluctuated with the imposed acoustic modulation. Such a variation may lead to the formation of hot spots in the presence of a flame. Other experimental and numerical studies under cold flow conditions also confirmed the presence of droplet density waves (Gajan et al. 2007), the dependence of droplet size distribution (Yang and Turan 2017), spray structure (Sujith 2005), and evaporation rate (Sujith et al. 2000) on the frequency and amplitude of the acoustic oscillation. A direct numerical simulation of an externally modulated bunsen spray flame by Pera and Reveillon (2007) showed that for droplets with significant Stokes number, the flame response was additionally affected by mixture fraction variations caused by preferential segregation of the droplets. Such droplet number densifications were also reported by Greenberg and Katoshevski (2012) in an oscillatory flow field leading to flame front pinching and a subsequent shape transformation. The effect of convective time delay associated with droplets on self-sustained instabilities was identified by Eckstein et al. (2006) on a swirl combustor equipped with an air-blast atomizer. The oscillation frequency, in this case, was found to be mainly dictated by the convection time of fuel from the atomizer lip to the flame zone. The convective time scales of the spray can be modified if there are wall interactions, as observed by Apeloig et al. (2015). During some parts of the acoustic cycle, the liquid droplet stream interacted with the swirler walls, forming a liquid film, which was further convected and subsequently re-atomized by the air flow. While at other instants, the droplets rebounded or were transported directly into the chamber from their injection point. The impact of spray-wall interaction on thermoacoustic instabilities was also emphasized by Lo Schiavo et al. (2020) through large eddy simulations (LES) on SICCA-Spray combustor equipped with an injector similar to the ones considered in the present investigation. The authors found that a slip boundary condition on the walls of the exit nozzle was unable to reproduce the experimental results. Whereas, considering film conditions accounted for the delay caused by the impingement of fuel droplets on the wall and the subsequent formation and atomization of the liquid film, nicely reproducing the experimental limit-cycle observations. Several other studies (see, for example, Zhu et al. (1999), de la Cruz García et al. (2009), Tachibana et al. (2015), Innocenti et al. (2017)) have also identified the effect of spray-flame coupling mechanisms, motivating further investigations in this domain. In a recent study by Lo Schiavo et al. (2021), the impact of spray injection angle was considered through the LES of SICCA-Spray. Even though the influence of spray angle on the stable flame was negligible, it completely altered the instability behavior —the system tended to become stable when the spray angle was diminished in the SICCA-Spray combustor. Using numerical modeling, it was shown that this variation of spray angle affected the film formation on the injector exit nozzle, modifying the film-acoustic coupling. Although it is not practically

feasible to change the spray angle, it is easier to shift the fuel atomizer location. In this way, one can modify the spray-wall interaction, in other words, the convective time scales associated with the fuel delivery and also the spatial distribution of spray. This technique is adopted in the present study to develop insights on the spray-flame dynamics leading to instabilities.

Understanding the effect of fuel injection position can also be motivated from the viewpoint of passive control of instabilities. Such a strategy was considered by Straub and Richards (1998) on a premixed can combustor, where experiments were carried out to study the effect of moving the fuel injection location along the axis of the premix nozzle. The instability regimes (both in amplitude and frequency) clearly depended on the fuel injection position, which was subsequently explained using a time lag model. By moving the fuel injection location, the distance and correspondingly the time taken for the air/fuel mixture to reach the flame front changes for a given nozzle velocity, thus affecting the phase between heat release rate and pressure. Although a stable operation of the combustor could not be achieved by simply changing the fuel injection location, it was possible to obtain a stable regime of operation by injecting the fuel from two axial fuel ports. With liquid rocket coaxial injectors, it was also found that the expansion rate of flames is notably augmented if the central channel conveying liquid oxygen is in recess with respect to the outlet (Juniper and Candel 2003). This is because the confined central stream becomes absolutely unstable, which possibly enhances the mixing and spreading rate. A slow active control method of damping instabilities based on varying the fuel spray properties using a Nanomizer^{TM} unit was successfully demonstrated by Lee et al. (2005). By varying the power input to the fuel injector, it was possible to change the droplet diameters, which resulted in modified stability behaviors. The above studies indicate the possibility of developing control techniques by altering the spray characteristics. This is achieved in the present study by modifying the fuel atomizer position with the aim of developing insights on the influence of spray dynamics on instabilities. As will be seen later, unlike in the study of Lee et al. (2005), the droplet distribution remains nearly the same in the present study, but the spray-wall interaction mechanism is altered, leading to different characteristic times and spatial dispersion for the spray when the fuel atomizer position is varied.

The current chapter is organized as follows. After a presentation of the experimental setup (Section 8.2), it reports the data obtained by systematically varying the fuel atomizer position (Section 8.3) in a combustor fueled by a spray of liquid heptane. A detailed analysis of the spray and flame structures is then carried out, and the observed regimes of self-sustained oscillations are interpreted by making use of measured flame describing functions (Section 8.4 and 8.5). An appendix is provided at the end to show the injector impedance measurement at different atomizer positions.

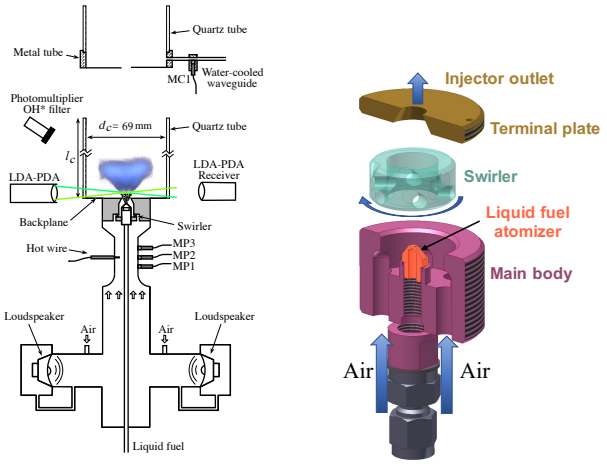

(a) *(b)*

Figure 8.1. *(a) Experimental setup of the SICCA-Spray test rig. (b) Exploded view of the injector unit. Reproduced from Chapter 1.*

8.2 Experimental setup

Experiments reported in this chapter are carried out in the SICCA-Spray combustor equipped with swirler 726 and operated with liquid heptane as fuel delivered by an atomizer. The experimental setup shown in Fig. 8.1 is only briefly described. More details may be found in Chapter 1. A movable atomizer is threaded onto the injector such that its position can be continuously varied along the injector axis, an arrangement that differs from the traditional setup where the atomizer position is fixed. The swirling air surrounding the atomizer assists in opening up the liquid spray cone and aids in breaking up the fuel jet. The injector houses the usual terminal plate with an exit diameter of $8\,\mathrm{mm}$. It is recalled that this component features a $5\,\mathrm{mm}$-long conical section followed by a $1\,\mathrm{mm}$-long cylindrical section. The swirler, fuel atomizer, and terminal plate (conical exit nozzle) together form the injector shown in Fig. 8.1 (b). In the present experiments, the test rig is operated at a thermal power of $\mathcal{P} = 6.4\,\mathrm{kW}$ and a global equivalence ratio of $\phi = 0.85$, corresponding to the operating point F1.

Two kinds of experiments are performed for this study. In the first set, the combustion chamber length is varied to produce self-sustained oscillations (SSOs) of different amplitudes and frequencies. Three chamber lengths are used in the present study, $l_c = 365\,\mathrm{mm}$, $265\,\mathrm{mm}$, and $215\,\mathrm{mm}$, all with a chamber inner diameter of $d_c = 69\,\mathrm{mm}$. At each chamber length, the atomizer position is varied continuously to identify the effect of fuel injection location. In the second set of experiments, the two driver units mounted at the bottom of the plenum modulate

the air flow at different frequencies and amplitudes to determine the flame describing function (FDF). During these experiments, the length of the chamber is fixed and equal to $l_c = 150\,\mathrm{mm}$ to avoid self-sustained oscillations. A wave generator connected to the driver units delivers frequency ramps between $250\,\mathrm{Hz}$ and $850\,\mathrm{Hz}$ at the rate of $4.5\,\mathrm{Hz\,s^{-1}}$ and at six amplifier voltages to produce different velocity fluctuation levels $u'_{c,r}/\overline{u}_{c,r}$ at the base of the flame.

The pressure signal is measured by microphone MC1 plugged on a water-cooled waveguide connected to the chamber through a brass ring of diameter $70\,\mathrm{mm}$ and a length of $15\,\mathrm{mm}$ mounted on the backplane. The microphone located at a distance of $276\,\mathrm{mm}$ from the waveguide port is protected from the high-temperature environment in the chamber, but this introduces a propagation delay of $0.79\,\mathrm{ms}$ in the measured acoustic pressure that is accounted for in the data processing. The chamber formed by a quartz tube provides the optical access needed for recording the chemiluminescence $I(OH^*)$ from the flame using a photomultiplier. Axial velocity measurement of the spray of heptane droplets is obtained using laser Doppler anemometry (LDA), and the droplet size profile is acquired using phase Doppler anemometry (PDA). The air velocity profiles reported in Section 8.4.1 for cold flow conditions are the only ones to include axial, radial and tangential velocity components. These are obtained using LDA by seeding the air flow with fine oil droplets having a small mean diameter of $2.5\,\mu\mathrm{m}$. More details on LDA and PDA measurements are given in Chapter 1. An intensified camera equipped with a UV lens and an OH^* filter centered at $308\,\mathrm{nm}$ is used to obtain the flame images. For heptane spray imaging, laser light sheet scattering images are recorded without chamber confinement to avoid parasitic reflections. The light-sheet is formed by a continuous Nd:YAG laser with a wavelength of $532\,\mathrm{nm}$ and the images are acquired using a *Panasonic* Lumix FZ38 digital camera.

8.3 Regimes of self-sustained oscillations (SSOs)

Pressure fluctuations are measured in SICCA-Spray for three chamber lengths $l_c = 365\,\mathrm{mm}$, $265\,\mathrm{mm}$, and $215\,\mathrm{mm}$, and at each length, the atomizer position is systematically varied. The atomizer recess h_r refers to the distance of this unit with respect to the chamber backplane. The atomizer is moved continuously from $h_r = 9.25\,\mathrm{mm}$ (lowest position) to $1.75\,\mathrm{mm}$ (highest position) in steps of $0.5\,\mathrm{mm}$ to obtain the instability characteristics at sixteen recess distances. At each position, the microphone MC1 measures the acoustic pressure level in the chamber, and the signals are sampled at a rate of 16,384 Hz for an acquisition time of at least $10\,\mathrm{s}$. Measurements are performed when the atomizer is moved upwards as well as downwards to check if there is any hysteresis effect. The recess distance is not reduced below $1.75\,\mathrm{mm}$ to avoid flame stabilization on the atomizer head, which would eventually damage this unit.

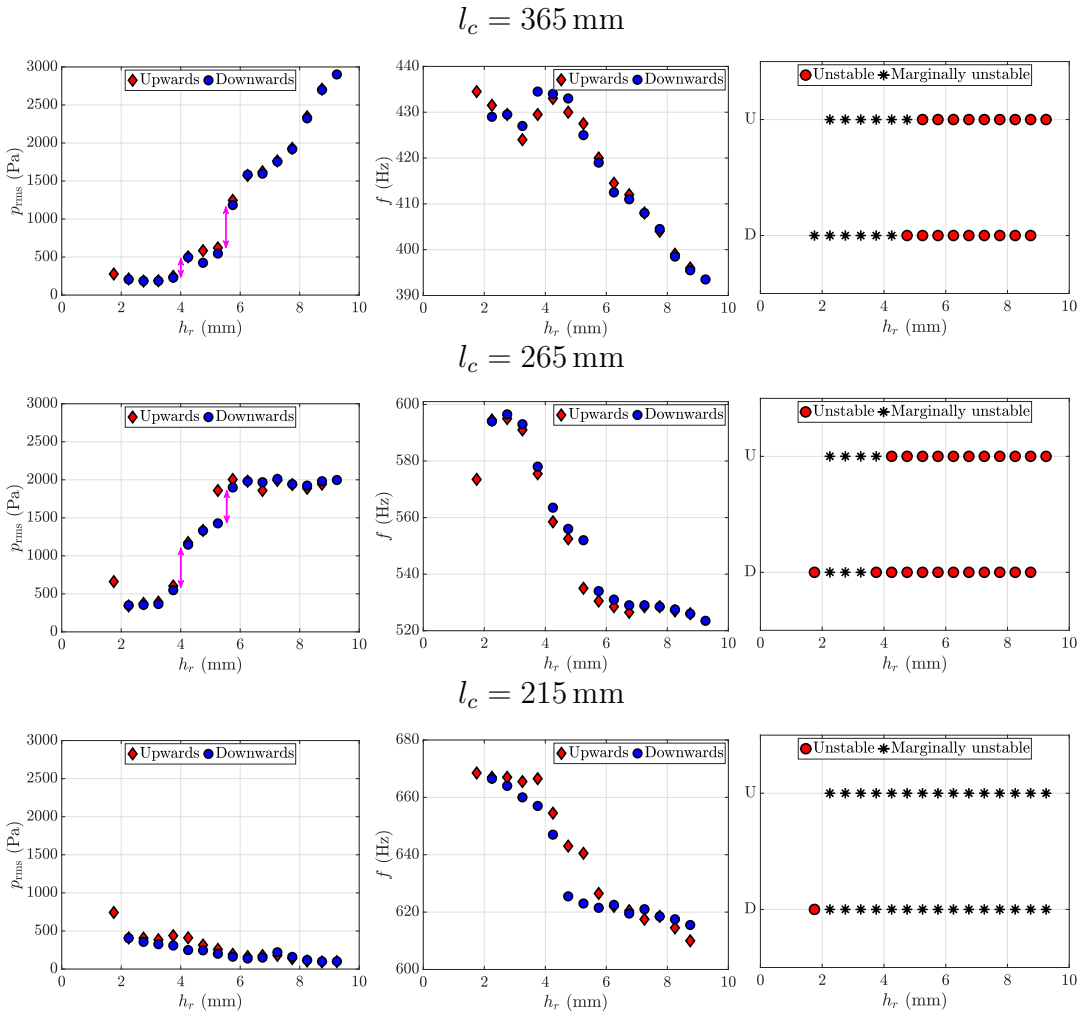

(a) Amplitude *(b) Frequency* *(c) Stability map*

Figure 8.2. *Amplitude (a) and frequency (b) of SSO at three chamber lengths* $365\,\mathrm{mm}$, $265\,\mathrm{mm}$ *and* $215\,\mathrm{mm}$ *and for different recess distances. The vertical arrows in (a) at* $365\,\mathrm{mm}$ *and* $265\,\mathrm{mm}$ *point to the jumps corresponding to changes in the system's state. (c) Stability map at different recess distances. U: Upwards; D: Downwards.*

Figure 8.2 (a) and (b) show the amplitude and frequency of SSO at different atomizer recess distances both for downward (increasing the recess distance) as well as upward movements (decreasing the recess distance). The frequency of oscillation is obtained by considering the peak frequency of the power spectrum, and the root mean square (RMS) pressure amplitude is calculated as the square root of the integrated power spectral density multiplied by the frequency resolution Δf.

At $l_c = 365\,\mathrm{mm}$ and $265\,\mathrm{mm}$, a general tendency of increased amplitude and decreased frequency can be observed as the recess distance h_r is augmented. From

the amplitude map, one distinguishes two jumps (represented by vertical arrows), resulting in three well-defined regions of operation. Each jump could be envisaged as a change in the state of the fuel injection geometry leading to a change in the system behavior. For both chamber lengths, one identifies three zones, the first between $1.75\,\mathrm{mm}$ and $3.75\,\mathrm{mm}$, the second between $4.25\,\mathrm{mm}$ and $5.25\,\mathrm{mm}$, and a final one between $5.75\,\mathrm{mm}$ and $9.25\,\mathrm{mm}$. Amplitude jumps are accompanied by frequency jumps, but this is less apparent in the $l_c = 365\,\mathrm{mm}$ case. No visible hysteresis is seen between the two operations as the system follows the same trajectory between downwards and upwards motion with minor differences existing at the jump locations. The tendency after these jumps is not necessarily the same between the two chamber lengths. At $l_c = 265\,\mathrm{mm}$, the amplitude in each zone appears to reach a plateau, whereas the frequency shows a continuous decrease. At $l_c = 365\,\mathrm{mm}$, the first two jumps result in the plateauing of the amplitude, whereas after the final jump, the amplitude does not plateau but keeps increasing. The frequency monotonically decreases in the first and third zones, whereas it remains nearly constant in the second zone. Although at each recess distance, the system has a slightly higher pressure amplitude at $265\,\mathrm{mm}$, the plateauing of amplitude in the final zone results in a smaller amplitude at the largest recess distance compared to $365\,\mathrm{mm}$, which has a higher amplitude at this state. On the other hand, the instability tendency at $l_c = 215\,\mathrm{mm}$ (third row of Fig. 8.2) differs from that found for the other two chamber lengths. The amplitude is much smaller and exhibits a reverse trend compared to the other two lengths, i.e., the instability amplitude is diminished when the recess distance is increased, and the RMS pressure tends to zero at higher recess distances, as seen from the third row of Fig. 8.2 (a). Unlike the other two cases, no distinct jumps are observed in the amplitude stability map, and the variation occurs gradually with changes in the recess distance. This is probably because the system is already close to its stability limit and any change caused by modifying the recess distance is not sufficient to drastically alter the system's stability domain. The frequency map shows a similar tendency as the other two chamber lengths and decreases when the atomizer recess distance is increased with a jump occurring at $h_r = 4.75\,\mathrm{mm}$.

The unstable regimes displayed in Fig. 8.2 (c) are identified with an instability criterion introduced in Chapter 6, in which the state of the system is compared to a stable baseline configuration corresponding to a chamber length $l_c = 115\,\mathrm{mm}$. Two metrics are computed: one related to RMS pressure amplitude and the other to peak prominence in the power spectrum. When only one of these two criteria is met, the system is deemed marginally unstable. The system is seen to move from a highly unstable operation (indicated by circles) to a marginal instability (indicated by stars) as the atomizer recess distance h_r is diminished at 365 and $265\,\mathrm{mm}$, and the recess distance at which this transition occurs is nearly the same for the two chamber lengths. At the smallest recess distance, p_{rms} is quite low, indicating that the system is approximately stable. At $215\,\mathrm{mm}$, the instability is only marginal at

all the recess distances except when the atomizer is at its closest position to the backplane, where the system becomes unstable.

In order to further understand the behavior of the system at each instability zone, three recess distances are selected at $h_r = 2.75\,\mathrm{mm}$, $4.75\,\mathrm{mm}$, and $6.75\,\mathrm{mm}$, corresponding to each zone. As will be seen later, the extent of spray-wall interaction at each of these locations changes, leading to a modified instability behavior of SICCA-Spray. Detailed measurements at these selected locations are presented in the following sections.

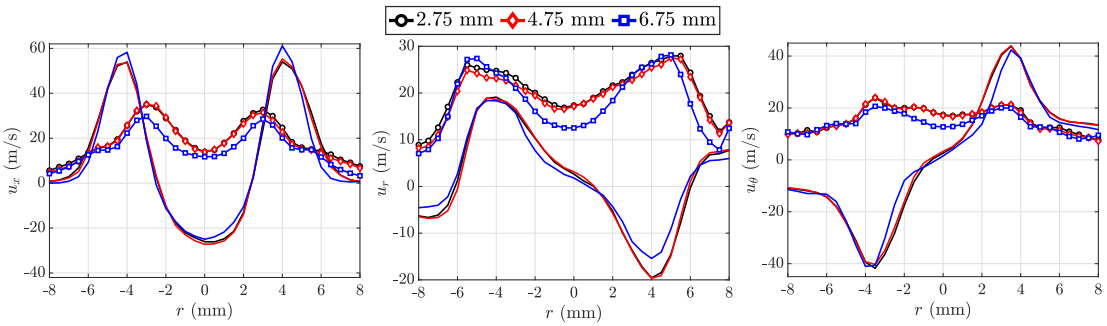

(a) Axial velocity *(b) Radial velocity* *(c) Tangential velocity*

Figure 8.3. *Velocity profiles of the air flow at different radii showing the evolution of the mean (solid line without marker) and RMS (solid line with marker) axial (u_x), tangential (u_θ), and radial (u_r) velocity components at three different recess distances. The measurements are made at* $2.5\,\mathrm{mm}$ *above the backplane with the quartz tube confinement under cold flow conditions with oil seeding.*

8.4 Measurements under steady conditions

It is instructive to successively examine velocity profiles under cold flow conditions, and spray configurations under cold and unconfined conditions using laser light scattering, droplet size distribution in the liquid spray under hot fire conditions, and the corresponding flame images at the three chosen atomizer positions.

8.4.1 Velocity profiles under cold flow conditions

The velocity profiles are measured with the PDPA system under cold flow conditions with a chamber length of $l_c = 150\,\mathrm{mm}$. The air flow is seeded with fine oil droplets to obtain three velocity components at different radii and at a height of $2.5\,\mathrm{mm}$ above the backplane. Figure 8.3 shows the mean and RMS profiles for axial (u_x), radial (u_r), and tangential (u_θ) velocity components. The mean velocity profiles are similar for the three recess distances except for minor differences in the peak of axial and radial components. Contrary to the mean profile, the RMS velocity profiles reveal two distinct categories: one corresponding to $6.75\,\mathrm{mm}$ and

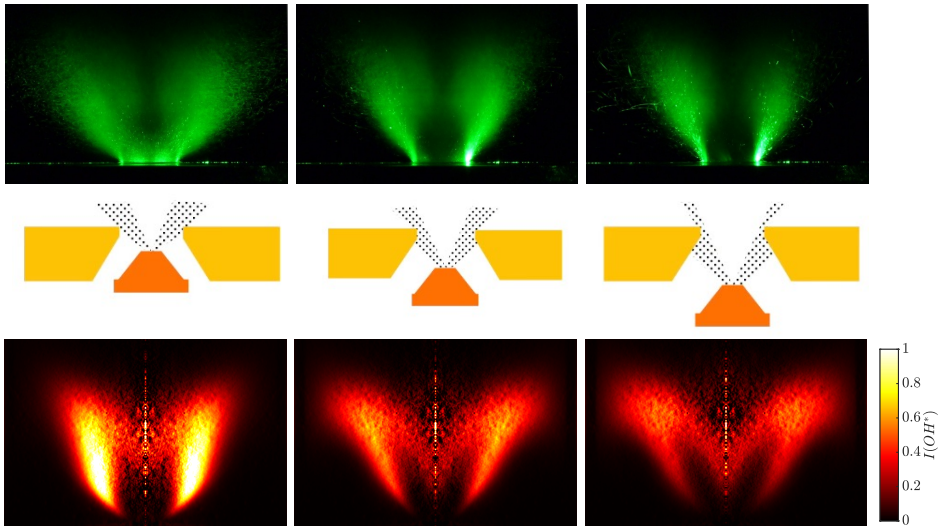

(a) $h_r = 2.75\,\mathrm{mm}$ *(b)* $h_r = 4.75\,\mathrm{mm}$ *(c)* $h_r = 6.75\,\mathrm{mm}$

Figure 8.4. *Top: Spray tomographic images at three atomizer positions obtained by illuminating the liquid spray with a laser light sheet. Middle: Schematic showing mean spray evolution at the three atomizer positions. Bottom: Flame images showing OH* chemiluminescence obtained under steady conditions. An Abel deconvolution algorithm is applied to the images captured by the camera and displayed in false colors.*

the second family belonging to the two smaller recess distances. At $6.75\,\mathrm{mm}$, the atomizer is slightly below the swirler head, but as the recess distance is decreased further, its presence in the air stream causes a minor interference in the flow.

From the measurements of the mean velocity evolution, the swirl number can be calculated by:

$$S_N = \frac{\int_0^{2R_{\mathrm{inj}}} \overline{u}_\theta \overline{u}_x r^2 dr}{R_{\mathrm{inj}} \int_0^{2R_{\mathrm{inj}}} \overline{u}_x^2 r dr} \qquad \text{(1.1 Rep.)}$$

where $R_{\mathrm{inj}} = 4\,\mathrm{mm}$ is the radius at the injector outlet. The swirl numbers calculated using the above equation are $S_N = 0.77$ at $2.75\,\mathrm{mm}$, $S_N = 0.75$ at $4.75\,\mathrm{mm}$, and $S_N = 0.72$ at $6.75\,\mathrm{mm}$. At $h_r = 6.75\,\mathrm{mm}$, the atomizer is slightly below the swirler level, but when the recess distance is further decreased, the atomizer is located in the path of the swirling air flow, likely resulting in a minor variation in swirl number. Although minor differences exist, the velocity profiles reveal no marked changes that might explain the observed behavior at the various recess distances. The next natural step is to explore the spray behavior, which is discussed in the subsequent sections.

8.4.2 Spray tomographic images

The spray images shown in Fig. 8.4 (top row) are obtained under cold flow conditions without chamber confinement. Additionally, an image (not shown here) is obtained by moving the atomizer almost in-level with the backplane to obtain a mean angle of the spray. The spray angle determined in this manner is then used to schematically plot the mean spray evolution as shown in Fig. 8.4 (middle row) at the different atomizer positions. At $h_r = 2.75\,\mathrm{mm}$, the laser sheet scattering images reveal the presence of droplets throughout the region above the backplane, whereas they are scarce close to the injector axis for $h_r = 4.75\,\mathrm{mm}$ and $6.75\,\mathrm{mm}$. This indicates that there are two regions in the spray: one close to the axis, where the droplets are directly issued from the atomizer, and a second close to the edge of the injector outlet, where the fuel spray originates after interaction with the conical section of the terminal plate as shown in Fig. 8.4 (middle row, (b) & (c)). At $h_r = 2.75\,\mathrm{mm}$, the spray directly exits into the chamber with only a small portion impacting the conical end piece. When $h_r = 4.75\,\mathrm{mm}$, the spray is displaced towards the injector periphery with only a small amount of droplets remaining in the central region. At $h_r = 6.75\,\mathrm{mm}$, most of the spray originates from the injector edge. When the atomizer recess is augmented, most of the initial spray hits the conical wall and exits into the chamber along the injector edge. Two possibilities can be envisaged when such a spray-wall interaction occurs. The spray particles hitting the wall might form a liquid film that undergoes secondary atomization due to the shearing action of the inner air flow on one side and by gases recirculating near the chamber backplane on the other side, producing small droplets that are convected away by the flow. This behavior has been modeled in the LES of a similar injector when the fuel injection angle is varied (Lo Schiavo et al. 2021). When the injection angle is augmented, spray-wall interactions lead to the formation of a film and a subsequent film-acoustic coupling that favors instability for certain operating points. The authors observed that when the spray angle is diminished and the spray is directly conveyed into the chamber, the level of instability is reduced, matching the experimental observations shown in the top row of Fig. 8.4. However, as will be seen in the next section, the droplet diameter distribution remains nearly the same at the injector exit at all three recess positions of the atomizer, which might not be the case if a liquid film undergoing subsequent atomization was present. The other outcome of spray-wall interaction might simply be the particles hitting the wall and bouncing back or sliding along the conical wall and being swept away by the air flow. One cannot be sure of the exact mechanism of the interaction, but whatever be the case, it is clear from the spray tomographic images in Fig. 8.4 (top row) that the spatial extent of the spray and possibly the convection time for any specific particle are modified. The laser sheet scattering images also indicate that the spray envelope spans a broad region when $h_r = 2.75\,\mathrm{mm}$, whereas it narrows down as the recess is increased (Fig. 8.4 top row).

8.4.3 Liquid droplet counts and size distributions

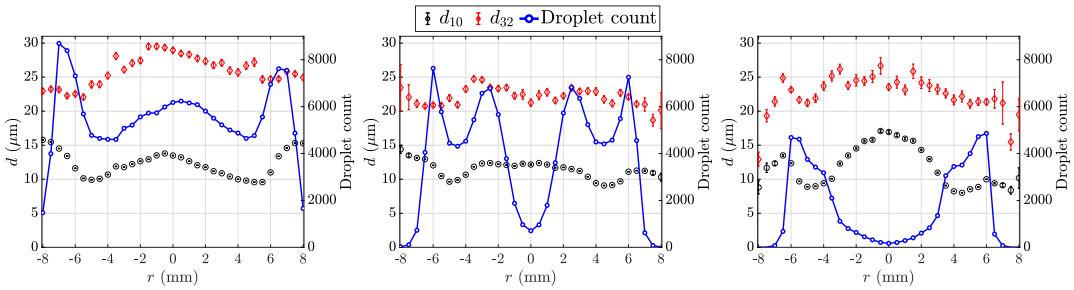

(a) $h_r = 2.75\,\mathrm{mm}$ *(b)* $h_r = 4.75\,\mathrm{mm}$ *(c)* $h_r = 6.75\,\mathrm{mm}$

Figure 8.5. *Granulometry profiles of the liquid spray showing mean diameter (d_{10}) and Sauter mean diameter (d_{32}) measured at different radii and three recess distances. The droplet count acquired by the PDPA system at each radial position is plotted in blue circles. The measurements are made at a height of* $2.5\,\mathrm{mm}$ *above the backplane.*

It is also instructive to examine the droplet profiles in terms of mean diameter (d_{10}) and Sauter mean diameter (d_{32}), as shown in Fig. 8.5 for the three recess values. Size distribution profiles and droplet counts in the spray are measured using PDA at a distance of $2.5\,\mathrm{mm}$ above the backplane. The d_{32} distributions are quite similar, except for $h_r = 2.75\,\mathrm{mm}$, where the spray features larger d_{32} values in the central region. The droplet counts confirm that the droplets are present in a broad region when the recess h_r is small (Fig. 8.5(a)) but that they are evacuated from the central region when h_r is augmented (Fig. 8.5(b)) and essentially absent when h_r takes its largest value (Fig. 8.5(c)). The diameter d_{10} remains nearly the same (around $10\,\mu\mathrm{m}$) at the three atomizer positions close to the injector outlet radius ($R_{\mathrm{inj}} = 4\,\mathrm{mm}$). The size is comparatively higher near the injector center at $6.75\,\mathrm{mm}$, but the droplet count is too low to substantially infer this.

8.4.4 Steady state flame images

The OH* chemiluminescence images of the flame under steady conditions are displayed in Fig. 8.4 (bottom row). These images are obtained by accumulating 35 frames and applying an Abel deconvolution algorithm. The flame images corresponding to the various atomizer recess distances show noticeable differences and can be primarily distinguished by three factors: overall flame shape, the appearance of the side branches, and light intensity. At the smallest recess distance $h_r = 2.75\,\mathrm{mm}$, the flame takes a relatively straight narrow-“M" shape. The flame is characterized by broad upright side branches that are luminous. When the recess distance is increased, the flame widens and takes a slant-“M" shape. The side branches reduce in thickness and have lower luminosity. At the largest recess distance of $h_r = 6.75\,\mathrm{mm}$, the flame widens further, and the side branches are thinner and more inclined. At this position, the flame retains an overall slanted “M" shape

with two low-intensity lobes at the top of the side branches. When the atomizer is close to the outlet, there is a greater density of droplets near the axis (see Fig. 8.5). As a result, combustion occurs in the central area, leading to narrower flames with higher intensity. This is also observed in the LES calculations of the SICCA-Spray combustor by Lo Schiavo et al. (2021).

8.5 Measurements with flame modulation

The previous section described the behavior of SICCA-Spray under steady operating conditions. It is next logical to identify the differences in the flame response through external acoustic modulation at the selected recess distances. This is done by first considering the flame images at different phase instants of the acoustic cycle. This is then followed by the determination of the FDF.

8.5.1 Flame images with acoustic modulation

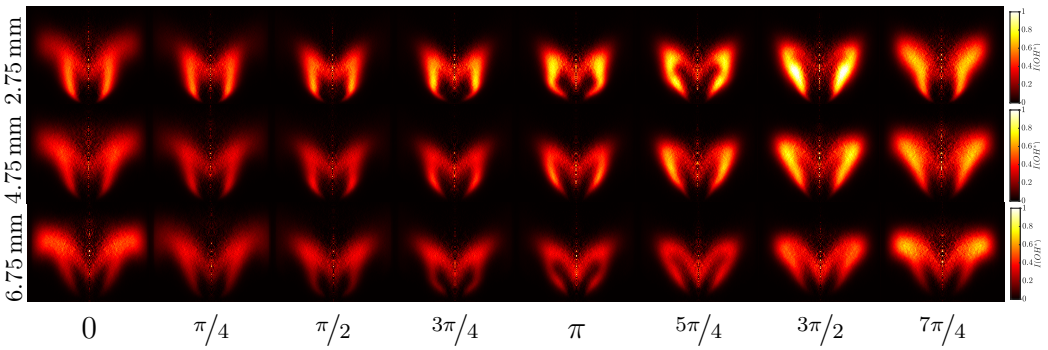

Figure 8.6. *Flame images showing OH* chemiluminescence obtained when modulating the flame at* $500\,\mathrm{Hz}$ *with* $u'_{c,r}/\overline{u}_{c,r} \approx 25\%$*. An Abel deconvolution algorithm is applied to the images captured by the camera and displayed in false colors. The images are plotted at different phase instants of the wave generator signal* φ_g*, mentioned at the bottom.*

Phase average flame images are obtained using the ICCD camera with an OH* filter when the flame is modulated at $500\,\mathrm{Hz}$ with an amplifier voltage of $3\,\mathrm{V}$ resulting in $u'_{c,r}/\overline{u}_{c,r} \approx 25\%$. Figure 8.6 shows the OH*-Abel transformed images at different phase instants of the wave generator signal φ_g. Overall, the flame size appears to diminish between $\varphi_g = \pi/4$ to $\varphi_g = \pi$, after which its size increases, as observed for all the atomizer positions. However, the flame shapes vary for the different recess values at any particular phase instant. The flames corresponding to h_r $=2.75\,\mathrm{mm}$ feature a "claw"-like shape near its anchor point at many phase instants. This feature is absent at $6.75\,\mathrm{mm}$, and it is weakly present at a few phase instants for $4.75\,\mathrm{mm}$. On the other hand, the flame at $6.75\,\mathrm{mm}$ features wings at its top, which are absent at $2.75\,\mathrm{mm}$, but feebly present at some phase instants

for $4.75\,\mathrm{mm}$. Thus, the flames at $4.75\,\mathrm{mm}$ possess the characteristics of flames at $2.75\,\mathrm{mm}$ and $6.75\,\mathrm{mm}$, which could not be previously identified in the steady flame images (Section 8.4.4).

8.5.2 Flame describing functions (FDFs)

Heat release rate fluctuations play a central role in combustion instability analysis. In spray flames, these fluctuations mainly caused by velocity and equivalence ratio disturbances and may be expressed as:

$$\dot{Q}'/\overline{\dot{Q}} = \mathcal{F}_v(u'_{c,r}/\overline{u}_{c,r}) + \mathcal{F}_\phi(\phi'/\overline{\phi}) \tag{8.1}$$

where $\mathcal{F}_v$ and $\mathcal{F}_\phi$ represent describing functions with respect to relative velocity and equivalence ratio fluctuations. As indicated in Chapter 4, the velocity fluctuation is measured at $r = 4\,\mathrm{mm}$, corresponding to the location where relative velocity fluctuations equal the relative volume flow rate fluctuations for swirler 726. At this point, the droplet count is sufficient to retrieve the RMS velocity, and the fuel droplets are small enough to follow the air flow with a negligible phase delay. Experiments described in Chapter 2 indicate that with a larger recess distance, the relative equivalence ratio fluctuations are weak compared to the velocity fluctuations, so that one may assume, as a first approximation, that the corresponding term may be neglected and link the relative fluctuations in heat release rate to the relative fluctuations in velocity only through: $\mathcal{F}_v(\omega, |u'_{c,r}/\overline{u}_{c,r}|) = (\dot{Q}'/\overline{\dot{Q}})/(u'_{c,r}/\overline{u}_{c,r})$. In the absence of equivalence ratio fluctuations, the light intensity fluctuations of the OH^* radical $I'(OH^*)/\overline{I}(OH^*)$ are known to approximately represent the relative fluctuations in heat release rate $\dot{Q}'/\overline{\dot{Q}}$. In essence, we consider that the spray flames operate in a quasi-premixed mode because the droplets sizes are small, heptane is highly volatile, and the atomizer is in recess with respect to the injector outlet. However, as shown in Chapter 2, when the recess is reduced to lower values, the equivalence ratio fluctuation level may become significant, and this is admittedly a limitation of the current measurements. Thus, the following describing function data are only meant as an approximate portrayal of the flame response to incident velocity disturbances.

Figure 8.7 shows the FDF in terms of gain G_F and phase φ_F at the three recess distances. Due to the difference in flame shape shown in Fig. 8.4, one naturally expects that differences will be manifested in the FDF as well. At $h_r = 2.75\,\mathrm{mm}$, the gain remains relatively flat until $600\,\mathrm{Hz}$, beyond which there is a moderate increase. The gain has a slightly higher value at $4.75\,\mathrm{mm}$ and takes the highest value when the atomizer is at $6.75\,\mathrm{mm}$. At this position, the gain notably depends on the fluctuation level. For the operating regimes considered here, there is almost no dependence of the phase on velocity fluctuation level, except close to $600\,\mathrm{Hz}$ for $2.75\,\mathrm{mm}$ and at low velocity fluctuation levels for $6.75\,\mathrm{mm}$. The phase curve

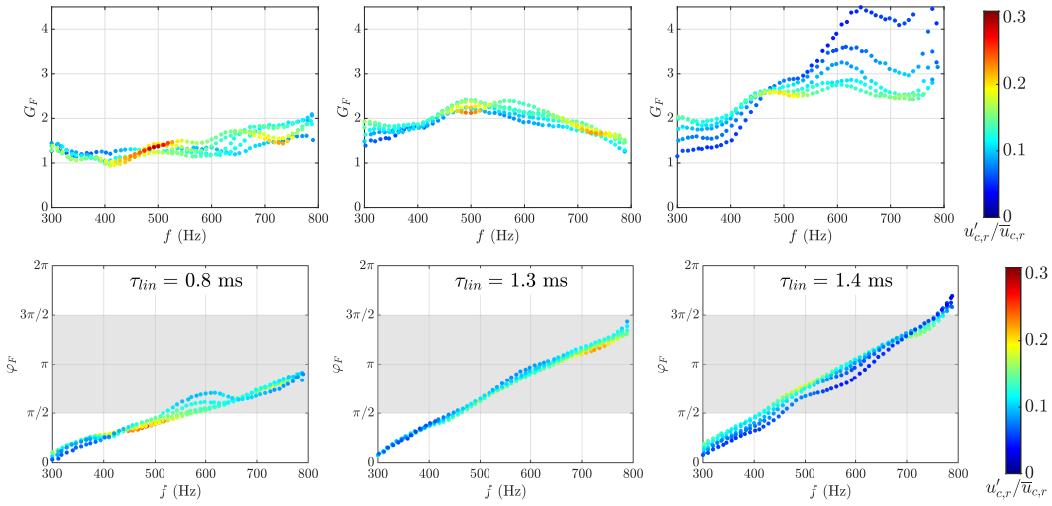

(a) $h_r = 2.75\,\mathrm{mm}$ *(b)* $h_r = 4.75\,\mathrm{mm}$ *(c)* $h_r = 6.75\,\mathrm{mm}$

Figure 8.7. *Flame describing function gain G_F (top) and phase φ_F (bottom) for the three atomizer recess positions. The color scale represents the level of velocity fluctuations measured at a radius of $r = 4\,\mathrm{mm}$ and at a height of $h = 2.5\,\mathrm{mm}$ from the backplane. $u'_{c,r}$ and $\overline{u}_{c,r}$ are respectively the RMS and mean velocity. The gray bands indicate the approximate location of unstable bands. The time delay τ_{lin} indicated in the bottom row is calculated by considering a linear evolution of the phase curve.*

slope changes at the various atomizer positions. By approximating a linear evolution, a time delay τ_{lin} can be calculated from the phase curves, and its values are indicated in Fig. 8.7. The delay is smallest at $2.75\,\mathrm{mm}$, while it is higher for the recess distances of $4.75\,\mathrm{mm}$ and $6.75\,\mathrm{mm}$. It is known that the phase evolution has a major impact on the instability of the system (Schuller et al. 2020), as it determines whether or not a particular frequency falls within an unstable band. With similar injectors that are weakly transparent to acoustic waves, it is shown in Chapter 5 that the unstable bands primarily depend on the phase of the impedance φ_ζ imposed by the injector at its outlet. Thus to obtain the unstable bands, the impedance is measured during an SSO with $l_c = 365$ and $265\,\mathrm{mm}$ (instability frequency in the range $420\,\mathrm{Hz}$–$600\,\mathrm{Hz}$), when the system mostly exhibits limit cycle oscillations. It is recalled here that ideally, the impedance measurements must be done when modulating the system from downstream, but the experiments are instead carried out under SSO due to the limitations of the test rig. The measured impedance details are given in Appendix 1, from where it can be seen that its phase is approximately $\varphi_\zeta \approx \pi$ at most frequencies. Considering this value for the impedance phase and using the model proposed in Chapter 5, the unstable band is located between $\pi/2$ to $3\pi/2$ (mod 2π) and superimposed on the phase curves in Fig. 8.7. At $h_r = 2.75\,\mathrm{mm}$, the phase curve enters the unstable band around $580\,\mathrm{Hz}$ when the velocity fluctuation level is highest. The instability frequency reported

in Section 8.3 at this atomizer position is below $590\,\mathrm{Hz}$ at $l_c = 365$ and $265\,\mathrm{mm}$, which is just at the lower limit of the unstable band. This potentially explains the marginal instability observed at this atomizer position. However, at $l_c = 215\,\mathrm{mm}$, the instability frequency is above $600\,\mathrm{Hz}$, and the FDF phase curves begin to fall inside the unstable band indicating why the SSO amplitude is slightly higher at this chamber length. At $h_r = 4.75$ and $6.75\,\mathrm{mm}$, the phase curves cross the unstable band at a lower frequency ($\approx$ 450 Hz), indicating that a system having an acoustic mode at frequencies higher than $450\,\mathrm{Hz}$ and lower than 750–800 Hz may develop a self-sustained oscillation, provided that the gain is sufficiently high, which is the case for these two atomizer positions. This corresponds to what is observed during the SSOs reported in Section 8.3.

However, this analysis does not explain the nearly-stable behavior when the recess distance is larger at $l_c = 215\,\mathrm{mm}$ (see third row and first column of Fig. 8.2). This discrepancy could perhaps be because the injector impedance is measured at a different frequency range, and the actual unstable bands corresponding to the eigenfrequencies of $215\,\mathrm{mm}$ could be lower. As seen in Chapter 6, the limits of the unstable band may depend upon the frequency/amplitude of oscillation for a particular swirler, and the lower limit can, in fact, be as low as $\pi/4$, in which case, the upper limit will be close to $5\pi/4$. In the higher frequency range, the unstable band is perhaps displaced to lower phase values, and the unstable range where the phase curve would cross the unstable band might not coincide with the frequency of oscillation corresponding to the chamber 1L mode, eventually resulting in a stable operation at larger recess distances.

8.6 Conclusions

This article describes the effects of spray dynamics on combustion instabilities through experiments carried out on a single swirl injector combustor fueled by a liquid-heptane pressure atomizer. By varying the fuel atomizer position in the axial direction, one observes three distinct instability zones, characterized by jumps in amplitude and frequency at two of the chamber lengths tested. The amplitude of instability decreases when the atomizer recess is diminished, indicating that the system can be stabilized by moving the atomizer towards the injector outlet. However, these observations are reversed at a chamber length corresponding to higher eigenfrequencies where the instability is only marginal and the amplitude increases when the atomizer recess is diminished. Light scattering images indicate that the spray interaction with the conical exit section of the injector plays a key role. When the atomizer is recessed deep inside the injector, the spray impinges on the conical section, whereas this process is reduced when the atomizer is closer to the outlet, thus modifying the spatial dispersion of the droplets and possibly the convection time of the particles. In turn, this is manifested in the flame shape, flame dynamics, and flame describing function. A smaller recess distance results

in a lower gain and a shorter delay. When the recess distance is increased, the delay is enhanced, and the FDF phase is within a band of instability for certain frequency ranges corresponding to the system's eigenmode. At the same time, the gain takes larger values, possibly explaining why the system becomes highly unstable. The present data indicate that small changes in the injector geometry can substantially impact the system dynamics. The extent of such variations depends on the operating regime. This study, therefore, constitutes an interesting test case in the development of instability prediction tools and may also serve in devising control techniques for instability suppression.

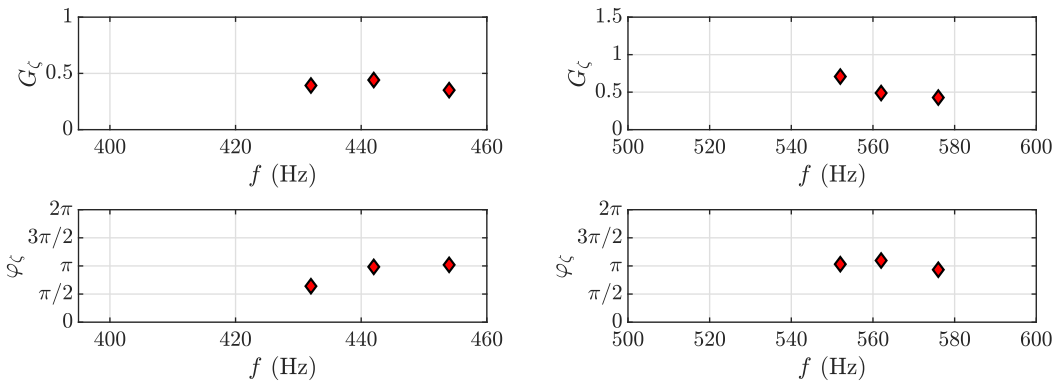

(a) $l_c = 365\,\mathrm{mm}$ *(b)* $l_c = 265\,\mathrm{mm}$

Figure 8.8. *The modulus* G_ζ *and phase* φ_ζ *of the injector impedance measured in SICCA-Spray at* $l_c = 365$ *and* $265\,\mathrm{mm}$*, and at frequencies corresponding to the three atomizer positions of* $h_r = 2.75$*,* 4.75*, and* $6.75\,\mathrm{mm}$*. The highest frequency at each chamber length corresponds to the lowest recess distance and so on.*

Appendix 1: Impedance at the injector outlet during self-sustained oscillations

As indicated earlier in this chapter, the injector impedance is measured when the system features limit cycle self-sustained oscillations at $l_c = 265\,\mathrm{mm}$ and $365\,\mathrm{mm}$. However, the measurements at $h_r = 2.75\,\mathrm{mm}$ are slightly less reliable, and the measurement is not performed at $l_c = 215\,\mathrm{mm}$, as the system only exhibits marginal instability in these cases. Figure 8.8 shows the impedance modulus G_ζ and phase φ_ζ measured at the injector outlet. These values are obtained with the two-step procedure described in Chapter 6. The highest frequency at each chamber length corresponds to the lowest atomizer recess distance and so on. The readers are referred to Fig. 8.2 for the relation between oscillation frequency and recess distance. The impedance phase decides the position of the unstable band and is mostly π in the frequency range considered except below $440\,\mathrm{Hz}$, where the phase is rather close to $\pi/2$. Nevertheless, in the simple analysis using FDFs described in Section 8.5.2, an impedance phase of π is considered to interpret the SSO behavior. The modulus of impedance is always close to 0.5 in the frequency range considered.

Chapter 9

Effect of fuel type on annular combustion dynamics: MICCA-Spray

Contents

This chapter is based in part on an article published as a full-length article with the title, "Effect of different fuels on combustion instabilities in an annular combustor" by Preethi Rajendram Soundararajan, Guillaume Vignat, Daniel Durox, Antoine Renaud and Sébastien Candel in the Journal of Engineering for Gas Turbines and Power, vol. 143, March 2021. Two appendices are included, which were not discussed in the publication. The experimental setup of the MICCA-Spray test rig comprehensively described in Chapter 1 is only briefly recalled in this chapter.

Readers who are familiar with the MICCA and SICCA test facilities can skip this part.

Combustion instability in annular combustors of jet engines is a standing issue. The characteristics of instabilities are investigated here for different fuels by combining the stability maps obtained in a laboratory-scale annular combustor equipped with multiple swirling spray injectors (MICCA-Spray) with flame describing functions (FDFs) determined in a single sector configuration (SICCA-Spray). Two types of liquid fuels are injected as hollow cone sprays: heptane, which is relatively volatile, and dodecane, which is less volatile. Experiments are also carried out with gaseous propane, perfectly premixed with air, which serves as a reference. Stability maps are systematically determined by varying the global equivalence ratio and thermal power. The data indicate that the amplitude and frequency of instabilities depend, for the same operating point, on the fuel injection conditions (premixed or spray) and fuel type. Overall trends show that premixed propane is unstable in a broad operating domain. Injection of liquid fuels induces changes in time lag that modify the unstable regions. For heptane, the stability map is closer to the propane reference map, whereas dodecane exhibits wider stable regions. An attempt is made to understand these features by examining the FDF, which gives the ratio of relative fluctuations in heat release rate to the relative fluctuations in velocity. The unstable bands obtained using a low-order theoretical analysis marked in the FDF phase diagrams are used to determine the stability limits of the annular combustor. In general, the change in time delay associated with the different fuels displaces the phase of the flame response with respect to the instability band, thus modifying the dynamical behavior of the annular combustor.

9.1 Introduction

Combustion instability is most often linked to a time delay between reactant injection and combustion. This delay is associated with convection, mixing, and chemical conversion, and under liquid injection, it is also linked to atomization, vaporization, and droplet momentum relaxation. The present investigation is focused on the role of changes in time lag linked with the injection of three different fuels in an annular combustor. In a reference case, propane premixed with air is injected. In two other cases, heptane and dodecane are atomized in the form of a spray of droplets. Thus, the time lag is modified, and this directly changes the instability characteristics.

At this point, it is worth reviewing the literature that considers delay effects (or equivalently phase effects) on the development of combustion instabilities. In a

pioneering work on the so-called "singing flame", Lord Rayleigh (Rayleigh 1878) provided a stability criterion indicating that acoustic pressure and unsteady heat release rate fluctuations have to be in phase for instabilities to grow. This may be translated in terms of a time delay between acoustic pressure oscillations and heat release rate fluctuations, providing a necessary condition for the growth of thermoacoustic instabilities. The importance of time lags was underlined in the early work on rocket engine instabilities, most notably by Crocco and his co-workers (Crocco 1951; Crocco 1952). It was recognized that the time delay involved in the conversion of liquid fuels to a gaseous state before burning and the additional time lag associated with mixing and reaction of propellants could be sensitive to the instantaneous conditions prevailing in the thrust chamber. This led to the sensitive time lag (STL) theory that was used in many investigations of combustion instabilities. The time lag was considered especially important in the case of liquid fuels as it results from complex processes such as the atomization of fuel droplets followed by vaporization and mixing. Many studies have relied on time lag concepts to derive methods that could be employed to suppress instabilities by suitably timing the liquid fuel injection or controlling other flow parameters, as successfully demonstrated by Lee et al. (2005) & Yu et al. (1998).

The role of the time lag associated with liquid fuel injection has been investigated in many different ways. Zhu et al. (1999), for example, employ numerical tools to analyze the fuel-spray dynamics when the pressure is fluctuating in an aero-engine combustor. It is concluded that the modulations of air flow rates affect the fuel droplet size distribution, thus modifying the fuel-air ratio and thereby changing the time delay. Experiments carried out by Eckstein et al. (2006) on an air-blast atomizer in a rich-quench-lean combustor indicate that the atomizer is sensitive to air velocity fluctuations in the injection unit, generating different droplet sizes, thus varying the combustion delay and related oscillations. Effects of air and liquid fuel flow modulations are examined by Gajan et al. (2007) and Kim et al. (2012) in non-reactive conditions. Gajan et al. (2007) show that modulations of the air stream influence the atomization process generating a droplet density wave with varying evaporation rates. Depending on the convection velocity of this wave, a time lag arises between pressure and heat release rate. Experiments reported by Apeloig et al. (2015) on a multi-point spray injector in an aeronautical combustor indicate that the air flow fluctuations in the injector perturb the atomization process, changing the time delay either amplifying or damping the instabilities. A numerical simulation by Pillai et al. (2020) considers thermoacoustic instabilities in a backward-facing step geometry in which liquid kerosene was injected as a jet in cross-flow. It was found that the fuel flow rate and atomization processes, modulated by the acoustic pressure fluctuations, amplified the instability. The large-eddy simulation (LES) reported by Tachibana et al. (2015) for a single sector aero-engine combustor operating at high pressure with liquid fuel (Jet-A) indicates that only a short time delay is linked to the evaporation and fuel-

air mixing processes. In an experimental investigation of a premixed prevaporized combustor fed with heptane, Bernier et al. (2004) found that the evaporation process occurs simultaneously with droplet convection to the combustion region so that this delay need not be added to the other delays in the analysis of combustion instability. Vignat et al. (2021) used an LES to study a self-sustained combustion oscillation in the single injector test rig, SICCA-Spray and reached a similar conclusion. However, this might not apply to fuels that are less volatile than heptane.

The preceding studies indicate that it is worth examining instability characteristics that may be linked to the nature and physical state of the fuel to identify the time lags' origins, comparing them with those of purely gaseous and premixed injection and sorting out consequences in terms of instability. Although time lag effects associated with liquid fuels are relatively well documented in the combustion instability literature, the number of studies that deal with liquid sprays in annular combustors is more limited. The annular configuration has, however, considerable importance because it is commonly found in jet engines and gas turbines. The presently studied MICCA-Spray annular combustor at the EM2C laboratory has been found to exhibit large amplitude azimuthal instabilities in the past when it is fed with liquid fuel (Prieur et al. 2018; Vignat et al. 2020). Another annular rig used by the team of Dawson & Worth at NTNU is only operated with gaseous fuel (Worth and Dawson 2013a; Worth and Dawson 2013b). Investigations carried out on these combustors have revealed different modes of azimuthal instabilities such as standing, spinning (clockwise or counterclockwise), and slanted (Bourgouin et al. 2015b). There are, in addition, some interesting LES of industrial annular combustors with spray injection (Wolf et al. 2009; Staffelbach et al. 2009) and a number of more theoretical investigations (Bauerheim et al. 2015; Ghirardo and Juniper 2013) of instabilities in annular chambers. The MICCA-Spray test rig has also been used (Prieur et al. 2017) to examine ignition dynamics under premixed propane, heptane, and dodecane injection, and it was concluded that the light-round time delay is maximum for less volatile fuel, indicating that evaporation induces additional time lags. As an extension to the previous studies, the current work focuses on azimuthal instabilities in the MICCA-Spray annular system using three different fuels. Propane (C_3H_8), fully premixed with air, is considered as the reference, as it features no mixing, atomization, or evaporation delays. Two liquid fuels are considered, heptane (C_7H_{16}) which is relatively volatile ($T_{\text{boil}} = 371\,\text{K}$) and is closer to the reference case, and dodecane ($C_{12}H_{26}$), a heavier fuel that is less volatile ($T_{\text{boil}} = 489\,\text{K}$) and hence has a longer vaporization time than heptane. Developing a complete understanding of the underlying mechanism of instabilities in an annular combustor is quite challenging, and hence it is worth examining the phenomenon in a simplified single-injector system that resembles one sector of the annular combustor. A familiar way to understand the flame dynamics and its response to acoustic perturbations is by measuring the flame transfer function (FTF) or flame describing function (FDF) (Dowling 1997; Noiray et al. 2008).

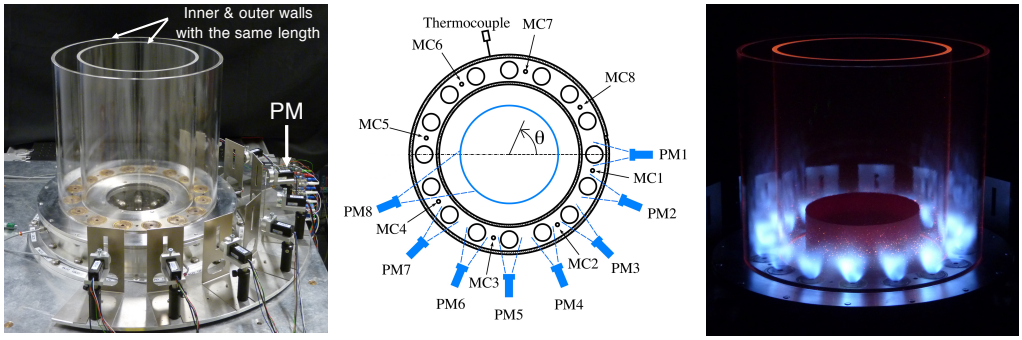

Figure 9.1. *From left to right: (a) Photograph of the MICCA-Spray test rig. (b) Schematic top view of the combustion chamber showing the locations of chamber microphones (MCx), the arrangement of photomultipliers (PMx), and the position of wall mounted thermocouple. The baseline for azimuthal angle is taken along the centerline of injector 1 and the positive angular direction is oriented in the counterclockwise direction. (c) Photograph of MICCA-Spray during operation. Reproduced from Chapter 1.*

The FDF determined in a single-sector configuration can then be used to interpret the observations in the MICCA-Spray configuration, similar to Chapter 7.

This chapter begins with a brief recollection of the experimental setup of the MICCA-Spray annular configuration and of single-injector arrangement (SICCA-Spray) that is used for FDF measurements. Readers who are familiar with the construction of these test rigs can skip this part. Results of instability experiments in MICCA-Spray are systematically examined by varying the fuel types, equivalence ratio, and thermal power. The next section describes the FDFs obtained for the different fuels at three operating conditions in SICCA-Spray. The relation between MICCA-Spray instabilities and FDF results is then explored using the simplified model discussed in Chapter 5. Appendix 1 shows the FDF measurement in SICCA-Spray with heptane and dodecane at F1 and F3. Appendix 2 discusses the stability maps of MICCA-Spray with other swirler units operated with the three fuels, and finally, Appendix 3 shows the flame images obtained in SICCA-Spray with different swirlers.

9.2 Experimental setup

The two experimental setups used in this chapter are briefly reviewed in what follows. For a detailed description, the readers are referred to Chapter 1.

9.2.1 MICCA-Spray

The MICCA-Spray setup (shown in Fig. 9.1) comprises sixteen injectors equipped with swirler 716 for the current study. The liquid fuels are delivered by the hollow-cone atomizer mounted at a distance of $h_r = 6.75\,\mathrm{mm}$ from the combustor backplane. While operating with premixed propane, this atomizer remains unused and gaseous propane is premixed with air before it enters the plenum. The combustion chamber consists of two concentric, cylindrical, and vertical quartz walls of height $400\,\mathrm{mm}$, each with a thickness of $8\,\mathrm{mm}$. Ignition is achieved by a spark plug introduced from the top of the chamber and removed before the measurements to ensure rotational symmetry in the system's geometry. The eight microphones in the chamber (MCx) and the four microphones in the plenum (MPx) record the acoustic pressure signals in the system at a sampling rate of $f_s = 32{,}768\ \mathrm{Hz}$. A set of eight PMs (PMx) records the light intensity fluctuations from the flames, but the acquired measurements are not used in the present study. Previous investigations in MICCA-Spray (Prieur et al. 2018) indicate that the instability depends on the wall temperature. This temperature and the thermal stability of the system are monitored with a K-type thermocouple mounted on the outer wall of the chamber.

9.2.2 SICCA-Spray

To interpret the self-sustained instabilities of MICCA-Spray, it is instructive to measure FDF in a single-sector device, namely SICCA-Spray. This setup uses the same injection unit as that of MICCA-Spray and operates with the same three fuels. A schematic of the experimental setup is shown in Fig. 9.2. When used in premixed conditions, propane is mixed with air at a distance of approximately $1\,\mathrm{m}$ from the plenum by a cyclone mixer. The combustion chamber of SICCA-Spray has an internal diameter of $69\,\mathrm{mm}$ and is $150\,\mathrm{mm}$ long for the experiments reported in this chapter. This length ensures that the flame operates in a stable fashion allowing external modulation. Three microphones (designated as MP1 to MP3) measure the acoustic pressure in the plenum and are also employed to deduce the acoustic velocity using the multi-microphone method (Chung and Blaser 1980; Seybert and Ross 1977). A hot wire anemometer complements the velocity measurements in the plenum. The measurements of velocity in the chamber with liquid fuels are carried out using a phase Doppler particle analyzer (PDPA) operating in laser Doppler anemometry (LDA) mode. These measurements are carried out directly on the spray of liquid droplets resulting in a “direct" FDF. However, for the case of premixed propane, flow seeding is not possible, and a two-step procedure is adopted to determine an “indirect" FDF. This method involves obtaining the injector describing function under cold flow conditions and separating this from the combined injector and flame describing function obtained in the presence of flame. The readers are referred to Chapter 4 for a discussion on direct and indirect FDFs. A photomultiplier equipped with an OH* filter measures the flame chemi-

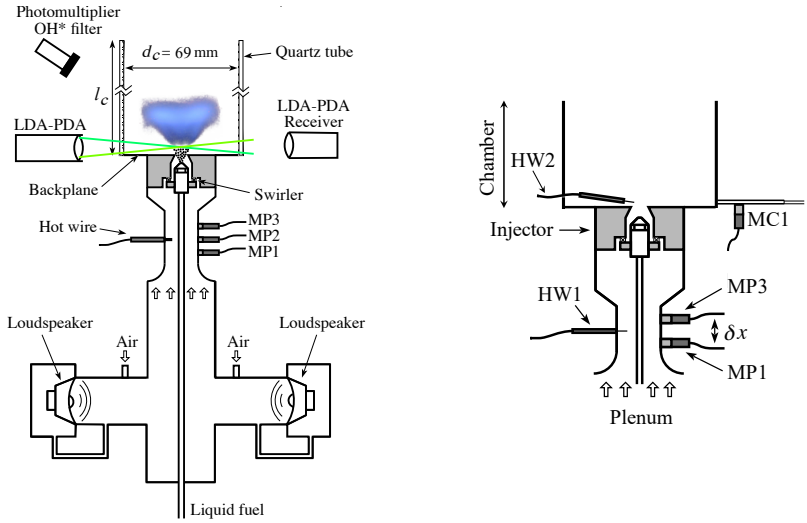

Figure 9.2. *(a) Schematic of the experimental setup SICCA-Spray used for direct FDF measurements. (b) Schematic of the experimental setup used for measuring injector describing function in SICCA-Spray. The measurements are obtained under cold conditions. Only the chamber and the plenum section containing the pressure and velocity measurement devices are shown. Reproduced from Chapter. 1.*

luminescence which is considered to approximately represent the heat release rate of the flame. In order to vary the amplitude of fluctuations for FDF measurements, the driver units mounted at the bottom of the plenum are modulated at six different voltage levels V_0 ($0.5\,\mathrm{V}$ to $3\,\mathrm{V}$ in steps of $0.5\,\mathrm{V}$), and a linear frequency sweep is performed from $250\,\mathrm{Hz}$ to $850\,\mathrm{Hz}$, at each level, for a time duration of $133\,\mathrm{s}$. This procedure defines different levels of acoustic velocity fluctuations at the base of the flame.

Additionally, an intensified CCD camera (PI-MAX) with an OH* filter and 1024×1024 spatial resolution is used to capture the time-averaged images of the flame shown in this chapter. The PDPA system is also used for measuring the droplet size when operating in phase Doppler anemometry mode. Measurements are performed at $z = 5\,\mathrm{mm}$ above the chamber backplane in cold, unconfined conditions at fuel and air mass flow rates corresponding to F1 ($\dot{m}_f = 520\,\mathrm{g\,h^{-1}}$ and $\dot{m}_a = 2.6\,\mathrm{g\,s^{-1}}$). Figure 9.3 shows the distribution of the mean diameter (d_{10}) and Sauter mean diameter (d_{32}) at different locations above the backplane of the injector. It can be observed that there is not much variability in the droplet diameters ensuing from the spray between heptane and dodecane. This eliminates the possibility of any variations between the two flames that could be due to a difference in the atomization quality.

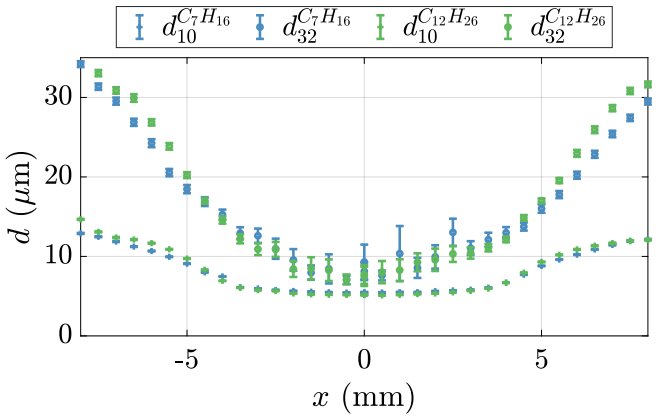

Figure 9.3. *Mean diameter (d_{10}) and Sauter mean diameter (d_{32}) at different radial locations and at a height of $z = 5\,\mathrm{mm}$ above the backplane of SICCA-Spray. $r = 0$ represents the center of the injector and the error bars on the plot represent the statistical standard errors in the measurements. These measurement are carried out under cold, unconfined conditions at flow rates corresponding to F1.*

9.3 Stability maps of MICCA-Spray

The stability maps of MICCA-Spray are determined from a total of thirty different operating points (in terms of global equivalence ratio, ϕ, and thermal power, $\mathcal{P}$) for the three fuels. The fuel flow rate is fixed for each thermal power, and the air flow rate is changed to sweep the range of global equivalence ratios or, equivalently, the range of fuel-air ratios. The translation between global equivalence ratio to fuel-air ratio can be obtained by multiplying ϕ by the fuel-air ratio at stoichiometric conditions, $\varkappa$. The value of $\varkappa$ is 0.0641 for propane, 0.0662 for heptane, and 0.0669 for dodecane. Different acoustic instabilities may appear in the combustion chamber depending on the operating points. There may be 1L type longitudinal modes or 1A-1L type azimuthal-longitudinal modes as the combustion chamber is open to the atmosphere. In the present study, the operating conditions corresponding to 1L modes were not considered. The operating points examined only resulted in stable operation or in oscillations coupled by 1A1L modes. It is convenient to recall that the acoustic pressure signal near the combustor backplane during an instability coupled by a 1A1L azimuthal mode is a combination of two waves:

$$p_c'(\theta,t) = A^+ \exp\left(\mathrm{i}\theta - \mathrm{i}\omega t\right) + A^- \exp\left(-\mathrm{i}\theta - \mathrm{i}\omega t\right) \qquad \text{(7.1 Rep.)}$$

Here, p_c' is the instantaneous pressure signal that can be obtained from the microphone measurements, A^+ and A^- represent the amplitudes of counterclockwise and clockwise spinning components of the 1A1L azimuthal acoustic mode, respectively, and θ is the azimuthal angle as defined in Fig. 9.1. From the reconstructed amplitude values of counterclockwise and clockwise waves, it is possible to de-

duce an instability amplitude that is spatially averaged over eight microphone signals and temporally averaged over $16\,\mathrm{s}$ recordings. This amplitude is proportional to the root mean square (RMS) amplitude averaged over the annular cross-section given by Vignat et al. (2020) and is calculated as

$$\mathcal{A} = (|A^+|^2 + |A^-|^2)^{1/2} \qquad \text{(7.2 Rep.)}$$

$\mathcal{A}$ is an indicator of the level of instability that is independent of the structure of the acoustic mode and is used here as a metric to compare the instability behavior of MICCA-Spray with the three fuels (similar to Chapter 7). The individual wave amplitudes are determined from the pressure signals measured by the eight chamber microphones (MC1-MC8). The microphone signals are bandpass-filtered between $500\,\mathrm{Hz}$ to $1100\,\mathrm{Hz}$, and the time-resolved analytical signals are constructed using the Hilbert transform. The wave amplitudes are determined with the method developed by Vignat et al. (2020) up to the third order in azimuthal harmonics for better fidelity in terms of pressure field reconstruction. The amplitude calculated using Eq. 7.2 Rep. at various operating points is interpolated to derive stability maps for MICCA-Spray, as shown in Fig. 9.4 (left). The case of 716 with heptane was already shown in Chapter 7 and is reproduced here to facilitate comparison. In the operating regime considered, premixed propane features broader unstable regions with higher $\mathcal{A}$ values (red & yellow shades). The maximum amplitude value $\mathcal{A} \approx 1460\,\mathrm{Pa}$ is reached at $\mathcal{P} = 110\,\mathrm{kW}$ and $\phi = 0.85$. Comparatively narrower regions of instability are found for heptane, but its maximum amplitude is the highest among the three fuels, $\mathcal{A} \approx 1670\,\mathrm{Pa}$, and corresponds to $\mathcal{P} = 110\,\mathrm{kW}$ and $\phi = 1.05$. Dodecane exhibits the narrowest unstable region with a maximum amplitude $\mathcal{A} \approx 1500\,\mathrm{Pa}$ occurring at $\mathcal{P} = 118\,\mathrm{kW}$ and $\phi = 0.9$. At the lowest global equivalence ratio ($\phi = 0.75$), the oscillation amplitude is low, indicating that the system is stable at this point irrespective of the fuel being used. For the lowest power ($\mathcal{P} = 93\,\mathrm{kW}$), propane is mostly unstable, whereas the liquid fuels are always stable (indicated by blue regions). For a given power ($\mathcal{P} = 110\,\mathrm{kW}$), propane features a high level of oscillation at a leaner point ($\phi = 0.9$), while heptane exhibits a maximum level at a richer condition ($\phi = 1.05$). Such a trend is not observed for dodecane. In summary, the stability maps indicate that, in the operating conditions and for the injector considered (i.e., swirler 716), the system is most unstable when operated with premixed propane and air, followed by heptane and then dodecane, and the extent of the instability region narrows down as the time delay associated with liquid fuel atomization, and vaporization is augmented.

The frequency of instability is deduced from the power spectral densities of pressure signals, which are calculated by averaging $M = 64$ periodograms using Hamming windows of $N = 4096$ data samples with 50% overlap, resulting in a frequency resolution $\Delta f \approx 2\,\mathrm{Hz}$. The interpolated frequency map is shown in Fig. 9.4 (right). Propane has a maximum frequency value of $840\,\mathrm{Hz}$, followed by heptane, which has a slightly lower peak frequency at $816\,\mathrm{Hz}$. Dodecane has the

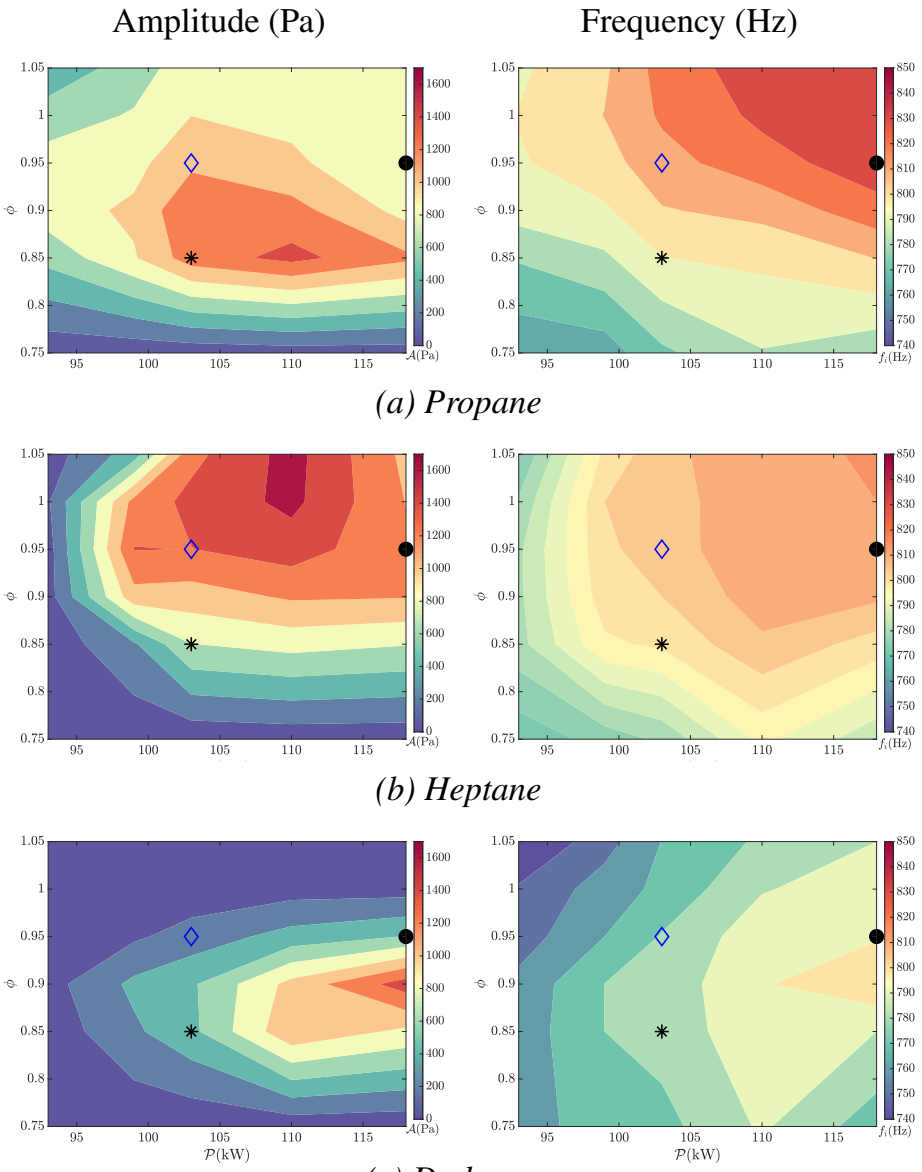

(a) Propane

(b) Heptane

(c) Dodecane

Figure 9.4. *Stability maps of MICCA-Spray showing the amplitude (left) and frequency (right) of instability at different operating points for the three fuels. The measurements are performed at five thermal powers ($\mathcal{P} \approx 93\,\mathrm{kW}$, $99\,\mathrm{kW}$, $103\,\mathrm{kW}$, $110\,\mathrm{kW}$, $118\,\mathrm{kW}$) and at each thermal power six equivalence ratios are considered ($\phi = 0.75, 0.85, 0.9, 0.95, 1.0, 1.05$). The black star, blue diamond and black circle respectively correspond to operating points F1, F2, and F3 used for FDF measurements in SICCA-Spray (Tab. 9.1).*

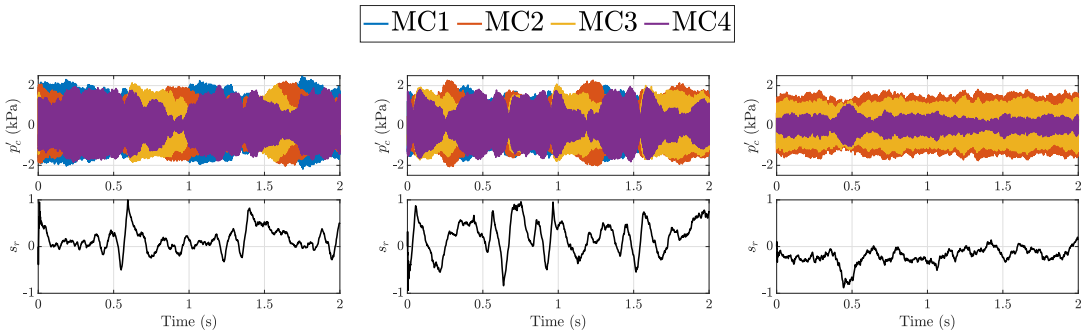

(a) Propane ($\mathcal{A} \approx 1274\,\mathrm{Pa}$ & $f_i = 813\,\mathrm{Hz}$)

(b) Heptane ($\mathcal{A} \approx 1227\,\mathrm{Pa}$ & $f_i = 813\,\mathrm{Hz}$)

(c) Dodecane ($\mathcal{A} \approx 1065\,\mathrm{Pa}$ & $f_i = 800\,\mathrm{Hz}$)

Figure 9.5. *A typical time evolution of MICCA-Spray chamber pressure signals and spin ratio at the same operating point ($\mathcal{P} = 110\,\mathrm{kW}$ and $\phi = 0.9$) for the three fuels. The amplitude and frequency of instability are also indicated for each fuel at this operating point.*

lowest maximum frequency value of $808\,\mathrm{Hz}$. It is next interesting to examine the spin ratio corresponding to the three fuel injection conditions. This ratio defined in Bourgouin et al. (2015b) is deduced from the wave amplitudes as

$$s_r = (|A^+| - |A^-|)/(|A^+| + |A^-|) \qquad \text{(7.3 Rep.)}$$

Its value is such that when $s = 0$, the mode is standing while $s = 1$ or $s = -1$ represents a spinning mode in counterclockwise or clockwise directions, respectively. A point is chosen in the stability map ($\mathcal{P} = 110\,\mathrm{kW}$ and $\phi = 0.9$) where the three fuels have nearly the same amplitude to present the typical pressure signals from the four chamber microphones (MC1-MC4) and the temporal evolution of spin ratio (Fig. 9.5). It should be noted that, for the same operating point, the adiabatic temperatures and laminar burning velocities are very close for the three fuels if all the fuels can be considered perfectly prevaporized and premixed with air during chemical conversion (Prieur et al. 2017). From the pressure signals, it can be seen that the oscillation is nearly at a limit cycle. One also finds that the spin ratio time series corresponding to the three fuels differ from each other, showing that the nature of the azimuthal modes coupling the oscillations is influenced by the fuel type.

9.4 Flame describing function measurements

The instabilities observed in MICCA-Spray can be further interpreted by measuring the response of a single flame to acoustic perturbations, as seen in Chapter 7. As already indicated, the FDF measurements are performed in SICCA-Spray at three operating points (shown in Tab. 9.1): two points at $\mathcal{P} \approx 6.4\,\mathrm{kW}$ and at an

Table 9.1. *Three operating conditions for FDF measurement in SICCA-Spray. The bulk velocity u_b, at the injector outlet, is calculated in cold flow conditions as $u_b = \dot{m}_{air}/(\pi\rho_0 R_{inj}^2)$. Reproduced from Chapter 1.*

Operating point	$\mathcal{P}_{\text{sicca}}$	ϕ	$\dot{m}_{\text{air}}$	u_b
	(kW)	(-)	($\mathrm{g\,s^{-1}}$)	($\mathrm{m\,s^{-1}}$)
F1	6.4	0.85	2.6	43
F2	6.4	0.95	2.3	38
F3	7.4	0.95	2.6	43

equivalence ratio of $\phi = 0.85$ and $\phi = 0.95$ (i.e., F1 and F2, respectively), corresponding to a thermal power of $103\,\mathrm{kW}$ in MICCA-Spray; and a third point at $\mathcal{P} \approx 7.4\,\mathrm{kW}$ and at an equivalence ratio of $\phi = 0.95$ (i.e., F3), corresponding to a thermal power of $118\,\mathrm{kW}$ in MICCA-Spray (see Fig. 9.4). Before discussing the FDF measurements, it is interesting to examine the flame images corresponding to the three fuels. The flame images displayed in Fig. 9.6 indicate that there are differences in flame shape between premixed and spray flames. On comparing the three fuels at F1, one sees that in the case of propane, the flame is full "M" shaped, and for heptane and dodecane, it is a hollow "M" with a central trough. The spray conveys the fuel outwards, and there is a relative absence of fuel close to the injector axis. This favors a hollow "M" flame for liquid fuel injection. However, in the case of propane and air, chemical reaction also occurs in the inner shear layer because the fresh mixture in this region has a suitable equivalence ratio, resulting in a full "M"-flame. On comparing the different operating points, the overall flame shape is preserved with some minor variations. The flames are generally more luminous at F2 and F3 than at F1, owing to the higher equivalence ratio of operation. The two central branches are visible for the two liquid fuels at F2 and F3 but are more pronounced in the case of heptane than dodecane. Between F2 and F3, the increase in thermal power causes the flame to be somewhat wider.

Now recalling the FDF definition, which provides the nonlinear response of the flame to the incoming acoustic velocity perturbation:

$$\mathcal{F}(\omega, |u'_{c,r}|) = \frac{\dot{Q}'/\overline{\dot{Q}}}{u'_{c,r}/\overline{u}_{c,r}} = G_F(\omega, |u'_{c,r}|)e^{i\varphi_F(\omega,|u'_{c,r}|)} \qquad \text{(6.1 Rep.)}$$

Here, $G_F = |\mathcal{F}|$ and $\varphi_F = \arg(\mathcal{F})$ are the FDF gain and phase. $\dot{Q}'$, the fluctuation in heat release rate (HRR), and $\overline{\dot{Q}}$, the mean HRR, are deduced from the light intensity of OH^*. As indicated in Chapter 4, the relative velocity fluctuation measurements for the FDF are to be obtained at a radial location of $r = 4\,\mathrm{mm}$ and at a height of $h = 2.5\,\mathrm{mm}$ for swirler 716 so that the equality between rela-

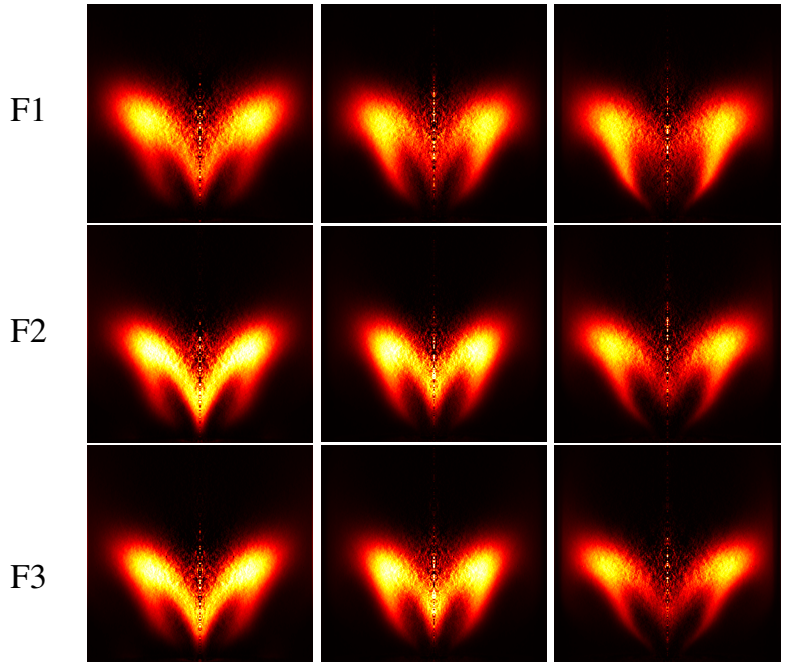

(a) Propane *(b) Heptane* *(c) Dodecane*

Figure 9.6. *SICCA-Spray flame images showing the chemiluminescence of OH* captured using an ICCD camera with the different fuels at all three operating points. A single image is obtained by time accumulation of 30 frames and an Abel transform is applied to these images.*

tive velocity fluctuations and relative volumetric flow rate fluctuations is satisfied. Different levels of velocity fluctuation are obtained during the frequency sweep at a rate of $4.5\,\mathrm{Hz\,s^{-1}}$ for different voltage levels (V_0) of a function generator. The transfer function is obtained from the acquired signals using Welch's periodogram method to calculate the cross-power spectral density between $u'_{c,r}$ and $\dot{Q}'$. The signals at each frequency are divided into 8 segments with Hamming windows and 50% overlap to obtain the gain and phase of the transfer function at f. As indicated earlier, the velocity measurements for the FDF determination are to be carried out at the base of the flame, especially for weakly-transparent injectors. This is straightforward to obtain for the two liquid fuels using LDA. As the spray droplets in the measurement location are small enough, the droplet velocity can be approximated to flow velocity (see Chapter 4) with both heptane and dodecane. However, this is not possible with gaseous propane premixed with air. Hence, the measurements are carried out in two steps to obtain the indirect FDF. In the first step, measurements are carried out with flame, and the velocity fluctuations upstream of the injector are recorded using the microphones and hot wire mounted in the plenum while also acquiring the photomultiplier signals. These data provide a lumped injector and flame describing function $\mathcal{F}_{IF}$ which is shown in Fig. 9.7 at different levels of plenum velocity fluctuation in the case of premixed propane operating at F1. Here, u'_p designates the acoustic velocity fluctuation determined from the two microphone technique or deduced from the hot wire signals, and $\overline{u}_p$ is the bulk velocity that is calculated from the mass flow rate and cross-sectional area in the hot wire section (Fig. 9.2) and takes a value of $2.9\,\mathrm{m\,s^{-1}}$ at F1. The inclusion of injector dynamics in this measurement introduces an injector phase φ_I and gain G_I that needs to be corrected in the FDF measurements. To measure this, two hot wires are used, one in the plenum (HW1–measuring u'_p) and another at a height of $2.5\,\mathrm{mm}$ above the backplane and at a distance of $4\,\mathrm{mm}$ from the axis of the injector (HW2–measuring $u'_{c,r}$), as shown in Fig. 9.2 (b). The measurements to obtain the injector describing functions are performed under cold flow conditions with $l_c = 150\,\mathrm{mm}$. A frequency sweep (same as for $\mathcal{F}_{IF}$ measurements) with varying levels of amplitude was performed, and the velocities from the two hot wires are measured. Figure 9.8 shows the variation of G_I and φ_I at F1 with respect to frequency for the various loudspeaker forcing voltages. From the figure, it can be seen that the value of the gain changes beyond $400\,\mathrm{Hz}$ when the amplifier voltage is different, but the value of the phase features only minor variations with amplifier voltage. It is recalled that a specific amplifier voltage establishes a particular level of relative velocity fluctuation in the plenum and at the injector outlet, depending on the frequency of modulation. Using these measurements, the describing function considering only the flame response to acoustic perturbations is obtained as follows:

$$G_F = \frac{G_{IF}}{G_I} \quad \& \quad \varphi_F = \varphi_{IF} - \varphi_I \tag{9.1}$$

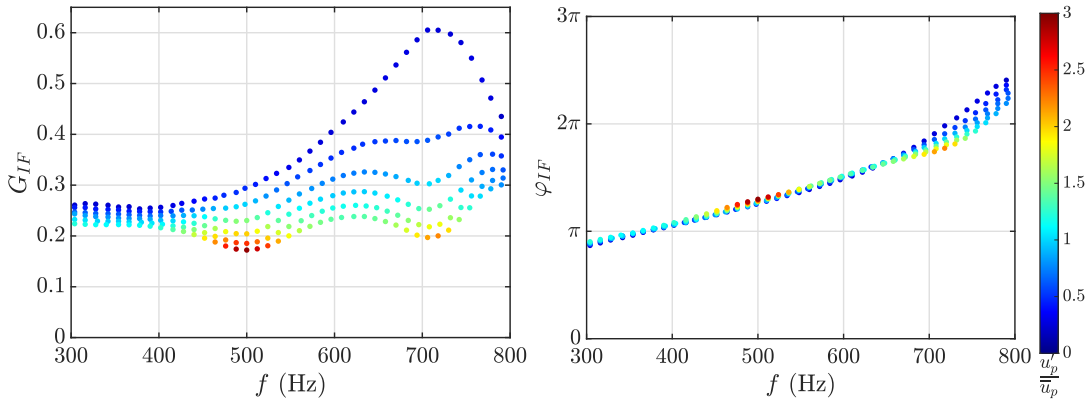

Figure 9.7. *FDF (gain and phase) results for measurements performed in SICCA-Spray for propane at F1 ($\mathcal{P}$ = 6.4 kW & ϕ = 0.85) with color axis representing the level of velocity fluctuations $u'_p/\overline{u}_p$ in the plenum. Here, u'_p is the RMS velocity fluctuations calculated using the two microphone method and $\overline{u}_p$ is the bulk velocity in the plenum at MP2 location (Fig. 9.2 (b)). The FDFs shown here include the response of the flame as well as the injection system dynamics (denoted by the subscript IF).*

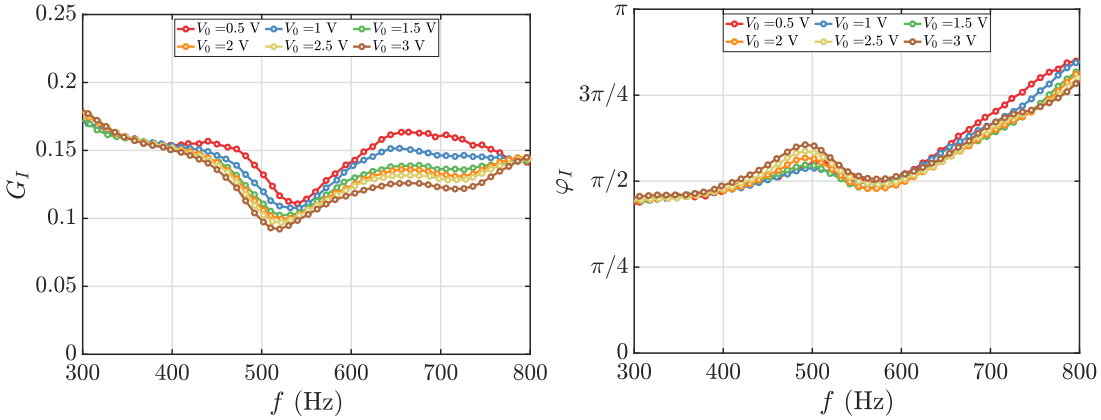

Figure 9.8. *Evolution of gain G_I and phase φ_I between the velocity measured in the plenum (u'_p marked as HW1 in Fig. 9.2 (b)) and at the injector outlet ($u'_{c,r}$ from HW2) with respect to frequency, for different loudspeaker excitation voltages. The measurements are carried out at an air flow rate of* $2.6\,\mathrm{g\,s^{-1}}$.

Now the indirect FDF is obtained by separating the injector describing function $\mathcal{F}_I$ (Fig. 9.8) from the injector + flame describing function $\mathcal{F}_{IF}$ (Fig. 9.7) using Eq. 9.1. The above procedure is carried out only for the case of premixed propane. For the liquid fuels, the FDF is obtained directly by measuring the relative fluctuations at the injector outlet. It is worth emphasizing here that an indirect measurement would result in a phase that is nearly the same as that determined from a direct FDF measurement, but there would be a non-negligible difference in the gain values (refer to Chapter 4). The resulting flame describing functions for the three fuels are shown in Fig. 9.9 at the operating point F1. These plots corresponding to the three fuels indicate that the gain G_F changes substantially with the amplitude of the incident fluctuations, especially with propane and heptane. The variation in gain with the velocity perturbation level is almost negligible in the lower frequency range until $500\,\mathrm{Hz}$, beyond which a strong nonlinearity is observed. This variation is less significant in the case of dodecane, and the curves corresponding to various velocity fluctuations levels nearly collapse except in the vicinity of $500\,\mathrm{Hz}$, where this difference is more apparent. On the contrary, there is almost no change in the phase φ_F at different excitation levels resembling the classical evolution of "M"-flames (Durox et al. 2009). Such behavior can be seen for all three fuels until $700\,\mathrm{Hz}$, beyond which a minor variation with respect to the relative velocity fluctuations can be observed. The phase also exhibits a linear evolution with frequency for heptane and dodecane, but for propane, the slope of the phase curve changes after $500\,\mathrm{Hz}$.

It is interesting to extract time delays from the FDFs phase plots. This may be accomplished in general by taking the derivative of the phase with respect to the angular frequency as $\tau_{u'-\dot{Q}'} = \Delta\varphi_{u'-\dot{Q}'}/\Delta\omega$. It can be seen in Fig. 9.9 that the slopes of the phase curves are in increasing order, first the premixed propane, then the heptane with a greater phase shift, and then dodecane. These different phase curve slopes can, in turn, be attributed to variations in time lags. For premixed propane, the associated time lag will just be the time taken by the reactants to reach the combustion zone, i.e., convection time delay τ_{conv} and the delay associated with the chemical conversion processes τ_{reac}. On the other hand, when liquid fuels are used, additional time-lags due to atomization τ_{atm}, vaporization τ_{vap}, and mixing τ_{mix} need to be considered. The case of heptane is likely to be close to propane, wherein the vaporization could be happening simultaneously with convection (Bernier et al. 2004; Vignat et al. 2021). However, in the case of dodecane, due to its lower volatility, the situation is likely to be dominated by the time delay associated with vaporization. Now assuming a rough linear evolution of the phase curve and without considering the dependence on the modulation level, a time delay can be calculated, and this is found to be $0.95\,\mathrm{ms}$ with premixed propane, $1.33\,\mathrm{ms}$ with liquid heptane, and $1.36\,\mathrm{ms}$ with liquid dodecane, thus confirming the earlier expectations. The FDF data set reported in this section will now be used together with the theoretical framework of Chapter 5 to interpret the instability be-

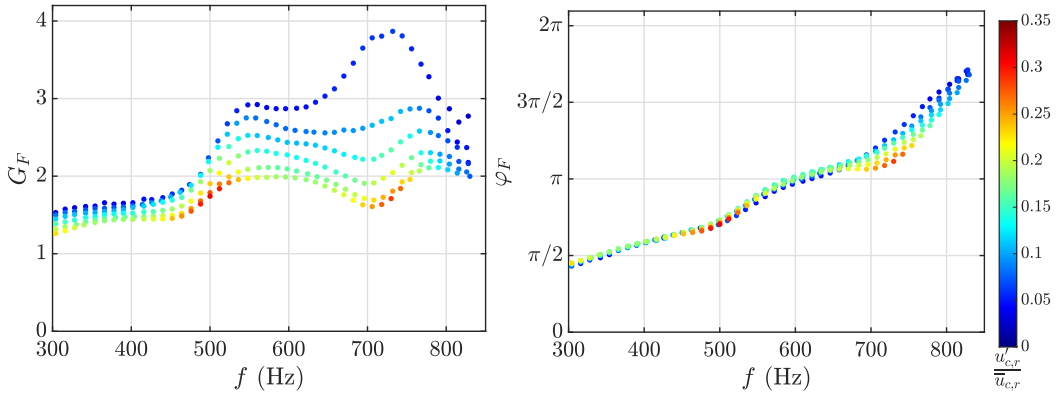

(a) Propane

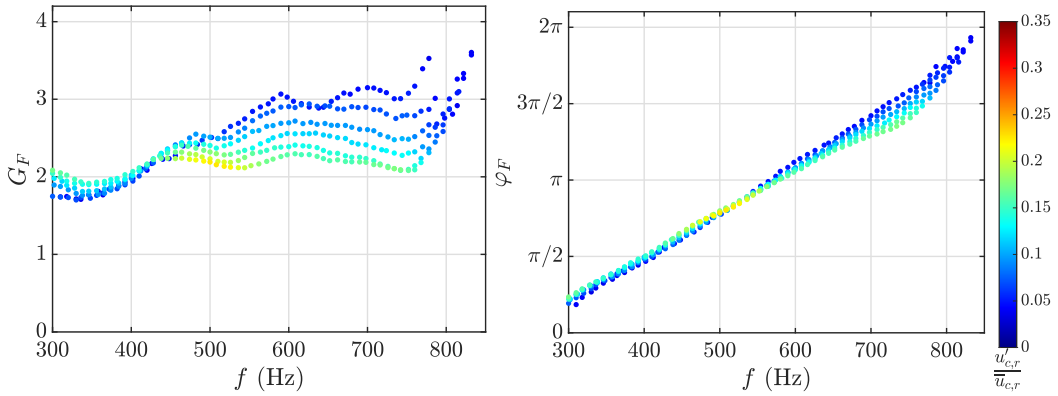

(b) Heptane

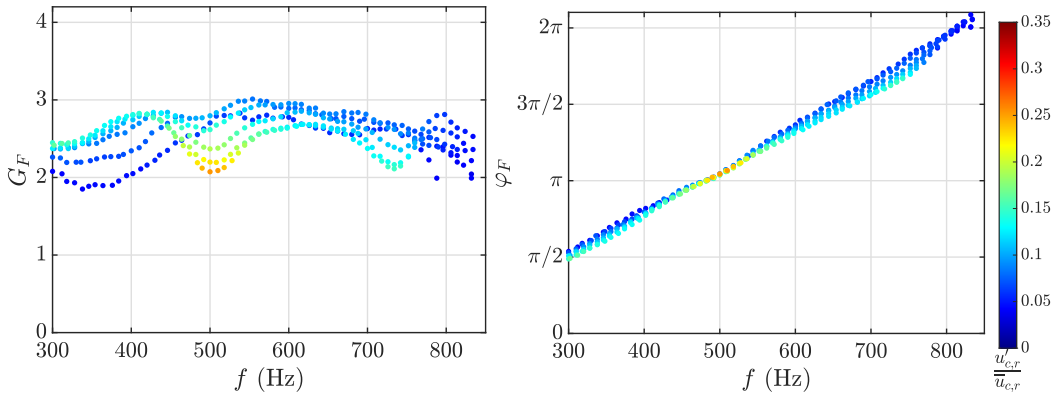

(c) Dodecane

Figure 9.9. *FDF (gain G_F and phase φ_F) of the flame describing function in SICCA-Spray for the three fuels ($\mathcal{P}$ = 6.4 kW & $\phi = 0.85$) with color axis representing the level of velocity fluctuations $u'_{c,r}/\overline{u}_{c,r}$. For the liquid fuels direct FDF is shown, while for the case of premixed propane indirect FDF is displayed. The data are smoothed using a five-point moving average.*

havior observed in the annular combustor, MICCA-Spray, a procedure previously adopted in Chapter 7.

9.5 Link between annular combustor instability & FDF measurements

An attempt is now made to link observations in MICCA-Spray and FDF measurements in SICCA-Spray. For propane, only the operating point F1 is considered as it is not feasible in these experiments to obtain a direct measurement of FDF and also because propane-air only constitutes a reference case. For the two liquid fuels, the other two operating points (F2 and F3) are also investigated, and their FDF evolution at different velocity fluctuation levels is shown in Appendix 1. A similar analysis of using the FDFs to interpret instabilities of an annular combustor equipped with acoustically transparent injectors (in an earlier version of MICCA the swirlers were formed by a set of blades) has been performed by Schuller et al. (2020). The method consists of unwrapping an annular combustor as an equivalent rectangular system and applying periodic boundaries on the lateral walls. This led to the standard unstable bands $\pi < \varphi_F < 2\pi, \mod 2\pi$ in the FDF phase diagram obtained from a single-injector setup. The current analysis is carried out in a similar fashion, but it is aimed at accounting for the impedance imposed by the injectors that are now weakly transparent to acoustic waves. As shown in Chapter 5, the impedance imposed by the injector at its outlet plays a pivotal role in deciding the unstable bands. Recollecting the impedance measured in SICCA-Spray with swirler 716 (Chapter 6), it is known that the impedance magnitude varies between 0.55-0.85, and the impedance phase φ_ζ has a lower limit slightly above $3\pi/4$ and an upper limit slightly above π in the frequency range of 395–$540\,\mathrm{Hz}$. Figure 9.10 shows the impedance measured in SICCA-Spray at F1 and F2 when it exhibits longitudinal self-sustained oscillations at different frequencies. The results corresponding to F1 are reproduced from Chapter 6. Although the impedance measurements were only carried out with heptane, they can be expected to be the same with the other two fuels as long as the injector remains the same. From the figure, it can be seen that both the gain and phase of impedance do not change with the operating point.

The impedance is, however, not known in the frequency range where MICCA-Spray is unstable, i.e., between 740–$850\,\mathrm{Hz}$. This is because SICCA-Spray does not exhibit any self-sustained instabilities in this frequency range. At this stage, it is useful to consider two cases, the first of which corresponds to a nearest neighbor extrapolation (case A), while the second consists of a linear extrapolation of the gain and a subsequent determination of the phase (case B):

- In case A, the impedance corresponding to the maximum possible limit

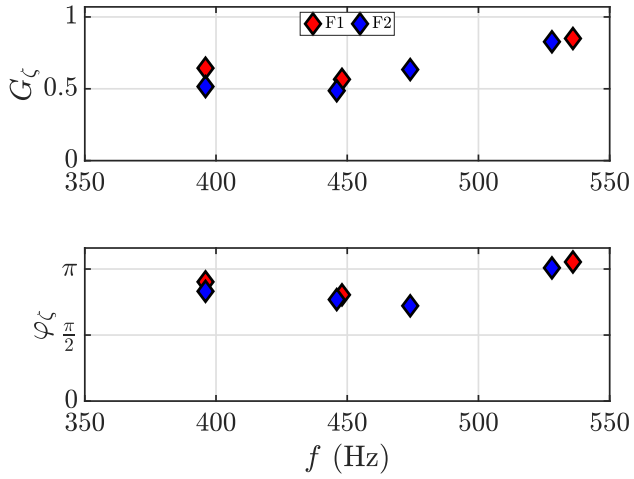

Figure 9.10. *The modulus G_ζ and phase φ_ζ of injector impedance measured when SICCA-Spray exhibits self-sustained oscillations with heptane at the two operating points F1 and F2. For details on the impedance measurement, the readers are referred to Chapter 6.*

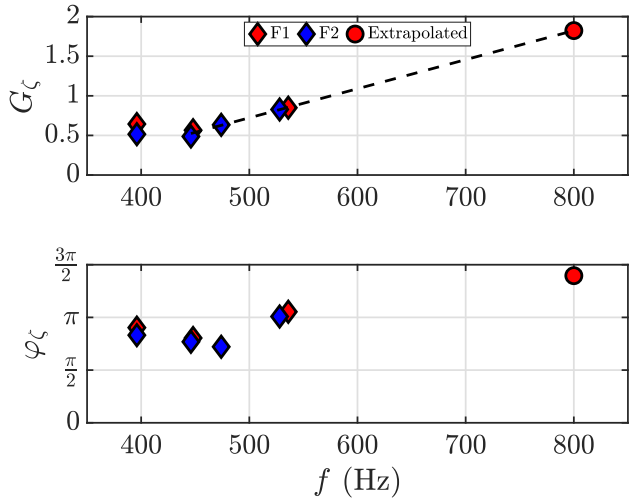

Figure 9.11. *The modulus G_ζ linearly extrapolated from low frequency data corresponding to heptane at the two operating points F1 and F2. The readers are referred to Section 9.5 for phase determination from the extrapolated gain value.*

cycle frequency of SICCA-Spray ($536\,\mathrm{Hz}$) is considered to represent the impedance in MICCA-Spray. At this frequency, the impedance magnitude is $G_\zeta \simeq 0.85$, and the impedance phase is $\varphi_\zeta \simeq 3.3\,\mathrm{rad}$ (nearly π). From the modal expansion method discussed in Chapter 5, the unstable bands are such that $-\pi/2 + \varphi_\zeta \leq \varphi_F \leq \pi/2 + \varphi_\zeta$, and in this case this band is defined by $\pi/2 \leq \varphi_F \leq 3\pi/2$.

- In case B, one first uses a linear extrapolation of the gain to a frequency of $800\,\mathrm{Hz}$ (see Fig. 9.11). This yields a value $G_\zeta \simeq 1.82$. It is then possible to

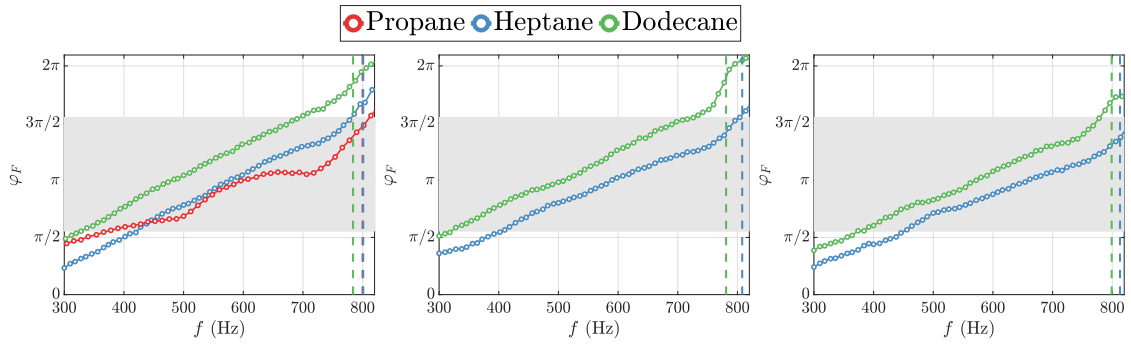

(a) F1 *(b) F2* *(c) F3*

Figure 9.12. *FTF for the three fuels at $V_0 = 3000\,\mathrm{mV}$ and at the three operating points F1 ($\mathcal{P} = 6.4\,\mathrm{kW}, \phi = 0.85$), F2 ($\mathcal{P} = 6.4\,\mathrm{kW}, \phi = 0.95$) and F3 ($\mathcal{P} = 7.4\,\mathrm{kW}, \phi = 0.95$). Unstable bands are obtained by considering the nearest neighboring impedance (case A) and shown in gray. The dashed vertical lines correspond to the instability frequency of MICCA-Spray. In (a), the dashed lines corresponding to heptane and propane coincide. The instability analysis of propane is only carried out at F1 as a reference case.*

estimate the impedance imaginary part ζ_i by assuming that the real part ζ_r remains constant and equal to that found when the phase angle is equal to π (where $\zeta_r + i\zeta_i = G_\zeta e^{i\varphi_\zeta}$). This may not be quite right, but it lies on the idea that the real part is essentially defined by Eq. 6.4 (p. 139) corresponding to an injector operating in a quasi-steady regime with $\zeta_r = -\kappa\overline{u}\sigma/c$. It is then assumed that κ does not evolve with frequency. One then obtains $\zeta_i \simeq -1.9$, and the phase angle is then $\varphi_\zeta \simeq 4\pi/3$. The unstable band is then shifted to $5\pi/6 \leq \varphi_F \leq 11\pi/6$.

One may now consider case A and plot the first band of instability in the FDF phase diagrams, as shown in Fig. 9.12. The dashed vertical lines represent the instability frequency of MICCA-Spray corresponding to the 1A1L mode with different fuels. At F1, the phase corresponding to propane-air remains inside the unstable band at the instability frequency $f_i = 800\,\mathrm{Hz}$, indicating a potential instability. The amplitude at this point is $\mathcal{A} = 1302\,\mathrm{Pa}$, thus confirming the tentative prediction. With liquid heptane, the instability frequency of MICCA-Spray is $801\,\mathrm{Hz}$ at F1, $808\,\mathrm{Hz}$ at F2, and $813\,\mathrm{Hz}$ at F3. In the FDF phase curves of Fig. 9.12 (a) at F1, the phase curve at $800\,\mathrm{Hz}$ is outside but close to the upper limit of the unstable band. As the phase curves exhibit mild nonlinearity around this frequency (see right side of Fig. 9.9 (b)), higher fluctuation levels would bring the phase values inside the unstable band. Thus, one can still expect instability in MICCA-Spray, as also observed in the experiments ($\mathcal{A} = 795\,\mathrm{Pa}$). At F2 and F3, the phases at the instability frequencies lie inside the band, matching the experimental instability observations in MICCA-Spray ($\mathcal{A} = 1398\,\mathrm{Pa}$ at F1 and $\mathcal{A} = 1241\,\mathrm{Pa}$ at

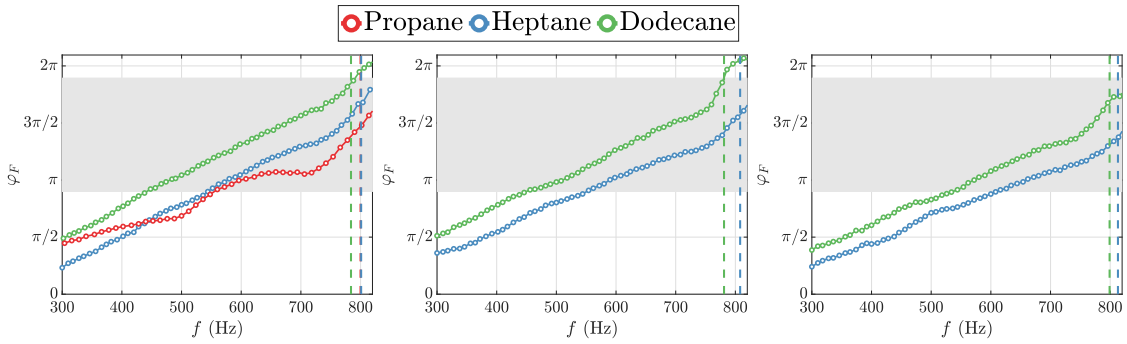

(a) F1 *(b) F2* *(c) F3*

Figure 9.13. *FTF for the three fuels at $V_0 = 3000\,\mathrm{mV}$ and at the three operating points F1 ($\mathcal{P} = 6.4\,\mathrm{kW}, \phi = 0.85$), F2 ($\mathcal{P} = 6.4\,\mathrm{kW}, \phi = 0.95$) and F3 ($\mathcal{P} = 7.4\,\mathrm{kW}, \phi = 0.95$). Unstable bands are obtained using a linear extrapolation of impedance gain (case B) and shown in gray. The dashed vertical lines correspond to the instability frequency of MICCA-Spray. In (a), the dashed lines corresponding to heptane and propane coincide. The instability analysis of propane is only carried out at F1 as a reference case.*

F2). The phase evolution of dodecane at F1 and F2 indicates that all the points beyond $700\,\mathrm{Hz}$ would escape the first unstable band, and hence, the frequencies of MICCA-Spray $f_i = 784\,\mathrm{Hz}$ and $781\,\mathrm{Hz}$ would be certainly stable. However, this prediction is not quite right, especially at F1, where the instability amplitude is $548\,\mathrm{Pa}$, and the system can be deemed unstable At F3, the phase value corresponding to the MICCA-Spray instability frequency of $799\,\mathrm{Hz}$ lies just close to the upper limit of the unstable band. A higher fluctuation level would shift the phase values inside the unstable band, which would then match the measurement ($\mathcal{A} = 608\,\mathrm{Pa}$). The above analysis only partially matches the experimental observations indicating that the impedance phase might not be exact. It is then interesting to consider case B.

The first instability band obtained by considering the impedance from case B is plotted in Fig. 9.13. It can be seen that these bands have now moved up, indicating that they will generally encompass the FDF phase curves at higher frequencies. At F1, the instability frequencies corresponding to both propane and heptane operation remain well inside the unstable band, thus indicating that MICCA-Spray will be potentially unstable with these two fuels. This is coherent with the experimental observations with the two fuels ($\mathcal{A} = 1302\,\mathrm{Pa}$ with propane and $\mathcal{A} = 795\,\mathrm{Pa}$) in the annular combustor. The case of dodecane at F1 is close to the upper limit but still inside the unstable band at $784\,\mathrm{Hz}$. The experimentally determined amplitude in MICCA-Spray is $\mathcal{A} = 548\,\mathrm{Pa}$, indicating a consistent prediction. The scenario with liquid fuels at F1 is notably different from that of case A where the FDF phase values at the instability frequencies fell either completely outside the unstable band or just at its upper limit, thus not fully explaining the experimental

observation. At the other two operating points (F2 and F3), the FDF phase curve corresponding to heptane remains well inside the unstable band at the respective frequencies of $808\,\mathrm{Hz}$ and $813\,\mathrm{Hz}$, indicating potential instability. With dodecane, the phase value at $f_i = 781\,\mathrm{Hz}$ falls just at the upper limit of the unstable band at F2. Thus, the annular combustor can be expected to be at a marginally unstable regime, which is confirmed by the comparatively lower amplitude of $\mathcal{A} = 285\,\mathrm{Hz}$, indicating that MICCA-Spray is only mildly unstable. However, it is pointed out that one cannot be sure of the potential instability prediction when the phase curve falls close to the limits of the band as even a small change, for example, in the velocity fluctuation level, can bring the FDF curves inside. At F3, the phase value of dodecane at $799\,\mathrm{Hz}$ falls well inside the band, pointing to a certainly unstable operation, which is in agreement with the observations in the annular combustor that exhibits an instability at $\mathcal{A} = 608\,\mathrm{Pa}$. As this analysis can only predict whether a particular case will be potentially unstable in the annular combustor, the difference in the instability amplitude between the three fuels cannot be reasoned with this approach. In addition, the impedance phases used in the two cases are only tentative, and they need to be experimentally validated. Nevertheless, from this analysis, one may infer that for a given injector, the change in time delay associated with the fuel type displaces the FDF phase curve location with respect to the unstable bands, and this modifies the dynamical behavior of the system.

The above analysis only predicts a potential instability based on whether the phase evolution lies inside the unstable band. To verify if the probed points are definitely unstable, one needs to obtain a growth rate and compare it with the damping rate in a way similar to the analysis in Chapter 6. However, this is not entirely possible for MICCA-Spray due to several limitations. Firstly, the maximum velocity fluctuation level achieved in SICCA-Spray at the injector exit in the instability range of MICCA-Spray ($740\,\mathrm{Hz}$–$850\,\mathrm{Hz}$) is only around 15% (shown in Fig. 9.9). Although the modulation level is much higher in the plenum (refer to Fig. 9.7), with the fluctuations being three times as high as the bulk velocity, this level is diminished upon transmission through the injectors that are weakly transparent to acoustic disturbances. Since the instability reaches high amplitude levels in MICCA-Spray (maximum amplitude of $1673\,\mathrm{Pa}$ with heptane), the velocity fluctuation level at the base of the flame can be expected to be relatively high. It is known from Chapter 3 that FDF can represent the self-sustained oscillations only when the fluctuation levels match. Thus, a quantitative comparison between the instabilities of the annular combustor and FDF cannot be made in the present case. To overcome this limitation, one has to modulate the single-injector system with higher-efficiency driver units that can produce enhanced values of velocity fluctuations at the injector exit even after passing through these weakly-transparent injectors. Secondly, the injector impedance in the range of MICCA-Spray instability frequencies is not well known. It can be seen from the impedance curve in Fig. 9.10 that there is a variation in both the gain and phase of the impedance with

respect to frequency. It has also been observed in the impedance measurements carried out using downstream transverse acoustic modulation in the TACC-Spray test rig at the CORIA laboratory that there is a dependence on the amplitude of fluctuations (personal communication with the team of Prof. Françoise Baillot, and the results are not shown here). Based on this, one might expect the impedance to change beyond $740\,\mathrm{Hz}$ at higher amplitudes, which would then modify the position of the unstable band. Thus, further studies are necessary in the single-injector combustor at higher modulation levels and close to the instability frequency of MICCA-Spray to obtain a definite value for the impedance. In addition, as will be discussed in the following chapter, it might also be necessary to carry out the FDF measurements in the newly developed three-injector combustor, TICCA-Spray, where the central flame is surrounded by neighboring side flames, an environment similar to that of MICCA-Spray. Despite the above limitations associated with experimentation, this simplified modeling effort helps gain a qualitative understanding of the instabilities in the annular system.

9.6 Conclusions

This chapter is focused on the effects of fuel properties and physical state on thermoacoustic instabilities coupled with azimuthal modes. Changes in fuel have a direct impact on the time lag. The shortest time lag corresponds to premixed propane and air. The time lag is augmented for heptane and takes its largest values for the less volatile dodecane. A database is obtained from systematic experiments on a laboratory-scale annular combustor (MICCA-Spray) for a wide range of operating points that vary in thermal power and global equivalence ratio. Results show that the largest instability domain is obtained for premixed propane. In comparison, the instability boundary defines a more compact unstable domain in the case of heptane and, correspondingly, a larger stable region. The stability of the system is further augmented when it is operated with dodecane. Hence, in this case, having a fuel that has a higher time lag makes the system more stable. A difference between the three fuels can be observed in the frequency of oscillation as well. At a point where the three fuels have nearly the same oscillation amplitude levels, it is found that propane and heptane have the same instability frequency, while dodecane features a lower instability frequency. An attempt is made to understand this dynamic behavior using flame describing functions (FDFs) measured in a single-sector configuration at three operating points in the stability map. Unstable bands obtained using the simple theoretical model proposed in Chapter 5 are combined with the injector impedance obtained from the single-injector configuration. In general, when the oscillation frequency corresponds to a phase that falls within the unstable band of the phase plots, the annular combustor is unstable. If the oscillation frequency is in the vicinity of one of its borders, then the amplitude appears comparatively lower. The variation in the instability behavior with the three

fuels can be explained by the changes in the associated time delay, which modifies the position of the FDF phase with respect to the fixed unstable band. In addition, the gain at a particular frequency is also modified depending on the fuel used, indicating a possible change in the instability amplitude. However, this observation does not extend to a few operating conditions, and one cannot expect to have a monotonic relation because the instability bands are defined in the linear regime while the observations in the annular combustor are made at the limit cycle. Also, the FDFs measured in the single-injector setup cannot reach a modulation level that is high enough due to the drop in amplitude of disturbances passing through the weakly-transparent injectors. Another limitation is associated with the lack of impedance measurements in the frequency range of interest. Nevertheless, the FDFs determined in the single sector configuration can be used to qualitatively interpret instability experiments in multiple-injector annular combustor systems.

Appendix 1: Flame describing function at different operating points

It is interesting, for completeness, to examine the results of the flame describing function measurements corresponding to operating point F2 (shown in Fig. 9.14) and F3 (shown in Fig. 9.15), when the fuel is delivered as a liquid spray of droplets. Measurements are not available for premixed propane and air at these two operating points. With heptane, the gain curves feature similar tendencies, especially between F1 (Fig. 9.9 (b)) and F3, with subtle differences. The gain level is slightly reduced both at F2 and F3 compared to F1. The phase curves show a slight dependence on the amplitude beyond $700\,\mathrm{Hz}$ at F2, somewhat like that of F1, whereas the phase evolution remains nearly linear at F3. As the equivalence ratio is changed while keeping the thermal power constant (i.e., between F1 and F2), the slope of the phase curve decreases, indicating a smaller time delay at the higher equivalence ratio point. The FDF gain slightly decreases as the equivalence ratio is increased. When changing the thermal power while keeping the equivalence ratio constant (i.e., between F2 and F3), a similar behavior is observed, and the time delay decreases when the thermal power is increased. The FDF gain increases to a higher value as the thermal power increases. With dodecane, the gain curves have slightly higher values at F2 and F3 compared to F1 (Fig. 9.9 (c)). As the equivalence ratio is increased at constant thermal power (between F1 and F2), the phase evolution remains nearly the same, with the phase curve at the higher equivalence ratio point exhibiting an increased dependence on the amplitude. The FDF gain values also remain nearly the same except for the lower velocity fluctuation levels, which result in higher gain values. At a constant equivalence ratio but higher thermal power (between F2 and F3), the phase curve slope decreases, indicating a smaller time delay, and the gain curves move towards higher values. On comparing heptane and dodecane, the time delay is always augmented with dodecane, as can be expected intuitively due to its lower volatility, thus increasing the time delay associated with the vaporization process.

Appendix 2: Stability maps for other swirlers

In addition to the results of azimuthal instabilities of MICCA-Spray described in this chapter for swirler 716 with different fuels, experiments were also carried out with the other swirling injectors defined in Chapter 7.

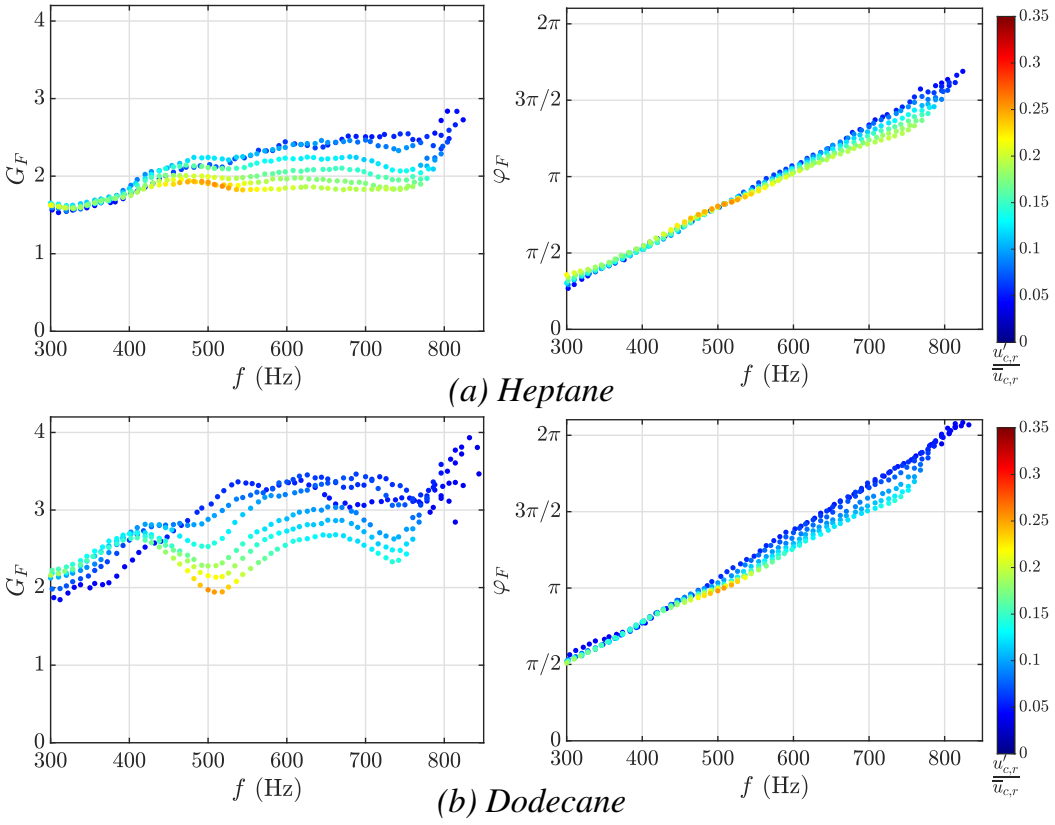

Figure 9.14. *FDF (gain G_F and phase φ_F) of the direct flame describing function in SICCA-Spray for the liquid fuels at F2 ($\mathcal{P}$ = 6.4 kW & $\phi = 0.95$) with color axis representing the level of velocity fluctuations $u'_{c,r}/\overline{u}_{c,r}$ at the injector outlet.*

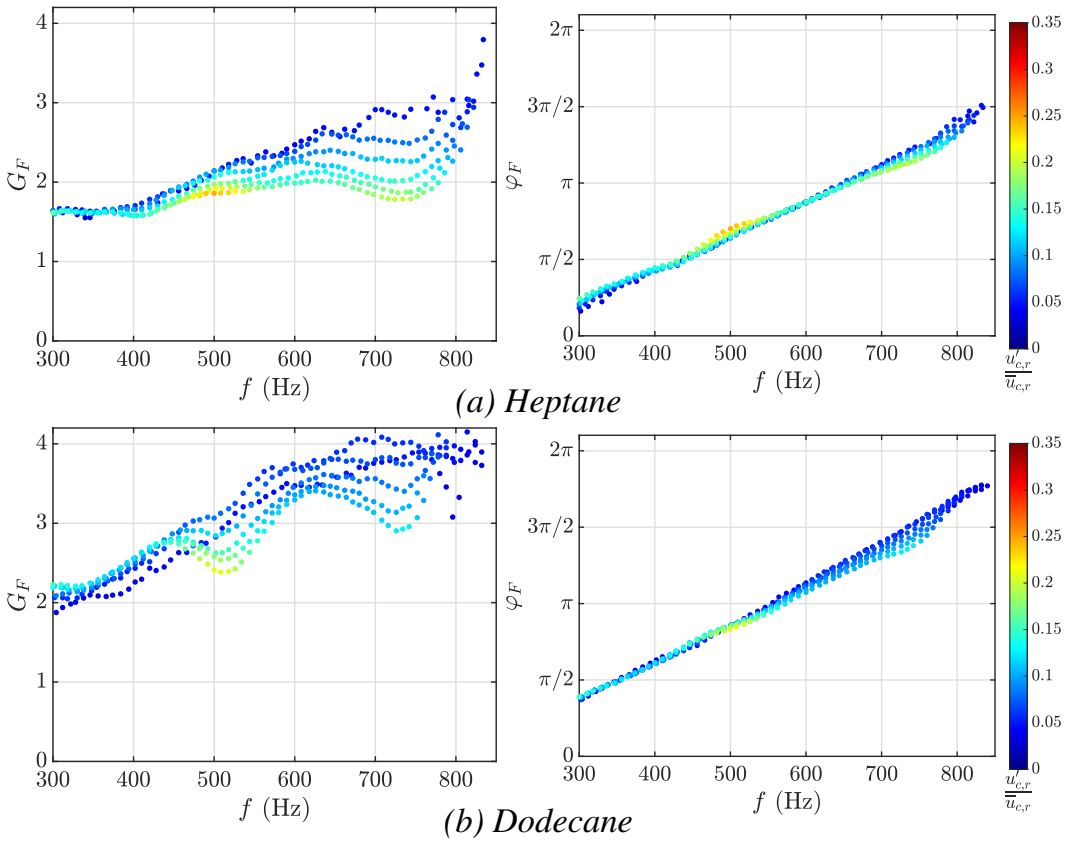

Figure 9.15. *FDF (gain G_F and phase φ_F) of the direct flame describing function in SICCA-Spray for the liquid fuels at F3 ($\mathcal{P}$ = 7.4 kW & $\phi = 0.95$) with color axis representing the level of velocity fluctuations $u'_{c,r}/\overline{u}_{c,r}$ at the injector outlet.*

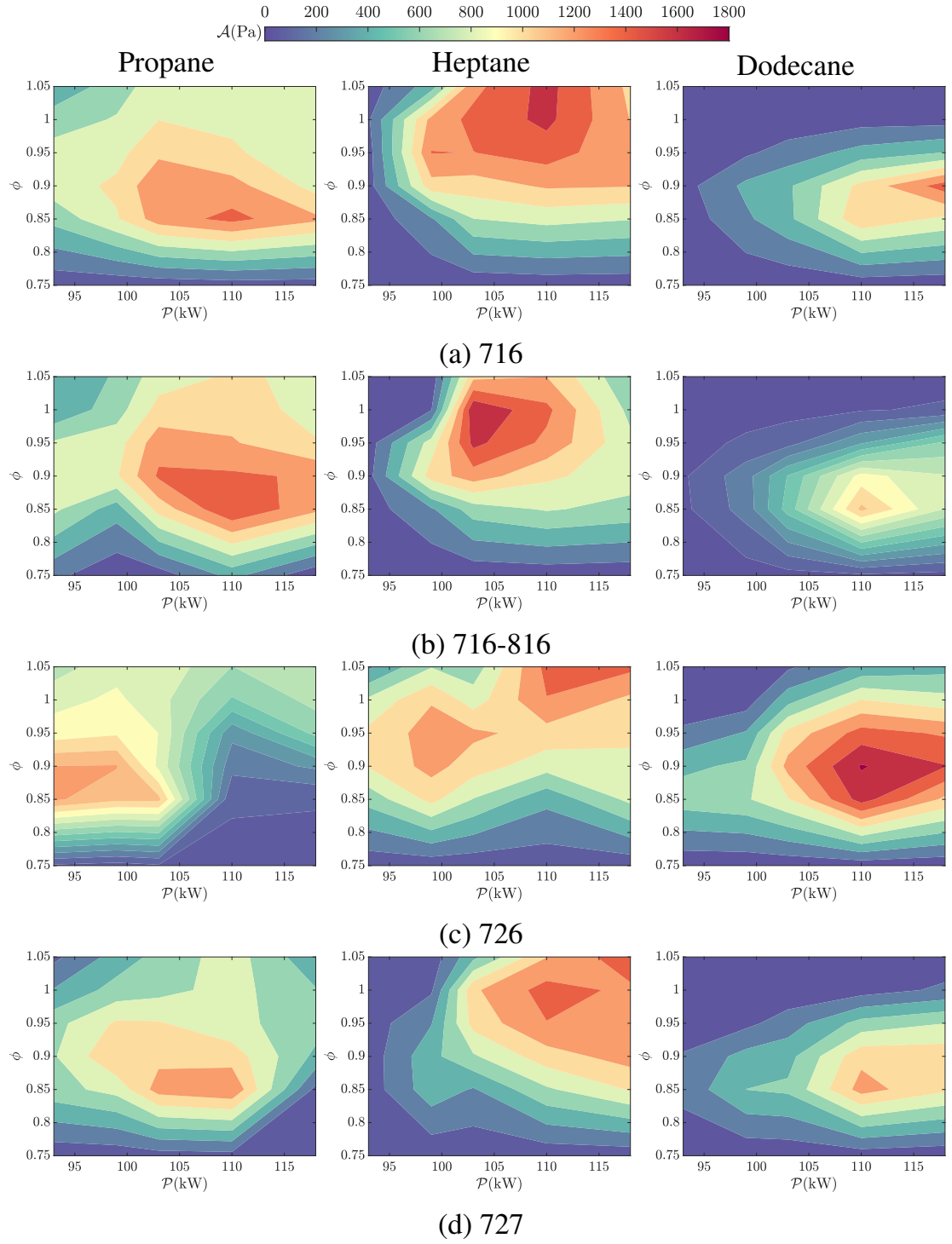

Figure 9.16. *Amplitude stability map of MICCA-Spray for the different swirlers in the higher-swirl category with the three fuels. The swirlers in the lower-swirl category (707 and 712) are always stable in the assessed operating zone and hence are not shown here.*

The case of heptane with different injectors discussed in Chapter 7 and the case of 716 with different fuels discussed in the present chapter is reproduced here to

facilitate comparison. The lower-swirl units (707 and 712) are always stable, even with premixed propane and dodecane, at the thirty operating points tested here, and the swirlers from the higher-swirl category (716, 726, 727) generally feature regions of instability. Figures 9.16 and 9.17 respectively show the amplitude and frequency stability maps for the higher-swirl units with the three fuels. It can be readily observed that the regions of instability depend on the fuel considered.

On comparing the amplitude stability map between the full CR configuration of 716 and the alternate CCR configuration of 716-816 (Fig. 9.16 (a) & (b)), one observes that for dodecane, the CCR domain of instability appears to be translated to lower thermal powers and lower equivalence ratios with respect to the CR domain, like in the case of heptane. However, the CR and CCR maps are quite similar for premixed propane. For both 716 ($\mathcal{A}_{\text{max}} = 1460\,\text{Pa}$) and 716-816 ($\mathcal{A}_{\text{max}} = 1596\,\text{Pa}$), the maximum amplitude of instability with propane occurs at the same operating conditions of $\mathcal{P} = 110\,\text{kW}$ and $\phi = 0.85$. A comparison between the different swirlers can now be carried out, considering 716 as the baseline configuration. In what follows, the discussion is majorly focused on propane and dodecane, as the case of heptane with different swirlers was already discussed in Chapter 7.

On comparing the case of 726 with the baseline 716, one notices that the instability regions and amplitudes starkly differ between the two cases. With propane, 726 exhibits higher instability amplitudes at the lower powers, contrary to 716, which is more unstable at higher powers. At higher powers, 726 is mostly stable at lower equivalence ratios but moderately unstable at higher equivalence ratios. With dodecane, 726 exhibits the highest instability amplitude of $\mathcal{A}_{\text{max}} \approx 1800\,\text{Pa}$ at $\{\mathcal{P} = 110\,\text{kW}, \phi = 0.9\}$ among the three fuels and exhibits wider unstable zones than with propane. This behavior is distinct from that of 716, which has wider unstable zones with propane than dodecane. This indicates that the instability behavior cannot be universally concluded with only the fuel, as it also depends on the specific configuration considered. The amplitude map (Fig. 9.16 (d)) of 727 closely resembles that of 716, with only minor differences with all three fuels. Instabilities are generally manifested at leaner equivalence ratios with propane and dodecane, while with heptane, the high-amplitude instabilities mostly occur at richer equivalence ratios. One can expect the changes described in this section to result from the variations in the corresponding FDFs, leading to the modification of instability zones, amplitudes, and frequencies.

The frequency of instability (Fig. 9.17 (a) & (b)) shows similar characteristics between the full CR and alternate CCR configurations for any particular fuel. The frequency maps of 726 generally exhibit a higher frequency compared to 716 or 727 with all three fuels. Although the frequency map of 727 (Fig. 9.17 (d)) is quite similar with the liquid fuels, there exists a slight deviation with propane only at higher thermal power.

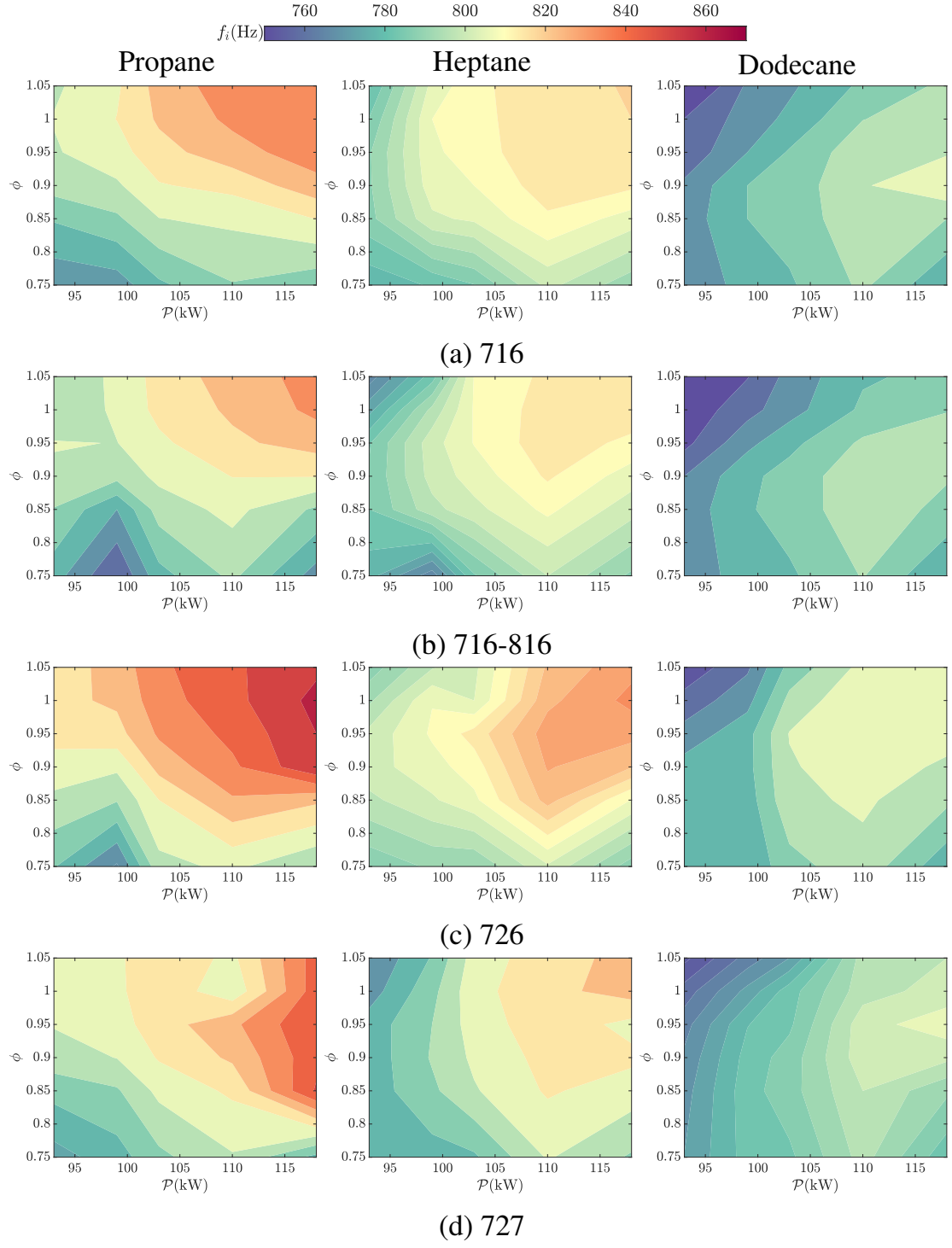

Figure 9.17. *Frequency stability map of MICCA-Spray for the different swirlers in the higher-swirl category with the three fuels. The swirlers in the lower-swirl category (707 and 712) are always stable in the assessed operating zone and hence are not shown here.*

Appendix 3: Flame images with the different injectors

The flame shapes formed by the various swirler units with the three fuels are shown in Fig. 9.18 at an equivalence ratio of $\phi = 0.85$ and thermal power of

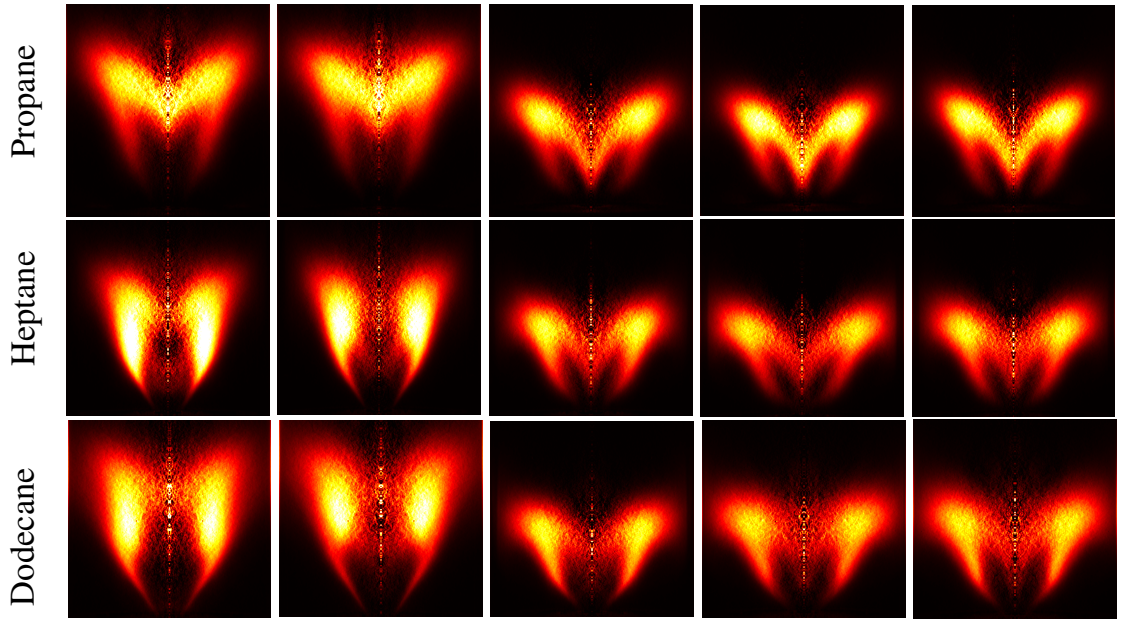

Figure 9.18. *Flame images showing OH* chemiluminescence captured in SICCA-Spray under stable conditions with different fuels. An Abel inversion is applied to the averaged images captured by the camera and are displayed in false colors.* $\mathcal{P}_{sicca} = 6.4\,\mathrm{kW}$ *and* $\phi = 0.85$*. The swirlers 707 and 712 belong to the lower-swirl category, while the other three swirlers (716, 726, 727) belong to the higher-swirl category.*

$\mathcal{P}_{\mathrm{sicca}} = 6.4\,\mathrm{kW}$ (operating point F1). These averaged images are obtained using an ICCD camera fitted with an OH* filter and performing an Abel deconvolution. The flame images of the different swirlers with heptane shown in Fig. 7.5 are recalled here for comparison.

Similar to the observation made with heptane in Chapter 7, the flame shapes formed by the lower-swirl units (707 and 712) notably differ from the high-swirl units (716, 726, and 727) with both propane and dodecane. The flame shapes of higher swirl units are overall similar with minor differences. As discussed in this chapter, the higher-swirl units, when operated with liquid fuels, take an “M" shape with a central hollow trough, which could be attributed to the hollow-cone spray produced by the atomizer resulting in only very few to no droplets at the center. The central trough is comparatively wider with dodecane, but with propane, these flames take a full “M" shape. While the flames formed by lower-swirl units take an overall “V" shape with the liquid fuels, the flames with propane take a lifted “M" shape. The lifted “M" shape could be attributed to the weaker recirculation zone of the lower-swirl units leading to a weaker stabilization of the propane flames. This was also observed by Durox et al. (2013) on a swirl combustor operated with pre-mixed methane where the blade angles can be continuously varied to modify the

swirl number. It was observed that the flames were lifted when the swirl number decreased. The flames, in general, appear wider with dodecane than with heptane.

Part III

FDF dependence on boundary conditions

Chapter 10

Comparison of FDFs in single and mutiple-injector configurations

Contents

This chapter is accepted for publication as a full-length article at the ASME Turbo Expo 2022 after peer-review with the title "Comparison of flame describing functions measured in single and multiple injector configurations" by Preethi Rajendram Soundararajan, Daniel Durox, Guillaume Vignat, Antoine Renaud, Jérome Beaunier, Sébastien Candel (paper no. GT2022-80577) and recommended for publication in the Journal of Engineering for Gas Turbines and Power. It comprises two additional appendices with supplementary data. The experimental

setup of the three test rigs described in Section 10.2 has already been discussed in Chapter 1 and familiar readers can skip this part. A few appendices at the end of this chapter show supplementary data.

Recent investigations of combustion instabilities in annular systems indicate that considerable insight may be gained by using information gathered in single-sector experiments. Such experiments are, for example, employed to measure flame describing functions (FDFs), which represent the flame response to incident perturbations. These data may be used in combination with low-order models to interpret instabilities in multiple injector annular systems. It is known, however, that the structure and dynamical behavior of an isolated flame do not necessarily coincide with those of a flame placed in an annular environment with neighboring side flames. It is then worth analyzing effects that may be induced by the difference in lateral boundary conditions and specifically examining the extent to which the FDF data from single-segment experiments portrays the dynamical response of the flame in the annular environment. These issues are investigated with a new setup, named TICCA-Spray, comprising a linear arrangement of three injectors. The central flame is surrounded by two identical side flames in a rectangular geometry with key dimensions, side-wall separation, and spacing between injectors identical to those of the annular system MICCA-Spray. The describing function of the central flame is determined with techniques recently developed in single sector experiments (SICCA-Spray). The FDFs obtained in the two configurations are compared for two swirler types having different swirl numbers and pressure drops. The effect of the swirl direction of the neighboring injectors is also explored by operating with co- and counter-swirl combinations. Differences between FDFs determined in the two test facilities, sometimes modest and not negligible in other cases, are found to depend on the flames' spatial extension and interactions. The general inference is that the FDFs measured in a single-injector combustor are better suited if the flame-wall interaction is weak and provided that the area is equivalent to that of a single sector of an annular combustor. Nonetheless, using a multi-injector system would be more appropriate for a more precise FDF determination.

10.1 Introduction

Controlling combustion instabilities in annular systems is still a challenge, especially in systems operating in the lean premixed mode in compact, weakly-damped geometries. These instabilities are caused by a coupling between the acoustics of the system and the dynamics of the flames. The acoustic modes can be longitudinal or, more often, azimuthal, corresponding to the largest dimension

of the annular chamber and consequently to the lowest frequencies where flames are most sensitive to disturbances. These instabilities are sustained by oscillations in the heat release rate (HRR) of the flames formed by the injection units (Krebs et al. 2002; Kunze et al. 2004; Staffelbach et al. 2009; Bourgouin et al. 2013; Worth and Dawson 2013a; Dawson and Worth 2014; O'Connor et al. 2015; Poinsot 2017; Prieur et al. 2017). It is generally considered that the transverse velocities that accompany azimuthal modes contribute to a lesser extent to the process, but some recent experiments indicate that when the oscillation level reaches large amplitudes, these velocities may extinguish flames located near the pressure nodal line (Prieur et al. 2018). In an annular combustor, if the flame dynamics are mainly driven by axial disturbances and well defined by the flow fluctuations in each injector (Staffelbach et al. 2009; Wolf et al. 2012), and if the damping rate of the system can be estimated, it is possible to determine the amplitude of the limit cycle and infer the nature of the azimuthal oscillation (standing or spinning) that prevails in the system as exemplified in Laera et al. (2017).

The analysis of these instabilities is usually based on low-order models accounting for the flame response to acoustic modulations in combination with a proper description of the injector dynamics and system acoustics (Schuller et al. 2020). The flame response is conveniently represented by the flame describing function (FDF) (Noiray et al. 2008) or at least by a flame transfer function (FTF). In general, the FDF is measured separately on a single-injector configuration equipped with an acoustic flow modulation system to obtain the stable flame response. Transfer or describing function concepts suitably represent the complex multidimensional dynamics of real flames if the combustion region is compact with respect to the wavelength and interactions between flames are weak. One must also make sure that the FDF measured in a single-injector setup reliably describes the flame response and that this knowledge can be transposed to the annular configuration.

For dynamical similarity, it is generally believed that the confinement ratio, *i.e.*, the ratio of the injection surface area to the backplane surface area A_I/A_{BP}, should take identical values in the single-sector and annular configurations. This alone, however, may be inadequate because there is a notable difference in boundary conditions: a rigid wall cannot properly reflect possible interactions between adjacent flames. Even if the interactions between the neighboring flames appear to be weak (Staffelbach et al. 2009; Wolf et al. 2012; Bourgouin et al. 2013), there is evidence that the proximity and arrangement of injection units (co- or counter-rotating) may influence the dynamics of the annular combustor (Worth and Dawson 2013a; Worth and Dawson 2019). In addition, the flames are generally swirling, causing a strong rotation of the burnt gases between the flames. These effects may be enhanced if the injectors are fitted with an outlet cup (Durox et al. 2016; Dolan et al. 2017).

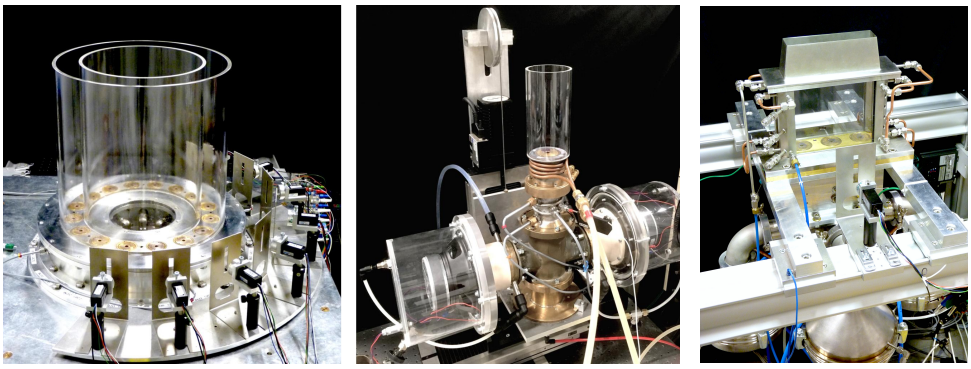

(a) MICCA-Spray (b) *SICCA-Spray* *(c) TICCA-Spray*

Figure 10.1. *(a) Photograph of the MICCA-Spray test rig. The mean diameter of the chamber is* $350\,\mathrm{mm}$ *and the walls are* $400\,\mathrm{mm}$ *long. (b) View of the SICCA-Spray test rig. The cylindrical flame tube has a* $69\,\mathrm{mm}$ *inner diameter and is* $200\,\mathrm{mm}$ *long. (c) The linear combustor, namely TICCA-Spray, equipped with three injectors. Acoustic actuators mounted inside metal enclosures are visible at the bottom of the photograph. A photomultiplier (in black) is installed in front of the quartz window, behind a mask with a vertical rectangular slot serving as a spatial filter.*

Several investigations carried out in linear geometries comprising a few swirling injectors indicate that relative injector positions (represented by the spacing-to-diameter ratio s_I/d_I) and flame shapes determine the level of interactions between neighboring flames (Kao et al. 2014; Kao et al. 2015; Dolan et al. 2015). If the flames are in close proximity and expanding sideways, strong interactions can occur between the reactive layers with significant variations in the instantaneous heat release rate (Worth and Dawson 2012; Worth and Dawson 2019; Lee et al. 2018; Lee et al. 2019). In Lee et al. (2019), it is shown in particular that two close flames do not have the same FTF as an isolated flame. Differences have been observed not just in the dynamical response of the flame but also in the lean blow-off limits, as indicated in a recent study (Ciardiello et al. 2021) conducted with a multi-burner linear combustor. One is led to think that the flame dynamics in an annular system will differ from the dynamics of a flame in a single-sector, even if the flame fronts are not in direct contact. This aspect was already considered in the past by Fanaca et al. (2008), Fanaca et al. (2010), and Smith et al. (2018). Additionally, the problem of assigning a surface area to the single-injector backplane was also discussed in Fanaca et al. (2010). It was found that to avoid interactions between the flame and wall in the single-sector configuration and to obtain a flame shape that matches with that found in the annular multiple injector system, the cross-sectional area of the single-injector combustor $A_{BP}|_{\mathrm{SIC}}$ has to be a few times that of a single segment in the annular chamber $A_{BP}|_{\mathrm{AC}}$, depending on the swirl number. However, such a large distortion in the surface area ratio

A_I/A_{BP} might not guarantee similar flame dynamics in the single-injector geometry and in the annular combustor. Smith et al. (2018) also consider the difference in flow and flame behaviors between single- and multi-injector configurations, but in contrast with what was initially expected, they find no significant changes in flame dynamics. However, this study was carried out at a single frequency, and the flames were only subjected to transverse acoustic modulations. Recent investigations carried out at the EM2C laboratory (Rajendram Soundararajan et al. 2021) indicate that FDFs measured in a single-injector cylindrical combustor (SICCA-Spray) having the same area as one segment of an annular combustion chamber (MICCA-Spray) can be used to analyze and approximately predict the instabilities observed in the annular combustor. However, it is also noted that the flame dynamics in the single-injector arrangement does not completely match that prevailing in the annular chamber.

Previous studies do not consistently conclude whether a single-injector configuration would sufficiently represent an annular combustor with multiple injectors. It is clearly important to investigate these issues in further detail and specifically aim at comparing FDFs obtained in single-sector and multiple-sector systems. The choice is made to conserve the same ratio between the injector outlet surface area and the backplane surface area A_I/A_{BP}, relative spacing s_I/d_I, and injector diameter in the single-sector and multiple-injector systems. A new test bench (designated as TICCA-Spray) was designed to complement the existing single-injector (SICCA-Spray) and annular combustor MICCA-Spray. TICCA-Spray comprises a set of three injectors in a rectangular geometry. The central flame is surrounded by two side flames in a geometry that portrays in a linear fashion the situation that prevails in the annular system.

This new experimental bench is described in Section 10.2, which also briefly discusses the related facilities: SICCA-Spray and MICCA-Spray. Section 10.3 is concerned with the FDF formulation and the treatment of the present spray flames as a single-input, single-output (SISO) system. Data gathered in this new facility are presented in Section 10.4 and compared in Section 10.5 with FDFs determined with the single-injector configuration. Two appendices are provided at the end, discussing further details on the FDF measurements. Appendix 1 shows the sensitivity of FDFs to the measurement location in TICCA-Spay, followed by Appendix 2, which discusses the repeatability and uncertainty of the measurements.

10.2 Experimental setup

It is natural to begin by briefly describing the MICCA-Spray annular combustor shown in Fig. 10.1 (a) since it forms the basis of the geometrical configurations for SICCA-Spray and TICCA-Spray. It is equipped with sixteen swirl-spray injectors and is now mainly fed with liquid heptane or dodecane. It may also be

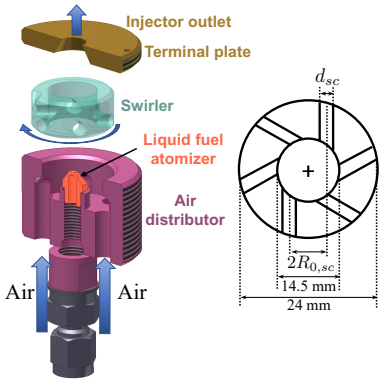

Figure 10.2. *The injector unit comprises an air distributor, a hollow cone atomizer, a swirler, and a terminal plate. The terminal plate features a converging conical shape having a diameter of* $8\,\mathrm{mm}$ *at the outlet. The schematic of the swirler is shown on the right. The channel diameter* d_{sc} *and radial location* $R_{0,sc}$ *can be varied to modify the swirl number and pressure drop.*

operated with a premixed flow of air and propane. The chamber is made of transparent quartz walls open to the atmosphere. The inner and outer diameters of the annulus are 300 and $400\,\mathrm{mm}$, respectively. Strong azimuthal instabilities were first observed with a $200\,\mathrm{mm}$ long inner tube and an outer tube $600\,\mathrm{mm}$ long (Prieur et al. 2018) or $700\,\mathrm{mm}$ long (Vignat et al. 2020), but in the recent studies (Rajendram Soundararajan et al. 2021), strong and persistent azimuthal instabilities were recorded with lateral tubes of equal length ($400\,\mathrm{mm}$). The instabilities of MICCA-Spray have until now been interpreted using FDFs measured in the single-injector facility, SICCA-Spray. This configuration is shown in Fig. 10.1 (b) and described in detail in Rajendram Soundararajan et al. (2022). The inner diameter of the flame tube is $69\,\mathrm{mm}$, which corresponds to the area of a single sector of the annular chamber. For FDF measurements, the flame tube is sufficiently short, with a typical length of $150\,\mathrm{mm}$, to avoid any longitudinal instabilities. Two driver units confined in cylindrical enclosures serve to oscillate the air flow at the injector outlet.

The same injector unit is used in MICCA-spray and SICCA-spray rigs, and its exploded view is shown in Fig. 10.2. Liquid heptane is delivered by an axial manifold to the hollow cone atomizer, which then sprays the fuel into the combustion chamber in the form of fine droplets. The atomizer is generally located at a distance of $6.75\,\mathrm{mm}$ from the combustor backplane. The air distributor delivers air around the atomizer to the six channels of the radial swirler. The geometrical parameters d_{sc} representing the swirler hole diameter and $R_{0,sc}$ representing the distance between the axis of the hole and the axis of the swirler can be suitably modified to obtain different swirl numbers and pressure drops. The injector assembly contains a terminal plate at its end, which has a conical hole of $8\,\mathrm{mm}$

Table 10.1. *Injector characteristics obtained under cold flow. Δp represents the pressure drop of the injector and S_N designates the experimentally obtained swirl number. The head loss coefficient σ is calculated using the equation $\Delta p = \frac{1}{2}\rho_0 \sigma u_b^2$, where u_b is the bulk velocity given by $\dot{m}_{air}/\pi\rho_0 R_{inj}^2$ and $R_{inj} = 4\,\mathrm{mm}$. d_{sc} is the diameter of the swirler channels and $R_{0,sc}$ is the distance between the axis of the hole and the axis of the swirler as shown in Fig. 10.2.*

Swirler	S_N	Δp		σ	d_{sc}	$R_{0,sc}$
	(-)	(kPa)		(-)	(mm)	(mm)
		F1	F2			
707/807	0.60	3.65	2.81	3.30	4.0	4.6
716/816	0.70	5.74	4.41	5.20	3.5	4.7

outlet diameter. Two distinct swirlers, designated as 707 and 716, having different swirl numbers and pressure drops, are investigated in what follows. These swirlers produce a clockwise rotation of the air flow, and their parameters are tabulated in Tab. 10.1. In addition, the counterclockwise version of the two swirlers, designated as 807 and 816, having identical geometries as their clockwise counterpart, are also investigated. It is pointed out that, in SICCA-Spray, the clockwise and counterclockwise counterparts cannot be distinguished as they possess the same characteristics.

The newly built TICCA-Spray linear combustor is shown in Fig. 10.1 (c). It comprises an array of three injectors, identical to those used in MICCA-Spray and SICCA-Spray, with a spacing of $69\,\mathrm{mm}$ between injectors. The choice of a system featuring three injectors is made so that the configuration remains simple enough but allows studying the effect of lateral boundary conditions on the flame dynamics. This is suitable as shown in Dolan et al. (2017), where it is found that the flow fields around the central injector in arrays with three or five injectors are quite close, provided that the spacing between injectors is kept constant. The combustion chamber is formed by four transparent windows that have a length of $205\,\mathrm{mm}$, a width of $50\,\mathrm{mm}$, and a height of $175\,\mathrm{mm}$. The width is equal to the distance between the two sidewalls in MICCA-Spray and the length to the curvilinear distance corresponding to three adjacent injectors in MICCA-Spray. The height of TICCA-Spray is chosen such that the flames are stable and also sufficiently confined as in the annular chamber. The central flame in the linear array is, therefore, in a configuration close to that of the annular chamber, with neighboring swirling flames on each side. A slightly converging metallic hat placed on top of the transparent chamber prevents entrainment of outside and its inflow into the chamber. The backplane and the metallic corner structures supporting the lateral windows

Table 10.2. *Operating conditions considered in this study. ϕ is the global equivalence ratio and u_b is the mean air flow velocity per injector at the outlet. Reproduced from Tab. 1.2.*

Operating point (-)	ϕ (-)	u_b (/injector) ($\mathrm{m\,s^{-1}}$)	P_{th} SICCA (kW)	P_{th} TICCA (kW)
F1	0.85	42.7	6.4	19.3
F2	0.95	37.7		

are cooled by circulating cold water. A sectional view passing through the axis of the central injector and perpendicular to the length of the chamber is shown in Fig. 10.3. The driver units for modulating the air flow are mounted inside metal enclosures and connected through elbow channels to the common air manifold (see Fig. 10.1 (c)). These are Monacor SP-6/108PRO HiFi speakers with a root mean square power rating of $100\,\mathrm{W}$ and an electrical impedance of $8\,\Omega$, capable of operating in the frequency range between 44 to $4500\,\mathrm{Hz}$. The driver units modulate the air flow longitudinally along the axis of the injectors. In this study, each injector is supplied with liquid heptane as fuel delivered by a central axial tube passing through the plenum. Both the air and fuel are supplied under ambient temperature. The FDF measurements in TICCA-Spray are carried out on the central flame and compared with FDFs determined in SICCA-Spray at two operating conditions defined in Tab. 10.2. These operating points, designated as F1 and F2, correspond to the same thermal power but differ in the global equivalence ratio ϕ. While F2 is close to stoichiometry ($\phi = 0.95$), F1 is leaner ($\phi = 0.85$).

The test rig is equipped with a photomultiplier (PM) with an OH^* filter centered at $308\,\mathrm{nm}$. A mask is placed in front of the PM such that it only collects the light emitted by the central flame (see Fig 10.1 (c)). The spray flames considered here did not show any significant spatial inhomogeneities of equivalence ratio during flow modulation in the frequency range of interest. This is because a large part of the spray impacts the conical wall of the terminal plate (see Fig. 10.2) before exiting into the chamber. This could cause strong secondary atomization under the action of the air flow, and this part of the fuel would then be approximately modulated in phase with the air pulsations. It might also be possible that the droplets interacting with the wall will slide along or bounce back and be swept away by the pulsating air flow. Whatever be the mechanism, it is seen in Chapter 2 that the fluctuation of the overall equivalence ratio (or mixture ratio) at the injector outlet is relatively weak compared to the fluctuation in velocity. One may thus consider that the spray flames investigated in the present experiments behave like

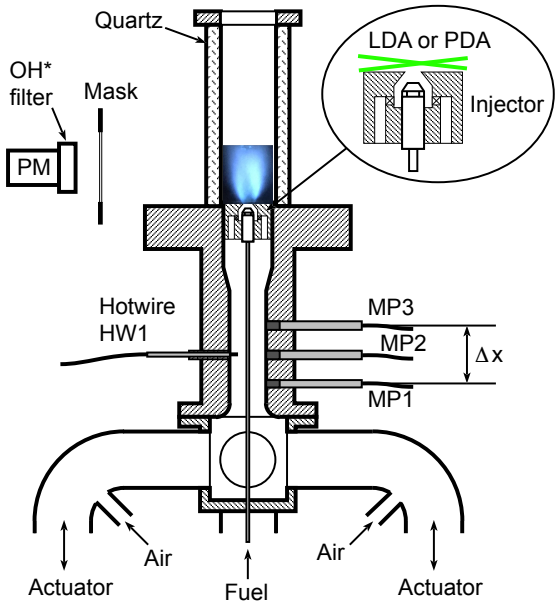

Figure 10.3. *Sectional view of the TICCA-Spray combustor in a plane perpendicular to the length and passing through the central axis of the burner.*

premixed flames, that their chemiluminescence characteristics are similar to those of premixed flames (Hurle et al. 1968; Ballester and García-Armingol 2010), and that the OH^* light emission may serve as an acceptable indicator of the HRR.

The velocity is measured using laser Doppler anemometry (LDA), the details of which are provided in Chapter 1. As seen in Chapter 4, the size of the spray droplets at the location of velocity measurements does not exceed a mean diameter of $5\,\mu\mathrm{m}$, resulting in low inertia for the droplets in the air flow. At an oscillation frequency of 500 Hz, a standard calculation indicates that the amplitude of the droplet velocity fluctuation is 0.95 that of the local velocity of the gas and that there is a small phase delay between the droplet and local gas velocities of about 0.05π. As a first approximation, it is, therefore, possible to consider that the droplet velocities correspond to the air velocities at the injector outlet in the frequency range of interest.

10.3 Determination of flame describing function

Generally, in flames that are formed by a spray of fuel conveyed by a stream of air, one expects to find equivalence ratio fluctuations together with velocity fluctuations. One would have to determine two describing functions, one pertaining to equivalence ratio disturbances and the other to velocity or volume flow rate

disturbances. One would write in general,

$$\dot{Q}'/\overline{\dot{Q}} = \mathcal{F}_\phi(\phi'/\overline{\phi}) + \mathcal{F}_v(\dot{q}_v'/\overline{\dot{q}_v}) \tag{10.1}$$

In the above equation, $\dot{q}_v$ is the volumetric flow rate, $\dot{Q}$ represents the HRR, $(\cdot)$' refers to fluctuations, and $\overline{(\cdot)}$ refers to the mean of a quantity. The flame would then have to be treated as a multiple-input single-output (MISO) system. However, as mentioned in Section 10.2, the relative equivalence ratio disturbances are an order of magnitude smaller than the volume flow rate (or velocity) disturbances in the present experiments (*i.e.*, $\phi'/\overline{\phi} \ll \dot{q}_v'/\overline{\dot{q}_v}$). One may then only consider the effects of volume flow rate disturbances (as a SISO system) and focus on the determination of $\mathcal{F}_v$. This is admittedly an approximation, but it is applicable in a situation where the relative HRR fluctuations are essentially induced by relative flow rate or equivalently velocity disturbances.

The FDF $\mathcal{F}_v$ gives the nonlinear response of the flame to the incoming acoustic perturbation, as shown in Eq. 10.2. In what follows, the subscript v is dropped and $\mathcal{F}$ is simply used to designate the FDF.

$$\mathcal{F}(\omega, \dot{q}_v') = \frac{\dot{Q}'/\overline{\dot{Q}}}{\dot{q}_v'/\overline{\dot{q}_v}} \tag{10.2}$$

where ω is the angular frequency. It is experimentally difficult to obtain a measure of flow rate fluctuations at the injector outlet, especially when there is a swirling flow with large shear zones. It is rather easier to measure the local velocity fluctuations instead by optical velocimetry techniques such as LDA or by hot wire anemometry. The FDF expression can then be rewritten as:

$$\mathcal{F}(\omega, |u_{c,r}'|) = \frac{\dot{Q}'/\overline{\dot{Q}}}{u_{c,r}'/\overline{u}_{c,r}} = G_F(\omega, |u_{c,r}'|)e^{i\varphi_F(\omega, |u_{c,r}'|)} \tag{10.3}$$

where, $G_F = |\mathcal{F}|$ and $\varphi_F = arg(\mathcal{F})$ represent the FDF gain and phase, and $u_{c,r}'$ is a reference acoustic velocity fluctuation determined at the base of the flame (subscript 'c' referring to the measurement in the chamber) at a certain distance r from the center of the injector and at a particular height h from the chamber backplane. Equations (10.2) and (10.3) are equivalent only if:

$$\dot{q}_v'/\overline{\dot{q}_v} = u_{c,r}'/\overline{u}_{c,r} \tag{10.4}$$

It is crucial that the velocity measurement at the injector outlet be obtained at a location where Eq. 10.4 is valid, and this has been carefully considered in Chapter 4.

As the velocity measurements by LDA require optical access, they are obtained at $h = 2.5\,\mathrm{mm}$ above the injector exit plane. It is also seen in Chapter 4 that the radial position r of the velocity measurement point that fulfills Eq. 10.4 nearly corresponds to the maximum of the mean axial velocity for the swirling injectors considered here. For swirlers 707 and 807, this radial location is at $r = 3.5\,\mathrm{mm}$, and for swirlers 716 and 816, this is at $r = 4\,\mathrm{mm}$. As shown in Appendix 1, the quality of the FDF determination is sensitive to the location where velocity fluctuations are being measured. Since the velocity at the injector outlet changes rapidly, even a small displacement with respect to the optimal point can significantly alter the equality in Eq. 10.4, thereby changing the determined FDF gain. One also finds that a shift of the measurement point is accompanied by a reduction in signal-to-noise ratio, producing phase values that are less reliable. This can be controlled by examining the coherence function and requiring that it be greater than a certain threshold, as indicated at the end of this section.

The FDF measurements are performed by subjecting the flame to different levels of acoustic velocity fluctuations induced by the four driver units located at the bottom of the plenum. A wave generator produces sinusoidal signals with an amplitude V_0 (peak to peak) ranging from $0.5\,\mathrm{V}$ to $2.9\,\mathrm{V}$ in steps of $0.3\,\mathrm{V}$, and a linear frequency sweep is performed from $250\,\mathrm{Hz}$ to $850\,\mathrm{Hz}$ for a time duration of $133\,\mathrm{s}$ at each amplitude level. Modulating the air flow with different amplifier voltages produces different velocity fluctuation levels at the injector exit. The processor of the LDA system simultaneously acquires the PM voltage while measuring the velocity. The signals are then interpolated and resampled to obtain the cross power spectral density between the relative HRR and velocity modulations. It is ensured that the number of droplets passing through the LDA measurement volume is high enough ($\approx 30\,\mathrm{kHz}$) to have a sufficient sampling rate. The coherence between the input relative velocity disturbances and output relative HRR disturbances is calculated, and the corresponding data are retained only if this coherence $\gamma^2 = |S_{\dot{Q}'u'_{c,r}}|^2/(S_{\dot{Q}'\dot{Q}'}S_{u'_{c,r}u'_{c,r}})$ is greater than a certain threshold. The choice is made to use $\gamma^2 \geq 0.9$, ensuring a signal-to-noise ratio of at least $9.5\,\mathrm{dB}$.

10.4 Results and discussion

It is interesting to first examine flame images recorded in TICCA-Spray and compare them with the images obtained in SICCA-Spray to uncover differences in terms of flame shapes. This will help interpret the FDF measurements corresponding to the different swirlers that are first shown for TICCA-Spray and then compared with the FDFs determined in SICCA-Spray.

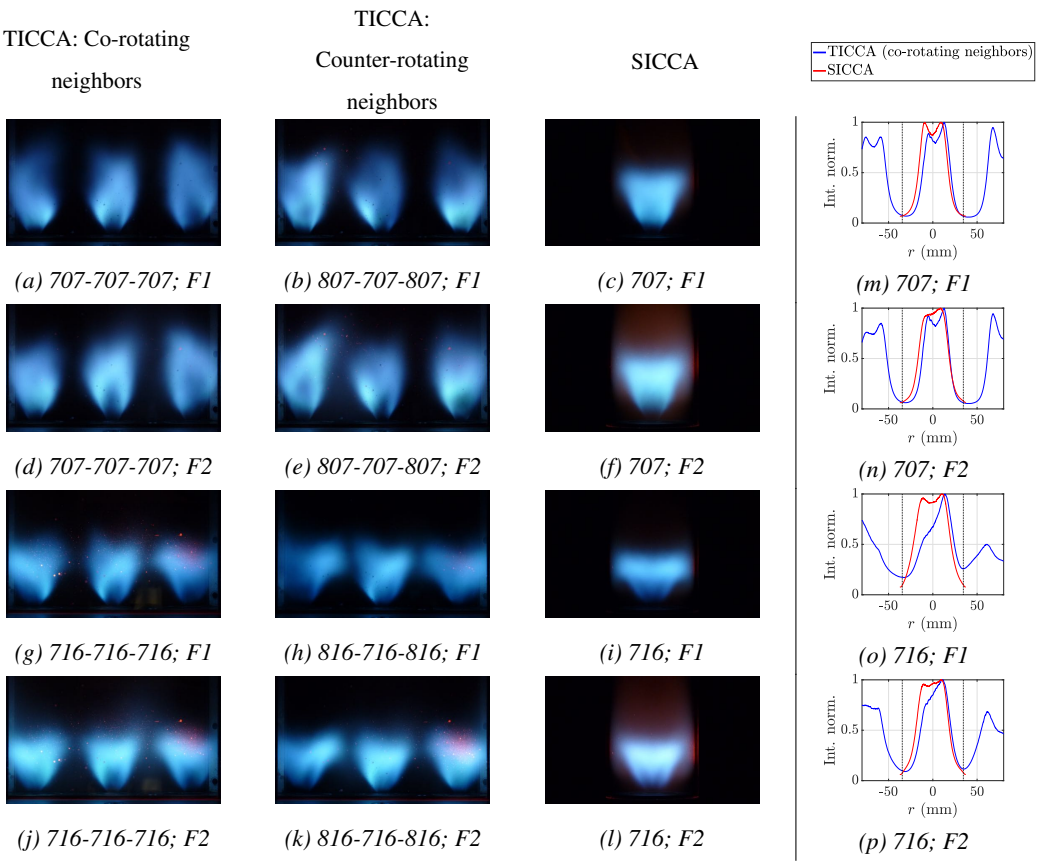

Figure 10.4. *Flame images in TICCA-Spray (first and second column) and SICCA-Spray (third column). In the first column, the neighboring injectors are co-rotating, while in the second column, the neighboring injectors are counter-rotating. Images are adjusted to have the same aspect ratio and scale. The fourth column shows the evolution of intensity integrated over an ensemble of vertical pixels at each horizontal coordinate in the flame zone normalized by its maximum value. The blue lines correspond to TICCA-Spray with co-rotating neighbors, and the red lines pertain to SICCA-Spray. Dotted black lines represent the chamber wall in SICCA-Spray. Here, the first and third rows correspond to the operating point F1, and the second and fourth rows correspond to F2.*

10.4.1 Flame images in TICCA-Spray and SICCA-Spray

The first three columns in Fig. 10.4 display the flame images of TICCA-Spray and SICCA-Spray formed by the different swirling injectors at the two operating points reported in Table 10.2. These images are recorded by a Panasonic Lumix FZ38 digital camera under steady conditions, and the driver units at the bottom of the test rigs are inoperative while recording these images. The fourth column is based on images captured by an intensified CCD camera equipped with a Nikon $105\,\mathrm{mm}$ UV lens and OH^* filter centered at $308\,\mathrm{nm}$. It shows the evolution of intensity integrated over all vertical pixels corresponding to each horizontal coordinate in the flame zone normalized by its maximum value. The flames formed by 707 (with adjacent co- or counter-rotating neighbors) in TICCA-Spray are, in general, longer and narrower with negligible interaction between the adjacent flames. This is apparent from the intensity plots in Fig. 10.4 (m) and (n), where the integrated intensity between the flames is quite low. Likewise, the flames of 707 in SICCA-Spray feature lesser interactions with the chamber walls but are comparatively shorter than in TICCA-Spray.

The flames established by 716 (with adjacent co- or counter-rotating neighbors) in TICCA-Spray are shorter and broader compared to 707, which results in augmented interaction with the neighboring flames. This can be seen at F1 in Fig. 10.4 (g) & (h), where the flame fronts touch their neighbors at the top. This is also apparent in the intensity plots in Fig. 10.4 (o) & (p), where the intensity level between flames is higher than for 707 (Fig. 10.4 (m) & (n)). The integrated intensity plots also indicate that the flames of 716 are broader than those of 707 in SICCA-Spray, indicating a higher flame-wall interaction with 716. The central flame of 716 is also less symmetric in TICCA-Spray (see Fig. 10.4 (o) & (p)), which could be due to the augmented interaction between flames and to the fact that all swirlers are co-rotating. At F2, the flames in TICCA-Spray are weakly interacting with the neighboring flames, and similarly, their interaction with the wall is reduced in SICCA-Spray. This is noticeable from Fig. 10.4 (p), where the intensity level between flames is lower in TICCA-Spray, and the flame is comparatively narrower in SICCA-Spray. With 716, the side flames of TICCA-Spray possess a shape similar to the wall-bounded flames of SICCA-Spray, which differs from the shape of the central flame in TICCA-Spray. The flames that interact with the wall feature wings on their sides that reach up to the lateral boundaries. The absence of this feature in the flames of 707 could be attributed to the reduced expansion of the flame and correspondingly reduced wall interaction. No obvious difference is visually observed in the flame images between co- and counter-rotating neighbors. For the two swirler arrangements, the flames at F2 are evidently brighter as they operate at a higher equivalence ratio. The general differences in the lateral extent of the flames between 707 and 716 may be linked to the higher swirl number of the latter, leading to a wider inner recirculation zone and an expanding flow field.

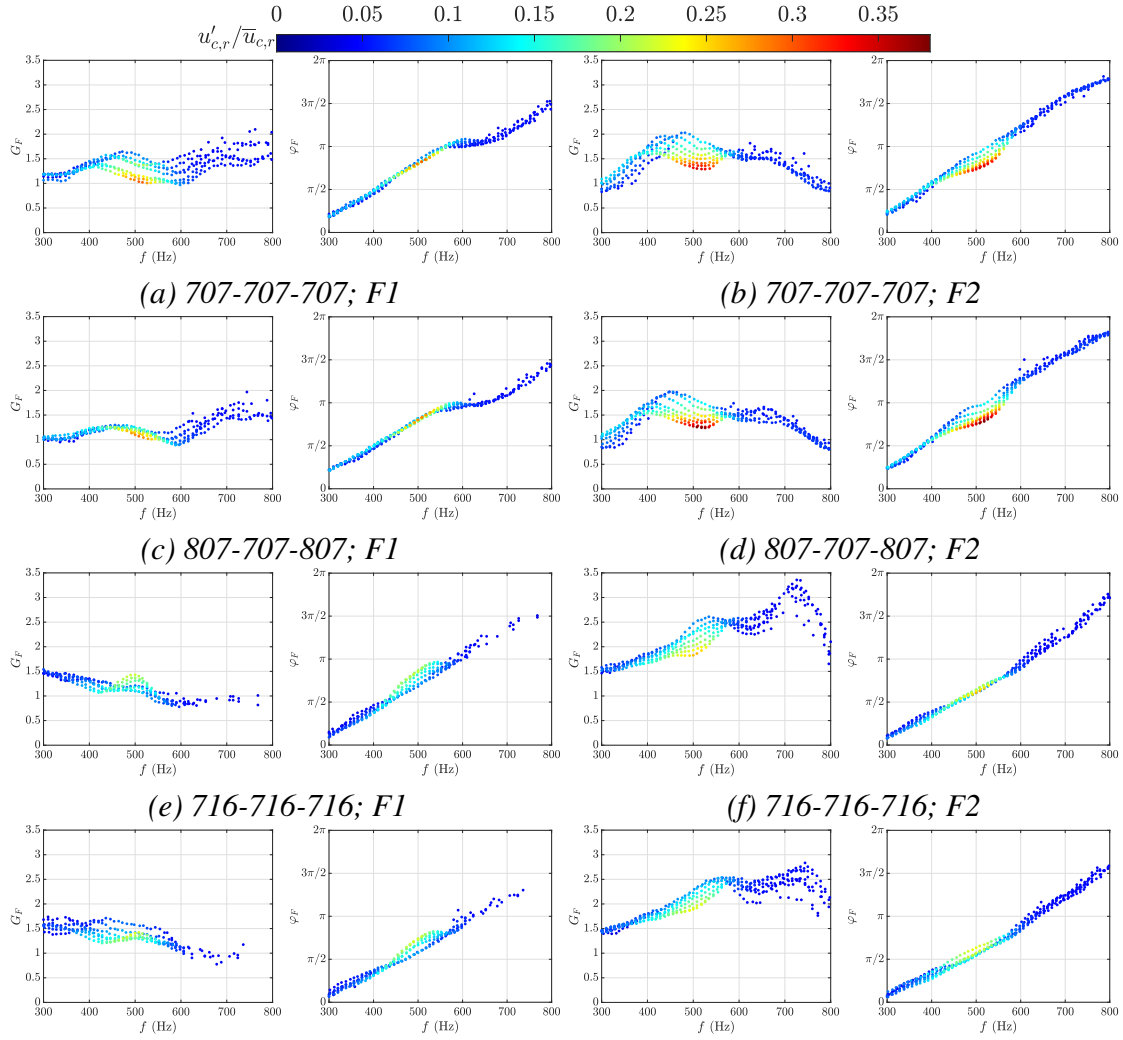

(a) 707-707-707; F1 *(b) 707-707-707; F2*

(c) 807-707-807; F1 *(d) 807-707-807; F2*

(e) 716-716-716; F1 *(f) 716-716-716; F2*

(g) 816-716-816; F1 *(h) 816-716-816; F2*

Figure 10.5. *Gain G_F and phase φ_F of FDFs measured in TICCA-Spray at the two operating conditions. The color scale represent the velocity fluctuation levels measured at the injector outlet.*

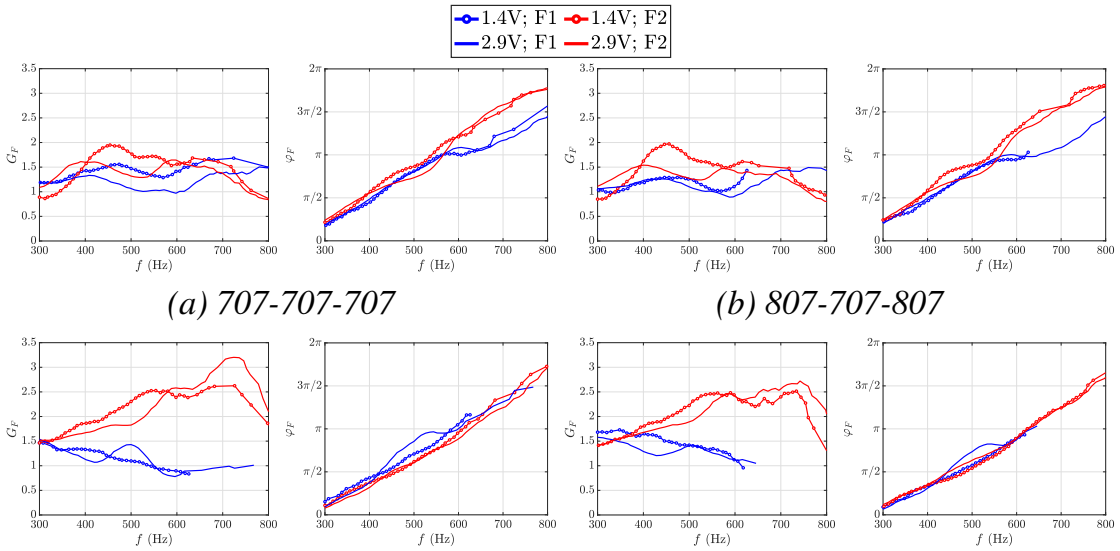

(a) 707-707-707 *(b) 807-707-807*

(c) 716-716-716 *(d) 816-716-816*

Figure 10.6. *Comparison between operating points: gain G_F and phase φ_F of the FDFs measured in TICCA-Spray showing the comparison between the two operating points for the different swirler combinations (F1: blue, F2: red). Results are only plotted at two amplifier voltages $V_0 = 1.4\,\mathrm{V}$ (solid line with marker) and $2.9\,\mathrm{V}$ (solid line without marker), to illustrate the differences.*

10.4.2 FDFs measured in the linear array facility TICCA-Spray

The FDFs measured in TICCA-Spray for the various swirlers and operating points are displayed in terms of gain G_F and phase φ_F in Fig. 10.5 for a range of frequencies and velocity fluctuation levels. Data are smoothed using a five-point moving average and shown only if the coherence γ^2 between HRR and velocity signals is at least 0.90. Experiments have also been repeated to ensure that the data reported can be reproduced reasonably well (see Appendix 2). Substantial variations in the velocity fluctuation amplitudes are obtained up to $600\,\mathrm{Hz}$, beyond which the system is only weakly responsive to acoustic perturbations. The modulation level remains relatively low ($\approx 5\%$) beyond $600\,\mathrm{Hz}$, and the signal levels are quite weak to consider any variation in the FDF. It might still be possible to analyze the flame dynamics linearly (as FTF) in this range, but caution is to be taken as the measurement uncertainties are expected to be comparatively higher in this region due to the lower signal-to-noise ratio (discussed in Appendix 2).

Nonlinearity, especially in the gain, is observed between $400\,\mathrm{Hz}$ and $600\,\mathrm{Hz}$ for all the operating conditions except for 707 with adjacent counter-rotating swirlers at F1 (Fig. 10.5 (c)). The phase, however, is mostly independent of the modulation amplitude except for 707 at F2 (Fig. 10.5 (b) and (d)) and 716 at F1 (Fig. 10.5 (e) and (g)) in the vicinity of $500\,\mathrm{Hz}$ (with both co- and counter-rotating neighbors). The change in equivalence ratio affects the FDF gain and phase, as seen

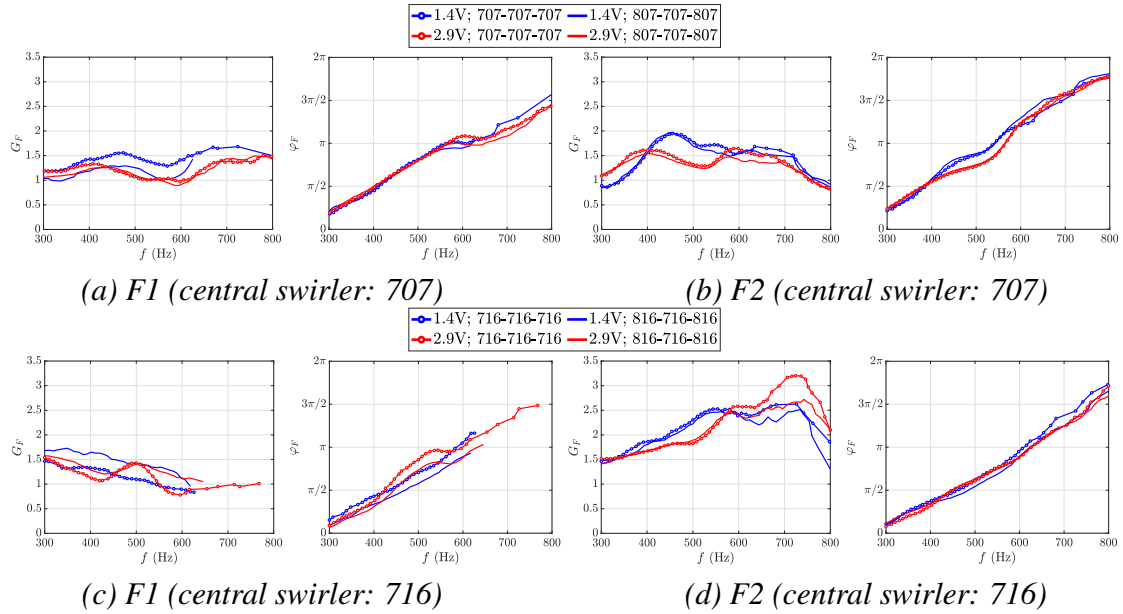

(a) F1 (central swirler: 707) *(b) F2 (central swirler: 707)*

(c) F1 (central swirler: 716) *(d) F2 (central swirler: 716)*

Figure 10.7. *Influence of neighboring swirlers: gain G_F and phase φ_F of the FDF measured in TICCA-Spray with co- (solid lines with marker) and counter-swirl (solid lines without marker) swirler combinations at the two operating points F1 and F2. Results are presented for two amplifier voltage $V_0 = 1.4\,\mathrm{V}$ and $2.9\,\mathrm{V}$ of the driver units.*

in Fig. 10.6. The results are presented only at two amplifier voltages for better clarity. The difference is comparatively modest in the gain of 707 with both adjacent co- and counter-rotating swirlers. This could be attributed to the absence of strong flame-flame interaction with this swirler. The phase evolution for 707 is nearly the same at F1 and F2 until $550\,\mathrm{Hz}$, beyond which the phase at F1 shows a plateau before increasing again. For 716, increasing the equivalence ratio from F1 to F2 leads to an increased gain, and at $700\,\mathrm{Hz}$, the gain at F2 is about three times that found at F1 (see, for example, Fig. 10.6 (c)). This variation in gain could be caused by the higher flame-flame interaction at F1 compared to F2 (see Fig. 10.4 (o) & (p)). The phase evolution nevertheless remains the same.

10.4.3 Comparison of FDF between co- and counter-rotating swirl

The TICCA-Spray test rig allows examining the effect of having counter-swirling flames next to the central flame rotating in the clockwise direction. Obviously, this effect cannot be examined in a single injector configuration. Figure 10.7 shows, on the same graphs, the comparison of FDFs plotted in terms of amplifier voltages for the two swirler units and operating points when having adjacent co- or counter-swirling flames. Although a representation in terms of amplifier voltage is not physically intuitive, it is reminded that they, in turn, are linked to velocity

modulation level. To read these values, one could refer to Fig. 10.5.

Overall, the FDF of 707 does not depend on the type of the adjacent swirlers. Both gain and phase generally remain the same with both co- and counter-rotating swirlers, except for a minor difference in gain at $V_0 = 1.4\,\mathrm{V}$. On the contrary, the FDF of 716 has a higher dependence on the neighboring flames, especially at F1. Both the FDF gain and phase moderately differ depending on whether the adjacent swirlers are 716 or 816 type. The gain with counter-rotating neighbors is slightly higher than that determined in the co-rotating case, whereas the phase takes slightly higher values with co-rotating swirlers. On the other hand, the difference in the FDF of 716 between co- and counter-rotating swirlers is only modest at F2, with minor variations in gain beyond $600\,\mathrm{Hz}$. However, in this region, the velocity fluctuation level is relatively low (refer to Fig. 10.5 (f) & (h)) to reasonably identify a difference.

The reason for this variation in the dynamic response of the flame depending on the adjacent swirlers can be well understood from the flame images shown in Section 10.4.1. Flames with 707 are narrower and have visibly weaker interactions with adjacent flames. Thus, the FDF of 707 is influenced to a lesser extent by the presence of a co- or counter-rotating neighbor. In contrast, 716 flames are wider, and the span of the neighboring flames evidently extends to the central flame, resulting in stronger interactions with the neighbors. This interaction is more pronounced at F1, as seen in Fig. 10.4 (g) & (h), where the wings of the neighbors touch the central flame (also seen in (o)). This is manifested in the FDF as a strong variation in gain and phase between co- and counter-swirling flames. However, at F2, the flame is comparatively narrower, and its interaction with the side flames is weaker, resulting in similar FDF evolution in configurations where the central flame that rotates in the clockwise direction is surrounded by counterclockwise neighbors.

10.5 Comparison of FDF measured in TICCA-spray and SICCA-spray

This section compares the FDF measured in the three-injector test rig TICCA-Spray against the measurements from the single-injector test rig SICCA-Spray. This comparison will identify the adequacy of the widely used procedure of obtaining the FDFs from a single-injector test rig, a procedure that is used, for example, in Rajendram Soundararajan et al. (2022) to explain observed instabilities. The comparison of the FDFs pertains to the central swirler in TICCA-Spray when the adjacent flames are of co-rotating type. Figure 10.8 shows the FDFs in terms of gain and phase between the two configurations. The FDFs obtained in SICCA-Spray are represented as solid lines with markers, and the FDFs de-

termined in TICCA-Spray are represented by solid lines without markers. These lines are colored according to the velocity fluctuation levels. The span of the FDF data obtained is represented by the colored bands, and the statistical uncertainties calculated by a bootstrapping method remain within this span (also discussed in Appendix 2). The levels of velocity fluctuations between the two systems match in the range from $300\,\mathrm{Hz}$ to $600\,\mathrm{Hz}$. Beyond 600 Hz, the signal level in TICCA-Spray is too weak, and the coherence between the input velocity and the output heat release rate modulations is low, unlike in SICCA-Spray. At F1, a difference in gain exists for both swirlers; while this difference is modest for 707, the gain of 716 is significantly higher in SICCA-Spray than in TICCA-Spray. The reason for the higher gain in SICCA-Spray could be attributed to the flame-wall interaction illustrated in Fig. 10.4 (i) & (o). Such interactions induce strong variations in the flame surface area, which, in turn, contribute to sound production, as shown by Candel et al. (2004). At a higher equivalence ratio, the flame of swirler 716 is narrower and features reduced interaction with the chamber walls in SICCA-Spray and adjacent flames in TICCA-Spray, possibly explaining similar gain values between the two systems at F2. The gain of 707 at F2 is nearly the same between the two systems except for some minor differences at low frequencies.

On comparing the phase curves, one observes that the phase of 707 takes lower values in TICCA-Spray than in SICCA-Spray but evolves in a nearly similar fashion for both operating points. The dependence of the phase on the input velocity fluctuation level is prominent for swirler 707 at F2. One also notices a deviation in phase beyond $550\,\mathrm{Hz}$ at F1, but the velocity fluctuation levels are much lower in this zone for TICCA-Spray than SICCA-Spray. With 716, the phase takes the same values between TICCA-Spray and SICCA-Spray at F1, thereby indicating similar values for the time delay between velocity and HRR fluctuations. On the other hand, the phase for the swirler 716 at F2 has a different behavior than at F1; although it has a similar evolution, the phase value measured with TICCA-Spray is lower than that measured with SICCA-Spray below $600\,\mathrm{Hz}$. This means that the time taken for the velocity fluctuations produced at the injector exit to reach the entire flame area will be the same between the two systems as at F1, except that the phase is shifted by a constant value, unlike at F1. The behavior at F2 is similar to the observations with swirler 707 but different from the behavior of swirler 716 at F1. Further diagnostics of the flow and flame behavior would be necessary to explain the observed differences.

The differences in FDFs between the two systems can be much appreciated by considering their impact on instability prediction using low-order modeling such as the one proposed in Chapter 5 for injectors that are weakly transparent to acoustic waves or in Schuller et al. (2020) for acoustically transparent injectors. As shown in these articles, the phase of the FDF often determines whether or not the system falls within an “unstable band” which can serve to predict a

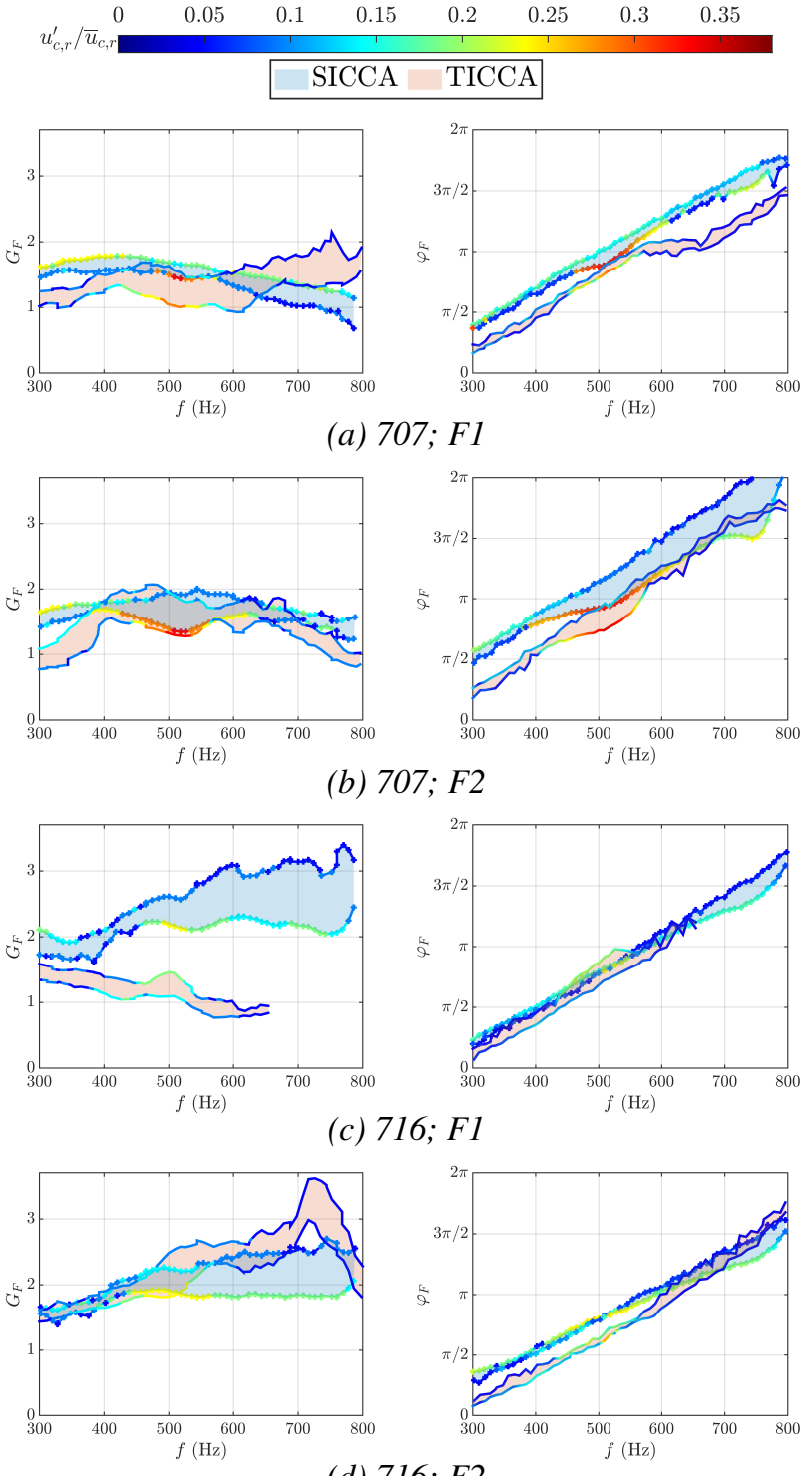

(a) 707; F1

(b) 707; F2

(c) 716; F1

(d) 716; F2

Figure 10.8. *Comparison of gain G_F and phase φ_F of the FDFs measured in the multiple-injector setup TICCA-Spray (solid lines without marker) with co-rotating neighbors and in the single-injector system SICCA-Spray (solid lines with marker) at the two operating points F1 and F2, and for the swirlers 707 and 716. The levels of velocity fluctuations $u'_{c,r}/\overline{u}_{c,r}$ are indicated by the color levels and the span of the FDF data is represented by the colored bands.*

potential instability in a particular frequency range. Furthermore, the gain of the FDF determines the growth rate, which relates to the amplitude of instability, provided the growth rate is originally higher than the damping rate imposed by the system. This indicates that, for swirler 707, one could reasonably obtain similar growth rates irrespective of whether the FDF is measured with an isolated flame or in an environment where the flame is surrounded by adjacent neighbors. Regarding the phase, it was shown that, despite having similar slopes, it takes lower values in TICCA-Spray than in SICCA-Spray. This introduces some uncertainty in assessing the instability potential. The phase curves in Fig. 10.8 (a) and (b) indicate a horizontal shift between the curves. This induces a $50\,\mathrm{Hz}$ displacement of the crossing point of the phase with one of the boundaries of the unstable region, causing a $50\,\mathrm{Hz}$ uncertainty on the range of frequencies where the instability might occur. Regarding swirler 716, the phase curves nearly coincide at F1, and the frequency range of potential instability can be assessed with smaller uncertainty. However, the differences in the FDF gains measured in SICCA-Spray and TICCA-Spray will give rise to notable changes in the growth rates. At F2, the differences observed in the FDF phase will result in some uncertainty in the frequency range of potential instability. Since the FDF gains are quite similar at F2, this will give rise to similar growth rates.

The above results indicate a moderate but non-negligible difference in the FDF between the two combustors. Also, whether the FDF measurement should be done in an isolated flame or a flame surrounded by the neighboring flames cannot be universally decided but rather depends on the flame geometry. In general, one would obtain an approximate prediction of the instability of an annular combustor using the FDF measured in a single-injector combustor if the flame-wall interaction is not too strong and provided that the backplane area is equivalent to that of a single sector of the annular combustor, *i.e.*, the area ratio A_I/A_{BP} is maintained. If A_I/A_{BP} is not conserved, the single-injector combustor will feature a different flow pattern, as can be seen in Fanaca et al. (2010). Nonetheless, a multi-injector system reflecting the flame-flame interaction found in the annular combustor would be worthwhile to get an accurate FDF and more precisely predict the instabilities. Since interactions between injector flows are mainly governed by the flame geometry, the results presented here, although demonstrated on a spray combustor, can be expected to be applicable to premixed injectors as well.

10.6 Conclusions

This article primarily reports flame describing functions (FDFs) measurements on a newly-developed three-injector linear test rig. In a first-of-its-kind study, FDFs measured in an isolated flame formed by a confined single-injector combustor are compared to those corresponding to a flame surrounded by neighboring side flames to identify the effect of lateral boundary conditions. Measurements of

FDFs are carried out with two swirlers varying in swirl intensity at two operating points differing in global equivalence ratio. The three-injector configuration allows to additionally study the effect of neighboring swirl direction on the FDF by placing either co- or counter-rotating swirlers in the lateral injectors.

Comparisons of FDFs measured in the single-injector SICCA-Spray and in the linear array TICCA-Spray reveal differences in gain and phase at a level that depends on the operating conditions. In general, larger differences arise in the gain in cases where flame-wall interactions are strong. In other cases where flame front interactions with lateral boundaries are less pronounced, the FDF gain remains almost the same between the two configurations. The phase curve corresponding to the multiple-injector situation features the same slope but exhibits an offset with respect to that determined in the single-injector system. This will have a moderate but non-negligible impact on predictions of instabilities based on FDFs measured in a single-injector combustor. The direction of rotation of the adjacent swirlers becomes particularly important when the flame fronts have pronounced interaction with their neighbors. If such interactions are negligible, the FDF is nearly the same with co- or counter-rotating neighbors.

The experiments reported in this chapter at eight operating conditions indicate that the decision on the suitability of measuring the FDF in an isolated flame or in an environment where a flame is surrounded by adjacent side flames has no single answer but rather depends on the flame geometry produced by the injector. In general, the FDFs measured with a single-injector combustor would approximately represent a multi-flame system if the flame-wall/flame-flame interaction is minor. In this case, an order-of-magnitude prediction of instability in an annular combustor can be obtained using the FDFs measured in a single-injector combustor, provided that the single-injector combustor possesses the same area as the single sector of the annular combustor. A multi-injector system will still be needed if one requires a more precise FDF measurement.

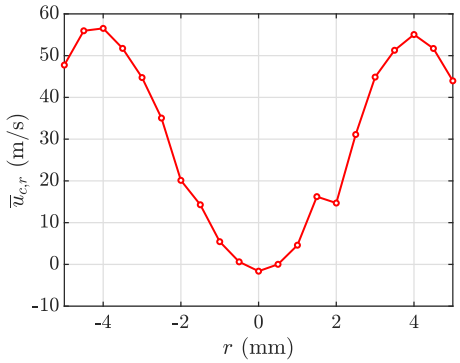

Figure 10.9. *Mean axial velocity profile of TICCA-Spray with 716 (co-rotating 716 neighbors) measured at F2 under steady conditions.*

Appendix 1: Sensitivity of FDF on the measurement location

As indicated in Chapter 4, for SICCA-Spray, the optimal point for measuring the relative velocity fluctuations was found to be close to the location of maximum mean axial velocity. In TICCA-Spray, this optimal position could be different due to the interaction of flow fields of the central swirler with the neighboring units. This may be examined by measuring the axial velocity in TICCA-Spray under steady conditions for the central injector at different radial locations to obtain the velocity profile with one of the swirlers, in this case, 716 (with co-rotating 716 neighbors). Measurements are performed using LDA directly on the heptane droplets in the presence of flame. Figure 10.9 shows the evolution of mean axial velocity at the operating point F2. The central recirculation zone is less pronounced like in the case of SICCA-Spray (Fig. 4.6 left) as only a small amount of large droplets are present in this region leading to reduced measurement accuracy. The velocity profile for the central injector evolves identically to that of an isolated injector in SICCA-Spray, indicating that the interaction between swirlers has not resulted in a significant modification of the flow field. The maximum mean axial velocity occurs at $r = 4\,\mathrm{mm}$ for 716, the same location as that of SICCA-Spray, and thus the FDF measurements are carried out at this location.

To further identify the sensitivity of the FDF on the radial location, measurements are carried out around the optimal position when the flame is modulated at an amplifier voltage of $V_0 = 2.9\,\mathrm{V}$. Figure 10.10 shows the evolution of the FDF gain and phase at different radial locations for swirler 707 (counter-rotating 807 neighbors) for which the optimal location is at $r = 3.5\,\mathrm{mm}$. These measurements are carried out at the operating point F2 in steps of $0.2\,\mathrm{mm}$ for the radial location. It can be seen that the gain changes rapidly with the radial location, while the phase evolves similarly if the radial location is such that $r < R_{\mathrm{inj}}$ until $550\,\mathrm{Hz}$ but

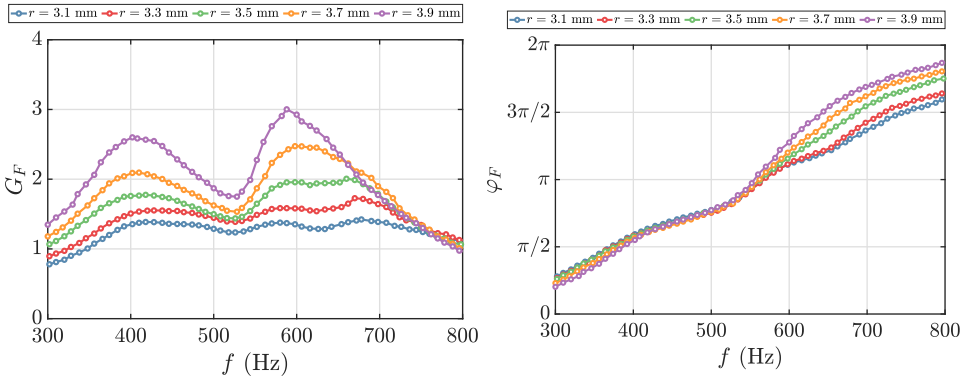

Figure 10.10. *Gain G_F and phase φ_F of FDF at different radial locations for swirler 707 (counter-rotating 807 neighbors). Measurements are carried out at F2, and an amplifier voltage of $V_0 = 2.9\,\mathrm{V}$.*

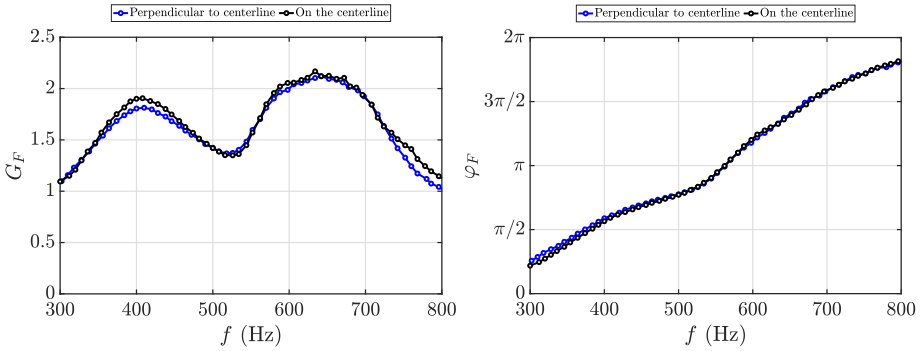

Figure 10.11. *Comparison of FDF with 707 (counter-rotating 807 neighbors) at F2 measured at two radial locations, one along the centerline of the LDA laser and another perpendicular to it. These measurements are carried out at an amplifier voltage of $V_0 = 2.9\,\mathrm{V}$.*

varies substantially from the optimum phase if the radial position crosses R_{inj}. This shows the importance of correctly positioning the velocity measurement location for FDF determination. In addition, it is also ensured that the FDF does not depend on the angular position as long as the measurements are carried out at the optimum radius. This is shown in Fig. 10.11, where measurements are carried out with 707 (counter-rotating 807 neighbors) at two positions, one at $r = 3.5\,\mathrm{mm}$ in the axial plane containing the centerline of the LDA laser and the other at $r = 3.5\,\mathrm{mm}$, in an axial plane perpendicular to that centerline.

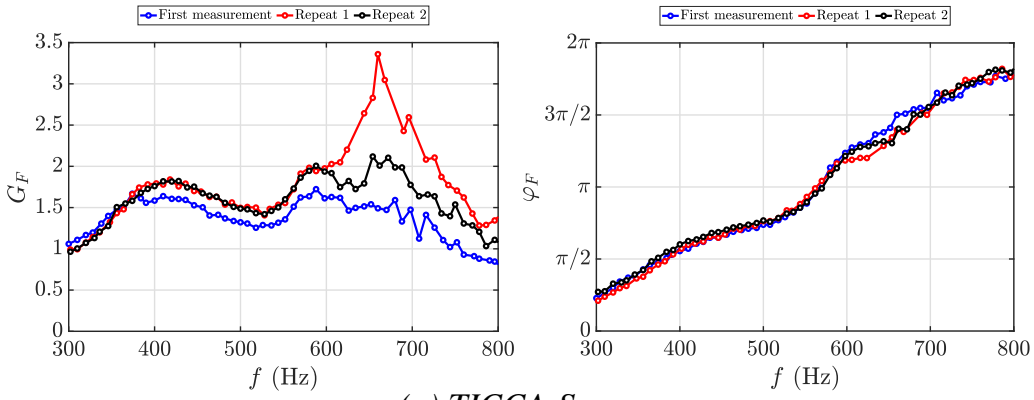

(a) TICCA-Spray

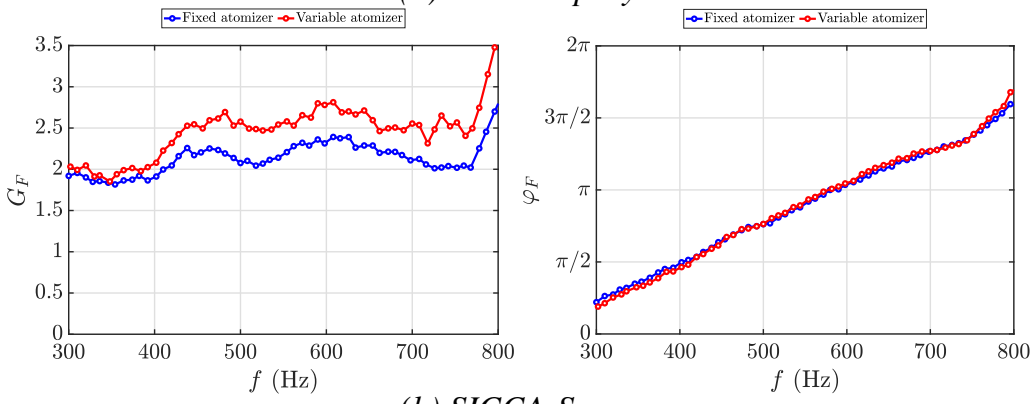

(b) SICCA-Spray

Figure 10.12. *(a) Gain G_F and phase φ_F of FDF in TICCA-Spray with 707 (co-rotating neighbors) at F2 measured three months apart. (b) FDF measurements carried out in SICCA-Spray with 726 at F1 at an amplifier voltage of $V_0 = 2.9\,\mathrm{V}$. The measurements are performed at an amplifier voltage of $V_0 = 2.9\,\mathrm{V}$ in TICCA-Spray and $3\,\mathrm{V}$ in SICCA-Spray to ensure the best possible signal quality.*

Appendix 2: Repeatability and uncertainty of FDF measurements

As pointed out by the reviewers of the full-length article forming this chapter, since the comparison of FDF is carried out between two different experimental setups, it is important to consider the repeatability and uncertainty of measurements in these two setups. Figure 10.12 (a) shows the evolution of gain and phase in three different data sets pertaining to 707 (co-rotating neighbors) at F2. The amplifier voltage is set at $V_0 = 2.9\,\mathrm{V}$ resulting in the highest attainable velocity modulation levels at the various frequencies and ensuring the best possible signal-to-noise ratio. Overall, the FDF gain curves evolve similarly, with a variation of less than 20% until $600\,\mathrm{Hz}$. One observes a non-negligible difference mainly between the repeat measurements in the frequency range from 600 to $700\,\mathrm{Hz}$. This could be attributed to the lower relative velocity modulation levels in TICCA-Spray beyond $600\,\mathrm{Hz}$, resulting in a reduced signal quality leading to a higher variability between the different measurements. This is noticeable from Fig. 10.5 (b) beyond $600\,\mathrm{Hz}$, where similar velocity fluctuation levels result in larger deviations in the gain values. In addition, as shown in the top row of Fig. 10.13, the uncertainties are slightly higher beyond $600\,\mathrm{Hz}$, indicating that the data is less reliable in this region. On the other hand, there is almost no variability in the FDF phase between the various measurements. In SICCA-Spray, the repeat measurements carried out with the same injector resulted in identical FDFs and are not shown here. Hence, repeatability analysis is considered with different manufactured specimens of the atomizer, one with a fixed atomizer and the other with a variable atomizer (discussed in Chapter 8) at the nominal recess distance of $h_r = 6.75\,\mathrm{mm}$ from the backplane. Figure 10.12 (b) shows the FDFs obtained with the two types of atomizers. It can be seen that the variations in gain are typically less than 20%, with the phase evolution remaining the same between the two measurements. From this discussion, it can be concluded that the measurements in both the experimental setups are reasonably repeatable.

For computing the statistical uncertainties associated with the FDF measurements, a bootstrapping method is used, and the associated error bars are shown in Fig. 10.13 with swirler 716 at the operating point F1. The uncertainties of SICCA-Spray are quite low in gain and phase and in the whole frequency range. The FDF gain of TICCA-Spray has lower uncertainties until $600\,\mathrm{Hz}$, beyond which the deviation is slightly higher for the few points that satisfy the coherence criterion $\gamma^2 > 0.9$. This can be attributed to the low velocity fluctuation levels (see Fig. 10.5) at these higher frequencies resulting in comparatively higher noise levels. The FDF phase of TICCA-Spray has only negligible uncertainties in the examined frequency range.

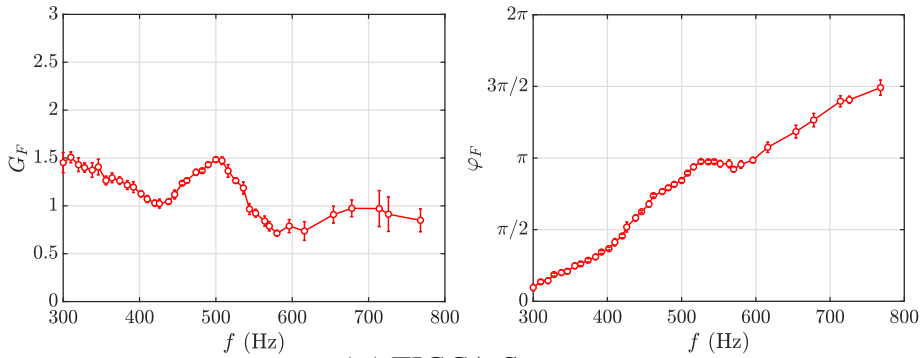

(a) TICCA-Spray

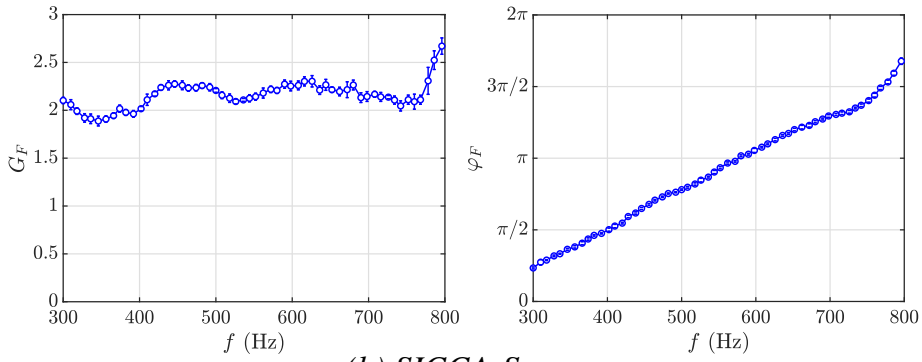

(b) SICCA-Spray

Figure 10.13. *Uncertainties in the FDF measurements obtained with a bootstrapping method. The results are shown for swirler 716 with co-rotating neighbors for (a) TICCA-Spray and with swirler 716 for (b) SICCA-Spray measured at the operating point F1 and maximum attainable amplifier voltage in both the cases.*

Conclusions and perspectives

Conclusions

The present investigation is meant to contribute to the domain of combustion dynamics by providing new data and developing models to understand, interpret, and predict combustion instabilities. The central theme of this investigation is to examine instabilities coupled with azimuthal modes, which most often arise in the annular combustors used in aircraft engines or gas turbines. It is known that azimuthal modes are the most dangerous because they are less well-damped and feature the lowest eigenfrequencies. These frequencies can fall in the range where flames are most sensitive to disturbances and respond with the highest gain to these disturbances. Understanding these instabilities has become even more critical in the present context of transitioning towards newer low-carbon fuels.

This work is mainly focused on flames formed by sprays of liquid fuel droplets and on injectors generating a swirling flow. These injection units feature essential characteristics found in aircraft combustors but in a simplified geometry. A choice was made to operate with liquid fuels that are simpler but similar to kerosene. The present investigation considers heptane, which is highly volatile, and dodecane, which is comparatively less volatile, to replace the more complex combination of molecules that compose the jet fuel. To deal with issues in a systematic fashion, it is logical to use pure liquid fuels instead of complex mixtures that are found in practical fuels.

For fundamental investigations, it is preferable to idealize the swirler and injector geometries to define a family of swirlers that allow simple geometrical variations. It has been possible to vary the head loss and swirl number and, in this way, sort out the main effects without dealing with the complexities found in real injection units. As a continuation of the previous investigations, the present work is aimed at examining the dynamical behavior of the injection units.

An original aspect of this research has been to establish a dialog between experiments carried out in three different environments, the first being that of an annular geometry allowing coupling between combustion and azimuthal modes (MICCA-

Spray), the second being a single sector comprising one injector placed in a cylindrical chamber (SICCA-Spray), and the third being a new facility equipped with a linear array of three injectors placed in a rectangular chamber (TICCA-Spray). This platform of three test rigs allows data exchanges and guides the choices of experiments to be carried out in the annular combustor. This also multiplies the configurations that can be used for validation and allows measurements that cannot be made in the more complex annular system. This research effort also requires that systematic experimentation be combined with modeling, which has been the central theme of this undertaking. The modeling relies on simplified representations of the flame response in terms of its describing function.

Here are a few conclusions gathered in a synthetic form. More details of these findings are available at the end of each chapter.

- One of the fundamental questions considered in this research is the possibility of representing the dynamics of a multi-dimensional combustion process with a flame describing function (FDF) relating an input, typically the incident volume flow rate fluctuations, and an output, namely the heat release rate fluctuations. The analysis indicates that the FDF, determined at the resonance frequency and input disturbance level of self-sustained oscillations (SSOs), does indeed coincide with the flame response during an SSO. This is valuable since much of the low-order modeling used in combustion dynamics assumes that the flame can be represented by a black-box input/output describing function. Although previous research efforts have successfully exploited these representations for instability predictions, direct experimental evidence is provided in the present thesis.

- The initial part of this work also deals with the response of the injection unit. In contrast with the more traditional injectors that allow transmission of acoustic disturbances with no impediment, it was found that the present injectors were only weakly transparent to acoustic waves. This characteristic is attributed to the high pressure drop and sharp area changes. One may then question whether the dynamics of such units may be represented with standard acoustic methods. This has consequences in terms of modeling and direct experimental determination of the FDFs.

- Concerning the determination of the FDF itself, it is found that reasonable estimates can be obtained by carefully choosing the point where velocity fluctuations need to be measured. When the velocity profile on the upstream side of the flame is nonuniform, this point should be such that the relative velocity disturbances coincide with the relative volumetric fluctuation rate. This choice is found to provide suitable values for the FDF.

- Using a family of injectors, it is found that the head loss and swirl number

define, to a large extent, the combustion dynamics of the system. It is observed that the swirler characteristics notably influence the FDF values, and this has a direct impact on the SSOs observed in the single-injector combustor SICCA-Spray.

- The experimental results gathered in SICCA-Spray with different injectors are then used to guide the low-order modeling aimed at identifying regimes of instability. It is shown that this requires a suitable representation of the injector response and that this can be conveniently achieved by assigning an impedance to the injector outlet. In turn, this impedance has to be measured or modeled or may be inferred from a combination of measurements and modeling. The model that combines experimentally determined FDFs, injector impedance and estimated damping rates is then used to predict the occurrence of unstable oscillations. One conclusion of this research effort is that the injector impedance determines the location of the unstable bands by shifting the boundaries of these bands in the FDF phase diagram. The head loss coefficient enters in the expression of the impedance's real part and thus directly impacts the instability boundaries.

- The knowledge gained from the single-injector experiments with different swirlers is used in a second stage to guide experimentation in the annular combustor and interpret instabilities coupled by azimuthal modes. It is found that a critical swirl number exists for this particular annular configuration below which the system is unconditionally stable. For the swirlers that were unstable, one observes that the pressure drop contributes to further variations in the amplitude and frequency of oscillations. By combining these results with the FDF information from the single-injector combustor, it is concluded that the pressure drop value influences the unstable band position, whereas the location of the FDF phase with respect to the unstable band depends on the swirl number value.

- Experiments carried out with a variable recess atomizer (an atomizer placed at various distances from the injector outlet) indicate that this parameter notably influences the behavior of the system. The change in fuel atomizer location modifies the spray shape and its spatial dispersion and possibly the droplet convective time, resulting in a change in the instability behavior.

- Experiments with different fuels carried out in this research indicate that the fuel composition and mode of combustion play a major role. The domains of instability boundaries are shifted, and the resonance frequencies are modified when the fuel is changed. These are indications that the main effect is linked to changes in the time lag between the input disturbances to the flame and its output in the form of heat release rate fluctuations. These experiments give access to the vaporization delay effects on the development of instabilities.

- Finally, in a first-of-its-kind study, comparisons are made between FDFs determined in the single-injector combustor (SICCA-Spray) and in the multiple-injector linear array system (TICCA-Spray). Results show that the choice of carrying out FDF measurements in a single- or multi-injector combustor depends upon the extent of flame-wall interaction or flame-flame interaction. In any case, one would at least obtain an order-of-magnitude FDFs using the single-injector combustor, but a multi-injector combustor is still needed for obtaining more precise FDF values. Of course, the linear array configuration is closer to the flame environment found in the annular combustor and is more suitable for future determinations of FDFs, provided that a higher modulation level, similar to the instability levels of the annular combustor, can be achieved in TICCA-Spray.

Perspectives

Advances made in this thesis open new areas of investigation. Several of these are listed below.

Examining the injection unit dynamics

- One area requiring further examination pertains to the injection unit. It is seen that this component determines to a large extent, the system dynamics. Experiments have shown that the swirl number has a notable effect on the FDF phase and subsequently on the combustion dynamics. It will be essential to pursue the characterization of injectors and develop a suitable modeling framework to represent the change in pressure and velocity fluctuations after the injector. This could be achieved by obtaining a transfer matrix for the injector that could include a frequency-dependent variable to represent the variation in fluctuation amplitude and phase across the injector. However, it will be important to see whether the transfer matrix method is applicable in cases where the injector induces a relatively large head loss and is therefore weakly transparent to acoustic waves. Thus, the corresponding model must be subsequently validated, for example, using simple impedance tube measurements. If such a model can be validated, then the velocity measured in the plenum using simple instrumentation can be transformed to obtain the velocity fluctuations at the base of the flame.

- Another aspect concerning the injection unit is the determination of impedance at the injector outlet. It was seen in this work that this value depended on the injector, particularly on its pressure drop value, which directly influences the position of the unstable bands. Thus a precise estimate of this impedance is needed to advance the proposed low-order modeling framework. In the present study, the injector outlet impedance is determined by making use of self-sustained oscillations as a source of acoustic waves, but this is not ideal. Thus, a downstream modulation system that can produce high amplitude disturbances might have to be implemented in the single-sector setup to obtain this value at different amplitudes and frequencies. It is also necessary to accurately determine this value in the frequency range where MICCA-Spray exhibits instabilities. The other alternative for such experimental determination is to use the injector transfer matrix model once such a representation is successfully developed.

- Another possibility to understand the injector behavior and obtain its impedance is using large eddy simulations (LES). Although this was begun in the present work with a validation study performed for a steady flame, this needs to be further pursued eventually for a modulated flame.

- Another aspect of injector impedance is determining whether this value is dependent on the experimental setup. Normally, the injector impedance also includes the acoustic state of the plenum, which is not identical between the simplified setups and the annular combustor. However, on comparing the measurements obtained in SICCA-Spray with the linear, transversely-modulated test rig at CORIA (TACC-Spray), it was found that this impedance takes similar values, even though the plenum configurations are entirely different in the two test rigs. It is thus essential to verify this point further so that the injector impedance measured in a simpler setup can be employed in the annular combustor configuration.

Flame describing function measurements

- FDFs in the current work are determined by approximating heat release rate fluctuations to light intensity fluctuations from OH^* chemiluminescence. Although this is proven suitable for the spray flames considered in this work due to their quasi-premixed operation (attributed to the atomizer recessed location and the subsequent spray-wall interactions), this is not generally valid for technically premixed flames. Thus, other possibilities of obtaining the heat release rate fluctuations from the flames need to be explored. One such way is measuring the velocities at the base of the flame and close to the chamber outlet and obtaining the FDF without the need for measuring the heat release rate. This method, which has been partially validated, could be adopted as an alternative technique for FDF determination. However, this approach would still require optical access to the base of the flame. Thus, it would be interesting to consider the flame transfer matrix (FTM) approach by combining the acoustic measurements made in the plenum and chamber. This has been widely used in many previous works with transparent injectors, but the validity of FTM for a weakly transparent injector needs to be established. This method also considers the measurement of an injector transfer matrix under cold conditions. One thus needs to verify whether such a matrix does reproduce the injector behavior in the presence of a flame.

- Obtaining a direct FDF measurement in this work was only possible for flames formed by a spray of fuel droplets, as particle seeding was not feasible. For further studies, the test rigs could be equipped with a particle seeding system for a direct FDF measurement of non-spray flames.

Limit cycle predictions

- The level of modulation to obtain the FDF in SICCA-Spray is sufficient for most of the longitudinal instabilities of this system. However, for certain operating conditions and possibly for the instabilities of MICCA-Spray, the

modulation system cannot reach a sufficient fluctuation level, similar to those found at the limit cycle. Thus, the FDF did not cover the full range of relative velocity fluctuations that may arise, especially in the annular combustor. This is also the case in TICCA-Spray, where the modulation levels are low in the frequency range where MICCA-Spray is unstable, with the maximum attainable level being only 7% beyond 600 Hz. Hence, the modulation level needs to be augmented, possibly by making use of higher-efficiency driver units that can produce higher velocity fluctuation levels even after crossing the weakly-transparent injection units. These elements would then help in suitably predicting the limit cycle amplitudes of MICCA-Spray.

Further investigations of annular combustor instabilities

- One aspect that needs to be considered in the instability prediction of MICCA-Spray is that, so far, only the FDFs measured in the single-injector combustor were used for interpreting the instabilities of the annular combustor. However, this work shows that one needs to use the FDFs from a multiple-injector combustor, especially when the flame-flame interactions are more pronounced, to better predict the annular combustor instability. Thus for future studies, the FDFs need to be measured in the multi-injector combustor after augmenting the modulation levels achieved by the driver units.
- An investigation that might perhaps be pursued concerns the azimuthal structure of the self-sustained modes of oscillation. It is observed that the spin ratio constantly fluctuates and exhibits different behavior when changing the fuel and injector. A variation in the azimuthal structure of the instabilities is also observed for a full co-swirl configuration as well as for a configuration where co- and counter-rotating swirlers are alternatively placed. These experiments have provided a large amount of data obtained by systematically varying several operating parameters, thus opening the possibilities of exploiting new processing techniques to understand the nature of these instabilities.

Impact of spray dynamics

- The study conducted using a variable recess atomizer reveals that a minor change in the atomizer position can modify the interaction of the spray with the injector exit nozzle, thus altering the instability regimes of the system. However, it was not entirely possible to probe the spray-wall interaction mechanism experimentally, and this phenomenon could be investigated in detail using LES simulations. Previous LES studies at CERFACS (Lo Schiavo et al. 2020; Lo Schiavo et al. 2021) and EM2C (Vignat et al. 2021; Vignat et al. 2021) have pursued this topic, and secondary atomization caused

by air blast of the liquid film formed on the injector wall was observed. Such secondary atomization would indicate a change in the droplet diameter in the chamber compared to a case with no spray-wall interaction. However, this is not experimentally observed in the studies reported in Chapter 8 with a variable-position atomizer. Thus, it might be necessary to improve the modeling of spray-wall interaction to have a more accurate description of the physical phenomena.

- The alteration of instability regimes achieved using a few millimeter variations of the atomizer location with respect to the injector outlet also indicates that some minor geometrical changes modify the system dynamics. One may then imagine new ways of designing injectors that would be less sensitive to disturbances, thus diminishing the propensity of the system to become unstable.

Future low-carbon fuels

- Another item that was seen to influence the stability characteristics of the system is the fuel composition. It is found that different fuels having markedly different volatility have a notable impact on the domains of instability and on the characteristics of the unstable modes. This question is of considerable interest at this point in time since near-future aviation fuels, designated as SAFs (or sustainable aviation fuels), may include molecules of widely different physical characteristics and, in particular, species that are highly volatile and other species that are not. It is then interesting to examine the instabilities of flames fed by mixtures resembling SAFs. The idea is to consider surrogates that have the same burning and physical characteristics as SAFs but are less complex, such as mixtures of iso-octane and dodecane.

- The second item of interest related to this subject is to examine the combustion dynamics of systems fed with hydrogen and air. This is considered for future gas turbines, and there are also plans to use hydrogen in aircraft engines. The injection device will have to be modified to allow for gaseous injection of a low molecular weight gas (hydrogen). The injection must also allow rapid mixing to prevent the formation of high-temperature regions, and at the same time, it will be important to consider the dynamics of this new system.

A concise version highlighting the most important conclusions of this study that also raises the scope for future work is tabulated in Tab. 10.3.

The general theme of model development for the prediction of instabilities remains of central interest, and this needs to be continued by capitalizing on the

Table 10.3. *Conclusions and perspectives: highlights.*

Issue	Finding	Future work
How does the fuel affect nature and level of instabilities?	Fuel composition and mode of combustion alter instability boundary and resonance frequencies. The time delay associated with fuels displaces the FDF phase with respect to the unstable bands and affects the FDF gain.	Further studies with newer low-carbon fuels: SAFs and hydrogen.
What is the link between injection unit and thermoacoustic coupling?	The swirler characteristics notably influence the FDF and impedance values. Correspondingly, the stability regimes of annular combustor are also modified; transition to instability mainly depends on the swirl number through its effect on the flame structure, and pressure drop adds to further variations in amplitude and frequency. The developed theoretical framework indicates the notable influence of injector impedance on unstable bands. In general, the pressure drop decides the position of unstable bands, and the swirl number determines the FDFs.	Further development of modeling framework to represent weakly transparent injectors & more accurate determination of injector impedance.
How do boundary conditions affect the FDF?	Depends on the extent of flame-flame and flame-wall interaction. An order-of-magnitude FDF can be obtained with a single-injector combustor, but for a more precise determination, it is necessary to use a multi-injector combustor idealizing flame-flame interactions that take place in the annular combustor.	Using FDFs measured in TICCA-Spray to interpret annular combustor instabilities while also augmenting the velocity modulation level. Developing FDF measurement technique using purely acoustic or non-optical methods.

knowledge that has been generated with further validation efforts. It will also be important to pursue the development of high-performance simulations as a tool for gaining a deeper understanding and guiding modeling efforts by combining them with experiments.

Appendix

Appendix A

An alternative determination of the flame describing function

Since FDFs play a crucial role, it is interesting to explore alternative ways for their determination. One possibility consists in using the relation representing the jump condition across the flame, which links velocity perturbations on the upstream and downstream sides of the flame to the heat release rate in the flame (repeated from Chapter 5):

$$S_2 u_3' - S_2 u_2' = \frac{\gamma - 1}{\rho_0 c_0^2} \dot{Q}' \tag{A.1}$$

where S_2 is the cross-sectional area at the flame section, u_3' and u_2' are the velocity fluctuations before and after the flame, and $\dot{Q}'$ designates the heat release rate fluctuations in the flame. The schematic representation of an idealized injector and combustion chamber is shown in Fig. A.1, depicting the various section jumps. The FDF is obtained at a point 'm' close to the injector exit, where relative velocity fluctuation matches the relative volume flow rate fluctuations. One may then write

$$\dot{Q}' = \overline{\dot{Q}} \mathcal{F} \frac{u_{1m}'}{\overline{u}_{1m}} \tag{A.2}$$

where $\overline{u}_{1m}$ and u_{1m}' are respectively the measured mean and fluctuation velocity at the nominal FDF measurement location, and this notation is equivalent to the convention $u_{c,r}$ adopted in the main text of this document.

Now, $\overline{\dot{Q}} = \rho_1 S_1 \overline{u}_1 \overline{c_p} (T_3 - T_2)$, where $\overline{u}_1$ is the bulk velocity at the injector exit, S_1 is the area of the injector exit section. T_2 and T_3 are the temperatures before

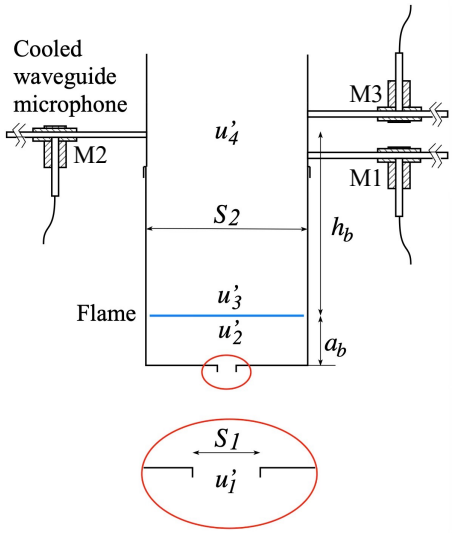

Figure A.1. *A schematic representation of the injector and combustion chamber. Also shown are the locations of the three chamber microphones.*

and after the flame, and $\overline{c_p}$ is such that $\overline{c_p}(T_3 - T_2) = \Delta h$, where Δh is the lower calorific value of the fuel. After substituting the above expressions in Eq. A.1 and adopting a treatment similar to the one in Chapter 5, the jump conditions becomes

$$S_2 u_3' - S_2 u_2' = \Xi\Gamma\Theta S_1 \mathcal{F} u_{1m}' \tag{A.3}$$

Here $\Xi = \overline{u}_1/\overline{u}_{1m}$, $\Theta = T_3/T_2 - 1$ is the volumetric expansion parameter across the flame and $\Gamma = \overline{c_p}/c_p$. Note that this expression is also obtained in Chapter 5, with the exception of Ξ parameter, as the velocities $\overline{u}_1$ and $\overline{u}_{1m}$ cannot be differentiated in a 1D model. The volume flow rate fluctuation at the injector exit is $\dot{q}_v' = S_2 u_2'$, assuming the volumetric flow rate fluctuation on the upstream side of the flame is conserved. As the measured relative velocity fluctuations at injector exit equals the volume flow rate fluctuation, i.e., $\dot{q}_v'/\bar{\dot{q}}_v = u_{1m}'/\overline{u}_{1m}$, one can write $S_1 \overline{u}_1 u_{1m}'/\overline{u}_{1m} = S_2 u_2'$ or $S_1 \Xi u_{1m}' = S_2 u_2'$. Using this expression, Eq. A.3 can be simplified as

$$S_2 u_3' - S_1 \Xi u_{1m}' = S_1 \Xi\Gamma\Theta \mathcal{F} u_{1m}' \tag{A.4}$$

The flame describing function $\mathcal{F}$ is then

$$\mathcal{F} = \frac{1}{\Xi\Gamma\Theta}\left[\frac{S_2}{S_1}\frac{u_3'}{u_{1m}'} - \Xi\right] \tag{A.5}$$

This expression can be used to obtain the flame describing function by measuring the velocities upstream and downstream of the flame without the need for measuring the heat release rate fluctuations, which are generally determined by making use of chemiluminescence emission intensity. The upstream velocity is measured

through LDA as described earlier in this document. The downstream velocity fluctuation u'_3 is deduced from pressure measurements by three microphones, M_1, M_2 and M_3 (shown in Fig. A.1) mounted on waveguides which are plugged on the downstream side of the flame at a distance of 110, 125 and $140\,\mathrm{mm}$ from the chamber backplane. The velocity determined from the microphone signals corresponds to section 4, where the central microphone M_2 is located. This section is at a distance h_b from the flame, and it is necessary to link sections 3 and 4 by considering acoustic propagation in a constant section channel. This is conveniently achieved by considering the transfer matrix between these two sections

$$\begin{bmatrix} \frac{p'_3}{\rho_c c_c} \\ u'_3 \end{bmatrix} = \begin{bmatrix} \cos k_c h_b & -i \sin k_c h_b \\ -i \sin k_c h_b & \cos k_c h_b \end{bmatrix} \begin{bmatrix} \frac{p'_4}{\rho_c c_c} \\ u'_4 \end{bmatrix} \tag{A.6}$$

where k_c is the wavenumber in the hot gases and h_b represents the distance between the flame barycenter and section 4 where the downstream velocity is being measured. One may then obtain an expression for $\mathcal{F}$ as

$$\mathcal{F} = \frac{1}{\Gamma\Theta}\left[\frac{1}{\Xi}\frac{S_2}{S_1}\frac{u'_4}{u'_{1m}}\cos k_c h_b - i\frac{1}{\Xi}\frac{S_2}{S_1}\sin k_c h_b \frac{p'_4}{\rho_c c_c u'_{1m}} - 1\right] \tag{A.7}$$

In the present case, it was verified that the fluctuations in equivalence ratio for these specific spray flames are negligible, and hence the chemiluminescence measurements reasonably represent the heat release rate. However, this is not always applicable for technically premixed flames, and the above equation might then be used to obtain the FDFs as it does not require an optical determination of the heat release rate but relies on an acoustic determination of the velocity downstream of the flame. It is then natural to compare the FDF estimates, one obtained using the chemiluminescence method and the other deduced from using the acoustic downstream velocity, to see if the direct acoustic method yields results that are compatible with those obtained from the more standard method.

For the FDF determination using Eq. A.7, one has to provide the temperature T_c in the chamber to calculate ρ_c, c_c and k_c. The temperature is estimated using an R-type thermocouple placed in the section corresponding to microphone M_2. Figures A.2 and A.3 show the FDFs obtained with the two methods for swirlers 707 and 716 at the operating point F1. The results are also shown at the recess distances $h_r = 2.75\,\mathrm{mm}$ and $6.75\,\mathrm{mm}$ and at an amplifier voltage of $V_0 = 3\,\mathrm{V}$ to ensure the best signal-to-noise acquisition. Only the results with a coherence value of minimum 0.9 (i.e., $\gamma^2 \geq 0.9$) are plotted in these figures. One observes that the phase evolution corresponding to the two methods matches quite well in the four cases. This further supports the FDF determination carried out in this work using the OH^* chemiluminescence and the subsequent instability analysis based on the corresponding phase curves. Although the gain values are close, having the same

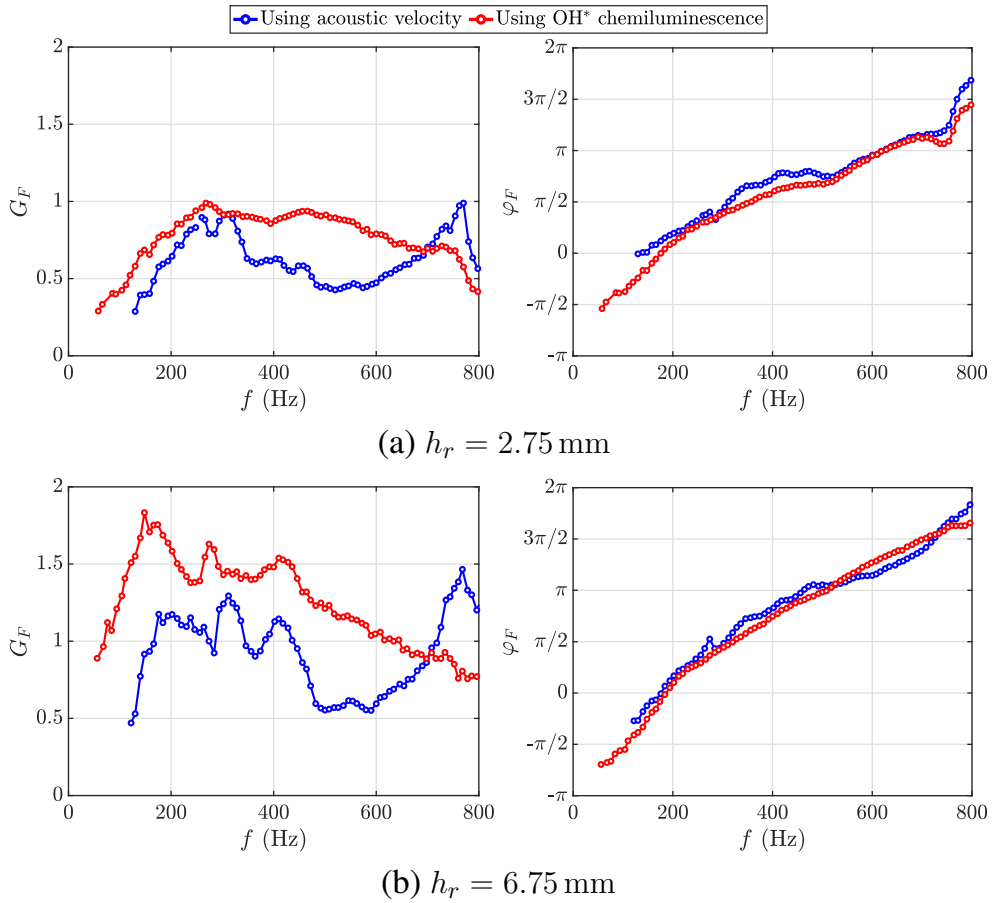

(a) $h_r = 2.75\,\mathrm{mm}$

(b) $h_r = 6.75\,\mathrm{mm}$

Figure A.2. *Comparison of flame describing function determined using an acoustic method and using OH* chemiluminescence for swirler 707. The results are shown in the top row for a recess distance of* $h_r = 2.5\,\mathrm{mm}$ *and in the bottom row for a recess distance of* $h_r = 6.75\,\mathrm{mm}$*. All the measurements are carried out at the operating point F1 and at an amplifier voltage of* $V_0 = 3\,\mathrm{V}$ *to ensure the best signal-to-noise acquisition.*

order of magnitude, non-negligible differences exist between the two methods. One possible reason for this mismatch could be in the determination of chamber temperature T_c. Although this is measured using an R-type thermocouple close to the measurement section of the chamber microphones, a temperature gradient exists in the chamber, and considering a single value might not be suitable. The other cause for this mismatch can be in the value of h_b, which represents the distance between the flame barycenter deduced from OH* light emission images and section 4, where the velocity is extracted from the microphone signals. One does not know if this location for the flame is exact. A sensitivity analysis is thus carried out to establish the dependence of the FDF on these two parameters, and the results are shown in Figs. A.4 and A.5. It appears that the phase determined using the acoustic method remains nearly the same, but the FDF gain is sensitive to both h_b and T_c, especially in the higher frequency range (beyond $600\,\mathrm{Hz}$). Further mea-

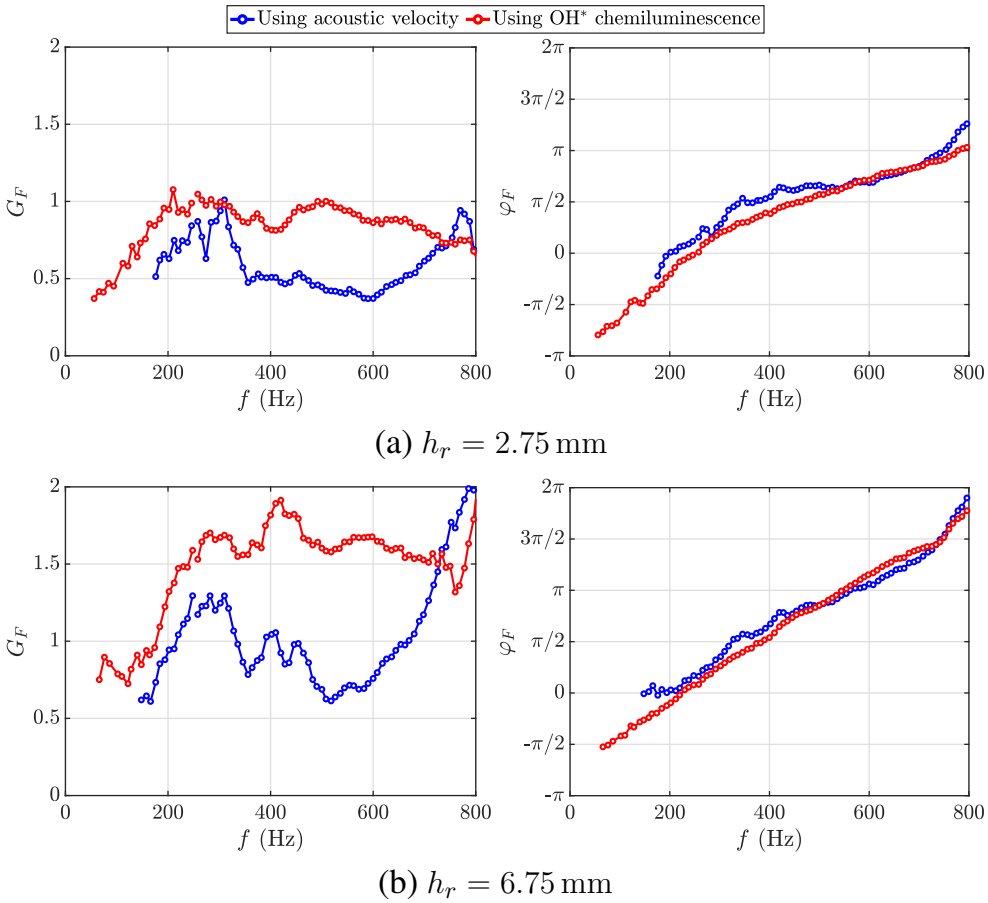

(a) $h_r = 2.75\,\mathrm{mm}$

(b) $h_r = 6.75\,\mathrm{mm}$

Figure A.3. *Comparison of flame describing function determined using an acoustic method and using OH* chemiluminescence for swirler 716. The results are shown in the top row for a recess distance of* $h_r = 2.5\,\mathrm{mm}$ *and in the bottom row for a recess distance of* $h_r = 6.75\,\mathrm{mm}$*. All the measurements are carried out at the operating point F1 and at an amplifier voltage of* $V_0 = 3\,\mathrm{V}$ *to ensure the best signal-to-noise acquisition.*

surements and analysis are required to assess the suitability of using the FDF gain determined by the acoustic method and are left as future work.

The alternate technique for FDF determination also poses certain practical difficulties. One such problem is that the chamber must be much longer than the flame to mount the different microphones and ensure sufficient spacing between them. The longer chamber imposes a risk of encountering self-sustained oscillations, which would then hinder obtaining the flame describing function, as these must be obtained by modulating a stable flame. This problem can be avoided when performing chemiluminescence measurement, as this only requires a chamber length sufficient enough to enclose the flame. In addition, the FDFs determined from the acoustic method have a sudden jump at higher frequencies. This might not be physical and could be caused by considering an incorrect value for

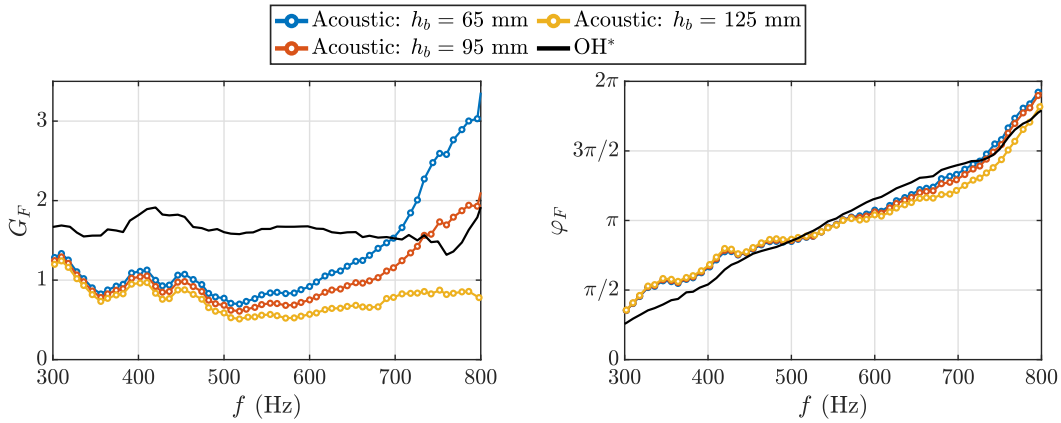

Figure A.4. *Sensitivity of flame describing function determined using an acoustic method to the distance h_b between flame section and microphone measurement section. Swirler: 716, $h_r = 6.75\,\mathrm{mm}$, operating point: F1, $V_0 = 3\,\mathrm{V}$.*

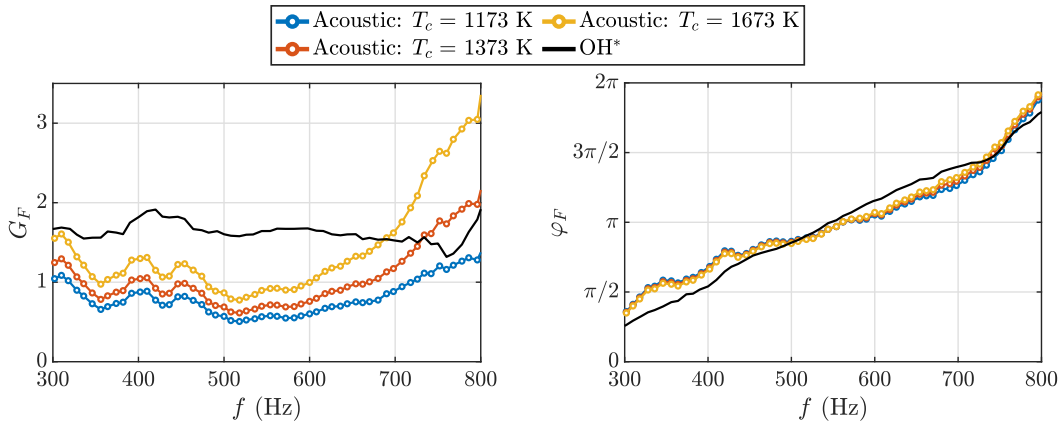

Figure A.5. *Sensitivity of flame describing function determined using an acoustic method to the temperature in the chamber T_c. Swirler: 716, $h_r = 6.75\,\mathrm{mm}$, operating point: F1, $V_0 = 3\,\mathrm{V}$.*

the temperature or distance between the downstream velocity section and flame, as shown in the sensitivity analysis. Accurate determination of these parameters is somewhat difficult, and the optical method considering chemiluminescence measurement might be more suitable in those scenarios.

Appendix B

A database of flame describing functions with different swirlers

This appendix gathers the flame describing functions measured in SICCA-Spray corresponding to the different swirling injectors operating with heptane at F1. The results corresponding to swirlers 707, 712, 716, 726 and 727 were shown in the main text of this manuscript but are reproduced here to facilitate comparison. It is recalled that the measurements of the relative velocity fluctuations are carried out at a point where it equals the relative volume flow rate fluctuations (see Chapter 4). This location is either at $r = 3.5\,\mathrm{mm}$ or $r = 4\,\mathrm{mm}$, depending on the swirler, and at a height of $h = 2.5\,\mathrm{mm}$.

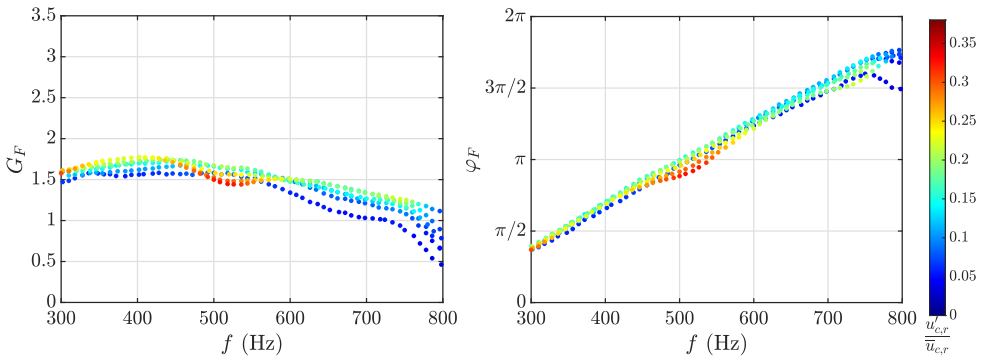

Figure B.1. *Flame describing function gain G_F (left) and phase φ_F (right) for swirler 707. Relative velocity fluctuations are measured at a radius $r = 3.5\,\mathrm{mm}$ from the injector center and a height of $h = 2.5\,\mathrm{mm}$ from the backplane.*

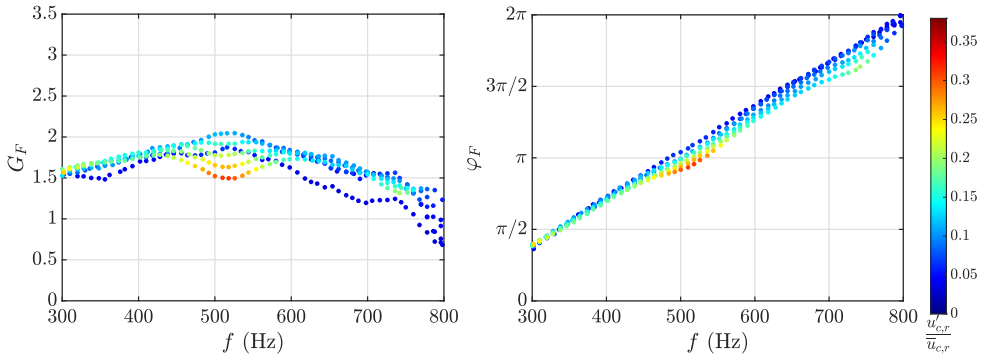

Figure B.2. *Flame describing function gain G_F (left) and phase φ_F (right) for swirler 712. Relative velocity fluctuations are measured at a radius $r = 3.5\,\mathrm{mm}$ from the injector center and a height of $h = 2.5\,\mathrm{mm}$ from the backplane.*

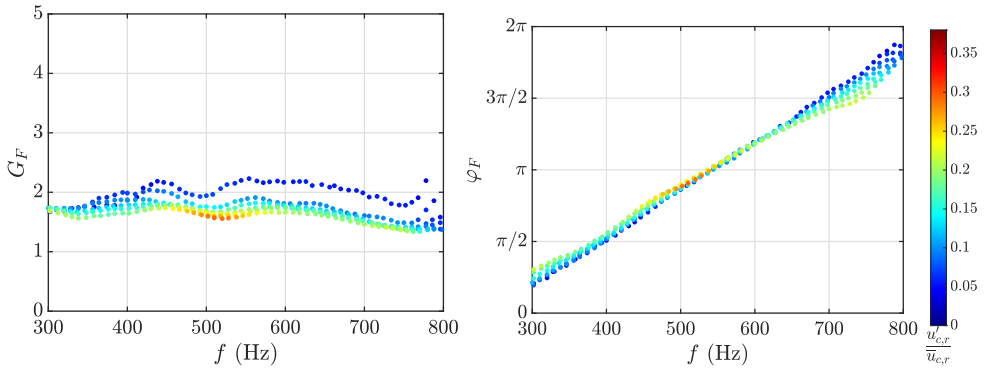

Figure B.3. *Flame describing function gain G_F (left) and phase φ_F (right) for swirler 713. Relative velocity fluctuations are measured at a radius $r = 3.5\,\mathrm{mm}$ from the injector center and a height of $h = 2.5\,\mathrm{mm}$ from the backplane.*

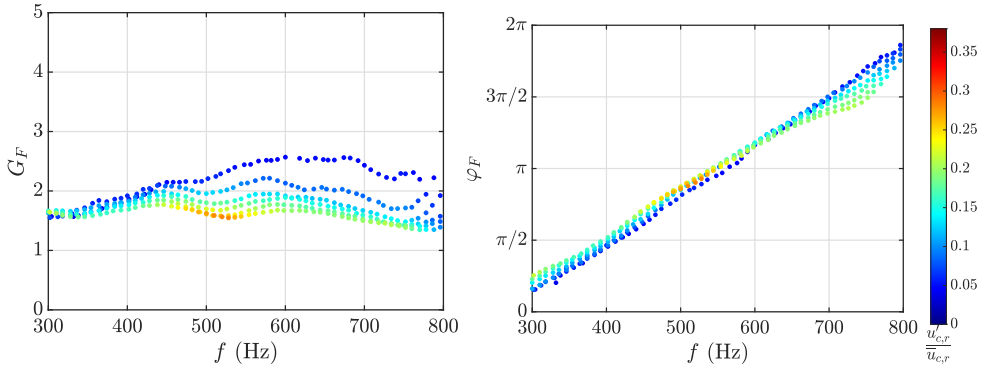

Figure B.4. *Flame describing function gain G_F (left) and phase φ_F (right) for swirler 714. Relative velocity fluctuations are measured at a radius $r = 3.5\,\mathrm{mm}$ from the injector center and a height of $h = 2.5\,\mathrm{mm}$ from the backplane.*

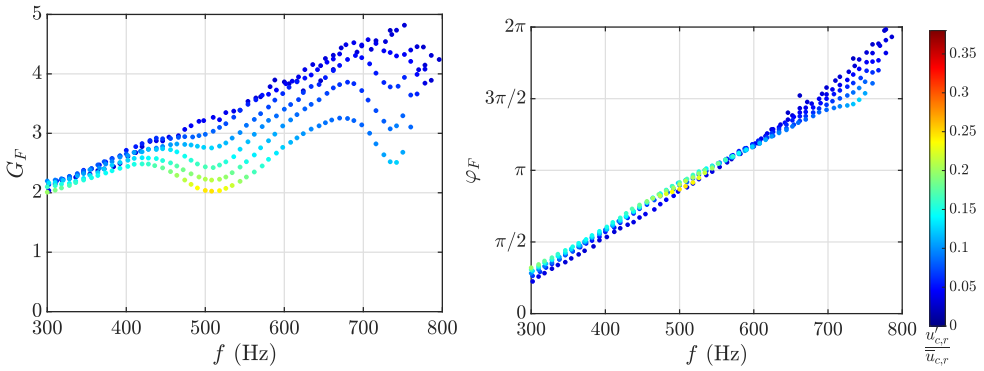

Figure B.5. *Flame describing function gain G_F (left) and phase φ_F (right) for swirler 715. Relative velocity fluctuations are measured at a radius $r = 4\,\mathrm{mm}$ from the injector center and a height of $h = 2.5\,\mathrm{mm}$ from the backplane.*

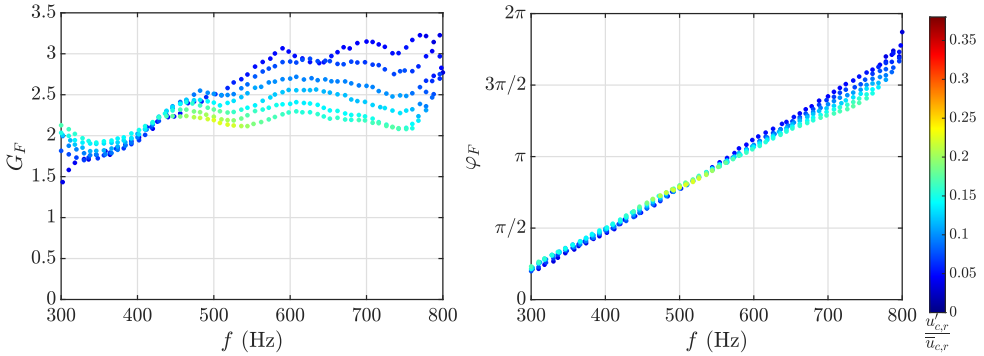

Figure B.6. *Flame describing function gain G_F (left) and phase φ_F (right) for swirler 716. Relative velocity fluctuations are measured at a radius $r = 4\,\mathrm{mm}$ from the injector center and a height of $h = 2.5\,\mathrm{mm}$ from the backplane.*

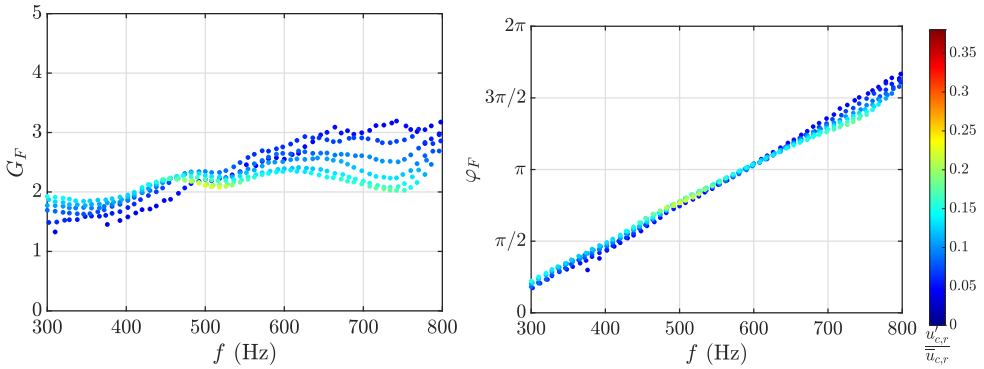

Figure B.7. *Flame describing function gain G_F (left) and phase φ_F (right) for swirler 726. Relative velocity fluctuations are measured at a radius $r = 4\,\mathrm{mm}$ from the injector center and a height of $h = 2.5\,\mathrm{mm}$ from the backplane.*

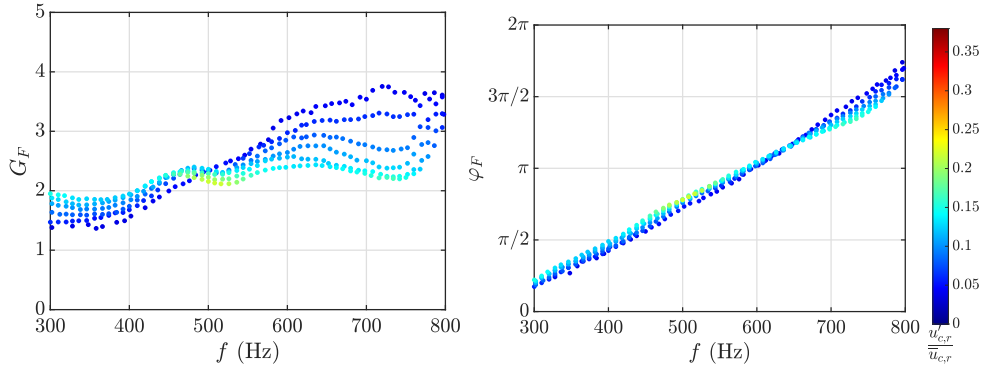

Figure B.8. *Flame describing function gain G_F (left) and phase φ_F (right) for swirler 727. Relative velocity fluctuations are measured at a radius $r = 4\,\mathrm{mm}$ from the injector center and a height of $h = 2.5\,\mathrm{mm}$ from the backplane.*

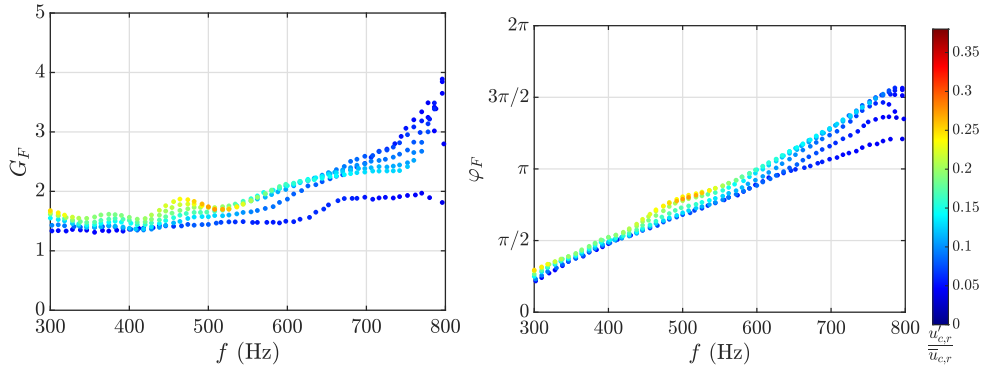

Figure B.9. *Flame describing function gain G_F (left) and phase φ_F (right) for swirler K. Relative velocity fluctuations are measured at a radius $r = 4\,\mathrm{mm}$ from the injector center and a height of $h = 2.5\,\mathrm{mm}$ from the backplane.*

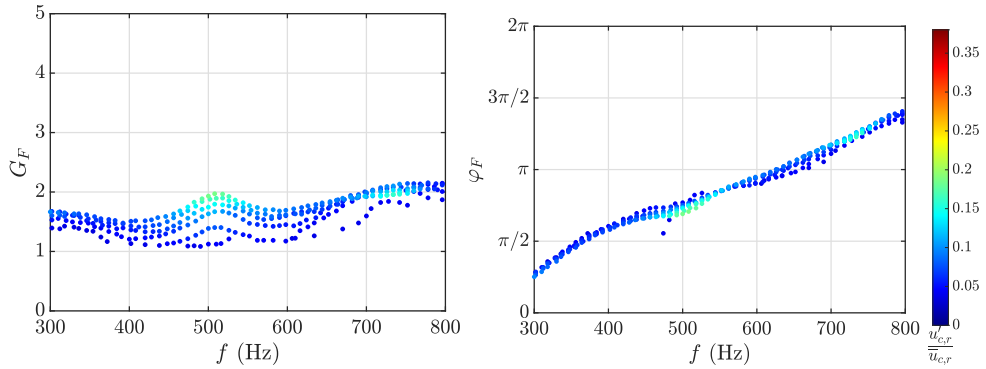

Figure B.10. *Flame describing function gain G_F (left) and phase φ_F (right) for swirler T. Relative velocity fluctuations are measured at a radius $r = 4\,\mathrm{mm}$ from the injector center and a height of $h = 2.5\,\mathrm{mm}$ from the backplane.*

Appendix C

A database of flame images with different swirlers

Mean flame images provide interesting indications about the structure and extent of the combustion region. This appendix gathers the corresponding data obtained in SICCA-Spray with different swirlers operated with different fuels. The images are obtained with an ICCD camera and correspond to the OH^* chemiluminescence emission from the flame. An Abel inversion is performed to remove the line-of-sight integration effect. The image frames roughly correspond to the dimensions $73\,\mathrm{mm} \times 71\,\mathrm{mm}$. The flame images are shown for the three operating conditions considered in this work.

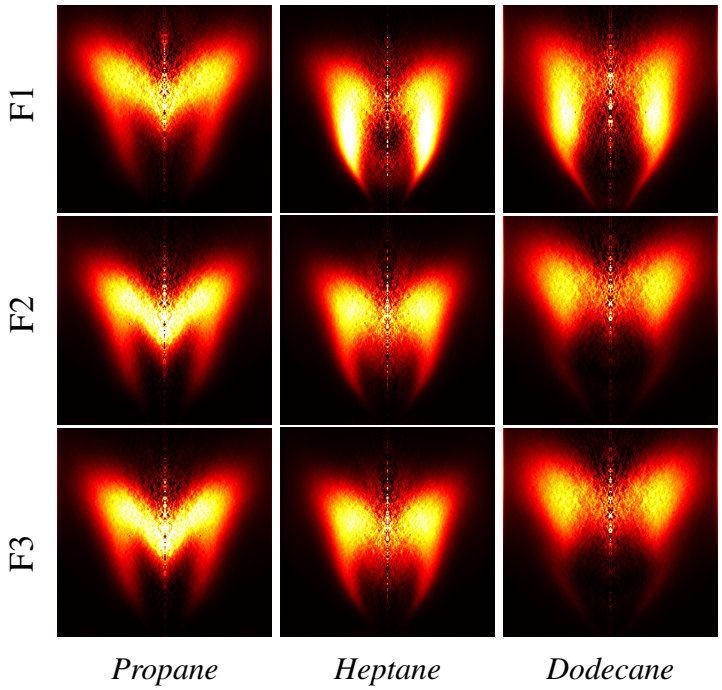

Figure C.1. *Swirler 707*

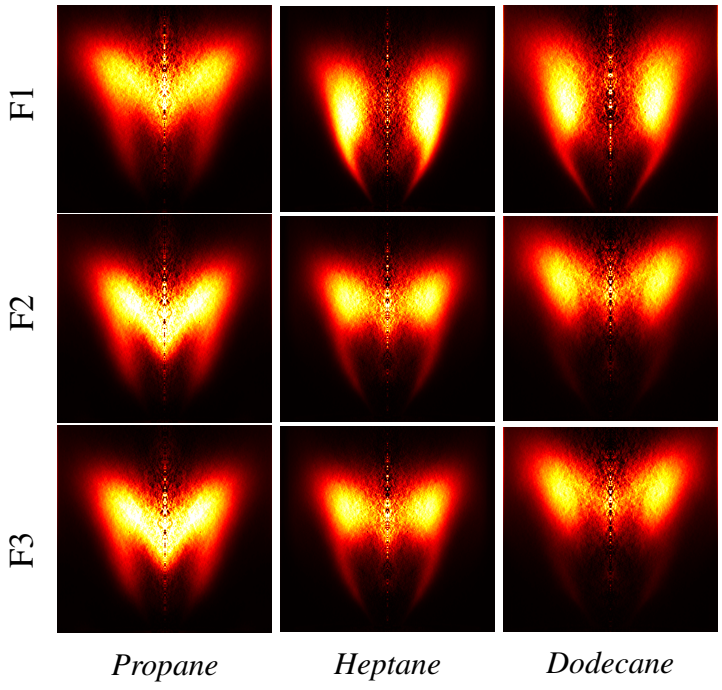

Figure C.2. *Swirler 712*

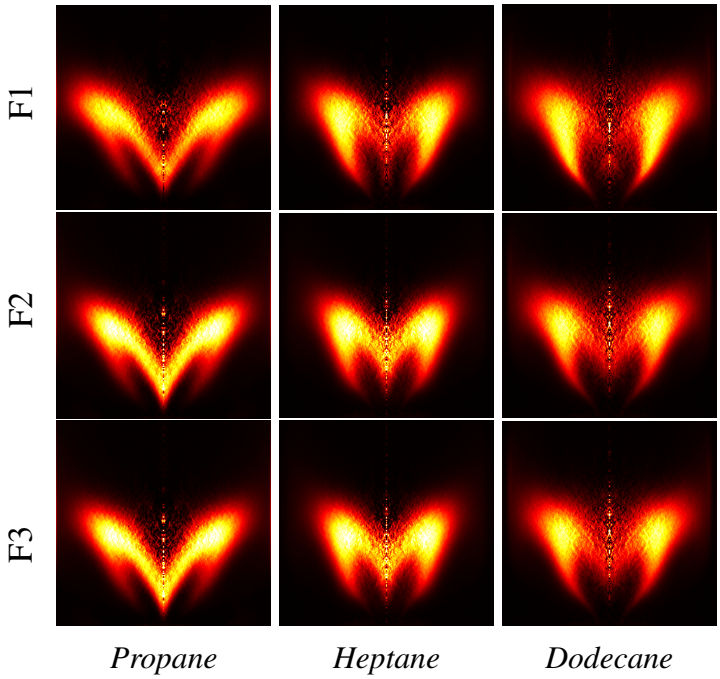

Figure C.3. *Swirler 713*

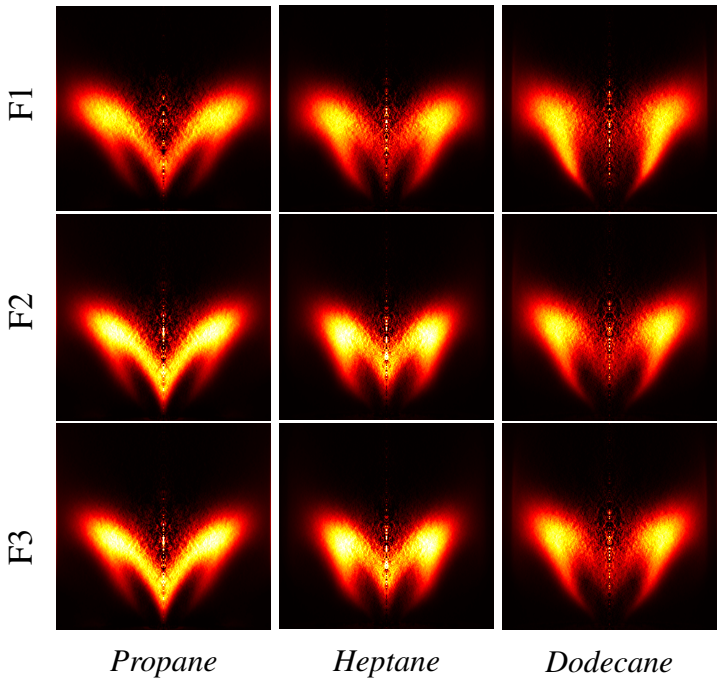

Figure C.4. *Swirler 714*

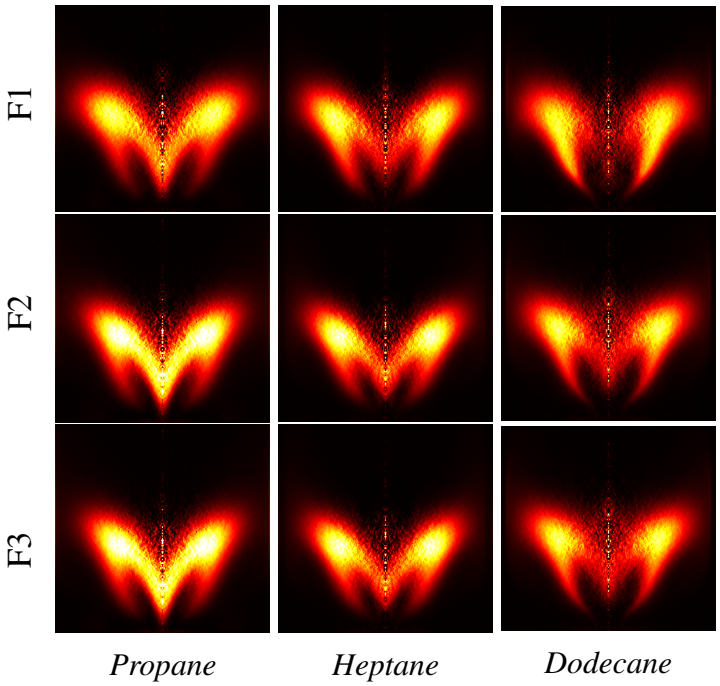

Figure C.5. *Swirler 715*

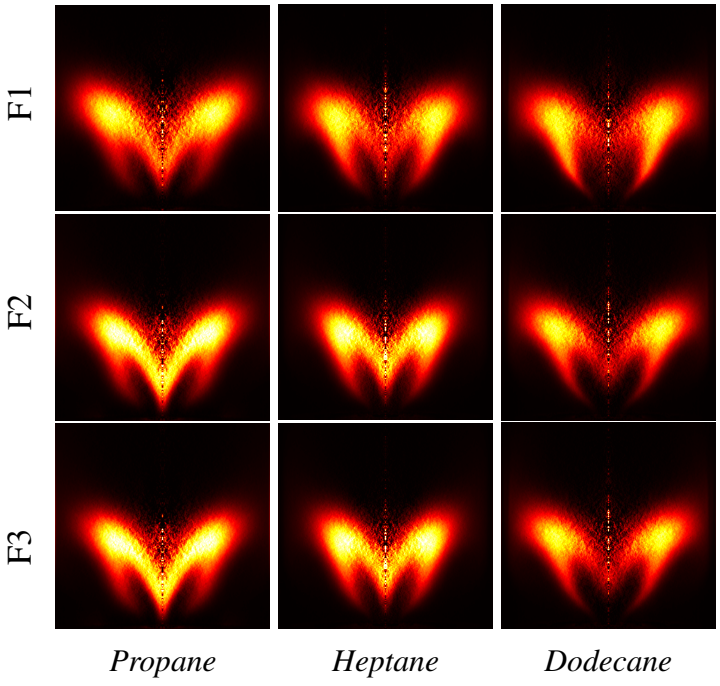

Figure C.6. *Swirler 716*

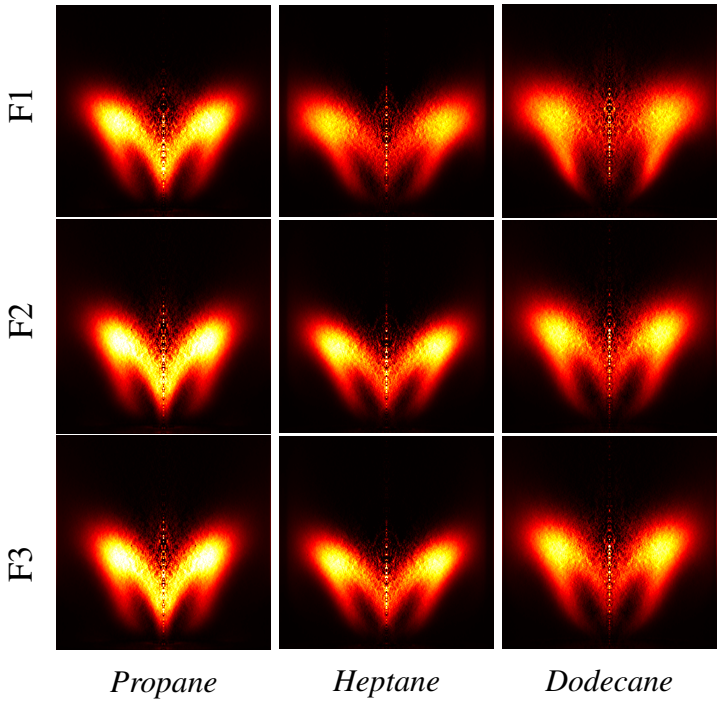

Figure C.7. *Swirler 726*

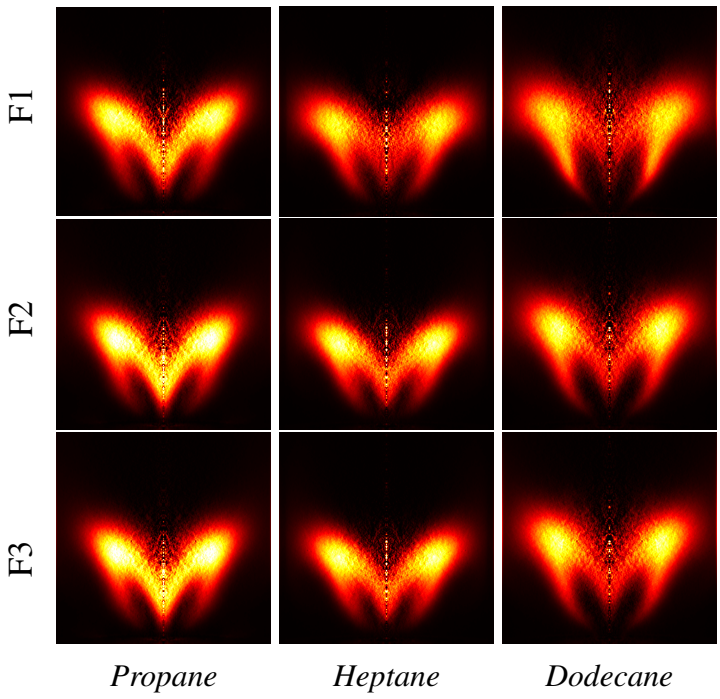

Figure C.8. *Swirler 727*

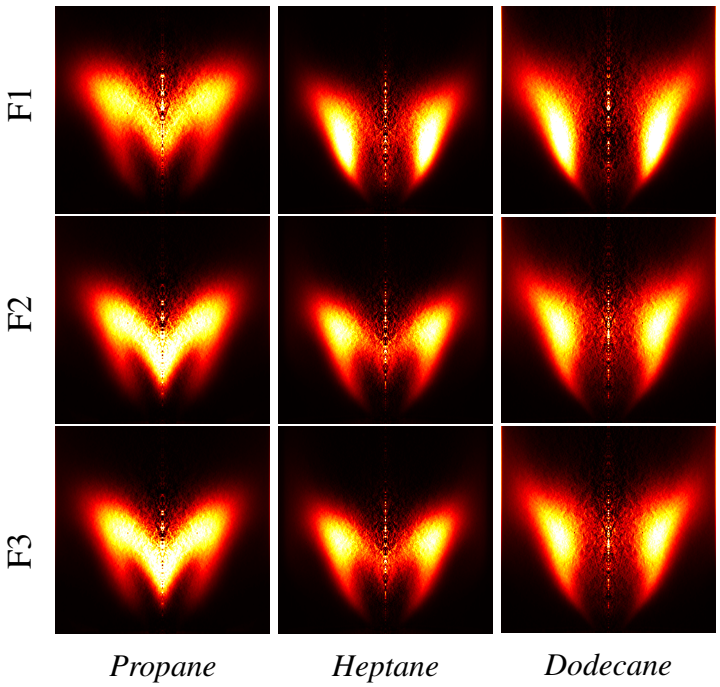

Figure C.9. *Swirler K*

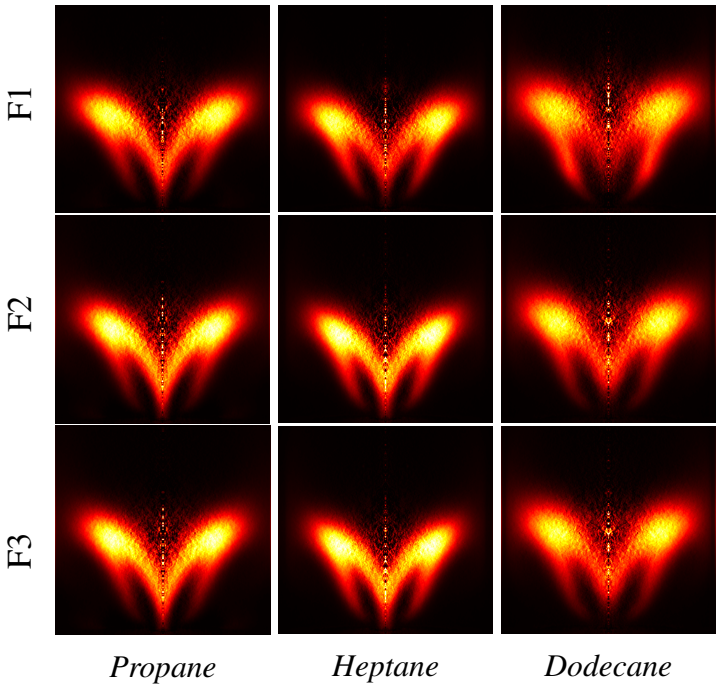

Figure C.10. *Swirler T*

Appendix D

Cold flow damping rate and stability map with different swirlers

Damping rate estimates are needed when one wishes to assess the dynamic stability of a system. It is generally not easy to obtain these estimates under hot-fire conditions. However, it is possible to extract cold flow damping rates from resonance curves. This appendix collects the damping rate values deduced from systematic experiments using SICCA-spray. Figure D.1 shows the cold flow damping rate measurements carried out under cold conditions with the different swirling injectors and complements the results discussed in Chapter 6.

Figure D.2 provides a comparison of the stability map of SICCA-Spray with two additional swirlers (726 and 727) to complement the results shown in Chapter 6. The stability maps of 707, 712, and 716 are reproduced here to facilitate comparison.

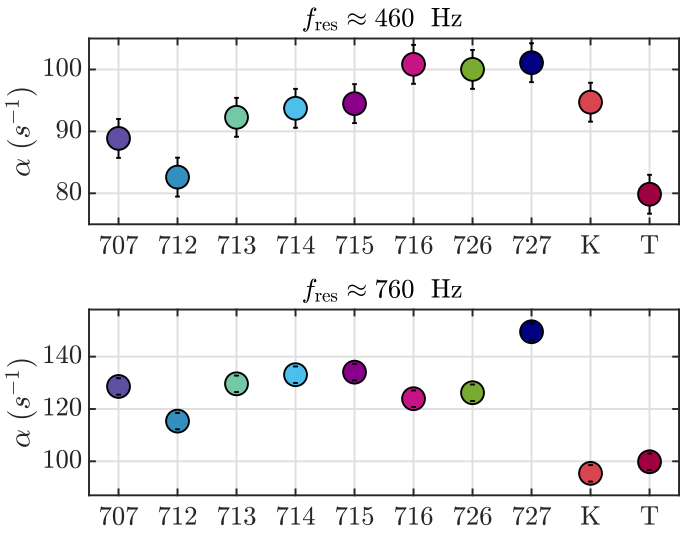

Figure D.1. *Top row shows the cold flow damping rate $\alpha = \pi\Delta f_r$ for the different swirlers at a frequency of* 460 Hz *with a chamber length of* 165 mm. *The bottom row shows damping at* 760 Hz *measured with a chamber length of* 315 mm. *The error bars indicate the uncertainty in damping rate determination from the frequency resolution in Welch's periodogram calculation, which is equal to* ± 1 Hz. *These measurements are carried out in SICCA-Spray under cold flow conditions using the resonance curve method discussed in Chapter 6.*

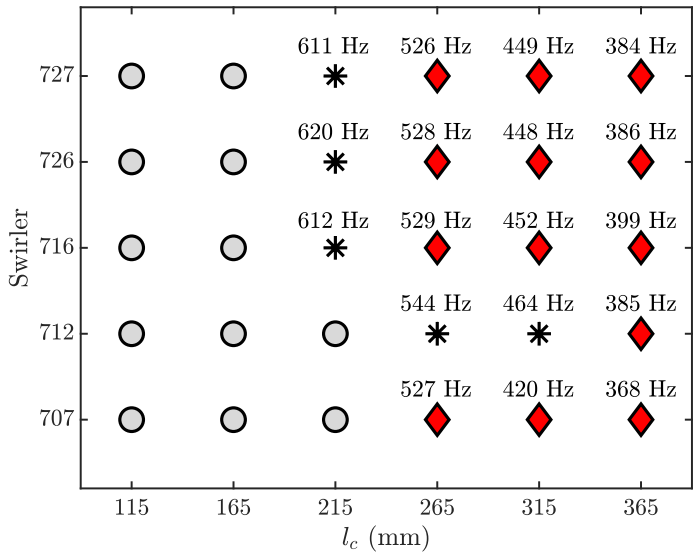

Figure D.2. *Stability map of SICCA-Spray with five different swirlers at F1.*

Appendix E

Low frequency FDFs at different atomizer positions

To complement the low frequency tendencies of the FDF described in Chapter 4, additional measurements are carried out with swirler 716 at three different atomizer positions and are shown in Fig. E.1. These measurements are performed at F1 when operating with liquid heptane. The FDFs between $50\,\mathrm{Hz}$ and $300\,\mathrm{Hz}$ are shown here for the first time, and the results beyond $300\,\mathrm{Hz}$ are reproduced from Chapter 4. It can be observed that the FDF phase tends towards $-\pi$ as the frequency vanishes at all the atomizer positions. The low frequency behavior of the FDF gain, on the other hand, depends on the atomizer positions. It takes a value of $G_F = 1$ at $h_r = 6.75\,\mathrm{mm}$ and $G_F = 0$ at $h_r = 2.75\,\mathrm{mm}$, as the frequency tends to zero. The gain at $h_r = 4.75\,\mathrm{mm}$ tends to $G_F = 0.5$ as if it exhibits a behavior that is in between the other two atomizer positions.

The FDF measurements discussed above are carried out at a lean equivalence ratio of $\phi = 0.85$. It is then interesting to see if the same behavior is retained at a rich equivalence ratio. To understand this, the measurements were carried out at an equivalence ratio of $\phi = 1.15$ while maintaining the same thermal power as F1, which is equal to $6.4\,\mathrm{kW}$. These experiments were carried out only at two recess distances 2.75 and $6.75\,\mathrm{mm}$, in the frequency range between $50\,\mathrm{Hz}$ and $350\,\mathrm{Hz}$, and the corresponding FDFs are shown in Fig. E.2.

Contrary to the behavior exhibited at $\phi = 0.85$, the phase in this case tends to $\varphi_F = 0$ and the gain tends to $G_F = 1$ as the frequency tends to $0\,\mathrm{Hz}$ at both the atomizer locations. Such behaviors are not completely understood and are left to be pursued as future work.

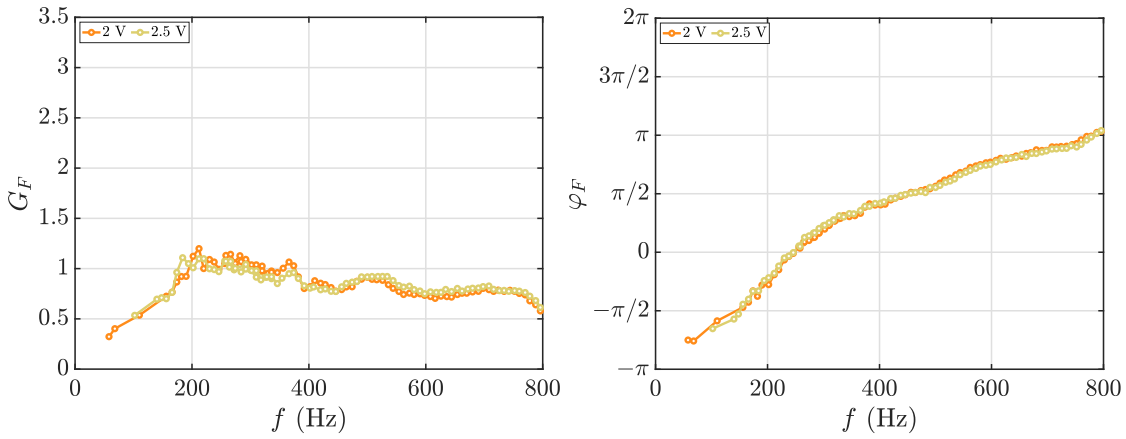

(a) $h_r = 2.75\,\mathrm{mm}$

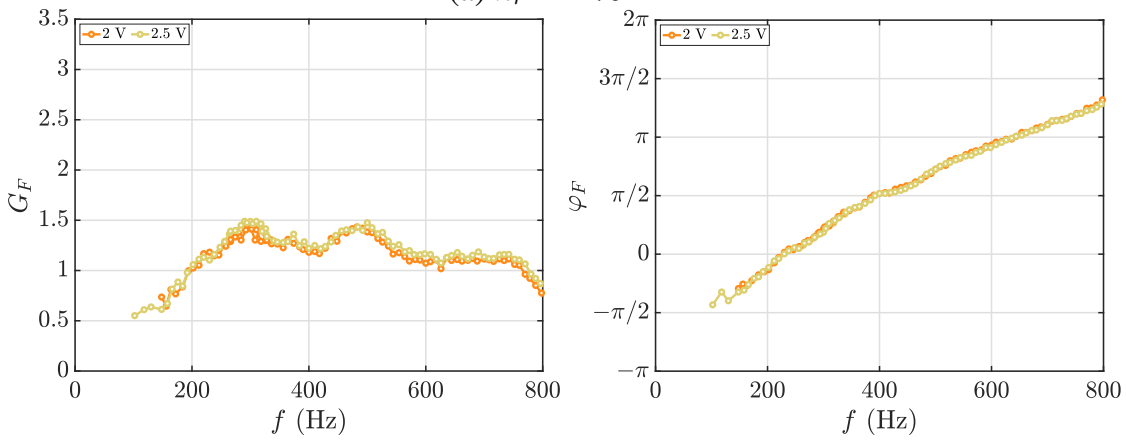

(b) $h_r = 4.75\,\mathrm{mm}$

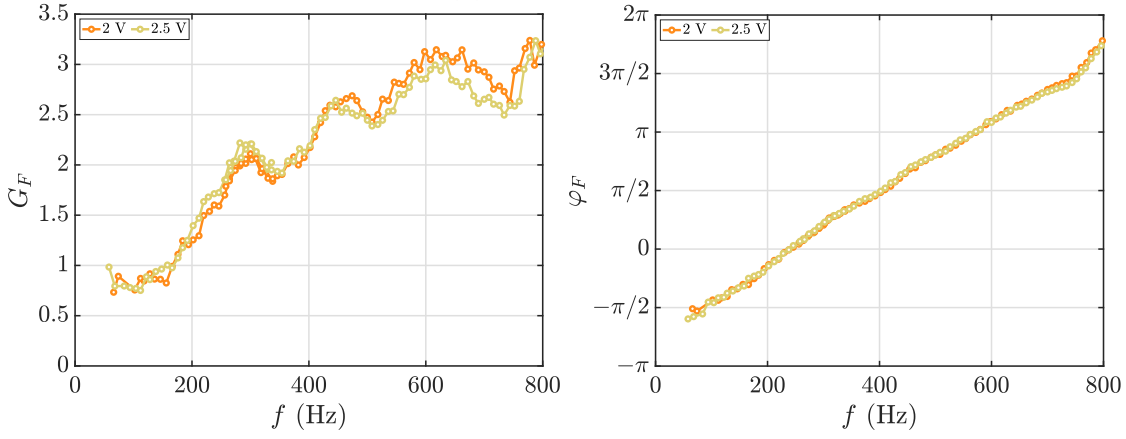

(c) $h_r = 6.75\,\mathrm{mm}$

Figure E.1. *Gain G_F and phase φ_F for swirler 716 with measurements carried out in the low frequency range between* 50 Hz *and* 300 Hz. *The results beyond* 300 Hz *are reproduced from Chapter 8. Operating point: F1 ($\phi = 0.85$).*

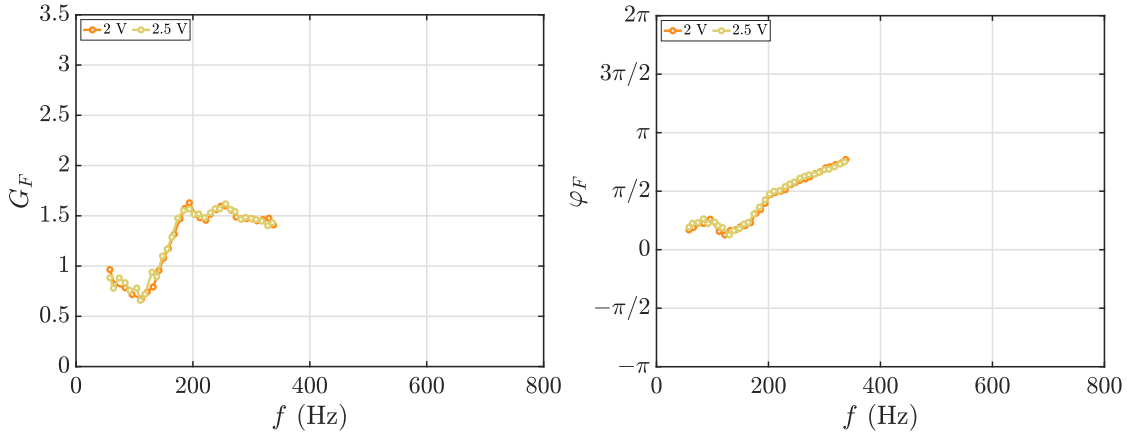

(a) $h_r = 2.75\,\mathrm{mm}$

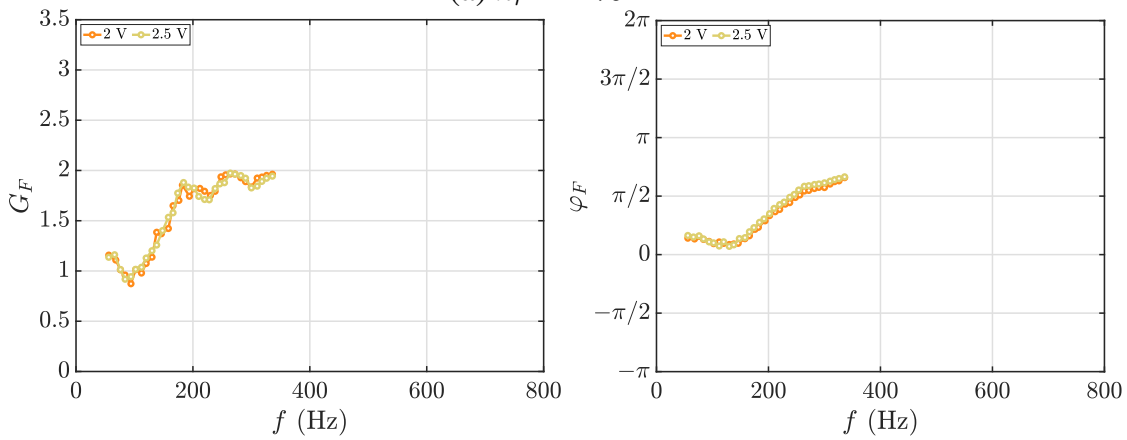

(b) $h_r = 6.75\,\mathrm{mm}$

Figure E.2. *Gain G_F and phase φ_F for swirler 716 in the low frequency range between* $50\,\mathrm{Hz}$ *and* $350\,\mathrm{Hz}$*. Measurements are performed at an equivalence ratio of* $\phi = 1.15$ *and at the same thermal power as F1 (*$6.4\,\mathrm{kW}$*).*

Appendix F

Large eddy simulations of steady flame in SICCA-Spray

A part of this work also involved performing large eddy simulations in collaboration with CERFACS using the AVBP[2] Navier Stokes flow solver. The eventual aim is to numerically obtain the flame response in SICCA-Spray, compare that response with experiments, and in this way, gain a better understanding of the injector dynamics. Because of the time constraints and broad experimental program, this could not be completed during the present thesis. However, the preliminary work aimed at steady state simulations is carried out with heptane, and detailed validation of the numerical results is performed by comparing with experimental measurements. Swirler 707 is used for this purpose, and the simulations are performed at an air mass flow rate of $\dot{m}_a = 2.3\,\mathrm{g\,s^{-1}}$ and fuel flow rate of $\dot{m}_f = 500\,\mathrm{g\,h^{-1}}$, resulting in an equivalence ratio of $\phi = 0.93$. The numerical setup used for this work is the same as that of Vignat (2020). The solver uses a two-step Taylor-Galerkin centered scheme (TTGC) (Colin and Rudgyard 2000) with a third-order precision in space and time along with Navier-Stokes characteristic boundary condition (NSCBC) imposing an atmospheric boundary condition in the far-field outlet (Poinsot and Lelef 1992). The chemical reactions are governed by a global two-step six-species 2S-C7H16-DP scheme with pre-exponential adjustment (PEA), and a thickened flame combustion model is adopted (Paulhiac et al. 2020). The liquid spray is modeled with a Lagrangian framework by adopting a FIMUR injection model (Lo Schiavo et al. 2020) with the droplet profile specified by a Rosin-Rammler distribution function. The droplet-wall interaction inside the injector is modeled using the FILM approach as suggested by Lo Schiavo et al. (2020).

[2]http://www.cerfacs.fr/avbp7x

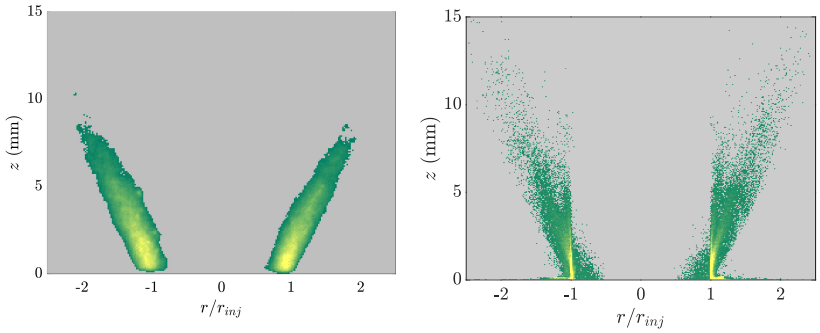

Experiment *Simulation*

Figure F.1. *Spray profile comparison between experiment and simulation. Mie scattering intensity obtained with a laser tomography is shown on the left image and square of mean droplet diameter which is proportional to Mie intensity (Boutier 2012) is shown in the right image.*

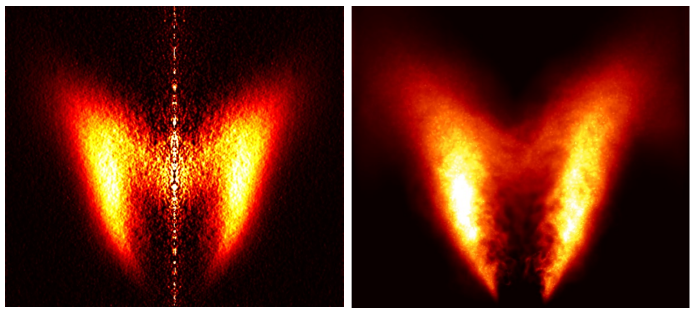

Experiment *Simulation*

Figure F.2. *Qualitative flame shape comparison between experiments (Abel-inverted OH^* chemiluminescence emission) and simulations (heat release rate).*

Some of the results obtained from this effort, along with a comparison of experimental measurements, are shown in Figs. F.1, F.3 and F.2. The flame pattern and diameter profiles are reasonably well retrieved, and this steady flame may be used to develop further investigations of modulated flames based on LES with the two liquid fuels, heptane and dodecane, and comparison with experimentally determined FDFs.

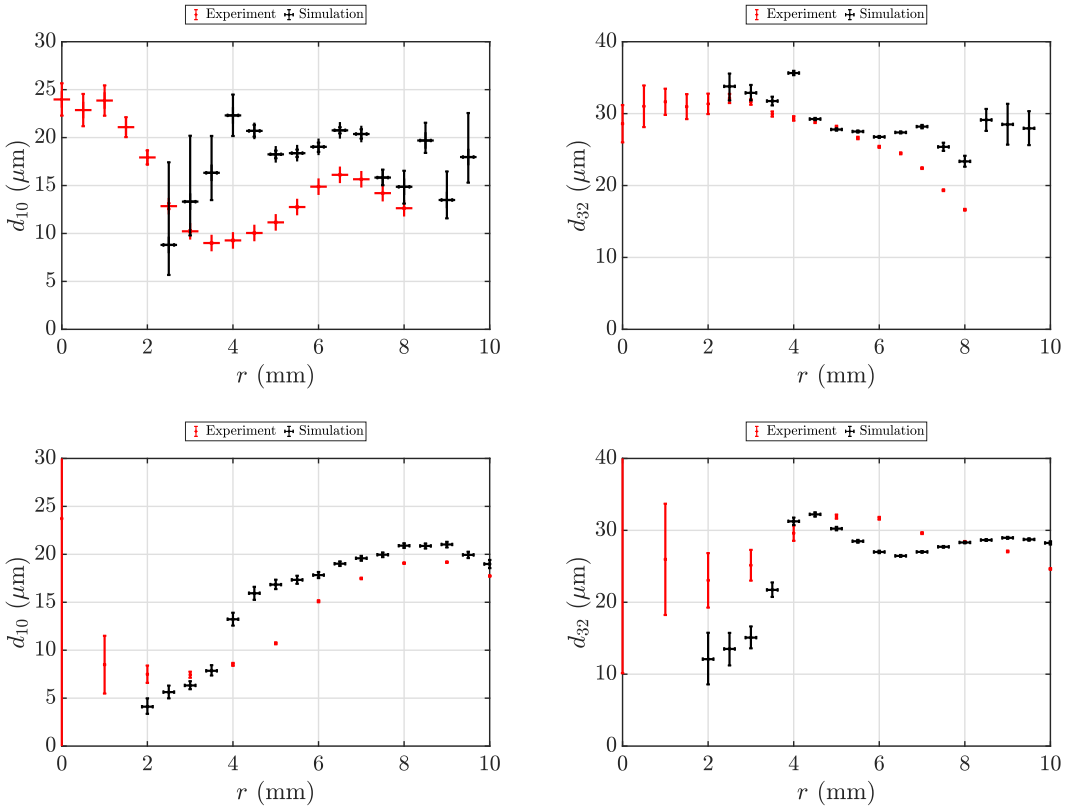

Figure F.3. *Comparison of spray droplet profiles showing mean diameter* d_{10} *and Sauter mean diameter* d_{32} *at different radial positions. Top:* $h = 5\,\mathrm{mm}$*, Bottom:* $h = 10\,\mathrm{mm}$ *above backplane.*

References

Aguilar, J. G., J. Dawson, T. Schuller, D. Durox, K. Prieur, and S. Candel (2021). Locking of azimuthal modes by breaking the symmetry in annular combustors. *Combustion and Flame 234*, 111639. *(p. 18, 145, 146)*

Ahn, B., T. Indlekofer, J. Dawson, and N. Worth (2021). Transient thermo-acoustic responses of methane/hydrogen flames in a pressurized annular combustor. *Journal of Engineering for Gas Turbines and Power 144*(1), 011018. *(p. 4)*

Albrecht, H.-E., N. Damaschke, M. Borys, and C. Tropea (2013). *Laser Doppler and phase Doppler measurement techniques*. Springer Science & Business Media. *(p. 36)*

Anikin, N., R. Suntz, and H. Bockhorn (2010). Tomographic reconstruction of the OH*-chemiluminescence distribution in premixed and diffusion flames. *Applied Physics B 100*(3), 675–694. *(p. 41)*

Annaswamy, A. M., M. Fleifil, J. P. Hathout, and A. F. Ghoniem (1997). Impact of linear coupling on the design of active controllers for the thermoacoustic instability. *Combustion Science and Technology 128*, 131–180. *(p. 57)*

Annaswamy, A. M. and A. F. Ghoniem (2002). Active control of combustion instability: Theory and practice. *IEEE Control Systems Magazine 22*(6), 37–54. *(p. 145)*

Apeloig, J. M., F.-X. d'Herbigny, F. Simon, P. Gajan, M. Orain, and S. Roux (2015). Liquid-fuel behavior in an aeronautical injector submitted to thermoacoustic instabilities. *Journal of Propulsion and Power 31*(1), 309–319. *(p. 171, 189)*

Ayoola, B., R. Balachandran, J. Frank, E. Mastorakos, and C. Kaminski (2006). Spatially resolved heat release rate measurements in turbulent premixed flames. *Combustion and Flame 144*(1-2), 1–16. *(p. 44)*

Bade, S., M. Wagner, C. Hirsch, T. Sattelmayer, and B. Schuermans (2013). Design for thermo-acoustic stability: modeling of burner and flame dynamics. *Journal of Engineering for Gas Turbines and Power 135*, 111502. *(p. 126)*

Baillot, F. and F. Lespinasse (2014). Response of a laminar premixed V-flame to

a high-frequency transverse acoustic field. *Combustion and Flame 161*(5), 1247–1267. *(p. 129)*

Balachandran, R., B. Ayoola, C. Kaminski, A. Dowling, and E. Mastorakos (2005). Experimental investigation of the nonlinear response of turbulent premixed flames to imposed inlet velocity oscillations. *Combustion and Flame 143*(1-2), 37–55. *(p. 41)*

Ballester, J. and T. García-Armingol (2010). Diagnostic techniques for the monitoring and control of practical flames. *Progress in Energy and Combustion Science 36*, 375 – 411. *(p. 41, 228)*

Bauerheim, M., M. Cazalens, and T. Poinsot (2015). A theoretical study of mean azimuthal flow and asymmetry effects on thermo-acoustic modes in annular combustors. *Proceedings of the Combustion Institute 35*(3), 3219–3227. *(p. 4, 190)*

Beita, J., M. Talibi, S. Sadasivuni, and R. Balachandran (2021). Thermoacoustic instability considerations for high hydrogen combustion in lean premixed gas turbine combustors: A review. *Hydrogen 2*(1), 33–57. *(p. 2)*

Bellucci, V., B. Schuermans, D. Nowak, P. Flohr, and C. O. Paschereit (2005). Thermoacoustic modeling of a gas turbine combustor equipped with acoustic dampers. *Journal of Turbomachinery 127*, 372–379. *(p. 4, 68, 69, 80, 81)*

Bernier, D., F. Lacas, and S. Candel (2004). Instability mechanisms in a premixed prevaporized combustor. *Journal of Propulsion and Power 20*(4), 648–656. *(p. 189, 203)*

Blimbaum, J., M. Zanchetta, T. Akin, V. Acharya, J. O'Connor, D. R. Noble, and T. Lieuwen (2012, dec). Transverse to Longitudinal Acoustic Coupling Processes in Annular Combustion Chambers. *International Journal of Spray and Combustion Dynamics 4*, 275–297. *(p. 4)*

Bothien, M. R., N. Noiray, and B. Schuermans (2015). Analysis of azimuthal thermo-acoustic modes in annular gas turbine combustion chambers. *Journal of Engineering for Gas Turbines and Power 137*(6). *(p. 4)*

Boudy, F., D. Durox, T. Schuller, and S. Candel (2011). Nonlinear mode triggering in a multiple flame combustor. *Proceedings of the Combustion Institute 33*, 1121–1128. *(p. 58)*

Boudy, F., D. Durox, T. Schuller, and S. Candel (2013). Analysis of limit cycles sustained by two modes in the flame describing function framework. *C. R. Mécanique 341*(1-2), 181–190. *(p. 75)*

Boudy, F., D. Durox, T. Schuller, G. Jomaas, and S. Candel (2011). Describing function analysis of limit cycles in a multiple flame combustor. *Journal of Engineering for Gas Turbines and Power 133*, 061502. *(p. 58)*

Bourgouin, J.-F. (2014). *Dynamique de flamme dans les foyers annulaires comportant des injecteurs multiples*. Ph. D. thesis, Ecole Centrale Paris. *(p. 2, 3, 104)*

Bourgouin, J.-F., D. Durox, J. P. Moeck, T. Schuller, and S. Candel (2013). Self-sustained instabilities in an annular combustor coupled by azimuthal and longitudinal acoustic modes. In *Proceedings of the ASME Turbo Expo, paper no. GT2013-95010*. *(p. 2, 18, 20, 24, 152, 223)*

Bourgouin, J.-F., D. Durox, J. P. Moeck, T. Schuller, and S. Candel (2015a). Characterization and modeling of a spinning thermoacoustic instability in an annular combustor equipped with multiple matrix injectors. *Journal of Engineering for Gas Turbines and Power 137*(2), 021503. *(p. 2, 18, 101, 145)*

Bourgouin, J.-F., D. Durox, J. P. Moeck, T. Schuller, and S. Candel (2015b). A new pattern of instability observed in an annular combustor: The slanted mode. *Proceedings of the Combustion Institute 35*, 3237–3244. *(p. 3, 18, 145, 190, 195)*

Bourgouin, J.-F., D. Durox, T. Schuller, J. Beaunier, and S. Candel (2013). Ignition dynamics of an annular combustor equipped with multiple swirling injectors. *Combustion and Flame 160*(8), 1398–1413. *(p. 3, 19)*

Candel, S. (2002). Combustion dynamics and control: Progress and challenges. *Proceedings of the Combustion Institute 29*, 1–28. *(p. 1, 57, 117)*

Candel, S., D. Durox, and T. Schuller (2004). Flame interactions as a source of noise and combustion instabilities. In *10th AIAA/CEAS Aeroacoustics Conference*, pp. 2928. *(p. 237)*

Candel, S., D. Durox, T. Schuller, J.-F. Bourgouin, and J. P. Moeck (2014). Dynamics of swirling flames. *Annual Review of Fluid Mechanics 46*, 147–173. *(p. 57, 117, 145)*

Chung, J. and D. Blaser (1980). Transfer function method of measuring in-duct acoustic properties. I. theory. *The Journal of the Acoustical Society of America 68*(3), 907–913. *(p. 34, 192)*

Ciardiello, R., R. S. Pathania, I. El Helou, and E. Mastorakos (2021). Lean blow-off investigation in a linear multi-burner combustor operated in premixed and non-premixed modes. *Applications in Energy and Combustion Science 9*, 100041. *(p. 224)*

Clark, T. P. (1958). *Studies of OH, CO, CH, and C2 radiation from laminar and turbulent propane-air and ethylene-air flames*. National Advisory Committee for Aeronautics. *(p. 41, 43)*

Colin, O. and M. Rudgyard (2000). Development of high-order taylor–galerkin schemes for les. *Journal of computational physics 162*(2), 338–371. *(p. 281)*

Crocco, L. (1951). Aspects of combustion stability in liquid propellant rocket motors part I: fundamentals. low frequency instability with monopropellants. *Journal of the American Rocket Society 21*(6), 163–178. *(p. 57, 189)*

Crocco, L. (1952). Aspects of combustion stability in liquid propellant rocket motors part II: Low frequency instability with bipropellants. high frequency instability. *Journal of the American Rocket Society 22*(1), 7–16. *(p. 57, 189)*

Crocco, L. and S. Cheng (1956). *Theory of combustion instability in liquid propellant rocket motors*. Butterworths Scientific Publications, New York. *(p. 57)*

Culick, F. E. and V. Yang (1995). Overview of combustion instabilities in liquid-propellant rocket engines. *(p. 1)*

Dawson, J. R. and N. A. Worth (2014). Flame dynamics and unsteady heat release rate of self-excited azimuthal modes in an annular combustor. *Combustion and Flame 161*(10), 2565–2578. *(p. 2, 4, 223)*

de la Cruz García, M., E. Mastorakos, and A. Dowling (2009). Investigations on the self-excited oscillations in a kerosene spray flame. *Combustion and Flame 156*(2), 374–384. *(p. 171)*

Degenève, A., R. Vicquelin, C. Mirat, B. Labegorre, P. Jourdaine, J. Caudal, and T. Schuller (2019). Scaling relations for the length of coaxial oxy-flames with and without swirl. *Proceedings of the Combustion Institute 37*, 4563–4570. *(p. 63)*

Ding, Y., D. Durox, N. Darabiha, and T. Schuller (2019). Chemiluminescence of burner-stabilized premixed laminar flames. *Combustion Science and Technology 191*(1), 18–42. *(p. 41)*

Docquier, N. and S. Candel (2002). Combustion control and sensors: a review. *Progress in Energy and Combustion Science 28*(2), 107–150. *(p. 41)*

Docquier, N., F. Lacas, and S. Candel (2002). Closed-loop equivalence ratio control of premixed combustors using spectrally resolved chemiluminescence measurements. *Proceedings of the Combustion Institute 29*(1), 139–145. *(p. 41)*

Dolan, B., R. Gomez, and E. Gutmark (2017, January, 9-13). Parametric study of alternating flow patterns in non-reacting multiple-swirl flows. In *55th AIAA Aerospace Sciences Meeting*, Number AIAA 2017-1956, Grapevine, Texas, USA. *(p. 223, 227)*

Dolan, B., R. V. Gomez, and E. Gutmark (2015, June 15 – 19). Optical measurements of interacting lean direct injection fuel nozzles with varying spacing. In *Proceegings of the ASME Turbo Expo 2015*, Number GT2015-43706, Montréal, Canada. *(p. 223)*

Dowling, A. P. (1997). Nonlinear self-excited oscillations of a ducted flame. *Journal of Fluid Mechanics 346*, 271–290. *(p. 58, 74, 119, 190)*

Dowling, A. P. and A. S. Morgans (2005). Feedback control of combustion oscillations. *Annual Review of Fluid Mechanics 37*, 151–182. *(p. 57)*

Ducruix, S., D. Durox, and S. Candel (2000). Theoretical and experimental determinations of the transfer function of a laminar premixed flame. *Proceegings of the Combustion Institute 28*, 765–773. *(p. 58)*

Durox, D., S. Ducruix, and F. Lacas (1999). Flow seeding with an air nebulizer. *Experiments in Fluids 27*(5), 408–413. *(p. 37, 82)*

Durox, D., J. P. Moeck, J.-F. Bourgouin, P. Morenton, M. Viallon, T. Schuller, and S. Candel (2013). Flame dynamics of a variable swirl number system and instability control. *Combustion and Flame 160*(9), 1729–1742. *(p. 117, 216)*

Durox, D., K. Prieur, T. Schuller, and S. Candel (2016). Different flame patterns linked with swirling injector interactions in an annular combustor. *Journal of Engineering for Gas Turbines and Power 138*(10), 101504. *(p. 18, 223)*

Durox, D., T. Schuller, and S. Candel (2005). Combustion dynamics of inverted conical flames. *Proceedings of the Combustion Institute 30*(2), 1717–1724. *(p. 128, 161)*

Durox, D., T. Schuller, N. Noiray, A. L. Birbaud, and S. Candel (2009, jan). Rayleigh criterion and acoustic energy balance in unconfined self-sustained oscillating flames. *Combustion and Flame 156*, 106–119. *(p. 132)*

Durox, D., T. Schuller, N. Noiray, and S. Candel (2009). Experimental analysis of nonlinear flame transfer functions for different flame geometries. *Proceedings of the Combustion Institute 32*, 1391–1398. *(p. 58, 201)*

Ebi, D., A. Denisov, G. Bonciolini, E. Boujo, and N. Noiray (2018). Flame dynamics intermittency in the bistable region near a subcritical hopf bifurcation. *Journal of Engineering for Gas Turbines and Power 140*, 061504. *(p. 124)*

Eckstein, J., E. Freitag, C. Hirsch, and T. Sattelmayer (2006). Experimental study on the role of entropy waves in low-frequency oscillations in a RQL combustor. *Journal of Engineering for Gas Turbines and Power 128*(2), 264–270. *(p. 171, 189)*

Fanaca, D., P. R. Alemela, F. Ettner, C. Hirsch, T. Sattelmayer, and B. Schuermans (2008, June 9-13). Determination and comparison of the dynamic characteristic of a perfectly premixed flame in both single and annular combustion chambers. In *Proceedings of the ASME Turbo Expo 2008*, Number GT2008-50781, Berlin, Germany. *(p. 224)*

Fanaca, D., P. R. Alemela, C. Hirsch, and T. Sattelmayer (2010). Comparison of the Flow Field of a Swirl Stabilized Premixed Burner in a Annular and a Single Burner Combustion Chamber. *Journal of Engineering for Gas Turbines and Power 132*(7). *(p. 224, 240)*

Fang, Y., Y. Yang, K. Hu, G. Wang, J. Li, and Y. Zheng (2021). Experimental study on self-excited thermoacoustic instabilities and intermittent switching of azimuthal and longitudinal modes in an annular combustor. *Physics of Fluids 33*(8), 084104. *(p. 4)*

Fischer, A., C. Hirsch, and T. Sattelmayer (2006). Comparison of multi-microphone transfer matrix measurements with acoustic network models of swirl burners. *Journal of Sound and Vibration 298*, 73–83. *(p. 79, 80, 81, 118)*

Fleifil, M., A. M. Annaswamy, Z. A. Ghoneim, and A. F. Ghoniem (1996). Response of a laminar premixed flame to flow oscillations: A kinematic model and thermoacoustic instability results. *Combustion and Flame 106*, 487–510. *(p. 58)*

Gajan, P., A. Strzelecki, B. Platet, R. Lecourt, and F. Giuliani (2007). Investigation of spray behavior downstream of an aeroengine injector with acoustic excitation. *Journal of propulsion and power 23*(2), 390–397. *(p. 171, 189)*

Gatti, M., R. Gaudron, C. Mirat, L. Zimmer, and T. Schuller (2019). Impact of swirl and bluff-body on the transfer function of premixed flames. *Proceedings of the Combustion Institute 37*, 5197–5204. *(p. 67)*

Gaudron, R. (2018). *Acoustic response of premixed flames submitted to harmonic sound waves*. Ph. D. thesis, Université Paris-Saclay. *(p. 32)*

Gaudron, R., M. Gatti, C. Mirat, and T. Schuller (2019a). Flame describing functions of a confined premixed swirled combustor with upstream and downstream forcing. *Journal of Engineering for Gas Turbines and Power 141*, 051016. *(p. 68)*

Gaudron, R., M. Gatti, C. Mirat, and T. Schuller (2019b). Impact of the acoustic forcing level on the transfer matrix of a turbulent swirling combustor with and without flame. *Flow, Turbulence and Combustion 103*(3), 751–771. *(p. 59, 69, 92)*

Ghirardo, G., M. Juniper, and J. P. Moeck (2016). Weakly nonlinear analysis of thermoacoustic instabilities in annular combustors. *Journal of Fluid Mechanics 805*, 52–87. *(p. 4, 58)*

Ghirardo, G. and M. P. Juniper (2013). Azimuthal instabilities in annular combustors: standing and spinning modes. *Proceedings of the Royal Society A: Mathematical, Physical and Engineering Sciences 469*(2157), 20130232. *(p. 4, 145, 190)*

Giuliani, F., P. Gajan, O. Diers, and M. Ledoux (2002). Influence of pulsed entries on a spray generated by an air-blast injection device: An experimental analysis on combustion instability processes in aeroengines. *Proceedings of the Combustion Institute 29*, 91–98. *(p. 171)*

Gopinathan, S. M., D. Iurashev, A. Bigongiari, and M. Heckl (2018). Nonlinear analytical flame models with amplitude-dependent time-lag distributions. *International Journal of Spray and Combustion Dynamics 10*, 264–276. *(p. 58)*

Greenberg, J. B. and D. Katoshevski (2012). Spray flame dynamics with oscillating flow and droplet grouping. *Combustion Theory and Modelling 16*(2), 321–340. *(p. 171)*

Gupta, A. K., D. G. Lilley, and N. Syred (1984). Swirl flows. *Tunbridge Wells*. *(p. 27)*

Haeringer, M., M. Merk, and W. Polifke (2019). Inclusion of higher harmonics in the flame describing function for predicting limit cycles of self-excited combustion instabilities. *Proceedings of the Combustion Institute 37*, 5255–5262. *(p. 58, 59, 75)*

Han, X., J. Li, and A. S. Morgans (2015). Prediction of combustion instability limit cycle oscillations by combining flame describing function simulations with a thermoacoustic network model. *Combustion and Flame 162*, 3632–3647. *(p. 58, 101)*

Han, X. and A. S. Morgans (2015). Simulation of the flame describing function of a turbulent premixed flame using an open-source LES solver. *Combustion and Flame 162*, 1778–1792. *(p. 58)*

Hardalupas, Y. and M. Orain (2004). Local measurements of the time-dependent heat release rate and equivalence ratio using chemiluminescent emission from a flame. *Combustion and Flame 139*(3), 188–207. *(p. 41, 43, 47)*

Harrje, D. J. and F. H. Reardon (1972). Liquid propellant rocket instability. Technical report, NASA, Report SP-194. *(p. 57, 117)*

Heckl, M. (2015). A new perspective on the flame describing function of a matrix flame. *International Journal of Spray and Combustion Dynamics 7*, 91–112. *(p. 58)*

Heckl, M. A. (2013). Analytical model of nonlinear thermo-acoustic effects in a matrix burner. *Journal of Sound and Vibration 332*, 4021–4036. *(p. 58)*

Higgins, B., M. McQuay, F. Lacas, and S. Candel (2001). An experimental study on the effect of pressure and strain rate on ch chemiluminescence of premixed fuel-lean methane/air flames. *Fuel 80*(11), 1583–1591. *(p. 41)*

Higgins, B., M. McQuay, F. Lacas, J.-C. Rolon, N. Darabiha, and S. Candel (2001). Systematic measurements of oh chemiluminescence for fuel-lean, high-pressure, premixed, laminar flames. *Fuel 80*(1), 67–74. *(p. 41)*

Howe, M. (1979). On the theory of unsteady high reynolds number flow through a circular aperture. *Proceedings of the Royal Society of London. A. Mathematical and Physical Sciences 366*(1725), 205–223. *(p. 92)*

Huang, Y. and V. Yang (2005). Effect of swirl on combustion dynamics in a lean-premixed swirl-stabilized combustor. *Proceedings of the Combustion Institute 30*(2), 1775–1782. *(p. 117, 146)*

Huang, Y. and V. Yang (2009). Dynamics and stability of lean-premixed swirl-stabilized combustion. *Progress in Energy and Combustion Science 35*(4), 293–364. *(p. 1, 57, 117, 145)*

Hubbard, S. and A. P. Dowling (2001). Acoustic resonances of an industrial gas turbine combustion system. *Journal of Engineering for Gas Turbines and Power 123*, 766–773. *(p. 57)*

Hurle, I. R., R. B. Price, T. M. Sugden, and A. Thomas (1968). Sound emission from open turbulent premixed flames. *Proceedings of the Royal Society of London Series A-Mathematical, Physical and Engineering Sciences 303*(1475), 409–427. *(p. 40, 41, 59, 228)*

Hutt, J. and M. Rocker (1995). *High-Frequency injection-coupled combustion instability, in: V. Yang, W.E. Anderson (Eds.), Liquid Rocket Engine Combustion Instability*. American Institute of Aeronautics and Astronautics. *(p. 129)*

Indlekofer, T., B. Ahn, Y. H. Kwah, S. Wiseman, M. Mazur, J. R. Dawson, and N. A. Worth (2021). The effect of hydrogen addition on the amplitude and harmonic response of azimuthal instabilities in a pressurized annular combustor. *Combustion and Flame 228*, 375–387. *(p. 4)*

Innocenti, A., A. Andreini, B. Facchini, and A. Peschiulli (2017). Numerical analysis of the dynamic flame response of a spray flame for aero-engine applications. *International Journal of Spray and Combustion Dynamics 9*(4), 310–329. *(p. 171)*

Juniper, M. P. and S. M. Candel (2003). The stability of ducted compound flows and consequences for the geometry of coaxial injectors. *Journal of Fluid Mechanics 482*, 257–269. *(p. 172)*

Kabiraj, L. and R. Sujith (2011). Investigation of subcritical instability in ducted premixed flames. In *Turbo Expo: Power for Land, Sea, and Air*, Volume 54624, pp. 969–977. *(p. 75)*

Kabiraj, L., R. Sujith, and P. Wahi (2011). Experimental studies of bifurcations leading to chaos in a laboratory scale thermoacoustic system. In *Turbo Expo: Power for Land, Sea, and Air*, Volume 54624, pp. 959–968. *(p. 75)*

Kao, Y.-H., M. Denton, X. Wang, S.-M. Jeng, and M.-C. Lai (2015, June 15 – 19,). Experimental spray structure and combustion of a linearly arranged 5-swirler array. In *Proceedings of the ASME Turbo Expo 2015*, Number GT2015-42509, Montréal, Canada. *(p. 223)*

Kao, Y.-H., S. Tambe, and S.-M. Jeng (2014, June 16-20,). Aerodynamics study of a linearly-arranged 5-swirler array. In *Proceedings of the ASME Turbo*

Expo 2014, Number GT2014-25094, Düsseldorf, Germany. *(p. 223)*

Kim, K. T. (2016). Combustion instability feedback mechanisms in a lean-premixed swirl-stabilized combustor. *Combustion and Flame 171*, 137–151. *(p. 117, 146)*

Kim, K. T., H. J. Lee, J. G. Lee, B. Quay, and D. Santavicca (2009, June 8-12). Flame transfer function measurement and instability frequency prediction using a thermoacoustic model. In *Proceedings of the ASME Turbo Expo 2009*, Number GT2009-60026, Florida, USA. International Gas Turbine Institute. *(p. 75)*

Kim, K. T. and D. Santavicca (2009). Linear stability analysis of acoustically driven pressure oscillations in a lean premixed gas turbine combustor. *Journal of Mechanical Science and Technology 23*(12), 3436–3447. *(p. 100)*

Kim, K. T. and D. A. Santavicca (2013). Generalization of turbulent swirl flame transfer functions in gas turbine combustors. *Combustin Science and Technology 185*, 999–1015. *(p. 58)*

Kim, T., M. Ahn, D. Lim, and Y. Yoon (2022). Flame describing function and combustion instability analysis of non-premixed coaxial jet flames. *Experimental Thermal and Fluid Science*, 110642. *(p. 101)*

Kim, W., S. Zhang, P. Palies, J. Cohen, S. Liljenberg, and D. Hautman (2012, June 11-15). The behavior of liquid fuel sprays in acoustically-forced air swirler flows. In *Proceedings of the ASME Turbo Expo 2012*, Number Copenhagen, Denmark. *(p. 189)*

King, L. V. (1914). On the convection of heat from small cylinders in a stream of fluid: Determination of the convection constants of small platinum wires with applications to hot-wire anemometry. *Philosophical transactions of the royal society of London. series A, containing papers of a mathematical or physical character 214*(509-522), 373–432. *(p. 33)*

Kojima, J., Y. Ikeda, and T. Nakajima (2000). Spatially resolved measurement of OH*, CH*, and C2* chemiluminescence in the reaction zone of laminar methane/air premixed flames. *Proceedings of the Combustion institute 28*(2), 1757–1764. *(p. 41, 43)*

Komarek, T. and W. Polifke (2010). Impact of swirl fluctuations on the flame response of a perfectly premixed swirl burner. *Journal of Engineering for Gas Turbines and Power 132*(6), 061503. *(p. 146)*

Kopitz, J., A. Huber, T. Sattelmayer, and W. Polifke (2005, June 6-9). Thermoacoustic stability analysis of an annular combustion chamber with acoustic low order modeling and validation against experiment. In *Proceedings of the ASME Conference*, Number GT2005-68797, Nevada, USA. *(p. 4)*

Kornilov, V. N., M. Manohar, and L. P. H. de Goey (2009). Thermo-acoustic behavior of multiple flame burner decks: transfer function decomposition.

Proceedings of the Combustion Institute 32, 1383–1390. *(p. 58)*

Krebs, W., P. Flohr, B. Prade, and S. Hoffmann (2002). Thermoacoustic stability chart for high-intensity gas turbine combustion systems. *Combustion Science and Technology 174*, 99–128. *(p. 223)*

Krebs, W., H. Krediet, E. Portillo, S. Hermeth, T. Poinsot, S. Schimek, and O. Paschereit (2013). Comparison of nonlinear to linear thermoacoustic stability analysis of a gas turbine combustion system. *Journal of Engineering for Gas Turbines and Power 135*(8). *(p. 57, 102)*

Krishnan, A., R. Sujith, N. Marwan, and J. Kurths (2021). Suppression of thermoacoustic instability by targeting the hubs of the turbulent networks in a bluff body stabilized combustor. *Journal of Fluid Mechanics 916*. *(p. 145)*

Kunze, K., C. Hirsch, and T. Sattelmayer (2004, June 14-17). Transfer function measurements on a swirl stabilized premix burner in an annular combustion chamber. In *Proceedings of the ASME Turbo Expo 2004*, Number GT2004-53106, Vienna, Austria. *(p. 223)*

Laera, D., T. Schuller, K. Prieur, D. Durox, S. M. Camporeale, and S. Candel (2017). Flame describing function analysis of spinning and standing modes in an annular combustor and comparison with experiments. *Combustion and Flame 184*, 136–152. *(p. 58, 145, 146, 160, 223)*

Lancien, T. (2018, Oct). *Numerical study of two-phase ignition in annular multi-burner combustors*. Ph. D. thesis, Université Paris-Saclay. *(p. 27)*

Lancien, T., K. Prieur, D. Durox, S. Candel, and R. Vicquelin (2018). Large eddy simulation of light-round in an annular combustor with liquid spray injection and comparison with experiments. *Journal of Engineering for Gas Turbines and Power 140*(2). *(p. 19)*

Lauer, M. and T. Sattelmayer (2010). On the adequacy of chemiluminescence as a measure for heat release in turbulent flames with mixture gradients. *Journal of Engineering for Gas Turbines and Power 132*(6). *(p. 42)*

Lawn, C. (2000). Distributions of instantaneous heat release by the cross-correlation of chemiluminescent emissions. *Combustion and Flame 123*(1-2), 227–240. *(p. 41)*

Lee, J.-Y., E. Lubarsky, and B. T. Zinn (2005). "slow" active control of combustion instabilities by modification of liquid fuel spray properties. *Proceedings of the Combustion Institute 30*(2), 1757–1764. *(p. 172, 189)*

Lee, T., J. Lee, J. Park, D. Han, and K. T. Kim (2018). Staggered swirler arrangement in two self-excited interacting swirl flames. *Combustion and Flame 198*, 363–375. *(p. 223)*

Lee, T., J. Park, D. Han, and K. Kim (2019). The dynamics of multiple interacting swirl-stabilized flames in a lean-premixed gas turbine combustor. *Proceedings of the Combustion Institute 37*(4), 5137–5145. *(p. 223)*

Leitgeb, T., T. Schuller, D. Durox, F. Giuliani, S. Köberl, and J. Woisetschläger (2013). Interferometric determination of heat release rate in a pulsated flame. *Combustion and Flame 160*(3), 589–600. *(p. 44)*

Lemaire, R. and S. Menanteau (2017). Assessment of radiation correction methods for bare bead thermocouples in a combustion environment. *International Journal of Thermal Sciences 122*, 186–200. *(p. 38)*

Li, J., D. Durox, F. Richecoeur, and T. Schuller (2015). Analysis of chemiluminescence, density and heat release rate fluctuations in acoustically perturbed laminar premixed flames. *Combustion and Flame 162*(10), 3934–3945. *(p. 44)*

Li, J. and A. S. Morgans (2016). Simplified models for the thermodynamic properties along a combustor and their effect on thermoacoustic instability prediction. *Fuel 184*, 735–748. *(p. 100)*

Li, J., F. Richecoeur, and T. Schuller (2012). Determination of heat release rate disturbances in unconfined flames based on fluctuations in the travel time of ultrasonic waves. *Combustion Science and Technology 184*(4), 533–555. *(p. 43)*

Lieuwen, T. (2003). Modeling premixed combustion-acoustic wave interactions: A review. *Journal of Propulsion and Power 19*, 765–779. *(p. 58)*

Lieuwen, T., H. Torres, C. Johnson, and B. T. Zinn (2001). A mechanism of combustion instability in lean premixed gas turbine combustors. *Journal of Engineering for Gas Turbines and Power 123*, 182–189. *(p. 57)*

Lieuwen, T. and V. Yang (Eds.) (2005a). *Combustion instabilities in gas turbine engines, Operational experience, Fundamental mechanisms, and modeling*, Volume 210 of *Progress in Astronautics and Aeronautics*. American Institute of Aeronautics and Astronautics, Inc. *(p. 57)*

Lieuwen, T. and B. T. Zinn (1998). The role of equivalence ratio oscillations in driving combustion instabilities in low NOx gas turbines. *Proceedings of the Combustion Institute 27*, 1809–1816. *(p. 57)*

Lieuwen, T. C. and V. Yang (2005b). Combustion instabilities in gas turbine engines: operational experience, fundamental mechanisms, and modeling. *American Institute of Aeronautics and Astronautics*. *(p. 1, 145, 170)*

Lo Schiavo, E., D. Laera, E. Riber, L. Gicquel, and T. Poinsot (2020). Effects of liquid fuel/wall interaction on thermoacoustic instabilities in swirling spray flames. *Combustion and Flame 219*, 86–101. *(p. 51, 171, 253, 281)*

Lo Schiavo, E., D. Laera, E. Riber, L. Gicquel, and T. Poinsot (2021). On the impact of fuel injection angle in Euler–Lagrange large eddy simulations of swirling spray flames exhibiting thermoacoustic instabilities. *Combustion and Flame 227*, 359–370. *(p. 171, 179, 180, 253)*

Magri, L., M. Bauerheim, and M. P. Juniper (2016). Stability analysis of thermo-acoustic nonlinear eigenproblems in annular combustors. part I. sensitivity. *Journal of Computational Physics 325*, 395–410. *(p. 4)*

Marble, F. E. and D. W. Cox Jr. (1953). Servo-stabilization of low frequency oscillations in a liquid bipropellant rocket motor. *Journal of the American Rocket Society 23*(63–74). *(p. 57)*

Matsui, Y. (1981). An experimental study on pyro-acoustic amplification of premixed laminar flames. *Combustion and Flame 43*, 199–209. *(p. 58)*

Mazur, M., Y. H. Kwah, T. Indlekofer, J. R. Dawson, and N. A. Worth (2021). Self-excited longitudinal and azimuthal modes in a pressurised annular combustor. *Proceedings of the Combustion Institute 38*(4), 5997–6004. *(p. 4)*

McManus, K. R., T. Poinsot, and S. Candel (1993). A review of active control of combustion instabilities. *Progress in Energy and Combustion Science 19*, 1–29. *(p. 57)*

Méry, Y. (2018). Dynamical response of a perfectly premixed flame and limit behavior for high power density systems. *Combustion and Flame 192*, 410–425. *(p. 117)*

Mirat, C., D. Durox, and T. Schuller (2014). Analysis of the spray and transfer function of swirling spray flames from a multi-jet steam assisted liquid fuel injector. In *Turbo Expo: Power for Land, Sea, and Air*, Volume 45684, pp. V04AT04A008. American Society of Mechanical Engineers. *(p. 42)*

Mirat, C., D. Durox, and T. Schuller (2015). Stability analysis of a swirl spray combustor based on flame describing function. *Proceedings of the Combustion Institute 35*(3), 3291–3298. *(p. 42)*

Moeck, J. P. and C. O. Paschereit (2012). Nonlinear interactions of multiple linearly unstable thermoacoustic modes. *International Journal of Spray and Combustion Dynamics 4*, 1–27. *(p. 59, 75)*

Mongia, H. C., T. Held, G. Hsiao, and R. Pandalai (2003). Challenges and progress in controlling dynamics in gas turbine combustors. *Journal of Propulsion and Power 19*(5), 822–829. *(p. 145)*

Morgans, A. S. and S. R. Stow (2007). Model-based control of combustion instabilities in annular combustors. *Combustion and Flame 150*(4), 380–399. *(p. 4, 57)*

Muruganandam, T., B.-H. Kim, M. Morrell, V. Nori, M. Patel, B. Romig, and J. Seitzman (2005). Optical equivalence ratio sensors for gas turbine combustors. *Proceedings of the Combustion Institute 30*(1), 1601–1609. *(p. 41, 43)*

Najm, H. N., P. H. Paul, C. J. Mueller, and P. S. Wyckoff (1998). On the adequacy of certain experimental observables as measurements of flame burning rate. *Combustion and Flame 113*(3), 312–332. *(p. 41, 44)*

Noiray, N., D. Durox, T. Schuller, and S. Candel (2008). A unified framework for nonlinear combustion instability analysis based on the flame describing function. *Journal of Fluid Mechanics 615*, 139–167. *(p. 58, 60, 66, 74, 119, 190, 223)*

Noiray, N., D. Durox, T. Schuller, and S. Candel (2009a). Dynamic phase converter for passive control of combustion instabilities. *Proceedings of the Combustion Institute 32*(2), 3163–3170. *(p. 145)*

Noiray, N., D. Durox, T. Schuller, and S. Candel (2009b). A method for estimating the noise level of unstable combustion based on the flame describing function. *International Journal of Aeroacoustics 8*, 157–176. *(p. 58, 138)*

Noiray, N., D. Durox, T. Schuller, and S. Candel (2009c). Mode conversion in acoustically modulated confined jets. *AIAA Journal 47*, 2053–2062. *(p. 59, 69, 81)*

Noiray, N. and B. Schuermans (2013). On the dynamic nature of azimuthal thermoacoustic modes in annular gas turbine combustion chambers. *Proceedings of the Royal Society A: Mathematical, Physical and Engineering Sciences 469*(2151), 20120535. *(p. 4)*

Nori, V. N. and J. M. Seitzman (2009). CH* chemiluminescence modeling for combustion diagnostics. *Proceedings of the Combustion Institute 32*(1), 895–903. *(p. 42)*

Obertacke, R., H. Wintrich, F. Wintrich, and A. Leipertz (1996). A new sensor system for industrial combustion monitoring and control using UV emission spectroscopy and tomography. *Combustion Science and Technology 121*(1-6), 133–151. *(p. 41)*

O'Connor, J., V. Acharya, and T. Lieuwen (2015). Transverse combustion instabilities: Acoustic, fluid mechanic, and flame processes. *Progress in Energy and Combustion Science 49*, 1–39. *(p. 129, 223)*

Oefelein, J. C. and V. Yang (1993). Comprehensive review of liquid-propellant combustion instabilities in F-1 engines. *Journal of Propulsion and Power 9*(5), 657–677. *(p. 1)*

Orchini, A. and M. P. Juniper (2016). Flame double input describing function analysis. *Combustion and Flame 171*, 87–102. *(p. 59, 75)*

Palies, P. (2010). *Dynamique et instabilités de combustion des flammes swirlées*. Ph. D. thesis, Ecole Centrale Paris. *(p. 90)*

Palies, P., D. Durox, T. Schuller, and S. Candel (2011). Nonlinear combustion instability analysis based on the flame describing function applied to turbulent premixed swirling flames. *Combustion and Flame 158*(10), 1980–1991. *(p. 30, 58, 67, 75, 100)*

Palies, P., D. Durox, T. Schuller, P. Morenton, and S. Candel (2009). Dynamics of premixed confined swirling flames. *C. R. Mécanique 337*, 395–405. *(p. 75)*

Palies, P., T. Schuller, D. Durox, and S. Candel (2011). Modeling of swirling flames transfer functions. *Proceedings of the Combustion Institute 33*, 2967–2974. *(p. 58)*

Pankiewitz, C. and T. Sattelmayer (2003). Time domain simulation of combustion instabilities in annular combustors. *Journal of Engineering for Gas Turbines and Power 125*(3), 677–685. *(p. 4, 145)*

Parmentier, J.-F., P. Salas, P. Wolf, G. Staffelbach, F. Nicoud, and T. Poinsot (2012). A simple analytical model to study and control azimuthal instabilities in annular combustion chambers. *Combustion and Flame 159*(7), 2374–2387. *(p. 4, 145)*

Paschereit, C. O., E. Gutmark, and W. Weisenstein (2000). Excitation of thermoacoustic instabilities by interaction of acoustics and unstable swirling flow. *AIAA Journal 38*(6), 1025–1034. *(p. 146)*

Paschereit, C. O., B. Schuermans, W. Polifke, and O. Mattson (2002). Measurement of transfer matrices and source terms of premixed flames. *Journal of Engineering for Gas Turbines and Power 124*(2), 239–247. *(p. 44, 57, 59, 68, 69, 80, 81)*

Patat, C., F. Baillot, J.-B. Blaisot, and E. Domingues (2021). Responses of lean swirling spray flames to acoustic pressure and transverse velocity perturbations. *Symposium on Thermoacoustics in Combustion: Industry meets Academia (SoTiC)*, paper 8499. *(p. 129, 139, 161)*

Patat, C., J.-B. Blaisot, E. Domingues, and F. Baillot (2021, 29 Aug. - 2 Sept. 2021). Response of a spray of n-heptane or dodecane at an acoustic pressure antinode in reactive conditions. In *15th ICLASS*, Edinburgh, UK,. *(p. 23)*

Paulhiac, D., B. Cuenot, E. Riber, L. Esclapez, and S. Richard (2020). Analysis of the spray flame structure in a lab-scale burner using large eddy simulation and discrete particle simulation. *Combustion and Flame 212*, 25–38. *(p. 281)*

Pera, C. and J. Reveillon (2007). Direct numerical simulation of spray flame/acoustic interactions. *Proceedings of the Combustion Institute 31*(2), 2283–2290. *(p. 171)*

Peterleithner, J., R. Basso, F. Heitmeir, J. Woisetschläger, R. Schlüßler, J. Czarske, and A. Fischer (2016). Comparison of flame transfer functions acquired by chemiluminescence and density fluctuation. In *Turbo Expo: Power for Land, Sea, and Air*, Volume 49767, pp. V04BT04A022. American Society of Mechanical Engineers. *(p. 44)*

Philip, M., M. Boileau, R. Vicquelin, E. Riber, T. Schmitt, B. Cuenot, D. Durox, and S. Candel (2015). Large eddy simulations of the ignition sequence of an annular multiple-injector combustor. *Proceedings of the Combustion Institute 35*(3), 3159–3166. *(p. 19)*

Philip, M., M. Boileau, R. Vicquelin, T. Schmitt, D. Durox, J.-F. Bourgouin, and S. Candel (2015). Simulation of the ignition process in an annular multiple-injector combustor and comparison with experiments. *Journal of Engineering for Gas Turbines and Power 137*(3). *(p. 3, 19)*

Pillai, A. L., J. Nagao, R. Awane, and R. Kurose (2020). Influences of liquid fuel atomization and flow rate fluctuations on spray combustion instabilities in a backward-facing step combustor. *Combustion and Flame 220*, 337–356. *(p. 189)*

Poinsot, T. (2017). Prediction and control of combustion instabilities in real engines. *Proceedings of the Combustion Institute 36*(1). *(p. 1, 57, 117, 145, 170, 223)*

Poinsot, T. and D. Veynante (2012). *Theoretical and numerical combustion*. R.T. Edwards. *(p. 135)*

Poinsot, T. J. and S. Lelef (1992). Boundary conditions for direct simulations of compressible viscous flows. *Journal of computational physics 101*(1), 104–129. *(p. 281)*

Polifke, W. (2020). Modeling and analysis of premixed flame dynamics by means of distributed time delays. *Progress in Energy and Combustion Science 79*, 100845. *(p. 57, 93)*

Polifke, W., A. Fischer, and T. Sattelmayer (2003). Instability of a premix burner with nonmonotonic pressure drop characteristic. *Journal of Engineering for Gas Turbines and Power 125*, 20–27. *(p. 118)*

Polifke, W. and C. Lawn (2007). On the low-frequency limit of flame transfer functions. *Combustion and Flame 151*(3), 437–451. *(p. 93, 96)*

Preetham, T. Sai Kumar, and T. Lieuwen (2006). Response of premixed flames to flow oscillations : unsteady curvature effects. *44th AIAA Aerospace Sciences Meeting and Exhibit Paper 2006-960*. *(p. 58)*

Preetham, H. Santosh, and T. Lieuwen (2008). Dynamics of laminar premixed flames forced by harmonic velocity disturbances. *Journal of Propulsion and Power 24*, 1390–1402. *(p. 58)*

Price, R. B., I. R. Hurle, and T. M. Sugden (1969). Optical studies of the generation of noise in turbulent flames. *Proceedings of the Combustion Institute 12*(1), 1093–1102. *(p. 41)*

Prieur, K. (2017). *Dynamique de la combustion dans un foyer annulaire multi-injecteurs diphasique*. Ph. D. thesis, Université Paris-Saclay. *(p. 2, 3, 5, 21, 26, 27, 32, 101, 128)*

Prieur, K., D. Durox, J. Beaunier, T. Schuller, and S. Candel (2017). Ignition dynamics in an annular combustor for liquid spray and premixed gaseous injection. *Proceedings of the Combustion Institute 36*(3), 3717–3724. *(p. 3, 19, 190, 197)*

Prieur, K., D. Durox, S. Schuller, and S. Candel (2018). Strong azimuthal combustion instabilities in a spray annular chamber with intermittent partial blow-off. *Journal of Engineering for Gas Turbines and Power 140*(3), 031503. *(p. 2, 19, 20, 27, 139, 190, 192, 223, 225)*

Prieur, K., D. Durox, T. Schuller, and S. Candel (2017). A hysteresis phenomenon leading to spinning or standing azimuthal instabilities in an annular combustor. *Combustion and Flame 175*, 283–291. *(p. 2, 18, 145, 223)*

Prieur, K., G. Vignat, D. Durox, T. Schuller, and S. Candel (2019). Flame and spray dynamics during the light-round process in an annular system equipped with multiple swirl spray injectors. *Journal of Engineering for Gas Turbines and Power 141*(6). *(p. 19)*

Puggelli, S., D. Veynante, and R. Vicquelin (2021). Impact of dynamic modelling of the flame subgrid scale wrinkling in large-eddy simulation of light-round in an annular combustor. *Combustion and Flame 230*, 111416. *(p. 19)*

Rajendram Soundararajan, P., D. Durox, A. Renaud, and S. Candel (2022). Azimuthal instabilities of an annular combustor with different swirling injectors. In *Accepted for publication at the Proceedings of ASME Turbo Expo 2022*. *(p. 146, 164)*

Rajendram Soundararajan, P., D. Durox, A. Renaud, G. Vignat, and S. Candel (2022). Swirler effects on combustion instabilities analyzed with measured FDFs, injector impedances and damping rates. *Combustion and Flame 238*(4), 111947. *(p. 60, 225, 237)*

Rajendram Soundararajan, P., G. Vignat, D. Durox, A. Renaud, and S. Candel (2021). Effect of different fuels on combustion instabilities in an annular combustor. *Journal of Engineering for Gas Turbines and Power 143*(3), 031007. *(p. 2, 19, 58, 145, 149, 170, 224, 225)*

Rayleigh, L. (1878). The explanation of certain acoustical phenomena. *Nature 18*, 319–321. *(p. 189)*

Richards, G. A. and M. C. Janus (1998, Apr). Characterization of oscillations during premix gas turbine combustion. *Journal of Engineering for Gas Turbines and Power 120*, 294–302. *(p. 57)*

Rienstra, S. and A. Hierschberg (2004). *An introduction to acoustics*. Report IWDE 92-06, Eindhoven University of Technology. *(p. 104)*

Roy, A., S. Singh, A. Nair, S. Chaudhuri, and R. Sujith (2021). Flame dynamics during intermittency and secondary bifurcation to longitudinal thermoa-

coustic instability in a swirl-stabilized annular combustor. *Proceedings of the Combustion Institute 38*(4), 6221–6230. *(p. 4)*

Schildmacher, K.-U., R. Koch, and H.-J. Bauer (2006). Experimental characterization of premixed flame instabilities of a model gas turbine burner. *Flow Turbulence and Combustion 76*, 177–197. *(p. 57)*

Schuermans, B., V. Bellucci, F. Guethe, F. Meili, P. Flohr, and C. O. Paschereit (2004). A detailed analysis of thermoacoustic interaction mechanisms in a turbulent premixed flame. *Turbo Expo: Power for Land, Sea, and Air paper no. GT2004-53831 1*, 539–551. *(p. 59, 68)*

Schuermans, B., V. Bellucci, and C. O. Paschereit (2003). Thermoacoustic modeling and control of multiburner combustion systems. In *ASME Conference Proceedings, Paper GT 2003-38688*. *(p. 92)*

Schuermans, B., F. Guethe, and W. Mohr (2010). Optical transfer function measurements for technically premixed flames. *Journal of Engineering for Gas Turbines and Power 132*(8). *(p. 44, 69)*

Schuller, T., S. Ducruix, D. Durox, and S. Candel (2002). Modeling tools for the prediction of premixed Flame Transfer Functions. *Proceedings of the Combustion Institute 29*, 107–113. *(p. 58)*

Schuller, T., D. Durox, and S. Candel (2003). A unified model for the prediction of laminar flame transfer functions : comparisons between conical and V-flame dynamics. *Combustion and Flame 134*, 21–34. *(p. 58)*

Schuller, T., D. Durox, P. Palies, and S. Candel (2012). Acoustic decoupling of longitudinal modes in generic combustion systems. *Combustion and Flame 159*, 1921–1931. *(p. 118)*

Schuller, T., T. Poinsot, and S. Candel (2020). Dynamics and control of premixed combustion systems based on flame transfer and describing functions. *Journal of Fluid Mechanics 894*, 1–95. *(p. 57, 66, 75, 100, 101, 102, 104, 109, 110, 132, 135, 138, 182, 203, 223, 239)*

Seybert, A. F. and D. F. Ross (1977). Experimental determination of acoustic properties using a two-microphone random-excitation technique. *The Journal of the Acoustical Society of America 61*(5), 1362–1370. *(p. 34, 192)*

Silva, C. F., F. Nicoud, T. Schuller, D. Durox, and S. Candel (2013). Combining a Helmholtz solver with the flame describing function to assess combustion instability in a premixed swirled combustor. *Combustion and Flame 160*, 1743–1754. *(p. 58)*

Singh, S., A. Roy, R. KV, A. Nair, S. Chaudhuri, and R. Sujith (2021). Intermittency, secondary bifurcation and mixed-mode oscillations in a swirl-stabilized annular combustor: Experiments and modeling. *Journal of Engineering for Gas Turbines and Power 143*(5). *(p. 4)*

Smith, T., I. Chterev, B. Emerson, D. Noble, and T. Lieuwen (2018). Comparison of single- and multinozzle reacting swirl flow dynamics. *Journal of Propulsion and Power 34*(2), 384–394. *(p. 224)*

Staffelbach, G., L. Gicquel, G. Boudier, and T. Poinsot (2009). Large eddy simulation of self excited azimuthal modes in annular combustors. *Proceedings of the Combustion Institute 32*(2), 2909–2916. *(p. 4, 23, 24, 129, 145, 190, 223)*

Steele, R. C., L. H. Cowell, S. M. Cannon, and C. E. Smith (2000). Passive control of combustion instability in lean premixed combustors. *Journal of Engineering for Gas Turbines and Power 122*(3), 412–419. *(p. 145)*

Steinberg, A. M., C. M. Arndt, and W. Meier (2013). Parametric study of vortex structures and their dynamics in swirl-stabilized combustion. *Proceedings of the Combustion Institute 34*, 3117–3125. *(p. 117)*

Steinberg, A. M., I. Boxx, M. Stöhr, C. D. Carter, and W. Meier (2010). Flow–flame interactions causing acoustically coupled heat release fluctuations in a thermo-acoustically unstable gas turbine model combustor. *Combustion and Flame 157*, 2250–2266. *(p. 117)*

Steinberg, A. M., I. Boxx, M. Stohr, W. Meier, and C. D. Carter (2012). Effects of flow structure dynamics on thermoacoustic instabilities in swirl-stabilized combustion. *AIAA Journal 50*(4), 952–967. *(p. 146)*

Stone, C. and S. Menon (2002). Swirl control of combustion instabilities in a gas turbine combustor. *Proceedings of the Combustion Institute 29*, 155–160. *(p. 117, 118)*

Straub, D. L. and G. A. Richards (1998). Effect of fuel nozzle configuration on premix combustion dynamics. *Turbo Expo: Power for Land, Sea, and Air*, paper 98–GT–492. *(p. 172)*

Sujith, R. (2005). An experimental investigation of interaction of sprays with acoustic fields. *Experiments in Fluids 38*(5), 576–587. *(p. 171)*

Sujith, R., G. Waldherr, J. Jagoda, and B. Zinn (2000). Experimental investigation of the evaporation of droplets in axial acoustic fields. *Journal of Propulsion and Power 16*(2), 278–285. *(p. 171)*

Syred, N. (2006). A review of oscillation mechanisms and the role of the precessing vortex core (PVC) in swirl combustion systems. *Progress in Energy and Combustion Science 32*, 93–161. *(p. 117)*

Tachibana, S., K. Saito, T. Yamamoto, M. Makida, T. Kitano, and R. Kurose (2015). Experimental and numerical investigation of thermo-acoustic instability in a liquid-fuel aero-engine combustor at elevated pressure: Validity of large-eddy simulation of spray combustion. *Combustion and Flame 162*(6), 2621–2637. *(p. 171, 189)*

Töpperwien, K., S. Puggelli, and R. Vicquelin (2022). Analysis of flame propagation mechanisms during light-round in an annular spray flame combustor: the impact of wall heat transfer and two-phase flow. *Combustion and Flame 241*(7), 112105. *(p. 19)*

Tran, N. (2009). *Influence of inlet acoustic boundary condition on large amplitude combustion instabilities: design of a robust impedance control system*. Ph. D. thesis, Ecole Centrale Paris. *(p. 34)*

Tsien, H. S. (1952). Servo-stabilization of combustion in rocket engines. *Journal of the American Rocket Society 22*(256–263). *(p. 57)*

Vignat, G. (2020). *Injection and combustion dynamics in swirled spray flames and azimuthal coupling in annular combustors*. Ph. D. thesis, Université Paris-Saclay. *(p. 2, 3, 5, 6, 21, 26, 27, 36, 40, 46, 54, 131, 132, 281)*

Vignat, G., D. Durox, K. Prieur, and S. Candel (2019). An experimental study into the effect of injector pressure loss on self-sustained combustion instabilities in a swirled spray burner. *Proceedings of the Combustion Institute 37*(4), 5205–5213. *(p. 118, 146)*

Vignat, G., D. Durox, A. Renaud, and S. Candel (2020). High amplitude combustion instabilities in an annular combustor inducing pressure field deformation and flame blow off. *Journal of Engineering for Gas Turbines and Power 142*(1), 011016. *(p. 19, 20, 149, 170, 190, 194, 195, 225)*

Vignat, G., D. Durox, T. Schuller, and S. Candel (2020). Combustion dynamics of annular systems. *Combust. Sci. Tech. 192*, 1358–1388. *(p. 118)*

Vignat, G., E. Lo Schiavo, D. Laera, A. Renaud, L. Gicquel, D. Durox, and S. Candel (2021). Dynamics of spray and swirling flame under acoustic oscillations: A joint experimental and les investigation. *Proceedings of the Combustion Institute 38*(4), 6015–6024. *(p. 51, 190, 203, 253)*

Vignat, G., P. Rajendram Soundararajan, D. Durox, A. Vié, A. Renaud, and S. Candel (2021). A joint experimental and LES characterization of the liquid fuel spray in a swirl injector. *Journal of Engineering for Gas Turbines and Power 143*, 081019. *(p. 253)*

Vogel, M., M. Bachfischer, J. Kaufmann, and T. Sattelmayer (2021). Experimental investigation of equivalence ratio fluctuations in a lean premixed kerosene combustor. *Experiments in Fluids 62*(5), 1–14. *(p. 50, 51)*

Wang, G., T. F. Guiberti, X. Xia, L. Li, X. Liu, W. L. Roberts, and F. Qi (2021). Decomposition of swirling flame transfer function in the complex space. *Combustion and Flame 228*, 29–41. *(p. 67)*

Wolf, P., R. Balakrishnan, G. Staffelbach, L. Y. Gicquel, and T. Poinsot (2012). Using LES to study reacting flows and instabilities in annular combustion chambers. *Flow, Turbulence and Combustion 88*(1), 191–206. *(p. 145)*

Wolf, P., G. Staffelbach, L. Y. Gicquel, J.-D. Müller, and T. Poinsot (2012). Acoustic and large eddy simulation studies of azimuthal modes in annular combustion chambers. *Combustion and Flame 159*(11), 3398–3413. *(p. 4, 24, 145, 152, 154, 163, 170, 223)*

Wolf, P., G. Staffelbach, A. Roux, L. Y. Gicquel, T. Poinsot, and V. Moureau (2009). Massively parallel LES of azimuthal thermo-acoustic instabilities in annular gas turbines. *CR Mécanique 337*(6-7), 385–394. *(p. 4, 190)*

Worth, N. and J. Dawson (2019). Characterisation of flame surface annihilation events in self excited interacting flames. *Combustion and Flame 199*, 338–351. *(p. 25, 223)*

Worth, N. A. and J. R. Dawson (2012). Cinematographic OH-PLIF measurements of two interacting turbulent premixed flames with and without acoustic forcing. *Combustion and Flame 159*(3), 1109–1126. *(p. 223)*

Worth, N. A. and J. R. Dawson (2013a). Modal dynamics of self-excited azimuthal instabilities in an annular combustion chamber. *Combustion and Flame 160*(11), 2476–2489. *(p. 4, 20, 25, 145, 152, 154, 155, 163, 166, 190, 223)*

Worth, N. A. and J. R. Dawson (2013b). Self-excited circumferential instabilities in a model annular gas turbine combustor: Global flame dynamics. *Procedings of the Combustion Institute 34*(2), 3127–3134. *(p. 2, 4, 145, 190)*

Xia, Y., D. Laera, W. P. Jones, and A. S. Morgans (2019). Numerical prediction of the flame describing function and thermoacoustic limit cycle for a pressurised gas turbine combustor. *Combustion Science and Technology 191*(5-6), 979–1002. *(p. 101)*

Yang, V. and W. Anderson (1995). *Liquid Rocket Engine Combustion Instability*. American Institute of Aeronautics and Astronautics. *(p. 57, 117)*

Yang, X. and A. Turan (2017). Simulation of liquid jet atomization coupled with forced perturbation. *Physics of Fluids 29*(2), 022103. *(p. 171)*

Yi, T. and D. A. Santavicca (2009). Flame spectra of a turbulent liquid-fueled swirl-stabilized lean-direct injection combustor. *Journal of Propulsion and Power 25*(5), 1058–1067. *(p. 42)*

Yu, K., K. Wilson, and K. Schadow (1998). Liquid-fueled active instability suppression. In *Symp. (Intl.) Comb.*, Volume 27, pp. 2039–2046. Elsevier. *(p. 189)*

Zhang, B., M. Shahsavari, Z. Rao, S. Yang, and B. Wang (2021). Thermoacoustic instability drivers and mode transitions in a lean premixed methane-air combustor at various swirl intensities. *Proceedings of the Combustion Institute 38*(4), 6115–6124. *(p. 146)*

Zhong, L., Y. Yang, T. Jin, Y. Xia, Y. Fang, Y. Zheng, and G. Wang (2021). Local flame and flow properties of propagating premixed turbulent flames during light-round process in a micca-type annular combustor. *Combustion and Flame 231*, 111494. *(p. 4)*

Zhu, M., A. Dowling, and K. Bray (1999). Combustion oscillations in burners with fuel spray atomisers. In *Turbo Expo: Power for Land, Sea, and Air*, Volume 78590, pp. V002T02A057. American Society of Mechanical Engineers. *(p. 171, 189)*

université PARIS-SACLAY | ÉCOLE DOCTORALE Sciences mécaniques et énergétiques, matériaux et géosciences (SMEMAG)

Titre: Etude des instabilités de combustion dans les foyers annulaires en considérant la dynamique des injecteurs et les fonctions descriptives des flamme déterminées dans des configurations simplifiées

Mots-clés: Instabilités de combustion, foyers annulaire, fonctions descriptives des flamme, injecteur swirlé, flamme de spray, dynamique des injecteurs

Résumé: Cette thèse aborde des questions centrales de la dynamique de la combustion des systèmes annulaires, en se concentrant essentiellement sur la compréhension, l'interprétation et la prédiction des instabilités de combustion couplées aux modes azimutaux. Ces modes sont les plus dangereux parmi ceux rencontrés dans les turbines à gaz et les moteurs d'avion car ils correspondent aux fréquences propres les plus basses où la combustion est la plus sensible aux perturbations auxquelles elle est soumise. Le travail considère spécifiquement le cas où les flammes établies dans la chambre de combustion sont formées par une atomisation du combustible liquide et sur les systèmes d'injection générant un écoulement «swirlé», en rotation idéalisant ceux des applications pratiques. Des expériences systématiques sont réalisées sur une chambre de combustion annulaire comportant des injecteurs multiples (MICCA-Spray), permettant un accès optique complet à la région de combustion et équipée de plusieurs microphones pour identifier le champ de pression. Ces expériences sont complétées par des mesures des fonctions descriptives de flamme (FDF) à l'aide d'une chambre de combustion à secteur unique (SICCA-Spray) et d'une autre installation comportant un réseau linéaire de trois injecteurs (TICCA-Spray) pour mieux représenter l'environnement de la flamme et les conditions aux limites correspondant à la configuration annulaire. Cette combinaison d'expériences permet d'explorer les effets de la géométrie d'injection et des paramètres de fonctionnement sur l'apparition d'instabilités de combustion. Les domaines d'instabilité sont documentés pour trois types de combustible (propane et air prémélangés, heptane et dodécane) et différentes valeurs de perte de charge d'injecteur et de nombre de swirl. De plus, les instabilités se révèlent également sensibles à la position de l'atomiseur par rapport à la sortie de l'injecteur. Plusieurs questions sont envisagées dans ce travail, dont la possibilité de représenter la réponse d'une flamme multidimensionnelle à l'aide d'une représentation par FDF et des méthodes permettant de déterminer convenablement les FDF pour la classe d'injecteurs utilisés, qui sont faiblement transparents aux ondes acoustiques. La comparaison entre les FDF mesurées dans le secteur unique et le réseau linéaire de trois injecteurs est réalisée pour révéler les limites des données obtenues dans le cas d'une flamme isolée dans la représentation de la dynamique de flammes entourées par d'autres flammes. L'interprétation des données basée sur la modélisation d'ordre réduit indique que beaucoup des caractéristiques observées expérimentalement peuvent être prédites en utilisant les FDF mesurées. Ceci nécessite cependant que les injecteurs swirlés soient convenablement représentés par une impédance d'injecteur et que le taux d'amortissement du système soit estimé. L'analyse souligne l'importance des paramètres de l'injecteur swirlé et des conditions d'injection sur l'apparition de l'instabilité de combustion et fournit des lignes directrices pour cerner leur influence.

Title: Investigation of combustion instabilities in annular combustors combining injector dynamics and flame describing functions determined in simplified configurations

Keywords: Combustion instability, annular combustors, flame describing function, swirling injector, spray flames, injector dynamics

Abstract: This thesis addresses some of the central issues in the combustion dynamics of annular systems, essentially focusing on understanding, interpreting, and predicting combustion instabilities coupled with azimuthal modes. These modes are the most detrimental among those encountered in gas turbines and aero-engines as they correspond to the lowest eigenfrequencies where the flame is most sensitive to incoming disturbances. The work specifically considers the case where the flames established in the combustor are formed by a spray of liquid fuel and on injection systems generating a swirling flow, idealizing those found in practical applications. Systematic experiments are carried out on a multiple-injector annular combustor (MICCA-Spray), allowing full optical access to the combustion region and equipped with multiple microphones for identifying the pressure field. These are complemented with measurements of flame describing functions (FDFs) using a single-sector combustor (SICCA-Spray) and another facility featuring an array of three injectors (TICCA-Spray) to better represent the flame environment and boundary conditions corresponding to the annular case. This combination of experiments is used to explore the effects of injection geometry and operating parameters on the occurrence of combustion instabilities. The domains of instability are documented for three fuel types (premixed propane and air, heptane and dodecane) and different values of injector head loss and swirl number. In addition, the instabilities are also found to be sensitive to the location of the atomizer with respect to the injector outlet. Several questions are considered in this work, including the possibility of representing the response of a multi-dimensional flame using the FDF framework and methods to suitably determine FDFs for the class of injectors used, which are weakly transparent to acoustic waves. The comparison between measured FDFs in the single sector and the linear array of three injectors is used to reveal the limitations of data corresponding to an isolated flame in representing the dynamics of flames surrounded by neighboring flames. The data interpretation based on low-order modeling indicates that many of the features observed experimentally can be predicted by making use of measured FDFs. This, however, requires that the swirling injectors be suitably represented by an injector impedance and that the damping rate be estimated. The analysis underlines the importance of the swirling injector parameters and injection conditions on the occurrence of combustion instability and provides guidelines in sorting out their influence.